

WA School of Mines, Mineral, Energy and
Chemical Engineering

School of Engineering
University of Aberdeen

Computational modelling of reactive processes in
lithium-metal batteries

Marcos Exequiel Arguello

This thesis is presented for the Degree of
Doctor of Philosophy
of
Curtin University of Technology
&
University of Aberdeen

November 2022

To the best of my knowledge and belief this thesis contains no material previously published by any other person except where due acknowledgement has been made. This thesis contains no material which has been accepted for the award of any other degree or diploma in any university.

Signature:

Marcos Exequiel Arguello

November 28, 2022

Acknowledgements

This project was carried out under the sponsorship of a Curtin International Postgraduate Research Scholarship (CIPRS) and the Aberdeen-Curtin Alliance PhD Scholarship. Their support during the time of this work is gratefully acknowledged.

Copyright statement

I have obtained permission from the copyright owners to use any third-party copyright material reproduced in the thesis (e.g. questionnaires, artwork, unpublished letters), or to use any of my own published work (e.g. journal articles) in which the copyright is held by another party (e.g. publisher, co-author).

Abstract

This Thesis presents a computational phase-field model to describe the electrodeposition process that forms dendrites within metal-anode batteries. We formulate, discretize, and solve the set of partial differential equations describing the coupled electrochemical interactions during a battery charge cycle using an open-source finite element library. The open-source library allows us to use parallel solvers and time-marching adaptivity.

The validity of the planar interface electrodeposition model is demonstrated through agreement between one-dimensional phase-field simulations and the theoretical sharp-interface Faradic reaction kinetics. Sensitivity analysis of changes in the phase-field interface thickness (0.5 to 10 μm) and under different applied voltages (-0.4 to -0.75 V), as well as spatial convergence analysis of mesh-induced errors, set the groundwork for two- and three-dimensional simulations of dendritic metal electrodeposition in batteries.

A set of two- and three-dimensional simulations, under different applied voltages (-0.45 to -1.5 V), are presented to validate the proposed formulation, showing their agreement with experimentally-observed lithium dendrite growth rates (0.03 to 0.4 $\mu m/s$), and morphologies reported in the literature. We simulate three-dimensional spike-like lithium structures that grow under high current density (fast battery charge); these structure's growth is dangerous for battery operation.

We study the three-dimensional distribution of the electric field and the lithium-ion concentration to understand the mechanism behind tip-growing lithium

morphologies better. Change of dendritic morphological behaviour is captured by a variation of the simulated inter-electrode distance (80 to 5000 μm). The analysis reveals that dendrite formation is connected to the competition between the lithium cation diffusion and electric migration, generating an uneven distribution of lithium ions on the electrode surface. This fact gives insight into strategies of dendrite suppression.

This work constitutes a relevant step towards physical-based, quantitative models to rationalize hazardous dendritic patterns needed to achieve the commercial realisation of lithium metal batteries.

Salient Points

- Planar electrode phase-field simulations in lithium-metal batteries
- Model verified by quantitative agreement with theoretical reaction kinetics
- Free energy formulation is favoured over grand canonical formulation
- Phase-field simulations of dendrite formation in lithium metal batteries
- Time-adaptive strategy produces energy stable results
- Analysis of 2D and 3D spike-like, symmetric, and highly-branched dendritic patterns
- Evaluation of modified lithium crystal surface anisotropy representation
- Analysis of 3D experimental-scale simulations
- Change of dendritic behaviour captured by variation of inter-electrode distance
- Simulations' consistency with experimental results reported in the literature

Contents

Acknowledgements	v
Copyright statement	vii
Abstract	ix
Salient Points	xi
Symbols	xvii
Abbreviations	xxi
1 Introduction	1
1.1 Background	1
1.2 Research problem	7
1.3 Objectives and significance	8
1.4 Thesis outline	9
2 Literature review	13
2.1 Experimental investigation of lithium dendrite formation	13
2.2 Computational models of dendrite formation	18
2.3 Phase-field models of dendrite growth	21

3	Methodology	29
3.1	Governing partial differential equations	29
3.1.1	Phase-field Butler-Volmer equation	31
3.1.2	Diffusion-migration	37
3.1.3	Electrostatic potential	41
3.1.4	Equations summary	42
3.2	Weak variational formulation and space-time discretization	44
3.2.1	Weak formulation	44
3.2.2	Time semi-discretization	44
3.2.3	Space discretization	47
3.3	Time-adaptive strategy	49
3.4	Implementation details	51
3.4.1	Numerical implementation	51
3.4.2	Phase-field diffuse interface thickness & mesh size: A dis- cussion	54
4	Phase-field simulations of planar interface electrodeposition in rechargeable lithium-metal batteries	57
4.1	System layout & properties	58
4.2	Spatial variation of variables	60
4.3	One-dimensional sensitivity analysis	63
4.3.1	Theoretical Faradic model	63
4.3.2	Applied overpotential	64
4.3.3	Phase-field interface thickness	65
4.4	Tafel plot: Sharp-interface Butler-Volmer	67
4.5	Convergence test	68

4.6	Conclusions on planar interface simulations	70
5	Phase-field simulations of dendrite formation in rechargeable lithium-metal batteries	73
5.1	System layout	74
5.2	Two-dimensional simulations of lithium dendrite formation	77
5.2.1	Lithium dendrite propagation rate: Consistency with experimental data	77
5.2.2	Bush-like lithium dendrite: Verification of 2D simulation results	81
5.3	Three-dimensional simulations of lithium dendrite formation	84
5.3.1	3D single nucleus simulation	84
5.3.2	3D multi-nuclei simulation	89
5.3.3	Phase-field interface thickness to mesh resolution ratio: A sensitivity analysis	96
6	Three-dimensional experimental-scale phase-field modelling of dendrite formation in rechargeable lithium-metal batteries	105
6.1	3D simulations using modified surface anisotropy	106
6.1.1	Surface anisotropy representation for phase-field electrodeposition models	106
6.1.2	Comparison of simulated patterns: Surface anisotropy model	108
6.1.3	Mesh orientation effect for different surface anisotropy representations	110
6.1.4	3D Orientation of lithium crystal: A surface anisotropy-based strategy	113

6.1.5	Mesh size effect for different surface anisotropy representations	114
6.2	Experimental-scale three-dimensional simulations of lithium dendrite formation	116
6.2.1	Meshing strategy for experimental-scale 3D simulations	117
6.2.2	Experimental-scale 3D simulations	120
7	Conclusions and research perspectives	133
7.1	Conclusions	133
7.2	Research outlook	141
	Appendices	145
	A Computational Framework	147
	B Copyright Information	169
	Bibliography	189

Symbols

Symbol	Description	Units
A^-	Anion species	$[-]$
a_i	Activity of species “i”	$[-]$
C_m^l	Site density electrolyte	$[mol/m^3]$
C_m^s	Site density electrode	$[mol/m^3]$
C_0	Bulk Li-ion concentration	$[mol/m^3]$
D^{eff}	Effective diffusivity	$[m^2/s]$
D^l	Diffusivity electrolyte	$[m^2/s]$
D^s	Diffusivity electrode	$[m^2/s]$
\vec{E}	Electric field vector	$[V/m]$
E_0	Energy density normalization constant	$[J/m^3]$
E^\ominus	Standard half-cell potential	$[V]$
F	Faraday constant	$[sA/mol]$
F_{mix}	Free energy of mixing	$[J]$
f_{ch}	Helmholtz free energy density	$[J/m^3]$
f_{grad}	Surface energy density	$[J/m^3]$
f_{elec}	Electrostatic energy density	$[J/m^3]$
$g(\xi)$	Double-well function	$[J/m^3]$
H	Dendrite height	$[m]$

Symbol	Description	Units
h	Mesh size	$[m]$
h_{\min}	Minimum mesh size	$[m]$
$h_p(\xi)$	Polynomial interpolation function	$[-]$
$h_s(\xi)$	Sigmoid interpolation function	$[-]$
h_0	Length normalization constant	$[m]$
i	Current density	$[A/m^2]$
\vec{i}	Current density vector	$[A/m^2]$
i_t	Theoretical current density	$[A/m^2]$
i_0	Exchange current density	$[A/m^2]$
\vec{J}	Flux of lithium species	$[mol/(m^2s)]$
\vec{J}_+	Flux of Li-ion species	$[mol/(m^2s)]$
L_η	Kinetic coefficient	$[1/s]$
L_σ	Interfacial mobility	$[m^3/(Js)]$
l_t	Phase-field interface position	$[m]$
l_x	Longitudinal battery cell size (x direction)	$[m]$
l_{x_u}	Region of interest	$[m]$
l_y	Lateral battery cell size (y direction)	$[m]$
l_z	Lateral battery cell size (z direction)	$[m]$
l_0	Anode initial thickness	$[m]$
M	Metal atom species	$[-]$
M^+	Cation species	$[-]$
n	Valence	$[-]$
R	Gas constant	$[J/(mol K)]$
\mathcal{R}	Phase-field interface thickness to mesh resolution ratio	$[-]$
T	Temperature	$[K]$
t	Time	$[s]$
t_0	Time normalization constant	$[s]$

Symbol	Description	Units
v	Lithium electrodeposition rate	$[m/s]$
W	Barrier height	$[J/m^3]$
α	Charge transfer coefficient	$[-]$
γ	Surface Energy	$[J/m^2]$
$\Delta\phi^{eq}$	Interfacial voltage at equilibrium	$[V]$
$\Delta\phi$	Electric potential difference	$[V]$
δ_{aniso}	Anisotropy strength	$[-]$
δ_{PF}	Phase-field diffuse interface thickness	$[m]$
δ_t	Computed phase-field interfacial thickness	$[m]$
ε	Relative error	$[\%]$
ϵ^l	Difference chemical potential “l” phase	$[J/mol]$
ϵ^s	Difference chemical potential “s” phase	$[J/mol]$
ζ	Li-metal concentration	$[mol/m^3]$
$\tilde{\zeta}$	Normalized Li-metal concentration	$[-]$
ζ_+	Li-ion concentration	$[mol/m^3]$
$\tilde{\zeta}_+$	Normalized Li-ion concentration	$[-]$
ζ_-	Anion concentration	$[mol/m^3]$
$\tilde{\zeta}_-$	Normalized anion concentration	$[-]$
η	Total overpotential	$[V]$
η_a	Activation overpotential	$[V]$
η_c	Concentration overpotential	$[V]$
κ	Gradient energy coefficient variable	$[J/m]$
κ_0	Gradient energy coefficient constant	$[J/m]$
λ	Electrodeposited film thickness	$[m]$
μ	Chemical potential	$[J/mol]$
μ_i^\ominus	Chemical potential specie “i” at ref. state	$[J/mol]$
$\tilde{\mu}$	Electrochemical potential	$[J/mol]$

Symbol	Description	Units
ξ	Phase-field order parameter	[–]
ρ_e	Charge density	[J/m^3V]
σ^{eff}	Effective conductivity	[S/m]
σ^l	Conductivity electrolyte	[S/m]
σ^s	Conductivity electrode	[S/m]
ϕ	Electric potential	[V]
ϕ_b	Charging voltage	[V]
χ	Susceptibility factor	[$mol^2/(J m^3)$]
Ψ	Gibbs free energy	[J]
Ω	Grand free energy functional	[J]
ω	Anisotropy mode	[–]

Abbreviations

Abbreviation	Meaning
ACR	Allen-Cahn reaction model
BC	Boundary Condition
BDF2	Second-order Backward Difference
BiCGStab	Biconjugate Gradient Stabilized Method
BV	Butler-Volmer
Cryo-STEM	Cryogenic Scanning Transmission Electron Microscopy
DFT	Density Functional Theory
EC-AFM	Electrochemical Atomic Force Microscopy
FEM	Finite Element Method
IC	Initial Condition
LIB	Lithium-ion Battery
LMB	Lithium-metal Battery
MD	Molecular Dynamics
MSM	Multiscale Model
NASM	Nonlinear Additive Schwarz Method
PDE	Partial Differential Equation
PF	Phase-field

Chapter 1

Introduction

This project is focused on the development of a computational framework to describe dendritic electrodeposition process within lithium-metal batteries. ¹

1.1 Background

Global energy demand continues to rise due to industrial activity and world's population expansion, with an average growth rate of about 1% to 2% per year since 2010 (pre-Covid19 pandemic levels) (IEA, 2021). The increasing consumption of non-renewable energy reserves, such as coal, gas, and oil (Smil, 2016), and awareness of climate change (IEA, 2022; Kumar, 2020), have triggered a steep growth in renewable energy sources (6% average annual growth worldwide over the past decade) (Hannah Ritchie and Rosado, 2020), along with an urgent need

¹Parts of the content of this Thesis are published in:

- Arguello, M. E., Gumulya, M., Derksen, J., Utikar, R., & Calo, V. M. (2022). Phase-field modeling of planar interface electrodeposition in lithium-metal batteries. *Journal of Energy Storage*, 50, 104627.
- Arguello, M. E., Labanda, N. A., Calo, V. M., Gumulya, M., Utikar, R., & Derksen, J. (2022). Dendrite formation in rechargeable lithium-metal batteries: Phase-field modeling using open-source finite element library. *Journal of Energy Storage*, 53, 104892.
- Arguello, M. E., Labanda, N. A., Calo, V. M., Gumulya, M., Utikar, R., & Derksen, J. (2022). Three-dimensional experimental-scale phase-field modelling of dendrite formation in rechargeable lithium-metal batteries. *Publication under review*.

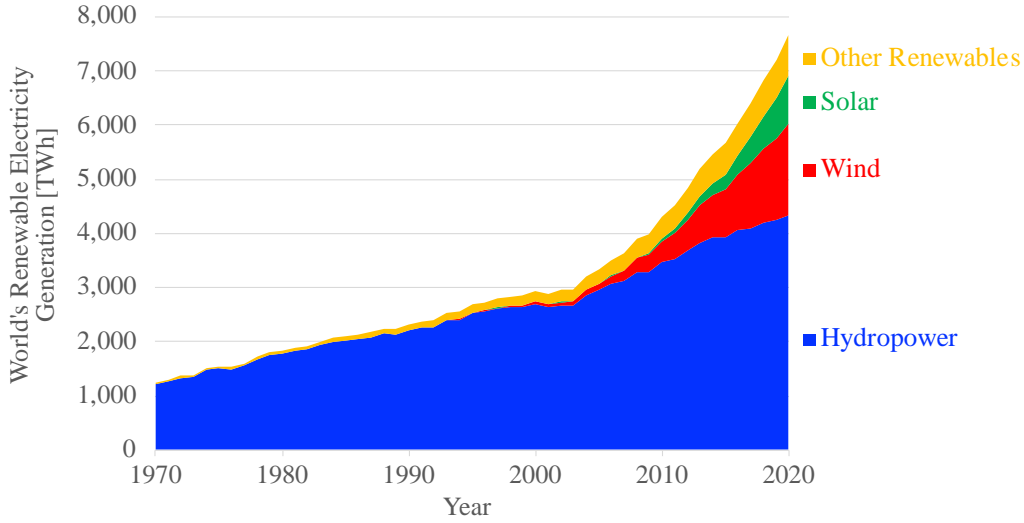


Figure 1.1: Plot of the development history of world’s renewable electricity generation (Hannah Ritchie and Rosado, 2020). ”Other renewable” refers to renewable sources including geothermal, biomass, waste, wave and tidal. Traditional biomass is not included.

for the development of improved energy storage systems (Pires et al., 2014) (see Figure 1.1). Globally, around one-quarter of our electricity comes from renewables, which includes hydropower, wind, solar, biomass, ocean energy, biofuel, geothermal (IEA, 2021).

Conventional lithium-ion batteries (LIB), based on intercalated graphite electrode, have dominated the rechargeable battery market since the late 1990s. However, these batteries are approaching their performance limit of about 300 Wh/kg (Xu et al., 2014; Fu et al., 2017). Novel chemistry and designs, such as metal anode batteries, are under active research to achieve a gravimetric energy density of 500 Wh/kg and manufacturing costs lower than \$100/kWh (Li and Lu, 2017). Despite enormous efforts, the highest gravimetric energy density achieved today remains below 400 Wh/kg, with an average growth rate of about 5% per year since 1970 (see Figure 1.2) (Winter et al., 2018).

Presently, metallic lithium (Li) is the most prominent anode material for pursuing high energy-density batteries, due to its superior theoretical gravimetric energy density (3862 mAh/g) and low reduction potential (-3.04 V vs. stan-

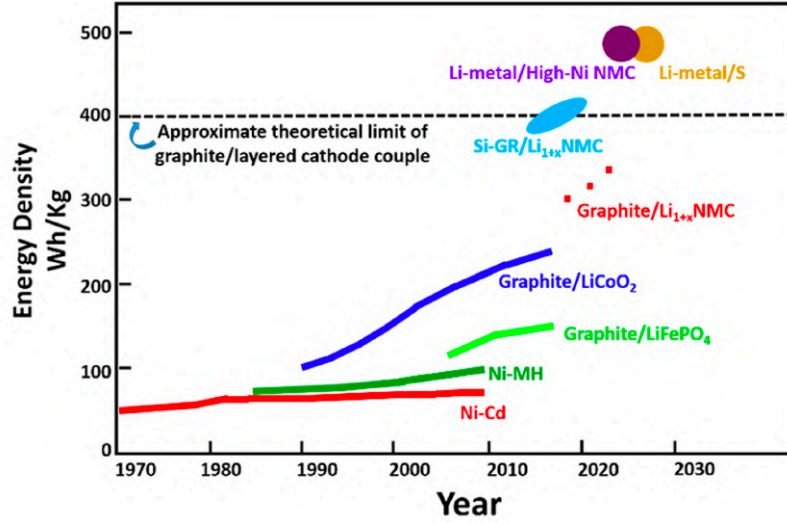


Figure 1.2: Diagram of the development history of batteries' gravimetric energy density (Winter et al., 2018). Reproduced with Journal's permission.

standard hydrogen electrode). Nonetheless, as the gravimetric energy density limitation (300 Wh/kg) of conventional lithium-ion batteries based on intercalated graphite anode cannot meet the current market demand, researchers are refocusing on lithium metal batteries (LMBs) (Zhang et al., 2020). Depending on the type of cathode materials, LMBs can be classified into three categories, namely: lithium-air batteries, lithium-sulfur batteries, and lithium-lithium intercalation compound batteries, all of them under active research (Wang et al., 2021). In LMBs, the anodic reaction consist of the dissolution (discharge) and deposition (charge) of the lithium metal on the electrode surface. Therefore, during battery charging process the Li-ions move across the electrolyte and are reduced on the anode surface by gaining electrons according to the following reaction: $\text{Li}^+ + e^- \rightarrow \text{Li}$. (see Section 3.1 for a detailed explanation on the reaction principles of the lithium electrodeposition process during battery charge).

Novel LMBs can achieve ultra-high energy densities (Figure 1.2) by avoiding the use of a graphite lattice to host Li^+ (intercalation process), as illustrated by the comparative schematic of Figure 1.3. The graphite material (host) drastically reduces the energy density of conventional Li-ion batteries, by adding extra weight to the battery-pack that does not participate in the electrochemical reaction.

Accounting for full battery-pack weight, the gravimetric energy density of LMBs is at least 440 Wh/kg (Winter et al., 2018; Lin et al., 2017).

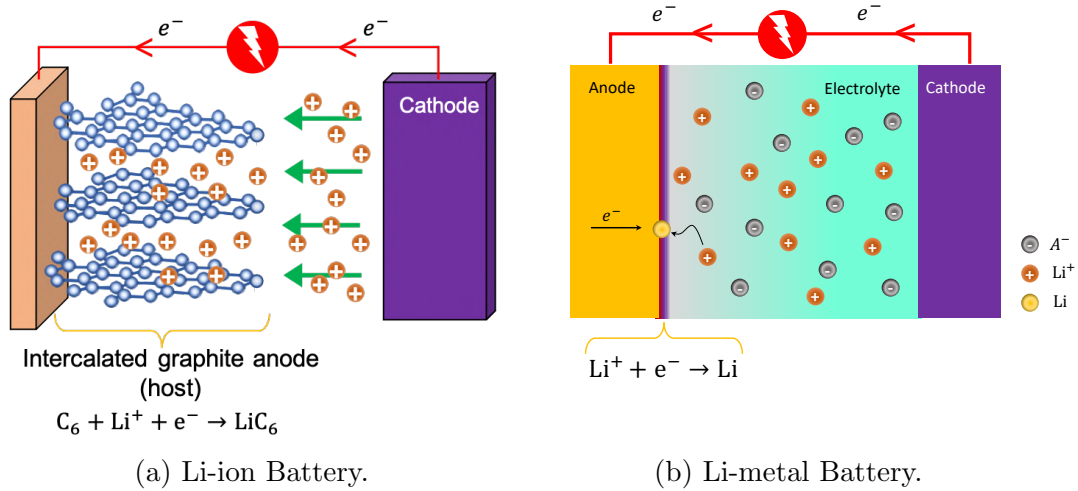


Figure 1.3: Comparative schematic of charging mechanism and anode’s structures between conventional Li-ion (a), and Li-metal (b) batteries. Grey, orange, and yellow spheres represent A^- anions, M^+ cations, and M atom, respectively.

Although lithium metal has been proposed as an attractive anode alternative in rechargeable batteries since early 1970s, its commercialization has been hindered due to several shortcomings. The greatest challenge to achieve the goal of commercial realisation of lithium-metal batteries is related to its stability and safety (Lin et al., 2017). Each of these issues are closely linked to the lithium anode problems, namely: dendrite formation due to the uneven deposition of lithium, dead lithium formed after dendrites breakage, anode corrosion due to highly negative redox potential leading to the formation of unstable solid electrolyte interphase (SEI), and volume expansion of the metal anode due to the loose structure of lithium dendrites, producing a disruption of battery interface and leading to the decay of the battery’s performance. It is widely accepted that the aforementioned mechanisms can interact causing a synergistic effect (Wang et al., 2021).

The formation of inert SEI on the surface of lithium deposits during the recharge cycle, caused by the high reactivity of Li with the electrolyte and subse-

quent continual consumption, resulting in low Coulombic efficiency (ratio of the total charge extracted from the battery to the total charge put into the battery over a full cycle). Due to the uneven deposition/dissolution of lithium metal, the SEI layer on the lithium surface is much less stable than in Li-ion batteries (Garche et al., 2013). The SEI layer breaks due to internal stresses during the operation of LMBs, and fresh lithium is exposed reacting with the electrolyte to form a new, uneven SEI (Dollé et al., 2002). Excess of Li, up to 300%, was used in the past for this issue (Xu et al., 2014).

Besides enhancing SEI formation, the unstable deposition of Li during the charge cycle, which often grows in a random and disordered way, leads to the formation of “dendrites” (Liu et al., 2018). This problem is compounded by the increase in the Li reactive area, which enlarges the SEI surface area (Bieker et al., 2015). Further, as Figure 1.4 illustrates, lithium dendrites can break due to internal stresses, disconnect from the anode, and SEI with poor electronic conductivity covers broken lithium. Thus, the broken lithium loses electrical connection with the anode generating “dead lithium” that do not participate in electrochemical reaction, resulting in further reduction in Coulombic efficiency (Adams et al., 2018; Wang et al., 2021). Coulombic efficiencies lower than 99.2% have been reported for lithium deposition/dissolution in non-aqueous electrolytes due to dendrite formation and dead lithium (Chen et al., 2019).

In the worst-case scenario, large dendrites can pierce the separator and contact the cathode leading to internal short-circuit and potential thermal runaway of the battery (Lu et al., 2015; Jiao et al., 2018). Rosso et al. (2006) reported a fuse effect of the first lithium dendrite reaching the opposite electrode, which melts due to high current density; before the major front of dendrites eventually connects the cathode and short-circuits the battery (producing an erratic potential).

In the case of solid-state batteries, lithium dendrites can also break under the compression of the electrolyte producing dead lithium compound, or cause dendritic cracking in solid electrolytes driven by lithium insertion (Klinsmann

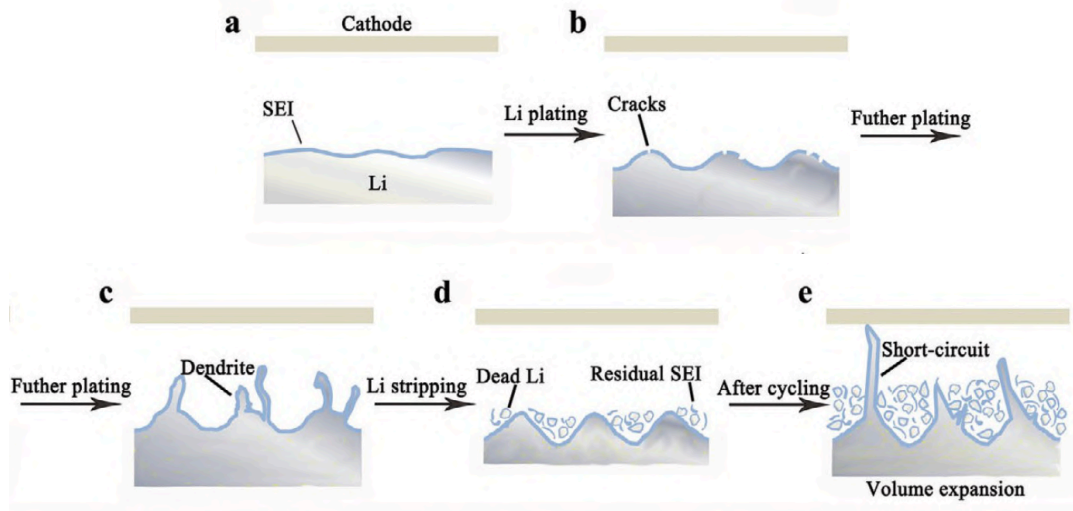


Figure 1.4: Schematic of lithium anode's failure process (Wang et al., 2021). Reproduced with Journal's permission.

et al., 2019). Furthermore, lithium dendrites are responsible for increasing the internal resistance of the battery due to interference mismatch and poor contact between the lithium anode and the solid electrolyte (Xu et al., 2018).

The critical shortcoming of dendrite formation during electrodeposition processes has triggered efforts on controlling the dendritic patterns and stabilizing the lithium anode to attain higher energy density rechargeable technologies, such as Li-air, Li-S, and Li-Li intercalation compound batteries (Bai et al., 2018; Bruce et al., 2012).

Different strategies for dendrite suppression have been proposed. Some of these strategies focus on the electrode (anode), including modifications in the electrode structure and porosity (Fan et al., 2018; Li et al., 2019; Zhang et al., 2018), electrode surface morphology (roughness and wavenumber) (Tikekar et al., 2014), and use of more stable interfacial coatings (Liu et al., 2017; Zhu et al., 2017). Other alternatives centre on the electrolyte, proposing different solvent and electrolyte composition (Sundström and Bark, 1995; Li et al., 2017; Zheng et al., 2017; Qian et al., 2015; Suo et al., 2013; Kim et al., 2018; Cheng et al., 2016), ionic mass transport and electrolyte management (Yang et al., 2005; Wang et al., 2019; Tan and Ryan, 2016; Crowther and West, 2008; Wlasenko et al., 2010;

Li et al., 2018; Iverson and Garimella, 2008; Parekh et al., 2020). Finally, some approaches address the battery operating conditions, such as implementation of pulsed charge-discharge cycle (Yang et al., 2014; Mayers et al., 2012; Aryanfar et al., 2014), controls of internal temperature and pressure (Gireaud et al., 2006; Akolkar, 2014; Yan et al., 2018).

Although the above strategies have shown a degree of effectiveness under certain operating conditions, the growth of Li dendrites is still observed at high current density (fast battery charge) (Steiger et al., 2015; Tang and Dillon, 2016; Zhu et al., 2019).

1.2 Research problem

Despite recent studies reporting successful operation of Lithium Metal Batteries (LMBs), they have reported short life cycle due to uneven and unstable deposition of lithium leading to the formation of dendrites, dead lithium, unstable SEI and volume expansion of lithium anode (Li et al., 2014; Liu et al., 2018).

Dendrite formation is the consequence of the uneven deposition of lithium, which can be associated to both thermodynamic and kinetic factors (Wang et al., 2021), such as the inhomogeneous distribution of Li-ion concentration and electric potential on the electrode surface. Furthermore, the morphology of the electrodeposited lithium is known to be influenced by different factors such as the magnitude and frequency of the applied current density, electrolyte concentration, temperature, pressure, ion transport and mechanical properties in the electrolyte (Frenck et al., 2019; Jana and García, 2017).

The investigation of lithium dendrite formation in rechargeable metal batteries becomes very challenging when based on experimental methods alone (Cheng et al., 2017). During the past decades, various computational models (thermodynamic and dynamic) have been developed to seek to understand better the fundamental mechanism of dendrite formation in metal anode batteries and guide the experiments (Liu et al., 2019; Jana and García, 2017; Tan et al., 2017).

The fundamental failure mechanism of lithium anode remains unclear and controversial (Wang et al., 2021). Due to the high reactivity of lithium, and lack of effective in-situ detection methods, it is difficult to study and characterize the lithium metal in native state, free from the influence of the SEI. Therefore, there is an urgent need for further investigation methods to characterize the behaviour of lithium anode and to guide experiments (Wang et al., 2021).

1.3 Objectives and significance

The following specific objectives will be pursued:

- Develop a computational model to describe reactive processes taking place within metal anode batteries, such as electrodeposition.
- Model verification with simulation results available in the literature and publicly available experimental data.
- Simulation of dendritic patterns to investigate the mechanisms dominating dendrite growth in rechargeable lithium-metal batteries and provide insight into strategies for dendrite’s suppression.

Controlling the morphology of the electrodeposited material is a serious challenge, which drastically affects the capacity, stability and safety of metal anode batteries under cycling. However, full theoretical comprehension of the lithium dendrite formation has not been developed owing to the complexity of the electrodeposition morphology. Therefore, developing a computational model to understand dendrite growth caused by electrodeposition has major technological significance for modern battery systems.

This work constitutes a step toward the physics-based, quantitative models to rationalize hazardous three-dimensional dendritic patterns needed to achieve the commercial realisation of Li-metal batteries. Herein, we use several computational efficiency improvements to deliver the 3D simulations at a reasonable cost,

such as time step adaptivity strategy, mesh rationalization, parallel computation, and balanced phase-field interface thickness to mesh resolution ratio. Moreover, the model results will ultimately lead to recommendations to improve lithium-metal battery long-term cyclability and energy efficiency (ratio of the total charge extracted from the battery to the total charge put into the battery over a full cycle).

Finally, beyond the metal electrodeposition in metal anode batteries, the computational framework developed in this project could be used to model other non-equilibrium systems in which the electrochemical reaction and charge mass transfer play important roles if involved time-dependent interfaces, such as electrochemical corrosion.

1.4 Thesis outline

The Thesis includes seven chapters presenting the relevant research work, developed method, modelling technique and simulation results to study the dendritic electrodeposition of lithium, in an effort to stabilize the lithium metal anode and optimize the battery performance.

Chapter 1: *Introduction*

This chapter introduces the background and research problem, followed by a description of the aims and significance of the research project.

Chapter 2: *Literature Review*

A comprehensive literature review is performed with focus on current research progress on lithium dendrite characterization, both experimental and computational. This review discusses existing computational models to describe reactive processes taking place within metal anode batteries. Different types of thermodynamic and dynamic models are presented, which are widely used to explore the mechanisms of lithium electrodeposition and dendrite suppression. Among these modelling strategies, phase-field method is discussed in detail, together with an analysis of its advantages, limitations, and reasons why this approach is selected

in this work.

Chapter 3: *Methodology*

This chapter covers a detailed description of the phase-field model used in this numerical study, along with underlying assumptions and parameters employed. I present the governing equations describing the electrodeposition process, boundary conditions as well as the numerical methods to solve them. I derive the weak variational statement and its numerical implementation. I describe the time-adaptive strategy and the parameters that deliver convergence and detail its implementation.

Chapter 4: *Phase-field Simulations of Planar Interface Electrodeposition in Rechargeable Lithium-metal Batteries*

In this chapter I simulate the coupled electrochemical interactions during a battery charge cycle using finite elements on open-source packages, allowing for parallel computation and time step adaptivity. A one-dimensional (planar interface) study compares the conventional free energy and grand canonical formulations. I investigate the effect of the applied overpotential (and the prediction's agreement with Faradic kinetics), as well as I analyze the prediction sensitivity to the phase-field interface thickness and mesh resolution. These simulation results set the groundwork for 2D and 3D simulations of dendritic metal electrodeposition in batteries.

Chapter 5: *Phase-field Simulations of Dendrite Formation in Rechargeable Lithium-metal Batteries*

This chapter discuss numerical simulations of lithium-anode battery dendrites growth. Firstly, a two-dimensional model is verified in terms of dendrite propagation rates and spatial distribution analysis of the system's variables in comparison with phase-field simulation results reported in the literature. Furthermore, I simulate three-dimensional spike-like lithium structures that grow under high current density (Ding, 2016; Tatsuma et al., 2001; Jana et al., 2019) (fast battery charge); these structure's growth is dangerous for battery operation. Single

and multiple nuclei numerical experiments are performed to study the 3D distribution of the electric field and the lithium-ion concentration to understand better the mechanism behind spike-growing lithium morphologies under short inter-electrode distance. Finally, a 3D sensitivity analysis of simulations under different mesh resolution and phase-field interface thickness is carried out.

Chapter 6: *Three-dimensional experimental-scale phase-field modelling of dendrite formation in rechargeable lithium-metal batteries*

This chapter addresses some of the shortcomings identified towards the goal of experimental scale simulations. Here, a modified surface anisotropy representation is introduced to the model. Firstly, numerical test are performed to gain insight into the benefits of this modification. Secondly, experimental-scale 3D simulations of lithium dendrite formation are carried using the modified anisotropy representation. Modification of lithium electrodeposition behaviour by increasing the inter-electrode distance are captured and discussed. Lithium dendrite propagation rates and morphologies obtained under different charging voltages are analysed.

Chapter 7: *Conclusions and research perspectives*

Conclusions are drawn based on the outcomes of the research project. Furthermore, I discuss the research perspectives, with potential developments and problems to be addressed in future work.

Chapter 2

Literature review

2.1 Experimental investigation of lithium dendrite formation

During the last decades, the research of electrochemical energy storage has developed rapidly, especially in rechargeable batteries (Wang et al., 2020). Investigation of dendrite formation in LMBs has been carried out by a combination of theory, experiment, and computation (Franco et al., 2019).¹

Extensive experimental investigation of microstructure evolution of lithium electrodeposit can be found in the literature (Steiger et al., 2015; Tang and Dillon, 2016; Ding, 2016; Zachman et al., 2018; Zhu et al., 2019; Zhang et al., 2020). The accurate high-resolution characterization of electrode-electrolyte interfaces is

¹Parts of the content of this chapter are published in:

- Arguello, M. E., Gumulya, M., Derksen, J., Utikar, R., & Calo, V. M. (2022). Phase-field modeling of planar interface electrodeposition in lithium-metal batteries. *Journal of Energy Storage*, 50, 104627.
- Arguello, M. E., Labanda, N. A., Calo, V. M., Gumulya, M., Utikar, R., & Derksen, J. (2022). Dendrite formation in rechargeable lithium-metal batteries: Phase-field modeling using open-source finite element library. *Journal of Energy Storage*, 53, 104892.
- Arguello, M. E., Labanda, N. A., Calo, V. M., Gumulya, M., Utikar, R., & Derksen, J. (2022). Three-dimensional experimental-scale phase-field modelling of dendrite formation in rechargeable lithium-metal batteries. *Publication under review*.

challenging owing the volatility of commonly used liquid electrolytes and the high chemical reactivity of lithium (Zachman et al., 2018). In-situ detection methods, such as optical microscopy (Steiger et al., 2015; Ding, 2016; Zhu et al., 2019), operando electrochemical atomic force microscopy (EC-AFM) (Tang and Dillon, 2016; Zhang et al., 2020) and cryo-scanning transmission electron microscopy (Cryo-STEM) (Zachman et al., 2018), have been recently used to map solid-liquid interfaces and dendrites in lithium-metal batteries. Figure 2.1a shows an illustration of symmetric lithium-metal coin cells used for the realisation of lithium dendrite experiments.

However, an important gap exists between practical lithium metal batteries and laboratory-grade batteries or coin-cells (Wang et al., 2021). For example, electrolyte consumption significantly reduces the cycling stability of Li metal anode batteries due to an increased resistance of ionic transmission; experimental coin cells instead have proportionally excess electrolyte (Li et al., 2020). Additionally, practical batteries have larger and more irregular reactive area, leading to faster failure of the lithium anode due to dendrite formation. It has been reported that, under identical test conditions, a practical pouch lithium metal battery can only achieve 10% to 33% of the lifespan of a coin cell (Yan et al., 2019). To achieve closer results to practical applications, some experimental studies have begun to use lean-electrolyte and practical pouch battery system in the test of lithium metal batteries (Wang et al., 2021).

In an effort to gain insight into the 3D morphology of lithium dendrite, Zachman et al. (2018) performed the reconstruction of the 3D dendrite microstructure from the cross sectional Cryo-STEM images as shown in Figure 2.1. Although, no spatial correlation was observed between the observed dendrites types, Cryo-STEM imaging revealed SEI layer on the type I dendrite (Figure 2.1b), approximately 300-500 nm thick, which was not present on the type II dendrite (Figure 2.1c).

Dendrite formation involves both, the nucleation process as well as the transi-

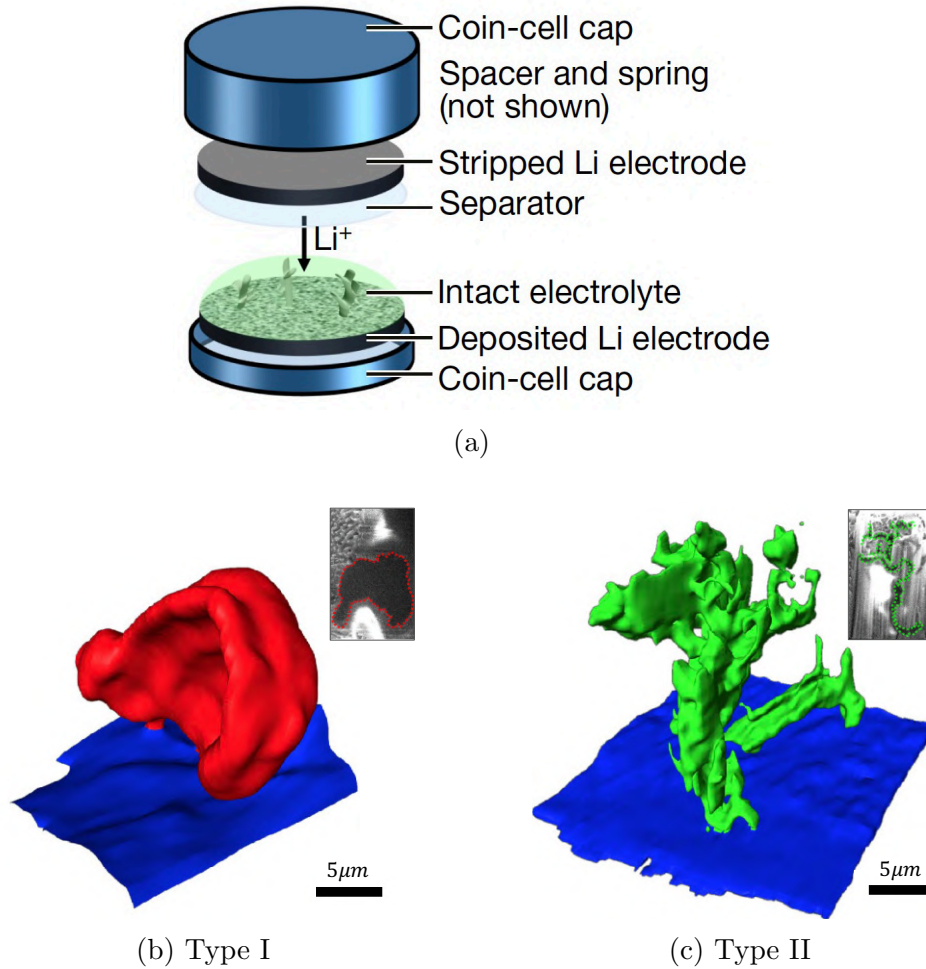


Figure 2.1: **a** illustrates a standard coin-cell arrangement used for the characterization of dendrite morphologies (Zachman et al., 2018). **b** and **c** correspond to three-dimensional reconstruction of two distinct experimental lithium dendrite morphologies, as performed by Zachman et al. (2018). The inset show the cross sectional Cryo-STEM imaging of the corresponding dendritic microstructures. Reproduced with Journal’s permission

tion to dendrite growth (Gao et al., 2020). Thus, the nucleation process define the dendrite’s location and number, which affects the battery capacity and lifespan. On the other hand, the dendrite growth process affects the breakage and formation of new SEI film, formation of dead Li compound, and battery short-circuit, leading to poor Coulombic efficiency and potential thermal runaway (Bieker et al., 2015; Adams et al., 2018; Chen et al., 2019).

Nishikawa et al. performed a series of experimental investigations of dendritic

electrodeposition of lithium as a function of the total charge (Nishikawa et al., 2010, 2011, 2012; Nishida et al., 2013). They reported dendrite growth rates between 0.01 and 0.55 [$\mu\text{m s}^{-1}$], for different current densities (0.1 – 10 [mA cm^{-2}]), electrolyte concentrations (0.5–1.5 M), and operating temperatures (–5–40°C); where larger current densities and higher temperatures produced faster propagation rates (Nishida et al., 2013). Furthermore, initiation periods for dendrite precursors to start to grow (become visible under optical microscope) were measured between 4 to 140 s (Nishida et al., 2013); where shorter times were obtained under larger applied current density.

The formation of dendrites in lithium anodes has been noted to vary considerably from one system to the other. Bai et al. (2016) noted the formation of mossy/whiskers-like morphologies at current densities lower than the intrinsic diffusion-limited current density (reaction limited regime, where lithium grows from the base). On the other hand, at higher current densities (greater than the diffusion-limited current density, i.e. transport or diffusion limited regime, where lithium grows from the tip), fractal dendritic morphology or finger-like structures are obtained. Transition from base-controlled mossy structure to tip-controlled dendrite growth was also observed experimentally when under limiting current condition. Further, various 2D numerical simulations have found the formation of spike-like or tree-like structures where dendrite growth was found to occur on multiple branches and in multiple directions. These types of formation, however, have not been observed widely experimentally due to instabilities at the branch structures and mass transfer rate limitations at these regions (Liu et al., 2019).

Jana and García (2017) expanded this observation and proposed 5 different regimes of lithium growth: thermodynamic suppression regime, incubation regime, tip-controlled growth regime, base-controlled growth regime, and mixed growth regime, based on various experimental observations over the years. While dendrite growth under tip-controlled regime (higher current densities) is highly influenced by local electrochemical gradients; on the other hand, irreversible me-

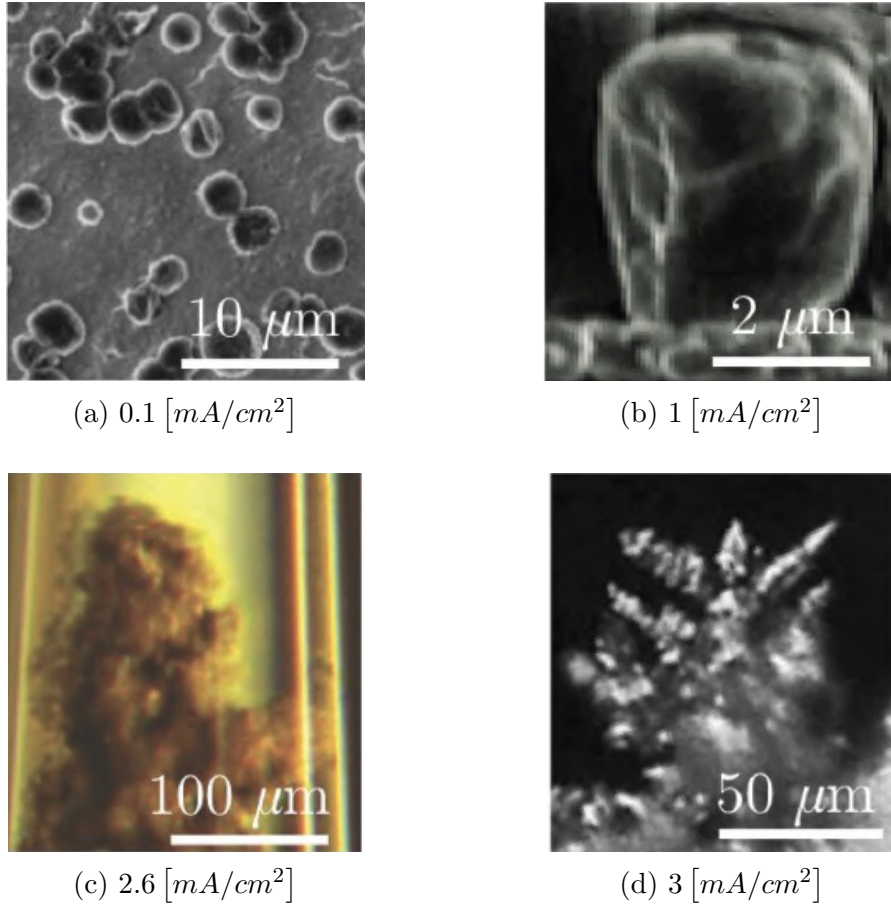


Figure 2.2: Photographs of experimental lithium electrodeposit microstructures demonstrates the effect of current density on dendrite morphology according to Jana et al. (2019). **a** corresponds to hemispherical lithium nuclei electrodeposited on top of a copper layer at $0.1 [mA/cm^2]$ for 1 hour, as performed by Pei et al. (2017). **b** corresponds to columnar growth of lithium on a copper substrate under a hollow carbon layer after 50 charge-discharge cycles at $1 [mA/cm^2]$, as shown by Zheng et al. (2014). **c** corresponds to mossy lithium electrodeposition on a copper substrate at $2.6 [mA/cm^2]$ for 0.5 hour in a liquid electrolyte column, as shown in experiments by Bai et al. (2016). **d** corresponds to branched/spike-like lithium dendrites electrodeposited on a lithium substrate from a gel-based electrolyte at $3 [mA/cm^2]$ for 1 hour, as performed by Tatsuma et al. (2001). Reproduced with Journal’s permission.

chanical deformation, such as, plastic deformation, can dominate dendrite growth under base-controlled regime (lower and battery-relevant current densities). Figure 2.2 presents a catalog of experimental lithium electrodeposit microstructures as classified by Jana et al. (2019), according to the effect of current density on

dendrite morphology.

In summary, experimental research has contributed significantly to a better understanding of the failure mechanisms of lithium anode batteries. Additionally, experimental outcomes on lithium dendrite characterization can guide the development and validation of computational models of dendrite formation. Among these findings we have the description of the parameters affecting dendrite formation (Frenck et al., 2019; Jana and García, 2017), classification of different regimes of lithium growth (Bai et al., 2016; Jana et al., 2019), identification of hazardous dendritic patterns, such as tree-like or spike-like lithium morphologies formed under fast battery charge (Tatsuma et al., 2001; Ding, 2016), and testing of different strategies of dendrite suppression (Li et al., 2021; Zhang and Qi, 2022). Furthermore, experimental data is valuable for model’s validation purpose, providing measurements of dendrite’s propagation rates under different electrodeposition conditions (Nishikawa et al., 2010, 2011, 2012; Nishida et al., 2013), and morphological characterization of dendrites’ shapes through volume-specific area and side branching analysis (Yufit et al., 2019).

2.2 Computational models of dendrite formation

The investigation of lithium dendrite formation in rechargeable metal batteries becomes very challenging when based on experimental methods alone (Cheng et al., 2017). Despite researchers’ efforts and current progress achieved in this field, experimental strategies suffer from its own limitations, namely, lack of effective in-situ detection methods to deal with the high reactivity of lithium (Wang et al., 2021), the gap between practical lithium metal batteries and laboratory-grade batteries or coin-cells (Yan et al., 2019; Li et al., 2020), and the higher cost and time consuming nature of experimental methods (Franco et al., 2019). Thus, experiments are combined with theoretical and computational investiga-

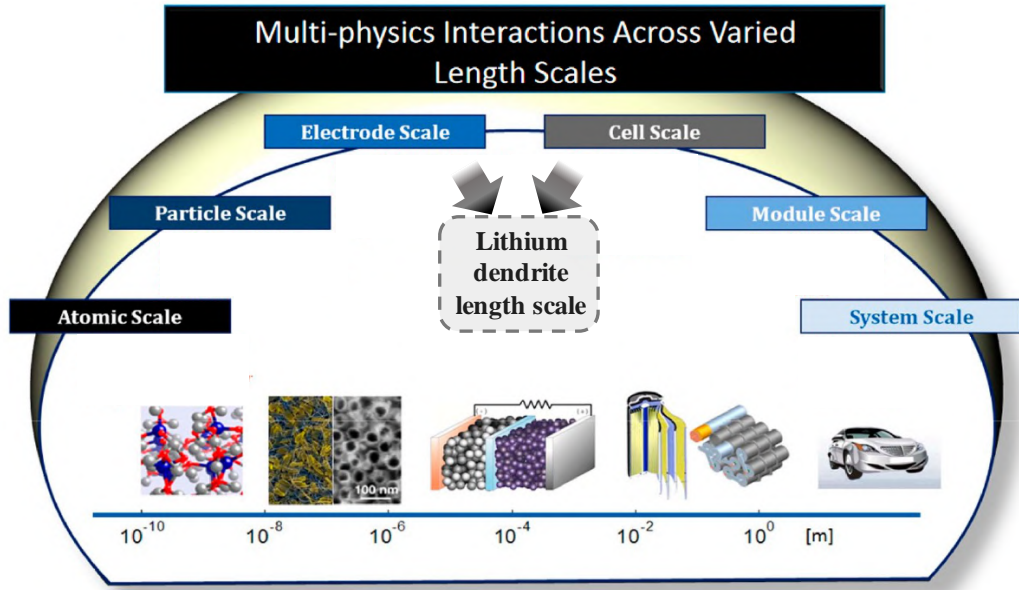


Figure 2.3: Schematic of length scale dependent physics impacting battery modelling (Abada et al., 2016). Reproduced with Journal’s permission.

tion, to reduce the research cost and accelerate the time-to-market of safe and high performance battery designs.

Recent improvements in battery models allow the description of processes such as electrochemical reactions, charge, mass, and heat transport, mechanical stresses, and electrode changes, at various time and length scales. Therefore, battery modelling may improve the available cells, their operation regimes and their constituent materials as well as forecast the performance properties of new cells (Franco et al., 2019). Typical battery models can be categorized as follows: electronic, atomistic, mesoscopic and continuum models. Figure 2.3 shows length-scale dependent physics affecting lithium battery simulation.

Various computational models seek to understand better the mechanisms of dendrite formation and growth in lithium anodes. Typically, we classify these models into two main groups: thermodynamic and dynamic (Liu et al., 2019; Jana and García, 2017; Tan et al., 2017). Since dendrite formation is a universal phenomenon in metal electrochemical deposition process (Li, Na, Zn, Cu, etc.), the first group focuses on the study of the intrinsic thermodynamic properties

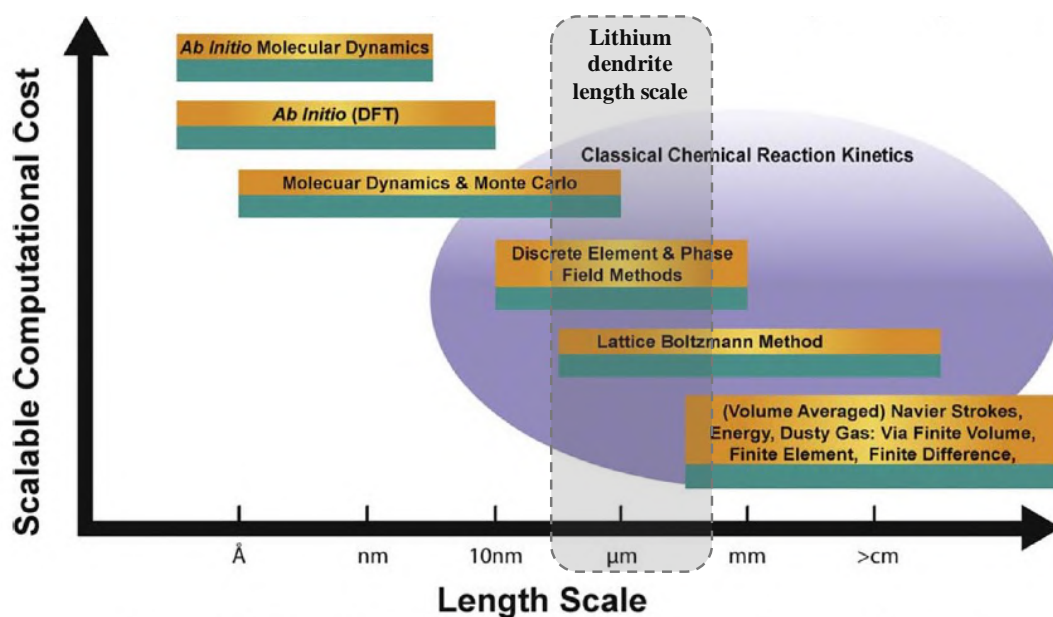


Figure 2.4: An overview of modelling techniques for battery-related applications (Grew and Chiu, 2012). Reproduced with Journal’s permission.

of the alkali metal anodes that lead to dendrite formation (Liu et al., 2019). The second group however, considers the influence of different electrochemical or environmental parameters affecting the deposition behaviour and dendrite growth in practical batteries, such as current density, electrolyte composition, operating temperature, as shown by experimental research (Frenck et al., 2019). Figure 2.4 compares the computational cost of these modelling techniques versus the typical length scales that they can solve.

Within the thermodynamic models, several surface nucleation models based on density functional theory (DFT) have been widely used to explore the mechanisms of lithium electrodeposition and dendrite suppression. Considering lithium dendrite growth as an inherent property of the metal, these models invoke surface energies and diffusion barriers as keys parameters in determining the specific metal structures growing on electrodes (Jäckle and Groß, 2014; Ling et al., 2012; Ozhabes et al., 2015).

On the other hand, various types of dynamic models have been used to describe the electrochemical propagation of dendrites; such as, space-charge (migration-

limited) models, proposing violation of electroneutrality (charge overcompensation) in the vicinity of dendrite tips that leads to high overpotentials and subsequent formation of ramified electrodeposits (Chazalviel, 1990). Furthermore, stress and inelastic deformation models have been developed to simulate dendrite’s surface-tension mitigated growth (Barton et al., 1962; Monroe and Newman, 2004). Additionally, film growth models, applying classical theory of film growth within lithium anode battery (Wang et al., 2016; Jiang et al., 2022), and diffusion-limited aggregation models (DLA), employing random-walk statistics to develop fractal shapes (Aryanfar et al., 2014), have also proven successful when applied at the condition of extremely low currents, and without considering surface energy.

Few attempts to simulate three-dimensional lithium dendrite growth can be found in the literature. For instance, Natsiavas et al. (2016) developed a 3D model of the growth of electrode–electrolyte interfaces in lithium batteries in the presence of an elastic prestress and used it for assessing the linearized stability of planar interface growth. Mu et al. (2020) performed parallel three-dimensional phase-field simulations of dendritic lithium evolution under different electrochemical states, including charging, suspending and discharging states (see Figure 2.5). Later, Jang and Yethiraj (2021) performed stochastic investigations of the three-dimensional effect of applied voltage and diffusion constant on the growth of lithium dendrites. Recently, Liu et al. (2021) presented a phase-field model to study the three-dimensional effect of exchange current density on electrodeposition behaviour of lithium metal, however, without focusing on dendritic morphologies.

2.3 Phase-field models of dendrite growth

Within the dynamic models, the phase-field method, based on classical chemical reaction kinetics, appears within the modelling techniques suitable for the study of mesoscale (μm) electro-kinetic phenomena, such as dendritic electrodeposition

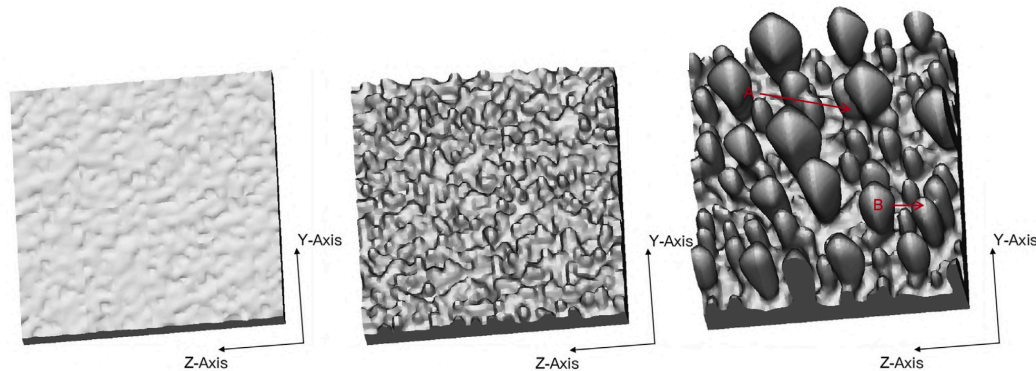


Figure 2.5: Three-dimensional simulation of dendritic evolution of lithium under an applied overpotential of $-0.3 [V]$, as performed by Mu et al. (2020). Reproduced with Journal’s permission.

of lithium, with a reasonable computational cost (see Figure 2.4). Phase-field (diffuse-interface) models can simulate the morphology evolution of Li electrodeposit due to reaction-driven phase transformation within metal anode batteries and rationalize morphology patterns of dendrites observed experimentally, under both low and high applied current densities (Guyer et al., 2004a,b; Shibuta et al., 2007; Okajima et al., 2010; Liang et al., 2012; Bazant, 2013; Liang and Chen, 2014; Ely et al., 2014; Zhang et al., 2014; Chen et al., 2015; Cogswell, 2015; Hong and Viswanathan, 2018; Yurkiv et al., 2018; Mu et al., 2019; Jana et al., 2019; Zhang et al., 2019; Guan et al., 2015, 2018; Liu and Guan, 2019; Gao and Guo, 2020; Mu et al., 2020; Chen and Pao, 2021; Zhang et al., 2021; Liu et al., 2021; Qiao et al., 2022). The vast amount of simulation work available is evidence of the effectiveness of the phase-field method for the investigation of lithium dendrite formation in rechargeable metal batteries.

The phase-field model tracks boundaries and interfaces implicitly using an auxiliary function (the phase-field order parameter, commonly identified with the Greek letter ξ , see Figure 2.6), avoiding the need for large mesh displacements with moving boundary conditions. The evolution of the phase-field variables satisfies local equilibrium (de Groot and Mazur, 1984) and free energy minimization (Steinbach et al., 1996), leading to nonlinear partial differential equations

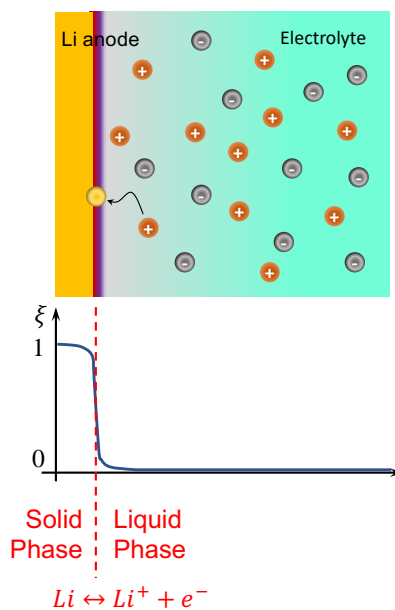


Figure 2.6: Illustration of a planar interface electrodeposition of lithium (solid) from a binary electrolyte (liquid). Continuous phase-field variable ξ tracks the evolution solid-liquid interface. Grey, orange, and yellow spheres represent A^- anions, M^+ cations, and M atom, respectively

(PDE's). These models incorporate interfacial energy, interface kinetics, and curvature-driven phase boundary movement. Another advantage is that it can simulate length scales comparable to the state-of-art characterization tools, such as scanning electron microscope (SEM) and transmission electron microscope (TEM), enabling direct comparison between experimental observations and simulation predictions (Hong and Viswanathan, 2020).

Different phase-field models of electrochemical systems describe the phase-field evolution by the Cahn-Hilliard equation (García et al., 2004; Han et al., 2004), the classical Allen-Cahn equation (Allen and Cahn, 1972), or a modified non-linear Allen-Cahn reaction model (Bazant, 2013). Thus, while some of these models assume linear kinetics (Guyer et al., 2004a,b; Shibuta et al., 2007; Ely et al., 2014), only applicable in the limit of minor deviations from equilibrium (current densities below the limiting current), others describe the nonlinear relation between the phase transformation rate and the thermodynamic driving force, following either Butler–Volmer (Okajima et al., 2010; Liang et al., 2012;

Bazant, 2013; Liang and Chen, 2014; Chen et al., 2015) or Marcus reaction kinetics (Cogswell, 2015).

In general, phase-field models of electrochemical systems combine a set of three different fields (variables) to simulate the metal electrodeposition process in rechargeable batteries, namely, the phase-field order parameter (solid-liquid phases), the concentration of metal-ions and the electrostatic potential (Guyer et al., 2004a,b; Shibuta et al., 2007; Bazant, 2013; Okajima et al., 2010; Liang et al., 2012; Ely et al., 2014; Zhang et al., 2014; Chen et al., 2015; Mu et al., 2020; Chen and Pao, 2021; Liu et al., 2021). Furthermore, while the derivation of the aforementioned models uses a free energy functional (Gibbs free energy), other models also adopt the grand canonical formulation (Plapp, 2011), exchanging concentration of metal-ion for chemical potential as the natural variable, to achieve better numerical stability at low concentration values (Cogswell, 2015; Hong and Viswanathan, 2018).

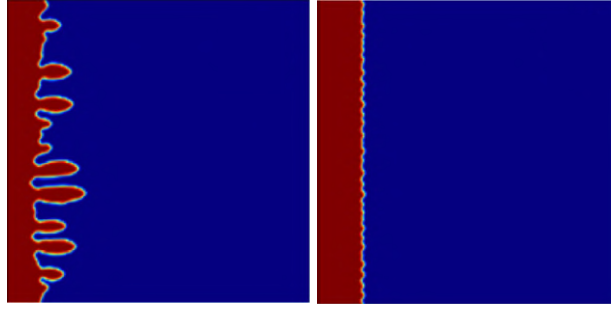
Recent works have coupled the phase-field model with an additional field to gain insight into a particular aspect of dendrite formation, such as heat transfer model to simulate the thermal effect during the lithium dendrite growth process (Yan et al., 2018; Qiao et al., 2022), flow field (forced advection) to study the effect of electrolyte hydrodynamics on the dendrite morphology in flow batteries (Wang et al., 2019), and electrochemical-mechanical phase-field models to explore the role of stress in lithium dendrites, such as the hydrostatic stress of lithium metal and residual stress in the SEI (Yurkiv et al., 2018; Liu and Guan, 2019; Jana et al., 2019; Zhang et al., 2021).

Typically, the charging conditions for a lithium battery either fix the applied electric potential or the charging current density. Different sets of boundary conditions (BC's) can represent each charging state through different electrodeposition models. In practice, Dirichlet BCs can effectively represent fixed electric potential charging state (Shibuta et al., 2007; Okajima et al., 2010; Liang and Chen, 2014; Zhang et al., 2014); in contrast, Neuman BCs at the lithium

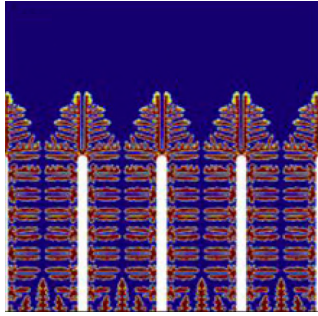
cation concentration (electrolyte side) represent fixed charging current density state (Chen et al., 2015; Cogswell, 2015; Yurkiv et al., 2018; Mu et al., 2019; Liu et al., 2021).

Another important feature of this problem is set by the way in which the initial perturbation (dendrite nuclei) is introduced in the simulation (initial condition); some models included initial seeds (artificial deformation imposed on the electrode surface) combined with surface anisotropy to propagate the dendrite shape (Okajima et al., 2010; Liang and Chen, 2014; Jana and García, 2017); alternatively other models combine surface anisotropy with Langevin noise at the phase-field interface, generating a random nucleation pattern (Cogswell, 2015; Yurkiv et al., 2018; Mu et al., 2019; de Groot and Mazur, 1984; Mu et al., 2020). It has been observed that either the shape of the initial seed as well as the noise level utilized can have a major effect on the simulated dendritic morphology (Chen et al., 2015; Yurkiv et al., 2018; Gao and Guo, 2020).

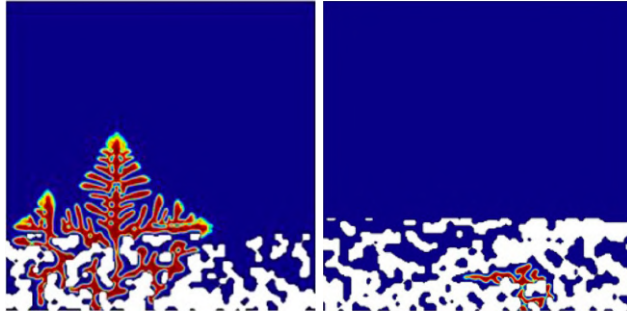
Although there has been a great advance in phase-field modelling of lithium dendrites in recent years, there are still several issues related to the evolution of dendritic patterns in lithium metal electrodes that continue unresolved (Chen and Pao, 2021). A significant effort seeks to develop two-dimensional models to rationalize three-dimensional dendritic patterns observed experimentally qualitatively. Furthermore, various strategies to suppress Li dendrites' growth and weaken the side reactions exist. Some of these strategies address the battery operating conditions, including pulse charging lithium dendrite suppression (Qiao et al., 2022) (Figure 2.7a), and control of internal temperature (Yan et al., 2018). Other alternatives focus on the electrode (anode), such as modelling of 3D conductive structured lithium metal anode (Zhang et al., 2019, 2022) (Figure 2.7b), and low porosity and stable SEI structure (Mu et al., 2019) (Figure 2.7c). Finally, other approaches centre on the electrolyte management and separator design, proposing a compositionally graded electrolyte (Hong and Viswanathan, 2018), dendrite suppression using flow field (forced advection) (Wang et al., 2019), study of sepa-



(a)



(b)



(c)

Figure 2.7: Examples of two-dimensional phase-field simulation of lithium dendrite suppression strategies. **a** corresponds to pulse charging lithium dendrite suppression, as performed by Qiao et al. (2022). Dendritic morphologies formed under pulse frequencies, $t_{ON} = 5$ ms, and $t_{OFF}/t_{ON} = 0.5$ (left), & $t_{ON} = 5$ ms, and $t_{OFF}/t_{ON} = 4$ (right), respectively; where an overpotential equal to -0.1 V is applied during the period of t_{ON} and 0 V during the period of t_{OFF} . **b** corresponds to dendritic morphologies after lithium electrodeposition in structured lithium metal anode with channel width equal to $50\mu m$, as performed by Zhang et al. (2019). **c** corresponds to lithium dendrite simulation through geometrically reconstructed porous SEI, as performed by Mu et al. (2019). Lithium dendrites are partially suppressed by low porosity and highly stable SEI structure. Reproduced with Journal's permission.

rator pore size inhibition effect on lithium dendrite (Li et al., 2022), etc. However, clarifying the numerical features behind phase-field models has attracted less interest.

Given the inherent three-dimensional nature of lithium dendrite morphologies (Jana et al., 2019; Ding, 2016; Tatsuma et al., 2001), it is critical the development of phase-field models that enable the study and understanding of the three-dimensional effects triggering the formation these patterns. This includes the exploration of differences between 2D and 3D simulations, such as free space effect on Li-ion diffusion to anode surface, surface anisotropy, electric field distribution, nuclei distribution and interaction between neighbouring dendrites; as well as assessing novel strategies to control lithium dendrite formation (e.g., 3D porous current collectors hosts with lithiophilic sites) (Yang et al., 2015; Zhang et al., 2019; Xu et al., 2021).

There is an urgent need for the development of fast numerical algorithms required to handle the phase field equations and perform efficient simulations. Currently, the vast majority of the phase-field works available in the literature use in-house codes or commercial software, such as widely used COMSOL Multiphysics (Multiphysics, 2022), offering user-friendly platforms, built-in CAD tools and combining different types of physics (Chen and Pao, 2021; Wang et al., 2015; Yan et al., 2018; Wang et al., 2019; Mu et al., 2019). However, there is a risk that commercial software can hinder the widespread use of the of phase-field simulations while also creating issues with data reproducibility and lack of flexibility (Hong and Viswanathan, 2020).

Open-source software arises as an attractive and powerful alternative to commercial software. Open-source is a decentralized way of developing software packages that embrace collaborations among a large number of developers, which is essential to the development of a diverse, inclusive modelling community (Powell and Arroyave, 2008). Among open-source software packages that have integrated phase-field capabilities we can mention FEniCS Project (Alnæs et al., 2015),

MOOSE (Lindsay et al., 2022), PRISMS-PF (DeWitt et al., 2020), SymPhas (Silber and Karttunen, 2022), FiPy (Wheeler et al., 2005), OpenPhase (Tegeler et al., 2017) and Sfepy (Cimrman et al., 2019). These software use either C++ or Python as their core programming language, and most of them make use of their own open-source finite differences, finite volumes, or finite elements tools. Reaching tens of thousands of commits, FEniCS and MOOSE are the most active open source phase-field open-source software to date (Hong and Viswanathan, 2020).

In conclusion, this review allows a overview understanding of existing computational models to describe reactive processes taking place within metal anode batteries, such as lithium dendrite formation. Among these modelling techniques, phase-field method was discussed in detail and regarded as the most suitable and cost-effective approach to simulate lithium dendrite growth in this work. The scarcity of three-dimensional phase field results observed in this review (Mu et al., 2020; Liu et al., 2021), is evidence of the large computational cost involved in solving the highly non-linear set of equations (PDE's) describing coupled electrochemical interactions during a battery charge cycle. This analysis guides our research focus, toward the development of a 3D phase field framework to describe hazardous three dimensional dendritic patterns needed to achieve the commercial realisation of Li-metal batteries.

Chapter 3

Methodology

3.1 Governing partial differential equations

This chapter ¹ presents the modelling of battery cells, composed of a solid metal anode made up of lithium, and a binary liquid electrolyte. The variables of interest are ζ , representing the concentration of lithium, and ϕ representing the electric potential. When an electro potential difference $\Delta\phi$, different than the equilibrium value $\Delta\phi^{eq}$, is imposed to the system (i.e. charging the battery), the binary electrolyte dissociates in M^+ cation and A^- anion species, being transported to the negative (anode) and positive (cathode) electrodes, respectively; developing an ionic concentration gradient (Xu et al., 2014). The overpotential η is described as,

$$\eta = \Delta\phi - \Delta\phi^{eq} , \quad (3.1)$$

¹Parts of the content of this chapter are published in:

- Arguello, M. E., Gumulya, M., Derksen, J., Utikar, R., & Calo, V. M. (2022). Phase-field modeling of planar interface electrodeposition in lithium-metal batteries. *Journal of Energy Storage*, 50, 104627.
- Arguello, M. E., Labanda, N. A., Calo, V. M., Gumulya, M., Utikar, R., & Derksen, J. (2022). Dendrite formation in rechargeable lithium-metal batteries: Phase-field modeling using open-source finite element library. *Journal of Energy Storage*, 53, 104892.

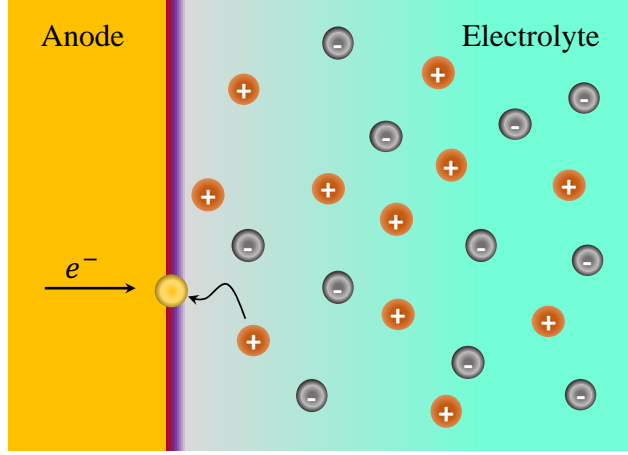


Figure 3.1: Schematic of lithium electrodeposition process. Grey, orange, and yellow spheres represent A^- anions, M^+ cations, and M atom, respectively.

where $\Delta\phi^{eq}$ is the electrode-electrolyte interfacial voltage at equilibrium, when the electrode electrochemical potential equals to that of the electrolyte, $\bar{\mu}_{\text{electrode}} = \bar{\mu}_{\text{electrolyte}}$ as determined via the Nernst equation (Bazant, 2013),

$$\Delta\phi^{eq} = E^\ominus + \frac{RT}{nF} \ln \frac{a_{M^{n+}} a_e^n}{a_M}, \quad (3.2)$$

where E^\ominus is the standard half-cell potential, $a_{M^{n+}}$ is the activity of M^+ ion in the electrolyte, a_e^n the activity of the electrons, and a_M the activity of the lithium atom. Furthermore, R, T, n , and F represent the gas constant, temperature, valence, and Faraday's constant, respectively. Thus, the total overpotential (3.1), can be explained as the sum of the activation $\eta_a = \Delta\phi - E^\ominus$, and the concentration $\eta_c = -\frac{RT}{nF} \ln \frac{a_{M^{n+}} a_e^n}{a_M}$.

As a result of the applied overpotential, Faradic reactions occurs, current passes through the electrode-electrolyte interface, a Li^+ cation gains an electron and deposits on the anode surface ($Li^+ + e^- \rightarrow Li$), as Figure 3.1 sketches.

The physical processes involved in the electrochemical deposition of lithium are charge and mass transport, where Butler-Volmer kinetics is the standard phenomenological model assumed to govern the charge and mass transport at the electrode-electrolyte interface (Vetter, 1967; Bard and Faulkner, 2001), also

known as the current-overpotential equation:

$$i = i_0 \left(e^{-\frac{\alpha n F \eta}{RT}} - e^{\frac{(1-\alpha) n F \eta}{RT}} \right), \quad (3.3)$$

where i is the current density and i_0 is the exchange current density (assumed constant in this case). The latter parameter is an indicator of the electron-transfer activity on the electrode surface at the equilibrium potential and has been identified as an intrinsic kinetic parameter (Liu et al., 2021). The first and second terms in brackets represent the oxidation and reduction reactions, respectively, where α is the charge transfer coefficient that characterizes the symmetry of the forward and reverse reactions (Kuznetsov and Ulstrup, 1999).

The lithium electrodeposition rate depends on the applied overpotential via a Faradic reaction (Nishikawa et al., 2011),

$$v = \frac{\partial \lambda}{\partial t} = \frac{i}{FnC_m^s} = \frac{i_0}{FnC_m^s} \left(e^{-\frac{\alpha n F \eta}{RT}} - e^{\frac{(1-\alpha) n F \eta}{RT}} \right), \quad (3.4)$$

where λ represents the electrodeposited film thickness over a time t . C_m^s represents the site density of lithium metal. The superscripts “s” and “l” are used to represent the solid-electrode and the liquid-electrolyte phases, respectively. At the mesoscale, the electrode phase is assumed as a pure solid (neglecting any solid phase nanoporosity). Furthermore, this model neglects the presence of a solid-electrolyte interface (SEI), thus neither species nor charge can be stored at the electrode-electrolyte interface.

3.1.1 Phase-field Butler-Volmer equation

Assuming a dilute electrolyte solution, the activity of lithium ions equals its concentration $a_{M^{n+}} = \tilde{\zeta}_+$, whereby electrons are assumed to always be supplied on the surface of the electrode, with an activity equal to unity $a_e = 1$ (Chen et al., 2015), then the electrode-electrolyte interfacial voltage at equilibrium (3.2)

becomes

$$\Delta\phi^{eq} = E^\ominus + \frac{RT}{nF} \ln \frac{\tilde{\zeta}_+}{a_M} . \quad (3.5)$$

The activity of M-atom a_M can be defined variationally by $a_i = e^{\frac{1}{RT} \frac{\delta F_{\text{mix}}}{\delta \zeta_i}}$, in terms of the free energy of mixing F_{mix} , where ζ_i represents the chemical species concentrations (e.g., lithium metal atom ζ , lithium cation ζ_+ , and anion ζ_- , respectively).

First, the Gibbs free energy of the system is computed as the summation of the Helmholtz free energy density f_{ch} , surface energy density f_{grad} , and electrostatic energy density f_{elec} (Guyer et al., 2004b; García et al., 2004; Han et al., 2004)

$$\Psi = \int_V [f_{\text{ch}}(\zeta_i) + f_{\text{grad}}(\nabla\zeta_i) + f_{\text{elec}}(\zeta_i, \phi)] dV , \quad (3.6)$$

The gradient energy density associated with the surface energy of the system is characterised as $f_{\text{grad}} = \frac{1}{2} \nabla\zeta_i \cdot \kappa(\zeta_i) \nabla\zeta_i$, and $f_{\text{elec}} = \rho_e \phi$ is the electrostatic energy density, where $\rho_e = \sum_i n_i F \zeta_i$ is the charge density. The Helmholtz free energy density is (Bazant, 2013; Chen et al., 2015),

$$f_{\text{ch}} = W\tilde{\zeta}^2 (1 - \tilde{\zeta})^2 + C_0 RT (\tilde{\zeta}_+ \ln \tilde{\zeta}_+ + \tilde{\zeta}_- \ln \tilde{\zeta}_-) + \sum_i \zeta_i \mu_i^\ominus , \quad (3.7)$$

with ζ being normalised against the site density of Lithium metal (C_m^s , inverse of molar volume), $\tilde{\zeta} = \zeta/C_m^s$, and ion concentrations, $\tilde{\zeta}_+ = \zeta_+/C_0$ and $\tilde{\zeta}_- = \zeta_-/C_0$, being normalised against the initial bulk concentration of Lithium in the electrolyte $C_0 = c_0 C_m^l$, where c_0 is the initial bulk Lithium molar ratio in the electrolyte, and C_m^l is the site density of the electrolyte phase.

The Helmholtz free energy density in (3.7), shows the contributions of the two equilibrium states (solid electrode and liquid electrolyte), the contribution of the lithium ions, and the summation of chemical potentials for each species at a reference state (μ_i^\ominus). For the equilibrium states, an arbitrary double-well function $g(\tilde{\zeta}) = W\tilde{\zeta}^2 (1 - \tilde{\zeta})^2$ is used, with $W/16$ representing the barrier height between

the two states.

The continuous phase-field variable ξ represents the dimensionless concentration of lithium atom $\tilde{\zeta}$, where $\xi = 1$ and 0 represent the pure electrode and electrolyte phases, respectively; ξ is a non-conserved order parameter in our model (Liang and Chen, 2014). Since the free energy has two local equilibria $\tilde{\zeta}_A$ and $\tilde{\zeta}_B$, then $\xi = \frac{\tilde{\zeta} - \tilde{\zeta}_A}{\tilde{\zeta}_A - \tilde{\zeta}_B}$ is the phase field with minima at $\xi = 1$ and $\xi = 0$, satisfying the Allen-Cahn reaction (ACR) model: $\frac{\partial \xi}{\partial t} = \mathcal{R} \left(\frac{\delta \Psi}{\delta \zeta_i} \right)$, a nonlinear generalization of the Allen-Cahn equation for chemical kinetics.

We express, in terms of ξ , the free energy of mixing F_{mix} relative to the standard state as (Bazant, 2013):

$$F_{\text{mix}} = f_{\text{ch}} + f_{\text{grad}} - \sum_i \zeta_i \mu_i^\ominus = W \xi^2 (1 - \xi)^2 + C_0 RT \left(\tilde{\zeta}_+ \ln \tilde{\zeta}_+ + \tilde{\zeta}_- \ln \tilde{\zeta}_- \right) + \frac{1}{2} \kappa(\xi) (\nabla \xi)^2 . \quad (3.8)$$

The surface energy anisotropy plays an important role in the morphology of the electrodeposit (Cogswell, 2015), which we implement using a standard approach (Kobayashi, 1993; Zhang et al., 2014) with $\kappa(\xi) = \kappa_0 [1 + \delta_{\text{aniso}} \cos(\omega\theta)]$, where κ_0 relates to the Lithium surface tension γ ; δ_{aniso} and ω , are the strength and mode of anisotropy, respectively (Tran et al., 2019; Zheng et al., 2020). θ is the angle between the surface normal and the crystallographic orientation of the lithium dendrite; aligned with the “ x ” direction of the cell stack for simplicity, as Figure 3.2 shows. We use four-fold anisotropy ($\omega = 4$) in agreement with lithium body centred cubic crystal structure Cogswell (2015). We make use of trigonometric identities to arrive to $\cos(4\theta) = 8n_1^4 - 8n_1^2 + 1$, where $n_1 = \nabla_x \xi / \|\nabla \xi\|$. Therefore, the 2D gradient coefficient is,

$$\kappa(\xi) = \kappa_0 [1 + \delta_{\text{aniso}} (8n_1^4 - 8n_1^2 + 1)] . \quad (3.9)$$

Figure 3.2 sketches (3.9), showing its preferred growth directions of a lithium electrodeposit ($\theta = 0^\circ, 90^\circ, 270^\circ$) due to four-fold surface energy anisotropy, tending to grow fractal or branched dendrites. In 3D, we use version of (3.9)

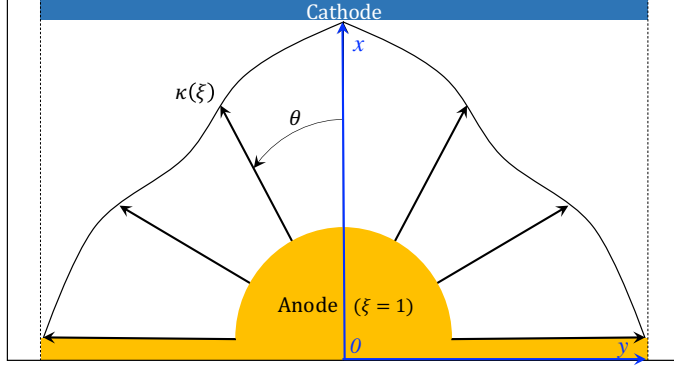


Figure 3.2: 2D schematic of Lithium electrodeposit, with four-fold surface energy anisotropy $\kappa(\xi)$ as a function of θ , defined as the angle between the surface normal and the crystallographic orientation “ x ”.

(four-fold anisotropy) derived by George and Warren (2002) to simulate crystal growth (Takaki et al., 2013)

$$\kappa(\xi) = \kappa_0 (1 - 3\delta_{\text{aniso}}) \left[1 + \frac{4\delta_{\text{aniso}}}{1 - 3\delta_{\text{aniso}}} (n_1^4 + n_2^4 + n_3^4) \right], \quad (3.10)$$

where $n_2 = \frac{\nabla_y \xi}{\|\nabla \xi\|}$ and $n_3 = \frac{\nabla_z \xi}{\|\nabla \xi\|}$, with “ y ” and “ z ” defined orthogonal to “ x ”.

From (3.8) we calculate the activity of M-atom variationally following (Chen et al., 2015):

$$a_M = e^{\frac{1}{RT} \frac{\delta F_{\text{mix}}}{\delta \xi}} = e^{\frac{g'(\xi) - \kappa(\xi) \nabla^2 \xi}{RT C_m^s}}. \quad (3.11)$$

Substituting (3.5) and (3.11) into (3.1), we obtain the total overpotential expression in terms of ξ :

$$\eta = \Delta\phi - E^\ominus - \frac{RT}{nF} \left(\ln \tilde{\zeta}_+ - \frac{g'(\xi) - \kappa(\xi) \nabla^2 \xi}{C_m^s RT} \right), \quad (3.12)$$

and substituting (3.12) into the Butler-Volmer (3.3), we arrive at:

$$i = i_0 \left\{ e^{-\frac{\alpha n F}{RT} \left[\eta_a - \frac{RT}{nF} \left(\ln \tilde{\zeta}_+ - \frac{g'(\xi) - \kappa(\xi) \nabla^2 \xi}{C_m^s RT} \right) \right]} - e^{\frac{(1-\alpha) n F}{RT} \left[\eta_a - \frac{RT}{nF} \left(\ln \tilde{\zeta}_+ - \frac{g'(\xi) - \kappa(\xi) \nabla^2 \xi}{C_m^s RT} \right) \right]} \right\}. \quad (3.13)$$

Finally, we obtain the phase-field evolution equation (Allen-Cahn reaction

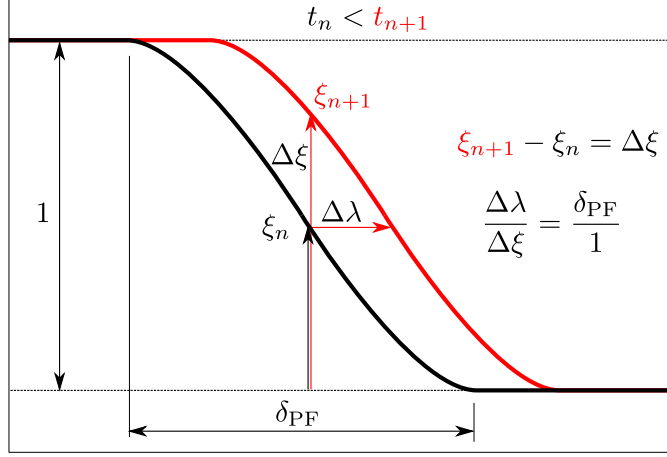


Figure 3.3: Geometry of the phase-field diffuse interface.

(ACR) equation) by matching the velocity of the sharp interface limit of the phase-field equation, with the current-overpotential equation as follows (Liang et al., 2012; Cogswell, 2015; Elder et al., 2001):

$$\frac{\partial \xi}{\partial t} = L_\eta \left\{ e^{-\frac{\alpha n F}{RT} \left[\eta_a - \frac{RT}{n F} \left(\ln \tilde{\zeta}_+ - \frac{g'(\xi) - \kappa(\xi) \nabla^2 \xi}{C_m^s RT} \right) \right]} - e^{\frac{(1-\alpha) n F}{RT} \left[\eta_a - \frac{RT}{n F} \left(\ln \tilde{\zeta}_+ - \frac{g'(\xi) - \kappa(\xi) \nabla^2 \xi}{C_m^s RT} \right) \right]} \right\}, \quad (3.14)$$

where L_η is the electrochemical reaction kinetic coefficient (Hong and Viswanathan, 2018). Figure 3.3 describes geometrically the phase-field interface position at two different time steps ($t_n < t_{n+1}$), elucidating the relationship between the phase-field derivative (3.13) and the lithium electrodeposition rate (3.4) as:

$$\frac{\partial \xi}{\partial t} = \frac{1}{\delta_{PF}} \frac{\partial \lambda}{\partial t}, \quad (3.15)$$

where δ_{PF} is the phase-field diffuse interface thickness.

We relate the Li surface energy (γ) and computed phase-field interfacial thickness (δ_t) to the model parameters according to: $\delta_t = \frac{2\kappa}{3\gamma}$ (Cahn and Hilliard, 1959), where $\delta_t \cong \frac{2}{3}\delta_{PF}$, thus $\delta_{PF} \cong \frac{\kappa}{\gamma}$. Now, by comparing Eqs.(3.4), (3.13) and (3.14), the electrochemical reaction kinetic coefficient becomes:

$$L_\eta = \frac{\gamma i_0}{n F \kappa C_m^s}. \quad (3.16)$$

When the system is far from equilibrium, the interface energy force is significantly smaller than the electrochemical reaction contribution, Liang et al. (2012) linearized the phase-field equation about the interface energy. Using a Taylor expansion, Chen et al. (2015) linearized the phase-field Butler-Volmer equation to obtain:

$$\frac{\partial \xi}{\partial t} = -L_\sigma \left[\frac{\partial g(\xi)}{\partial \xi} - \kappa(\xi) \nabla^2 \xi \right] - L_\eta \frac{\partial h(\xi)}{\partial \xi} \left[e^{\left(\frac{(1-\alpha)nF\eta_a}{RT}\right)} - \tilde{\zeta}_+ e^{\left(\frac{-\alpha nF\eta_a}{RT}\right)} \right]. \quad (3.17)$$

The standard half-cell potential E^\ominus is set as 0 for Li/Li+ equilibrium, thus our activation overpotential becomes: $\eta_a = \phi$. Moreover, $h(\xi)$ is an interpolation function that smooths the diffuse interface in the current implementation. The interpolation function satisfies $h(0) = 0$, $h(1) = 1$, $\partial h(0)/\partial \xi = \partial h(1)/\partial \xi = 0$, ensuring that $\partial f_{\text{ch}}/\partial \xi = 0$ when $\xi = 0$ and $\xi = 1$, for any electric potential value.

A popular choice is a polynomial interpolation function $h_p(\xi) = \xi^3(6\xi^2 - 15\xi + 10)$, (Boettinger et al., 2002), which satisfies these properties. Herein, we also use a sigmoid interpolation function (Chai et al., 2017):

$$h_s(\xi) = \frac{e^{\varsigma(\xi - \frac{1}{2})}}{1 + e^{\varsigma(\xi - \frac{1}{2})}}. \quad (3.18)$$

where ς is a parameter that determines the interface thickness of the interpolation function; we use $\varsigma = 20$, for interpolation between $\xi = 0$ and $\xi = 1$. Figure 3.4 plots these interpolation functions.

Besides satisfying the above-mentioned properties, the sigmoid function (3.17) is bound to the range between 0 and 1 for all possible values of ξ . This property is especially useful to deal with numerical overshoots of the phase-field variable ($\xi < 0$ and $\xi > 1$) that are frequent in these simulations. Our experience show that the sigmoid function delivers better the computational efficiency; thus, we use it in all of our simulations.

The interface mobility L_σ can be expressed as (Chen et al., 2015):

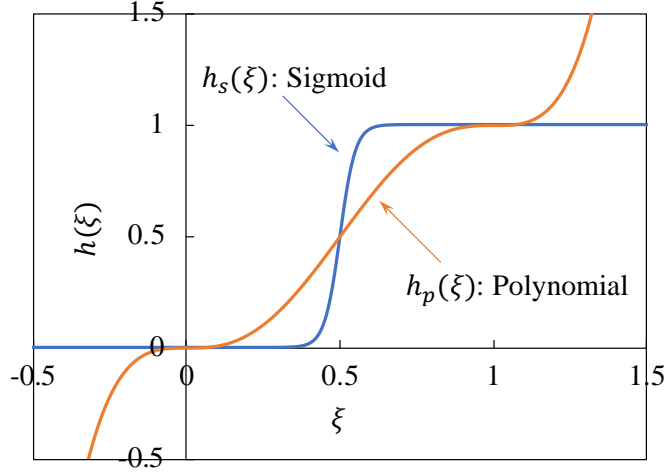


Figure 3.4: Comparison between sigmoid vs polynomial interpolation functions.

$$\begin{aligned}
 L_\sigma &= \beta \left\{ \alpha e^{-\alpha \left[\frac{nF\phi}{RT} - \ln \tilde{\zeta}_+ \right]} + (1 - \alpha) e^{(1-\alpha) \left[\frac{nF\phi}{RT} - \ln \tilde{\zeta}_+ \right]} \right\} \\
 &= \beta \left\{ \alpha \frac{\tilde{\zeta}_+^\alpha}{e^{\alpha \frac{nF\phi}{RT}}} + (1 - \alpha) \frac{e^{(1-\alpha) \frac{nF\phi}{RT}}}{\tilde{\zeta}_+^{(1-\alpha)}} \right\}, \tag{3.19}
 \end{aligned}$$

where $\beta = \frac{i_0 \gamma}{RT n F \kappa(\xi) C_m^s}$. Replacing constant values in (3.19), Figure 3.5 plots the exponential variation of L_σ within the range of charging voltages relevant for lithium dendrite electrodeposition ($\phi = 0$ to -3 [V]), and Li-ion concentration ranging $0 \leq \tilde{\zeta}_+ \leq 1$.

Figure 3.5 shows that L_σ (assumed constant for each simulation) needs to be adjusted to the selected voltage that charges the battery. Furthermore, the L_σ dependency on $\tilde{\zeta}_+$ is lower, but not insignificant. Therefore, selecting an adequate value for L_σ is vital to achieve the right balance between the phase-field interface energy term and the electrochemical reaction contribution. This adjustment avoids the unphysical broadening of the phase-field interface when simulating larger electro potential values, see Figure 3.6

3.1.2 Diffusion-migration

A diffusion-migration equation describes the motion of charged chemical species (lithium-ion) in the fluid electrolyte. The temporal evolution of $\tilde{\zeta}_+ = \zeta_+/C_0$,

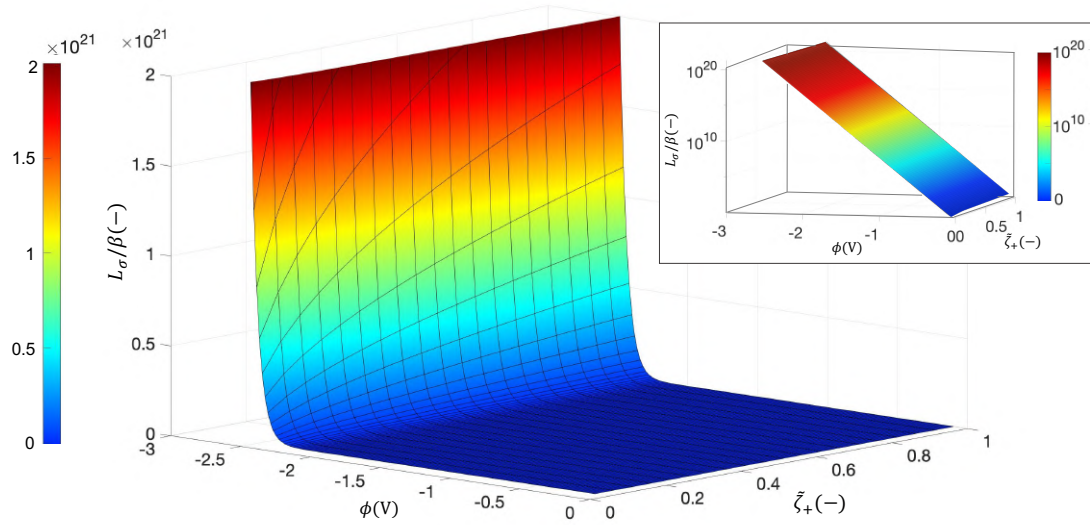


Figure 3.5: Interfacial mobility (L_σ/β) value within the range of charging voltages relevant for dendritic electrodeposition of lithium ($\phi = 0$ to -3 [V]), and range of Li-ion concentration ($0 \leq \zeta_+ \leq 1$). The inset plots L_σ/β in logarithmic scale for better appreciation.

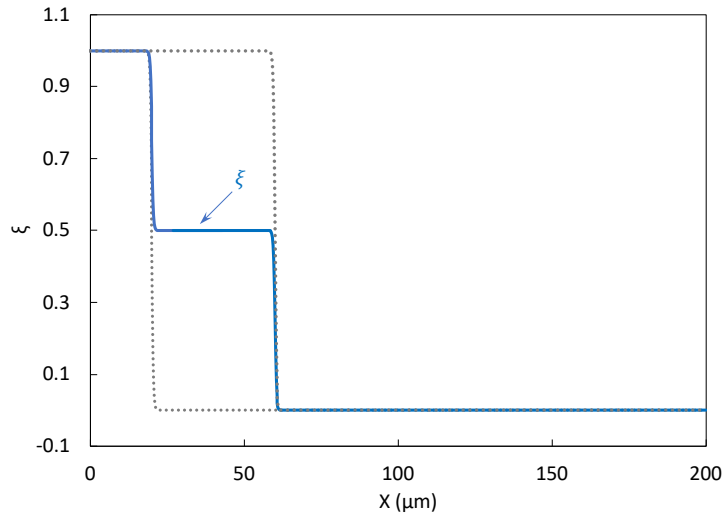


Figure 3.6: “Step-like” diffuse interface due to the imbalance between interface energy term (L_σ) and electrochemical reaction contribution. X: direction normal to phase-field interface.

satisfies the modified Nernst-Planck diffusion equation, which describes the flux of Li-ions under the influence of both a concentration gradient ($\nabla\zeta_+$) and an electric field ($\nabla\phi$) (Chazalviel, 1990)

$$\frac{\partial\zeta_+}{\partial t} = -\nabla \cdot \vec{J}_+ , \quad (3.20)$$

where the flux of lithium-ion species is:

$$\vec{J}_+ = -D^{\text{eff}}(\xi) \left(\nabla\zeta_+ + \frac{nF}{RT}\zeta_+\nabla\phi \right) . \quad (3.21)$$

Herein, the effective diffusivity is interpolated by $D^{\text{eff}}(\xi) = D^s h(\xi) + D^l [1 - h(\xi)]$, where D^s and D^l are the electrode and electrolyte diffusivities, respectively.

Moreover, an additional term $\frac{C_m^s}{C_0} \frac{\partial\xi}{\partial t}$ needs to be included in the Nernst-Planck diffusion equation, to account for the amount of Lithium-ion elimination in the electrolyte solution, due to electrodeposition on the solid phase (metal electrode). Thus, diffusion equation is finally expressed as:

$$\frac{\partial\tilde{\zeta}_+}{\partial t} = \nabla \cdot \left(D^{\text{eff}}(\xi) \nabla\tilde{\zeta}_+ + D^{\text{eff}}(\xi) \frac{nF}{RT}\tilde{\zeta}_+\nabla\phi \right) - \frac{C_m^s}{C_0} \frac{\partial\xi}{\partial t} , \quad (3.22)$$

Alternatively, Plapp (Plapp, 2011) demonstrated that exchanging concentration ζ for chemical potential μ as one of the dependent variables ensures constant chemical potential at equilibrium; in addition, simulations are more robust at low concentration values. This grand canonical formulation was recently applied to other phase-field models of electrokinetic (Cogswell, 2015; Hong and Viswanathan, 2018). The grand free energy functional of an electrochemical system is (Cogswell, 2015):

$$\Omega = \int_V [f_{\text{ch}}(\xi, \mu) + f_{\text{grad}}(\nabla\xi) + f_{\text{elec}}(\mu, \phi)] dV , \quad (3.23)$$

which represents the grand canonical version of (3.6). Thus, by making use of the Nernst-Einstein relation ($\nabla\zeta = \zeta\nabla\mu/RT$), the flux equation of all lithium

species can be written as follows:

$$\vec{J} = -\frac{D^{\text{eff}}(\xi) \zeta_{\text{Li}}}{RT} (\nabla\mu + nF\nabla\phi) , \quad (3.24)$$

where the concentration of Lithium species ζ_{Li} has the contribution from the electrode and electrolyte phases. However, derivation of diffusion equation by Hong and Viswanathan (2018) does not consider the effect of Li-metal diffusivity in the flux of Lithium species, by assuming it to be much smaller than the diffusivity of Li-ion; thus $\vec{J} \cong -\frac{D^l \zeta_+}{RT} (\nabla\mu + nF\nabla\phi)$, where the concentration of Li-ion is interpolated in terms of ξ and μ as (Cogswell and Carter, 2011):

$$\zeta_+(\mu, \xi) = \tilde{\zeta}_+(\mu, \xi) C_0 = C_m^l \zeta^l(\mu) [1 - h(\xi)] = C_m^l \frac{e^{\left(\frac{\mu - \epsilon^l}{RT}\right)}}{1 + e^{\left(\frac{\mu - \epsilon^l}{RT}\right)}} [1 - h(\xi)] , \quad (3.25)$$

with $\zeta^l(\mu)$ as the local Lithium molar ratio at liquid phase, and $\epsilon^l = \mu^{0l} - \mu^{0N}$ as the difference in the chemical potential of lithium and neutral components at the initial equilibrium state in the liquid phase. The flux assumption creates an inconsistency in the diffusion equation via the grand canonical approach; where the chemical potential of all lithium species μ only considers the contribution of the flux of lithium-ion species \vec{J}_+ . The grand canonical formulation used this assumption when it was initially derived as a solidification model for phase-field processes (Plapp, 2011), and then adapted to model metal electrodeposition (Cogswell, 2015; Hong and Viswanathan, 2018), where only the charged species are affected by the electric field (ϕ).

The diffusion equation in terms of the chemical potential (μ), following Hong and Viswanathan (2018), becomes:

$$\frac{\partial\mu}{\partial t} = \frac{1}{\chi} \left[\nabla \cdot \frac{D^l \tilde{\zeta}_+ C_0}{RT C_m^l} (\nabla\mu + nF\nabla\phi) - \frac{\partial h}{\partial t} \left(c^s \frac{C_m^s}{C_m^l} - c^l \right) \right] , \quad (3.26)$$

where the susceptibility factor χ is:

$$\chi = \frac{\partial c^s}{\partial \mu} h \frac{C_m^s}{C_m^l} + \frac{\partial c^l}{\partial \mu} (1 - h) . \quad (3.27)$$

3.1.3 Electrostatic potential

We account for the electrostatic potential distribution ϕ using the charge continuity equation (Guyer et al., 2004b)

$$\frac{\partial \rho}{\partial t} = -\nabla \cdot \vec{i} , \quad (3.28)$$

where \vec{i} is the current density vector and $\rho = \sum_i n_i F \zeta_i$ is the charge density. Experimental observations support the assumption that space-charge effects do not affect the stability of electrodeposits (Elezgaray et al., 1998). Therefore, herein we ignore the effects of the double-layer structure and assume electroneutrality, (i.e. $\tilde{\zeta}_+ = \tilde{\zeta}_-$, $\mu_+ = \mu_-$). Thus, electroneutrality means that $\rho^l = 0$ and $\rho^s = -nF\zeta$, where $\zeta = C_m^s \tilde{\zeta}$, so that $\Delta\rho$ represents the electrons required to create neutral ζ from ζ_+ in the electrolyte. Another benefit of the electroneutrality assumption is the model simplification that only needs to track the lithium cation Li^+ movement. Therefore, making use of Ohm's law in the continuity equation, $\vec{i} = \sigma \vec{E}$, where σ is the conductivity and $\vec{E} = -\nabla\phi$ is the electric field, we obtain the Poisson equation, including the source term to represent the charge that enters or leaves the system due to the electrochemical reaction:

$$\nabla \cdot [\sigma^{\text{eff}}(\xi) \nabla \phi] = nFC_m^s \frac{\partial \tilde{\zeta}}{\partial t} . \quad (3.29)$$

Since the phase-field variable ξ correspond to the lithium atom concentration $\tilde{\zeta}$, we can express the previous equation as (Chen et al., 2015)

$$\nabla \cdot [\sigma^{\text{eff}}(\xi) \nabla \phi] = nFC_m^s \frac{\partial \xi}{\partial t} . \quad (3.30)$$

We interpolate the effective conductivity by $\sigma^{\text{eff}}(\xi) = \sigma^s h(\xi) + \sigma^l [1 - h(\xi)]$, where σ^s and σ^l are the electrode and electrolyte phase conductivity respectively. This last, is the final equation to model our physical problem.

3.1.4 Equations summary

We collect the equation system that models the physical process in the following box.

Box 1: Dendrite growth model

Lithium-battery dendrite growth process based on phase-field theory. *Find*

$\Xi = (\xi, \tilde{\zeta}_+, \phi)$ fulfilling

$$\left\{ \begin{array}{ll} \frac{\partial \xi}{\partial t} = -L_\sigma \left[\frac{\partial g(\xi)}{\partial \xi} - \nabla \cdot (\kappa(\xi) \nabla \xi) \right] \\ \quad - L_\eta \frac{\partial h(\xi)}{\partial \xi} \left[e^{\left(\frac{(1-\alpha)nF\phi}{RT}\right)} - \tilde{\zeta}_+ e^{\left(\frac{-\alpha nF\phi}{RT}\right)} \right], & \text{in } V \times I \\ \frac{\partial \tilde{\zeta}_+}{\partial t} = \nabla \cdot \left[D^{\text{eff}}(\xi) \nabla \tilde{\zeta}_+ + D^{\text{eff}}(\xi) \frac{nF}{RT} \tilde{\zeta}_+ \nabla \phi \right] \\ \quad - \frac{C_m^s}{C_0} \frac{\partial \xi}{\partial t}, & \text{in } V \times I \\ nFC_m^s \frac{\partial \xi}{\partial t} = \nabla \cdot [\sigma^{\text{eff}}(\xi) \nabla \phi], & \text{in } V \times I \\ \xi = \xi_D, & \text{on } \partial V_D \times I \\ \tilde{\zeta}_+ = \tilde{\zeta}_{+D}, & \text{on } \partial V_D \times I \\ \phi = \phi_D, & \text{on } \partial V_D \times I \\ \nabla \xi \cdot \mathbf{n} = 0, & \text{on } \partial V_N \times I \\ \nabla \tilde{\zeta}_+ \cdot \mathbf{n} = 0, & \text{on } \partial V_N \times I \\ \nabla \phi \cdot \mathbf{n} = 0, & \text{on } \partial V_N \times I \\ \xi(\mathbf{x}, t_0) = \xi_0, & \text{in } V \\ \tilde{\zeta}_+(\mathbf{x}, t_0) = \tilde{\zeta}_{+0}, & \text{in } V \\ \phi(\mathbf{x}, t_0) = \phi_0, & \text{in } V \end{array} \right.$$

where V is the problem domain with boundary $\partial V = \partial V_N \cup \partial V_D$, the subscript N and D related to the Neumann and Dirichlet parts, with outward unit normal \mathbf{n} , and I is the time interval.

3.2 Weak variational formulation and space-time discretization

3.2.1 Weak formulation

We now state the weak variational formulation (Hughes, 2012; Pardo et al., 2021) of the system of equations as: *Find* $\Xi = (\xi, \tilde{\zeta}_+, \phi)$ such that $\forall V = (v, w, p)$

$$\underbrace{\langle v, \dot{\xi} \rangle_V + \langle w, \dot{\tilde{\zeta}}_+ \rangle_V + \left\langle w, \frac{C_m^s}{C_0} \dot{\xi} \right\rangle_V + \langle p, \dot{\xi} \rangle_V}_{M(V, \dot{\Xi})} = \underbrace{a(v, \xi, \tilde{\zeta}_+, \phi) + b(w, \xi, \tilde{\zeta}_+, \phi) + c(p, \xi, \phi)}_{A(V, \Xi)} \quad (3.31)$$

where $\dot{\bullet} = \frac{\partial \bullet}{\partial t}$ denotes the time derivative of the variable $\bullet = \xi, \tilde{\zeta}_+$, $\langle u, w \rangle_V = \int_V w u \, dV$ expresses the inner product, and the functions on the right-hand side are

$$\begin{aligned} a(v, \Xi) &= - \int_V L_\sigma \left[\frac{\partial g(\xi)}{\partial \xi} v + \kappa \nabla \xi \cdot \nabla v \right] dV \\ &\quad - \int_V L_\eta \frac{\partial h(\xi)}{\partial \xi} \left[e^{(\frac{(1-\alpha)nF\phi}{RT})} - \tilde{\zeta}_+ e^{(\frac{-\alpha nF\phi}{RT})} \right] v \, dV, \\ b(w, \Xi) &= - \int_V \left[D^{\text{eff}}(\xi) \nabla \tilde{\zeta}_+ \cdot \nabla w + D^{\text{eff}}(\xi) \frac{nF}{RT} \tilde{\zeta}_+ \nabla \phi \cdot \nabla w \right] dV, \\ c(p, \Xi) &= - \frac{1}{nFC_m^s} \int_V \sigma^{\text{eff}}(\xi) \nabla \phi \cdot \nabla p \, dV. \end{aligned} \quad (3.32)$$

We use standard finite element spaces where each function and its gradient are square integrable.

3.2.2 Time semi-discretization

We use a second-order backward-difference (BDF2) time marching scheme with an adaptive time step size. BDF2 is an implicit time marching method that requires the solution at two previous time instants; the initial step uses a first-order backward-difference method (BDF1). BDF2 has second-order accuracy and numerically damps the highest frequencies of the solution, unlike the conservative

Crank-Nicolson method Hughes (2012). Liao et al. Liao et al. (2020) showed that BDF2 is an effective time integrator for the phase-field crystal model, especially when coupled with an adaptive time-step strategy.

We discretize the time interval into $t_0 < t_1 < \dots < t_n < \dots < t_f$ and define the time-step size as $\Delta t_n = t_n - t_{n-1}$, approximate $\xi(t_n)$, $\dot{\xi}(t_n)$, $\tilde{\zeta}_+(t_n)$ and $\dot{\tilde{\zeta}}_+(t_n)$, respectively, as ξ_n , $\dot{\xi}_n$, $\tilde{\zeta}_{+n}$ and $\dot{\tilde{\zeta}}_{+n}$, and express the time increments as $\Delta \bullet = \bullet_{n+1} - \bullet_n$ for $\bullet = \xi, \dot{\xi}, \tilde{\zeta}_+, \dot{\tilde{\zeta}}_+$. We use a second-order approximation of the time derivative at t_{n+1} as follows (Celaya et al., 2014),

$$\frac{\partial \bullet_{n+1}}{\partial t} = \left(\frac{1 + 2\omega_{n+1}}{1 + \omega_{n+1}} \right) \frac{\bullet_{n+1} - \frac{(1+\omega_{n+1})^2}{1+2\omega_{n+1}} \bullet_n + \frac{\omega_{n+1}^2}{1+2\omega_{n+1}} \bullet_{n-1}}{\Delta t_{n+1}}, \quad (3.33)$$

with $\omega_{n+1} = \frac{\Delta t_{n+1}}{\Delta t_n}$, and $\bullet = \xi, \tilde{\zeta}_+$.

Then using this definition and letting $V_v = (v, 0, 0)$, we define the ξ -residual as

$$\begin{aligned} 0 = R_\xi(V_v, \Xi_{n+1}) &= M(V_v, \dot{\Xi}_{n+1}) - A(V_v, \Xi_{n+1}) \\ &= \langle v, \xi_{n+1} \rangle_V + \underbrace{\left\langle v, \frac{(1 + \omega_{n+1})^2}{1 + 2\omega_{n+1}} \xi_n - \frac{\omega_{n+1}^2}{1 + 2\omega_{n+1}} \xi_{n-1} \right\rangle_V}_{\ell_\xi(v) \text{ (known at } t_n)} \\ &\quad - \beta_{n+1} \Delta t_{n+1} a(v, \Xi_{n+1}) \end{aligned} \quad (3.34)$$

with $\beta_{n+1} = \frac{1+\omega_{n+1}}{1+2\omega_{n+1}}$. We now approximate $a(v, \Xi_{n+1})$ as a Taylor series expansion from Ξ_n to obtain

$$a(v, \Xi_{n+1}) = a(v, \Xi_n) + a'_\xi(v, \Delta \xi; \Xi_n) + a'_{\tilde{\zeta}_+}(v, \Delta \tilde{\zeta}_+; \Xi_n) + a'_\phi(v, \Delta \phi; \Xi_n) + \mathcal{O}(\Delta t_{n+1}^2) \quad (3.35)$$

where $\mathcal{O}(\Delta^2)$ represents neglected higher-order terms in the expansion and

$$f'_\bullet(v, \Delta \bullet; \bullet_n) = \frac{d}{d\epsilon} f(v, \bullet_n + \epsilon \Delta \bullet) \Big|_{\epsilon=0} \quad (3.36)$$

represents the directional Gâteaux derivative of the functional f in the direction \bullet . Combining (3.34) and (3.35), we obtain a linear equation system to solve, that

is

$$\begin{aligned}
0 = R_\xi(V_v, \Xi_n) + \langle v, \Delta\xi \rangle_V \\
+ \beta_{n+1} \Delta t_{n+1} \left[a'_\xi(v, \Delta\xi; \Xi_n) + a'_{\tilde{\zeta}_+}(v, \Delta\tilde{\zeta}_+; \Xi_n) + a'_\phi(v, \Delta\phi; \Xi_n) \right]
\end{aligned} \tag{3.37}$$

Similarly, we define the weighting functions $V_w = (0, w, 0)$ and $V_p = (0, 0, p)$; the residuals \mathcal{R}_\bullet with $\bullet = \tilde{\zeta}_+, \phi$ and linearize the resulting residuals to obtain the linearized system of equations to update the Newton iteration. We collect the linearized equation system that models the physical process in the following box.

Box 2: Linearized equation system

Discrete linearized equations for lithium-battery dendrite growth process based on phase-field theory. Find $\Xi_{n+1} = (\xi_n, \tilde{\zeta}_{n+1}, \phi_n) + (\Delta\xi, \Delta\phi, \Delta\tilde{\zeta}_+)$ such that

$$\left\{ \begin{aligned}
0 = R_\xi(V_v, \Xi_n) + \langle v, \Delta\xi \rangle_V \\
+ \beta_{n+1} \Delta t_{n+1} \left[a'_\xi(v, \Delta\xi; \Xi_n) + a'_{\tilde{\zeta}_+}(v, \Delta\tilde{\zeta}_+; \Xi_n) + a'_\phi(v, \Delta\phi; \Xi_n) \right] \\
0 = \mathcal{R}_{\tilde{\zeta}_+}(V_w, \Xi_n) + \left\langle w, \Delta\tilde{\zeta}_+ + \frac{C_m^s}{C_0} \Delta\xi \right\rangle_V \\
+ \beta_{n+1} \Delta t_{n+1} \left[b'_\xi(w, \Delta\xi; \Xi_n) + b'_{\tilde{\zeta}_+}(w, \Delta\tilde{\zeta}_+; \Xi_n) + b'_\phi(w, \Delta\phi; \Xi_n) \right] \\
0 = \mathcal{R}_\phi(V_p, \Xi_n) + \langle p, \Delta\xi \rangle_V + \beta_{n+1} \Delta t_{n+1} \left[c'_\xi(p, \Delta\xi; \Xi_n) + c'_\phi(p, \Delta\phi; \Xi_n) \right]
\end{aligned} \right. \tag{3.38}$$

We only expand c in the directions $\Delta\xi$ and $\Delta\phi$ as it is independent of $\Delta\tilde{\zeta}_+$, see (3.32).

For completeness, we summarize the Gâteaux derivatives in (3.38) in the following box.

Box 3: Gâteaux derivatives

$$\begin{aligned}
a'_\xi(v, \Delta\xi; \Xi_n) &= \int_V L_\sigma \left[\frac{\partial g^2(\xi)}{\partial \xi^2} \Big|_{\xi_n} \Delta\xi v + \left(\kappa(\xi_n) \nabla \Delta\xi + \frac{\partial \kappa(\xi)}{\partial \xi} \Big|_{\xi_n} \Delta\xi \nabla \xi_n \right) \cdot \nabla v \right] dV \\
&\quad + \int_V L_\eta \frac{\partial h^2(\xi)}{\partial \xi^2} \Big|_{\xi_n} \left[e^{\left(\frac{(1-\alpha)nF\phi_n}{RT}\right)} - \tilde{\zeta}_{+n} e^{\left(\frac{-\alpha nF\phi_n}{RT}\right)} \right] \Delta\xi v dV \\
a'_{\tilde{\zeta}_+}(v, \Delta\tilde{\zeta}_+; \Xi_n) &= \int_V L_\eta \frac{\partial h(\xi)}{\partial \xi} \Big|_{\xi_n} e^{\left(\frac{-\alpha nF\phi_n}{RT}\right)} \Delta\tilde{\zeta}_+ v dV \\
a'_\phi(v, \Delta\phi; \Xi_n) &= \int_V L_\eta \frac{\partial h(\xi)}{\partial \xi} \Big|_{\xi_n} \frac{nF}{RT} \left[(1-\alpha) e^{\left(\frac{(1-\alpha)nF\phi_n}{RT}\right)} + \alpha \tilde{\zeta}_{+n} e^{\left(\frac{-\alpha nF\phi_n}{RT}\right)} \right] \Delta\phi v dV \\
b'_\xi(w, \Delta\xi; \Xi_n) &= \int_V \frac{\partial D^{\text{eff}}(\xi)}{\partial \xi} \Big|_{\xi_n} \Delta\xi \left(\nabla \tilde{\zeta}_{+n} + \frac{nF}{RT} \tilde{\zeta}_{+n} \nabla \phi_n \right) \cdot \nabla w dV \\
b'_{\tilde{\zeta}_+}(w, \Delta\tilde{\zeta}_+; \Xi_n) &= \int_V D^{\text{eff}}(\xi_n) \left(\nabla \Delta\tilde{\zeta}_+ + \frac{nF}{RT} \Delta\tilde{\zeta}_+ \nabla \phi_n \right) \cdot \nabla w dV \\
b'_\phi(w, \Delta\phi; \Xi_n) &= \int_V D^{\text{eff}}(\xi_n) \frac{nF}{RT} \tilde{\zeta}_{+n} \nabla \Delta\phi \cdot \nabla w dV \\
c'_\xi(p, \Delta\xi; \Xi_n) &= \frac{1}{nFC_m^s} \int_V \frac{\partial \sigma^{\text{eff}}(\xi)}{\partial \xi} \Big|_{\xi_n} \Delta\xi \nabla \phi_n \cdot \nabla p dV \\
c'_\phi(p, \Delta\phi; \Xi_n) &= \frac{1}{nFC_m^s} \int_V \sigma^{\text{eff}}(\xi_n) \nabla \Delta\phi \cdot \nabla p dV
\end{aligned} \tag{3.39}$$

3.2.3 Space discretization

We discretize the domain $V \subset \mathbb{R}^3$ with Dirichlet boundary condition ∂V_D and Neumann boundary condition ∂V_N using finite elements. We express the domain as the union of non-overlapping elements, K_i ; thus, $V_h = \bigcup_{i=1}^M K_i$. We define continuous piecewise polynomial functions over the discrete domain. In particular, we use linear functions over simplexes (i.e., triangles in 2D, tetrahedra in 3D). Since the three variables share the spatial distribution of the boundary conditions, we use the shape functions $N_A(\mathbf{x})$ for each degree of freedom \bullet_A^n at t_n satisfying the Dirichlet boundary conditions to discretize each degree of freedom $\bullet = X, Z, Y$

corresponding to the variables $\xi, \tilde{\zeta}_+, \phi$, respectively; thus, we have

$$\begin{aligned} \xi_n^h &= \sum_{i=1}^S N_A(\mathbf{x}) X_A^n & \tilde{\zeta}_{+n}^h &= \sum_{i=1}^S N_A(\mathbf{x}) Z_A^n & \phi_n^h &= \sum_{i=1}^S N_A(\mathbf{x}) Y_A^n \\ \Delta \xi^h &= \sum_{i=1}^S N_A(\mathbf{x}) \Delta X_A & \Delta \tilde{\zeta}_+^h &= \sum_{i=1}^S N_A(\mathbf{x}) \Delta Z_A & \Delta \phi^h &= \sum_{i=1}^S N_A(\mathbf{x}) \Delta Y_A \end{aligned} \quad (3.40)$$

where S corresponds to the total number of unknowns in each solution variable. We define the weighting spaces using test spaces using the same functions but restricting those with support on ∂V_D to be zero, thus

$$v^h \in \text{span} \{N_B\}_{B=1}^W \quad w^h \in \text{span} \{N_B\}_{B=1}^W \quad p^h \in \text{span} \{N_B\}_{B=1}^W \quad (3.41)$$

where W corresponds to the total number of weighting functions for each variable.

Using these spatial discretizations, we obtain the fully discrete algebraic problem:

$$\underbrace{\begin{Bmatrix} \Delta \mathcal{R}_\xi \\ \Delta \mathcal{R}_{\tilde{\zeta}_+} \\ \Delta \mathcal{R}_\phi \end{Bmatrix}}_{\Delta \mathcal{R}} = \underbrace{\left(\begin{bmatrix} \mathbb{M}_{\xi\xi} & \mathbf{0} & \mathbf{0} \\ \mathbb{M}_{\tilde{\zeta}_+\xi} & \mathbb{M}_{\tilde{\zeta}_+\tilde{\zeta}_+} & \mathbf{0} \\ \mathbb{M}_{\phi\xi} & \mathbf{0} & \mathbf{0} \end{bmatrix} + \beta_{n+1} \Delta t \begin{bmatrix} \mathbb{K}_{\xi\xi} & \mathbb{K}_{\xi\tilde{\zeta}_+} & \mathbb{K}_{\xi\phi} \\ \mathbb{K}_{\tilde{\zeta}_+\xi} & \mathbb{K}_{\tilde{\zeta}_+\tilde{\zeta}_+} & \mathbb{K}_{\tilde{\zeta}_+\phi} \\ \mathbb{K}_{\phi\xi} & \mathbf{0} & \mathbb{K}_{\phi\phi} \end{bmatrix} \right)}_{\mathbb{J}} \cdot \underbrace{\begin{Bmatrix} \Delta \mathbf{X} \\ \Delta \mathbf{Z} \\ \Delta \mathbf{Y} \end{Bmatrix}}_{\Delta \mathbf{X}}. \quad (3.42)$$

Box 4: Matrix blocks

The mass matrix blocks are

$$\mathbb{M}_{AB}^{\xi\xi} = \mathbb{M}_{AB}^{\tilde{\zeta}_+ \tilde{\zeta}_+} = \mathbb{M}_{AB}^{\phi\xi} = \sum_{k=1}^M \int_{K_k} N_A N_B dK_k \quad \text{and} \quad \mathbb{M}_{AB}^{\tilde{\zeta}_+ \xi} = \sum_{k=1}^M \int_{K_k} \frac{C_m^s}{C_0} N_A N_B dK_k \quad (3.43)$$

while stiffness matrix blocks are

$$\left\{ \begin{array}{l} \mathbb{K}_{AB}^{\xi\xi} = \sum_{k=1}^M \int_{K_k} L_\sigma \left[\frac{\partial g^2}{\partial \xi^2} \Big|_{\xi_n^h} N_A N_B + \left(\kappa(\xi_n^h) \nabla N_A + \frac{\partial \kappa}{\partial \xi} \Big|_{\xi_n^h} N_A \nabla \xi_n^h \right) \cdot \nabla N_B \right] dK_k \\ \quad + \sum_{k=1}^M \int_{K_k} L_\eta \frac{\partial h^2}{\partial \xi^2} \Big|_{\xi_n^h} \left[e^{\left(\frac{(1-\alpha)nF\phi_n^h}{RT} \right)} - \tilde{\zeta}_{+n} e^{\left(\frac{-\alpha nF\phi_n^h}{RT} \right)} \right] N_A N_B dK_k \\ \mathbb{K}_{AB}^{\xi \tilde{\zeta}_+} = \sum_{k=1}^M \int_{K_k} L_\eta \frac{\partial h}{\partial \xi} \Big|_{\xi_n^h} e^{\left(\frac{-\alpha nF\phi_n^h}{RT} \right)} N_A N_B dK_k \\ \mathbb{K}_{\xi\phi} = \sum_{k=1}^M \int_{K_k} L_\eta \frac{\partial h}{\partial \xi} \Big|_{\xi_n^h} \frac{nF}{RT} \left[(1-\alpha) e^{\left(\frac{(1-\alpha)nF\phi_n^h}{RT} \right)} + \alpha \tilde{\zeta}_{+n} e^{\left(\frac{-\alpha nF\phi_n^h}{RT} \right)} \right] N_A N_B dK_k \\ \mathbb{K}_{AB}^{\tilde{\zeta}_+ \xi} = \sum_{k=1}^M \int_{K_k} \frac{\partial D^{\text{eff}}}{\partial \xi} \Big|_{\xi_n^h} N_A \left[\nabla \tilde{\zeta}_{+n} + \frac{nF}{RT} \tilde{\zeta}_{+n} \nabla \phi_n^h \right] \cdot \nabla N_B dK_k \\ \mathbb{K}_{\tilde{\zeta}_+ \tilde{\zeta}_+} = \sum_{k=1}^M \int_{K_k} D^{\text{eff}}(\xi_n^h) \left[\nabla N_A + \frac{nF}{RT} N_A \nabla \phi_n^h \right] \cdot \nabla N_B dK_k \\ \mathbb{K}_{AB}^{\tilde{\zeta}_+ \phi} = \sum_{k=1}^M \int_{K_k} D^{\text{eff}}(\xi_n^h) \frac{nF}{RT} \tilde{\zeta}_{+n} \nabla N_A \cdot \nabla N_B dK_k \\ \mathbb{K}_{AB}^{\phi\xi} = \frac{1}{nFC_m^s} \sum_{k=1}^M \int_{K_k} \frac{\partial \sigma^{\text{eff}}}{\partial \xi} \Big|_{\xi_n^h} N_A \nabla \phi_n^h \cdot \nabla N_B dK_k \\ \mathbb{K}_{AB}^{\phi\phi} = \frac{1}{nFC_m^s} \sum_{k=1}^M \int_{K_k} \sigma^{\text{eff}}(\xi_n^h) \nabla N_A \cdot \nabla N_B dK_k \end{array} \right. \quad (3.44)$$

3.3 Time-adaptive strategy

Time step adaptivity is highly useful in this problem, where the time step requirement varies significantly at different simulation stages. For example, initially, the simulation requires small time steps to achieve convergence during the devel-

opment of the phase-field interface and thereon, their size grows a few orders of magnitude (i.e., from $\Delta t = 10^{-6}$ [s] up to $\Delta t = 10^{-1}$ [s]) depending on the parameters (e.g., mesh size, electrodeposition rate).

Following (Vignal et al., 2017; Labanda et al., 2022), we express the local truncation error for BDF2 using Taylor expansions as follows

$$\tau^{\text{BDF2}}(t_{n+1}) = \frac{\Delta t_{n+1}^2 (\Delta t_n + \Delta t_{n-1})}{6} \ddot{u}(t_{n+1}) + \mathcal{O}(\Delta t^4), \quad (3.45)$$

where $u = \xi, \tilde{\zeta}_+$, since ϕ 's time derivative does not appear explicitly in the formulation. We use the solutions u_{n+1}, u_n, u_{n-1} and u_{n-2} from the BDF2 scheme to estimate the truncation error of (3.45) using the third-order backward difference formula (BDF3)

$$\ddot{u}(t_{n+1}) \approx \frac{1}{\Delta t_{n+1}^2} \left[\frac{u_{n+1} - u_n}{\Delta t_{n+1}} - \left(1 + \frac{\Delta t_{n+1}}{\Delta t_n} \right) \frac{u_n - u_{n-1}}{\Delta t_n} + \frac{\Delta t_{n+1}}{\Delta t_n \Delta t_{n-1}} (u_{n-1} - u_{n-2}) \right]. \quad (3.46)$$

Thus, we estimate BDF2's local truncation error by substituting (3.46) into (3.45) to obtain

$$\begin{aligned} \tau^{\text{BDF2}}(t_{n+1}) \approx & \frac{\Delta t_n + \Delta t_{n-1}}{6} \left[\frac{u_{n+1} - u_n}{\Delta t_{n+1}} - \left(1 + \frac{\Delta t_{n+1}}{\Delta t_n} \right) \frac{u_n - u_{n-1}}{\Delta t_n} \right] \\ & + \frac{\Delta t_n + \Delta t_{n-1}}{6} \left[\frac{\Delta t_{n+1}}{\Delta t_n \Delta t_{n-1}} (u_{n-1} - u_{n-2}) \right]. \end{aligned} \quad (3.47)$$

Finally, we compute the weighted local truncation error as an error indicator (Hairer and Wanner, 2010)

$$E_u(t_{n+1}) = \sqrt{\frac{1}{N} \sum_{i=1}^N \left(\frac{\tau_i^{\text{BDF2}}(t_{n+1})}{\rho_{abs} + \rho_{rel} \max(|u_{n+1}|_i, |u_{n+1}|_i + |\tau^{\text{BDF2}}(t_{n+1})|_i)} \right)^2}, \quad (3.48)$$

where ρ_{abs} and ρ_{rel} are user-defined parameters that define the absolute and relative tolerances, respectively. In our examples we set these parameters to $\rho_{abs} = \rho_{rel} = 10^2$. The time error is computed using the maximum time error of

time-dependent variables

$$E(t_{n+1}) = \max\left(E_{\xi}(t_{n+1}), E_{\tilde{\zeta}_+}(t_{n+1})\right), \quad (3.49)$$

and the time-step adaptivity simply follows (Gómez et al., 2008; Lang, 1995)

$$\Delta t_{n+1}^{k+1}(t_{n+1}) = \mathbf{F}(E(t_{n+1}), \Delta t_{n+1}^k, \text{tol}) = \rho_{tol} \left(\frac{\text{tol}}{E(t_{n+1})}\right)^{\frac{1}{2}} \Delta t_{n+1}^k, \quad (3.50)$$

where k is the time-step refinement level and ρ_{tol} is a safety factor parameter set to 0.9 in our simulations. We summarize the time-adaptive scheme in Algorithm 1, where we define two tolerances tol_{max} and tol_{min} that limit the range of reduction or increments of the time-step size.

Allen-Cahn and Cahn-Hilliard equations are designed in such a way that they are gradient flows for the energy (Allen and Cahn, 1972; Gomez and van der Zee, 2017). This means that the construction of the phase-field model satisfies an a priori nonlinear stability relationship, expressed as a time-decreasing free-energy functional; nevertheless, standard discrete approximations do not inherit this stability property (Gomez and Hughes, 2011; Sarmiento et al., 2018; Wu et al., 2014; Hawkins-Daarud et al., 2012; Vignal et al., 2017). Thus, the evolution of the Gibbs free energy of the system Ψ , see (3.6), needs to be analysed along with our simulation results to verify that the total systems' discrete free energy does not increase with time (discrete energy stable results).

3.4 Implementation details

3.4.1 Numerical implementation

This section briefly discusses the implementation aspects and details the step-by-step calculations. We perform all the numerical experiments using the open-source FEniCS environment (Alnæs et al., 2015) using the FIAT package (Kirby,

2004) to integrate numerically and assemble the matrices and vectors. We use two-node linear elements in 1D, four-node quadrilateral elements in 2D and eight-node hexahedral elements in 3D; in all cases, we use consistent Gaussian quadrature. We use a passing interface package MPI4py (Dalcin and Fang, 2021; Dalcin et al., 2011; Dalcín et al., 2008, 2005) for parallelization and solve nonlinear equations using SNES combined with BiCGStab for each linear system, including a Nonlinear Additive Schwarz methods (NASM) for parallel solution (Balay et al., 2021). Table 3.1 summarizes the parameters we use.

Table 3.1: Numerical parameters summarize

Description	Symbol	Value
Max. iteration number for SNES	it_{\max}	8
Relative tolerance for SNES	tol	10^{-8}
Max. iteration number for Krylov	it_{Kr}	1000
Relative tolerance for Krylov	tol_{Kr}	10^{-22}
Max. tolerance for time-adaptive scheme	tol_{\max}	10^{-5}
Min. tolerance for time-adaptive scheme	tol_{\min}	10^{-7}
Safety factor for time-adaptive scheme	ρ_{tol}	0.9
Relative scale factor for time-error computation	ρ_{rel}	10^2
Absolute scale factor for time-error computation	ρ_{abs}	10^2

We compute the time increment by gathering the unknown vectors at the master core, estimating the error for the current time step, adapting the time step size, and broadcasting its value to the other cores. This straightforward implementation is practical given the small number of processors used. We initialize the simulations using a first-order backward difference formula (BDF1) until \bullet_{n-2} is different from null. We perform the simulations using a laptop with a 2.4 GHz processor with 8-core Intel Core i9 and 16 GB 2667 MHz DDR4 RAM, obtaining satisfactory results using a regular computer. Algorithm 1 sketches the time marching scheme, where *rank* is the core number, and *master* is the master core used as the communicator.

Algorithm 1: Dendrite growth model based on phase-field theory with time adaptivity

Data: $\bullet_n, \bullet_{n-1}, \bullet_{n-2}, \dot{\bullet}_n, \Delta t_{n+1}, \Delta t_n, \Delta t_{n-1}$
Result: updated variables $\bullet_{n+1}, \dot{\bullet}_{n+1}, \Delta t_{n+1}$

- 1 Initialize $\bullet_n = \bullet_0$, with $\bullet = \xi, \zeta, \phi$;
- 2 **while** $t_{n+1} \leq t_f$ **do**
- 3 Solve non-linear problem (3.42) ;
- 4 Gather $\Delta \mathbf{X}$ in master core and calculate temporal error $\tau^{\text{BDF2}}(t_n + \Delta t_{n+1})$ with (3.47) ;
- 5 **if** $\text{rank} == \text{master}$ **then**
- 6 Calculate $E_u(t_n + \Delta t_{n+1})$ with (3.48) ;
- 7 Take the maximum error with (3.49) ;
- 8 **if** $E(t_n + \Delta t_{n+1}) \leq \text{tol}_{\max}$ **then**
- 9 Update current time step $t_{n+1} \leftarrow t_n + \Delta t_{n+1}$;
- 10 Update \bullet_{n+1} and $\dot{\bullet}_{n+1}$;
- 11 Update $\bullet_{n-2} \leftarrow \bullet_{n-1}, \bullet_{n-1} \leftarrow \bullet_n, \bullet_n \leftarrow \bullet_{n+1}$ and $\dot{\bullet}_n \leftarrow \dot{\bullet}_{n+1}$;
- 12 **if** $E(t_n + \Delta t_{n+1}) < \text{tol}_{\min}$ **then**
- 13 Increase delta step for next time increment
 $\Delta t_{n+1} \leftarrow \mathbf{F}(E(t_{n+1}), \Delta t_{n+1}, \text{tol}_{\min})$ using (3.50) ;
- 14 **end**
- 15 Broadcast to rest of ranks all variables $\Delta t_{n+1}, \bullet_{n-2}, \bullet_{n-1}$ and $\dot{\bullet}_n$;
- 16 **else**
- 17 Reduce time-step size $\Delta t_{n+1} \leftarrow \mathbf{F}(E(t_{n+1}), \Delta t_{n+1}, \text{tol}_{\max})$
 using (3.50) ;
- 18 Broadcast to rest of ranks only Δt_{n+1} ;
- 19 **end**
- 20 **end**
- 21 **end**

3.4.2 Phase-field diffuse interface thickness & mesh size:

A discussion

The interface thickness between the lithium electrode and the electrolyte is about 5 nm (ichi Morigaki, 2002). Simulating this thickness is impractical due to the computational cost (Guyer et al., 2004a,b); the smaller the interface thickness, the finer the grid resolution (mesh size) used, causing the simulation time to increase significantly. Therefore, broadening the interface for computational reasons (thin interface formulations) is essential in our model (Karma, 2001; Echebarria et al., 2004). However, the thickness selection must follow reasonable criteria since using an oversized interface deviates the simulation from reality (Zhao et al., 2018).

An analysis of the published data reveals that the interface thickness used in phase-field simulations of electrodeposition are varied, from less than 0.1 nm – 1D (Guyer et al., 2004b) up to 50 μm (Yan et al., 2018), although this thickness is often not reported (Zhang et al., 2014; Chen et al., 2015; Yurkiv et al., 2018; Mu et al., 2019); this fact shows the lack of agreement in criteria in the definition of the phase-field interface. In our phase-field model (3.17), the phase-field diffuse interface thickness (δ_{PF}) results from the interaction between two opposite effects on the interfacial energy term ($\frac{\partial g(\xi)}{\partial \xi} - \kappa \nabla^2 \xi$), as Figure 3.7 shows. On the one hand, the reduction of the volume of material where ξ is between 0 and 1 (proportional to $W \propto \gamma$), and on the other hand, the diffusion of the interface to minimize the energy relative to the gradient of ξ (proportional to κ) (Cahn and Hilliard, 1959; Boettinger et al., 2002). Two different expressions for W and κ are common in phase-field models of electrokinetics available depending on the definition of phase-field thickness (δ_t). Boettinger et al. (2002) characterized the characteristic thickness (δ_B) from an equilibrium solution: $\xi(x) = \frac{1}{2} \left[1 - \tanh \left(x \sqrt{\frac{W}{2\kappa}} \right) \right]$ (the term multiplying x , $2\delta_B = \sqrt{\frac{2\kappa}{W}}$); alternatively, Cahn and Hilliard (1959) used the slope at $x = 0$ to estimate an interface thickness (δ_{CH}). Table 3.2 summarizes different expressions for W and κ ; that relate these phase-field interface thicknesses: $\delta_{CH} = 4\delta_B$.

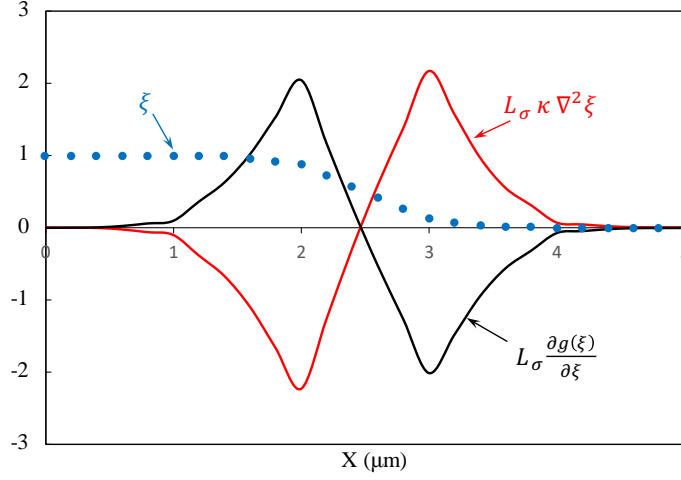


Figure 3.7: Schematic of phase-field diffuse interface (blue dotted line) as a result of the equilibration of the opposing effects of the energy barrier ($\frac{\partial g(\xi)}{\partial \xi}$) and the gradient energy ($\kappa \nabla^2 \xi$).

Table 3.2: Comparison between different expressions for W and κ in literature (Cahn and Hilliard, 1959; Boettinger et al., 2002).

Variable name	Symbol	Cahn and Hilliard (1959)	Boettinger et al. (2002)
Theoric Interfacial thickness	δ_t	$2\sqrt{\frac{2\kappa}{W}}$	$\sqrt{\frac{\kappa}{2W}}$
Barrier height	W	$12\frac{\gamma}{\delta_{CH}}$	$3\frac{\gamma}{\delta_B}$
Gradient energy coefficient	κ	$\frac{3\gamma\delta_{CH}}{2}$	$6\gamma\delta_B$

Section 4.3.3 further analyses the effect of the phase-field interface thickness on the electrodeposition rate simulation results, which ultimately control the temporal evolution of the electrodeposits.

Chapter 4

Phase-field simulations of planar interface electrodeposition in rechargeable lithium-metal batteries

This chapter ¹ presents simulations describing the coupled electrochemical interactions during a battery charge cycle using finite elements on open-source packages, allowing for parallel computation and time step adaptivity. A one-dimensional (planar interface) study compares the conventional free energy and grand canonical formulations. The effect of the applied overpotential (and the prediction's agreement with Faradic kinetics) is investigated, as well as analysis of the prediction sensitivity to the phase-field interface thickness and mesh resolution. These simulation results set the groundwork for 2D and 3D simulations of dendritic metal electrodeposition in batteries.

¹The content of this chapter is published in: Arguello, M. E., Gumulya, M., Derksen, J., Utikar, R., & Calo, V. M. (2022). Phase-field modeling of planar interface electrodeposition in lithium-metal batteries. *Journal of Energy Storage*, 50, 104627.

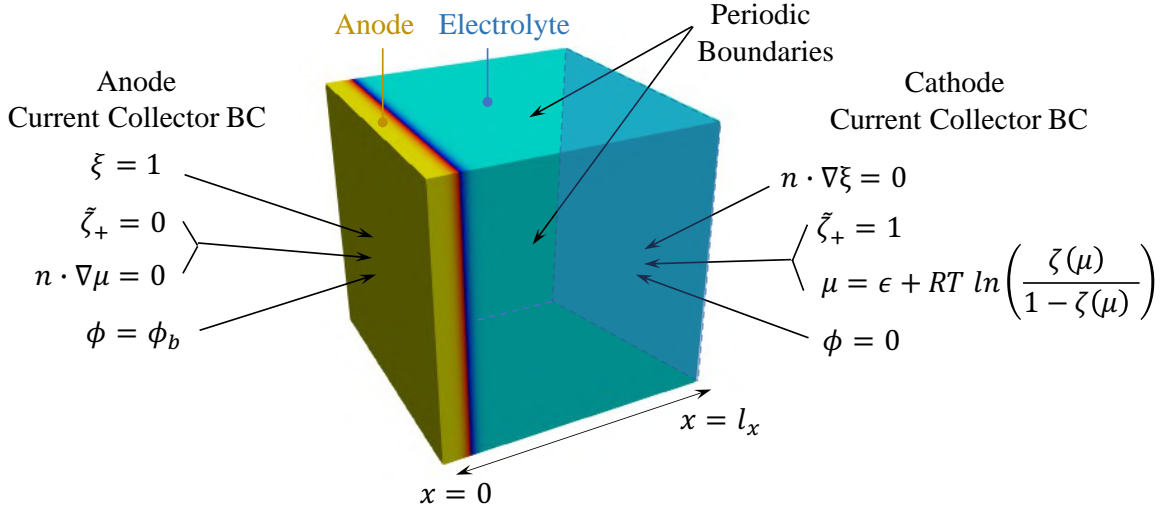


Figure 4.1: Boundary conditions for planar interface battery charge simulation.

4.1 System layout & properties

Generally, the computational domain for a battery simulation comprises the anode and cathode regions and the space between the electrodes filled with electrolyte (Trembacki et al., 2019). However, for most phase-field simulations of metal electrodeposition, including those performed herein, the cathode region is reduced into a current collector boundary condition on the electrolyte side of the domain (Figure 4.1).

We model a battery cell, with a traditional 1D sandwich architecture, and an initial interelectrode distance of $180 \mu\text{m}$, undergoing a recharging process under fixed applied electric potential status. The initial structure consists of a $20 \mu\text{m}$ -thick metal anode ($l_0 = 20\mu\text{m}$), made up of pure lithium, separated from the liquid electrolyte by a smooth interface, as Figure 4.1 shows. The initial condition drives from the equilibrium solution for a one-dimensional transition zone between solid ($\xi = 1$) and liquid ($\xi = 0$), where our variables $(\xi, \tilde{\zeta}_+, \phi)$ vary in the “x” spatial direction normal to the interface according to: $\frac{1}{2} \left[1 - \tanh \left(x \sqrt{\frac{W}{2\kappa}} \right) \right]$ (Boettinger et al., 2002).

On the cell’s right side, the liquid electrolyte is assumed as 1M LiPF_6 EC/DMC 1:1 volume ratio solution, including Li^+ cation and PF_6^- anion species. We com-

pute the site density of the electrolyte (C_m^l) using the density ($1.3 [g/cm^3]$) and molar mass ($90 [g/mol]$) of the electrolyte; similarly, the site density of the electrode C_m^s uses the density ($0.534 [g/cm^3]$) and molar mass ($6.941 [g/mol]$) of pure Lithium (Hong and Viswanathan, 2018).

We use a Dirichlet boundary condition $\xi = 1$ on the left boundary for the phase-field order parameter (solid electrode phase) and a non-flux Neumann boundary condition on the right boundary, which allows the electrodeposition process (ξ changing from 0 to 1) when the reaction front approaches the right boundary (cathode).

For the Li-ion concentration, we apply Dirichlet boundary conditions, $\tilde{\zeta}_+ = 0$ and $\tilde{\zeta}_+ = 1$, to the left and right cell boundaries, respectively. Thus, the Li-ion flows into the battery (electrolyte side), ensuring that the amount of lithium deposited at electrode-electrolyte interface equals the amount of Li^+ supplied on the electrolyte side, thus avoiding quick Li-ion depletion and keeping the electrodeposition process running for the entire simulation time.

Alternatively, when solving for the chemical potential μ , instead of $\tilde{\zeta}_+$, we apply a non-flux Neumann boundary condition on the left boundary (electrode phase), indicating a constant lithium molar ratio, while we apply a time-varying Dirichlet boundary condition on the electrolyte side (right boundary), allowing for a change on the chemical potential value when the reaction front approaches the right boundary. Table 4.1 summarizes our set of boundary conditions.

Table 4.1: Boundary Conditions (1D Problem).

Variable	Electrode ($x = 0$)	Electrolyte ($x = l_x$)
Phase-field	$\xi = 1$	$\nabla \xi \cdot \mathbf{n} = 0$
Li-ion Concentration	$\tilde{\zeta}_+ = 0$	$\tilde{\zeta}_+ = 1$
or		
Chemical Potential	$\nabla \mu \cdot \mathbf{n} = 0$	$\mu = \epsilon + RT \ln \left(\frac{\zeta(\mu)}{1 - \zeta(\mu)} \right)$
Electrostatic Potential	$\phi = \phi_b [V]$	$\phi = 0 [V]$

Additionally, Table 4.2 presents the parameters used in the current phase-field model. The normalization constants for length, time, energy and concentration scales are set as $h_0 = 1 [\mu m]$, $t_0 = 1 [s]$, $E_0 = 2.5 \times 10^6 [J/m^3]$, and $C_0 = 1 \times 10^3 [mol/m^3]$, respectively.

Table 4.2: Planar Electrode Simulation Parameters

Description	Symbol	Real Value	Normalized	Source
Exc. current density	i_0	$30 [A/m^2]$	30	Monroe and Newman (2003)
Surface tension	γ	$0.556 [J/m^2]$	0.22	Vitos et al. (1998); Tran et al. (2016)
Phase-field interface thickness	δ_{PF}	$1 \times 10^{-6} [m]$	1	selected
Barrier height	W	$W = \frac{12\gamma}{\delta_{PF}} = 6.67 \times 10^6 [J/m^3]$	2.67	computed
Gradient energy coefficient	κ_0	$\kappa_0 = \frac{3\gamma\delta_{PF}}{2} = 8.34 \times 10^{-7} [J/m]$	0.335	computed
Kinetic coefficient	L_η	$L_\eta = i_0 \frac{\gamma}{n_F C_m^s} = 2.71 \times 10^{-3} [1/s]$	2.71×10^{-3}	computed
Difference in chem. pot. electrode	ϵ^s	$\epsilon^s = \mu^{0s} - \mu^{0N}$	-13.8	Hong and Viswanathan (2018)
Difference in chem. pot. electrolyte	ϵ^l	$\epsilon^l = \mu^{0l} - \mu^{0N}$	2.63	Hong and Viswanathan (2018)
Site density electrode	C_m^s	$7.64 \times 10^4 [mol/m^3]$	76.4	Hong and Viswanathan (2018)
Site density electrolyte	C_m^l	$1.44 \times 10^4 [mol/m^3]$	14.4	Hong and Viswanathan (2018)
Bulk Li-ion concentration	C_0	$10^3 [mol/m^3]$	1	computed
Conductivity electrode	σ^s	$10^7 [S/m]$	10^7	Chen et al. (2015)
Conductivity electrolyte	σ^l	$1.19 [S/m]$	1.19	Valoen and Reimers (2005)
Diffusivity electrode	D^s	$7.5 \times 10^{-13} [m^2/s]$	0.75	Chen et al. (2015)
Diffusivity electrolyte	D^l	$3.197 \times 10^{-10} [m^2/s]$	319.7	Valoen and Reimers (2005)

Table 4.2 shows that although the electrode and electrolyte materials can exhibit Li/Li⁺ dependent conductivities and diffusivities, their values are set constant across each phase for simplicity (Hong and Viswanathan, 2018; Cogswell, 2015).

4.2 Spatial variation of variables

We study the spatial variation of the phase-field, Li-ion concentration, and electric potential at the initial stage and two different times (100[s] and 200[s]) for a

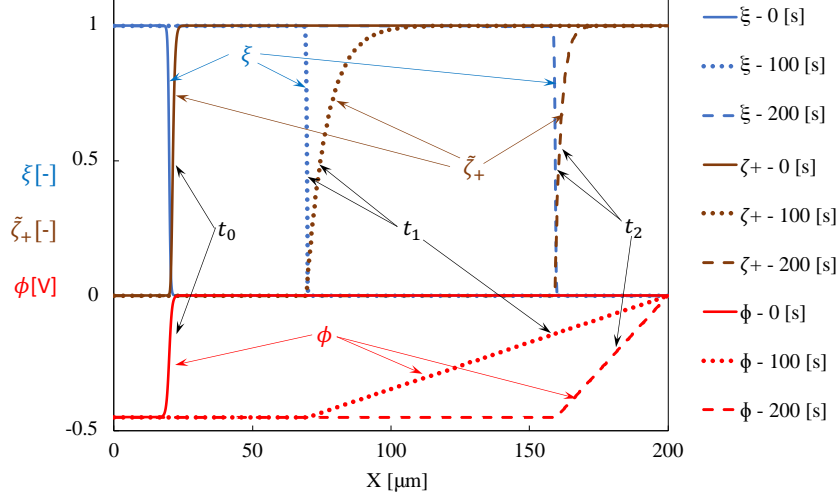


Figure 4.2: Spatial variation of phase-field (ξ), Li-ion concentration ($\tilde{\zeta}_+$), and electric potential (ϕ) in electrode-electrolyte system during charging ($\phi_b = -0.45$ [V]) at $t_0 = 0$ [s] (solid), $t_1 = 100$ [s] (dotted), and $t_2 = 200$ [s] (dashed).

flat interface (one-dimensional simulation) as Figure 4.2 shows. These results illustrate our set of initial conditions, as well as the evolution of our system's variables $\Xi = (\xi, \tilde{\zeta}_+, \phi)$ by solving three coupled (3.17), (3.22), (3.30). This model corresponds to a phase-field derivation from a free energy functional. The growth of Li deposit starts when we apply a negative voltage ($\phi_b = -0.45$ [V]) to the cell (charging state). We use a phase-field interface thickness of $\delta_{\text{PF}} = 1$ [μm], with spatial resolution of $h = 0.25$ [μm] (mesh size) combined with time step adaptivity (Labanda et al., 2022; Hairer and Wanner, 2010).

Figure 4.2 shows that the electrode-electrolyte interface moves as lithium deposits on the electrode surface as time progresses. The electrodeposition evolution results in a steeper distribution of Li-ion concentration at the electrode-electrolyte interface (compare the concentration profile at $t_1 = 100$ [s] and $t_2 = 200$ [s]), due to the increase of the electric potential gradient (migration forces) as the inter-electrode distance shortens. Finally, in agreement with the experimental observations of Nishikawa et al. (2011), the electrodeposition velocity increases over time (compare the interface position at $t_1 = 100$ [s] and $t_2 = 200$ [s]). The planar interface simulation presented here took about 5 minutes to be completed using

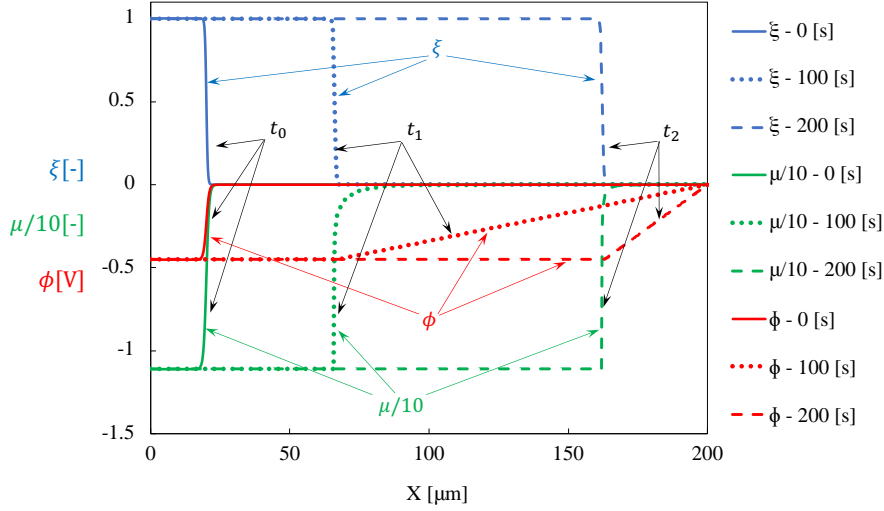


Figure 4.3: Spatial variation of phase-field (ξ), chemical potential (μ), and electric potential (ϕ) in electrode-electrolyte system during charging ($\phi_b = -0.45$ [V]) at $t_0 = 0$ [s] (solid), $t_1 = 100$ [s] (dotted), and $t_2 = 200$ [s] (dashed).

a regular computer (laptop with a 2.4 GHz processor with 8-core Intel Core i9 and 16 GB 2667 MHz DDR4 RAM).

We repeat the simulation switching lithium-ion concentration ($\tilde{\zeta}_+$) for chemical potential (μ) as a dependent variable (grand canonical formulation) (Yan et al., 2018; Hong and Viswanathan, 2018; Plapp, 2011). Even though the grand canonical approach was recently applied to other phase-field models of electrokinetics (Cogswell, 2015; Hong and Viswanathan, 2018), to the best of our knowledge, there was no evidence comparison between the performance of each formulation in this field. Thus, we verify the agreement between simulation results and identify advantages and disadvantages of each approach. Figure 4.3 shows the initial conditions for the grand canonical approach, as well as the evolution of our system's variables (ξ, μ, ϕ) by solving three coupled equations. Again, we apply a negative voltage ($\phi_b = -0.45$ [V]) to the cell (charging state). These results show a distribution of field variables similar to that of the free energy approach.

Furthermore, Figure 4.4 shows the agreement between the lithium-ion concentration ($\tilde{\zeta}_+$) at different phase-field interface positions (l_t), using the free energy formulation and the grand canonical approach when using sigmoid smoothing

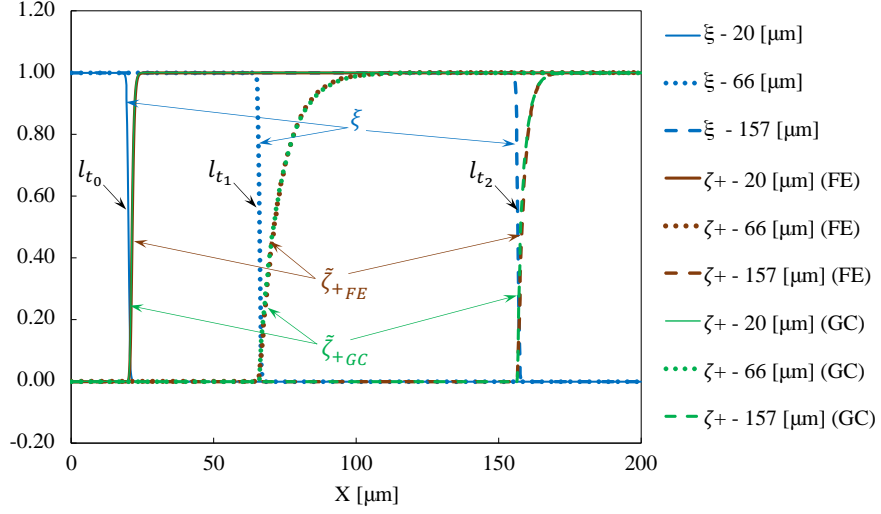


Figure 4.4: Lithium-ion concentration ($\tilde{\zeta}_+$) comparison between free energy (FE) and grand canonical (GC) approaches using sigmoid smoothing (4.1). Phase field (ξ) (blue) for reference; Charge: $\phi_b = -0.45$ [V]; $l_{t_0} = 20$ [μm] (solid), $l_{t_1} = 66$ [μm] (dotted), and $l_{t_2} = 157$ [μm] (dashed).

(Plapp, 2011):

$$\tilde{\zeta}_+ = \frac{C_m^l}{C_0} e^{\left(\frac{\mu - \epsilon^l}{RT}\right)} \left[1 + e^{\left(\frac{\mu - \epsilon^l}{RT}\right)} \right]^{-1}. \quad (4.1)$$

Figure 10 shows a steeper Li^+ concentration distribution as the front approaches the opposite electrode ($l_{t_2} > l_{t_1}$); since proximity induces a higher electric potential gradient ($\nabla\phi$) as the model approaches the battery short-circuit condition. This produces an increase of the Li^+ concentration at the electrode-electrolyte interface ($\xi = 0.5$), from $\tilde{\zeta}_+ = 0.03$ at $l_{t_1} = 66$ [μm], to $\tilde{\zeta}_+ = 0.06$ at $l_{t_2} = 157$ [μm], leading to faster rates of lithium electrodeposition according to (3.17).

4.3 One-dimensional sensitivity analysis

4.3.1 Theoretical Faradic model

We compare our planar interface phase-field results against the theoretical Faradic model, used to theoretically interpret the growth rate of a uniform deposited film

(Nishikawa et al., 2011; Akolkar, 2013). The theoretical operating current density across the flat electrode surface is $i_t = \phi_b / \left(\frac{l_t}{\sigma^s} + \frac{l_x - l_t}{\sigma^l} \right)$, where ϕ_b , σ^s , σ^l , l_x and l_t , are the applied voltage, electrode and electrolyte conductivities, battery cell size, and the electrode surface position at time t , respectively. Therefore, we compute the theoretical electrodeposited film thickness, $\lambda = l_t - l_0$, integrating Faraday's law 3.4 over time as follows:

$$\lambda = \frac{\int_0^t i_t dt}{nFC_m^s}. \quad (4.2)$$

In (4.2), we define a set of electrode positions $\{l_{t_i} \in \mathbb{R} \text{ s.t. } l_0 \leq l_{t_i} \leq l_x\}$, using a small interval size between these positions (i.e., $\Delta l_t = 0.01 [\mu m]$ achieves convergence). We calculate the theoretical current density $i_{t_i}(l_{t_i})$ for each position, and estimate the Faradic electrodeposition rate, $v(t_{n+1})$, using the forward Euler method:

$$v = \frac{\lambda(t_{n+1}) - \lambda(t_n)}{t_{n+1} - t_n} = \frac{l_t(t_{n+1}) - l_t(t_n)}{t_{n+1} - t_n}. \quad (4.3)$$

Thus, solving for t_{n+1} from (4.3), we obtain a set of t_i vs l_{t_i} values that allows for comparison with phase-field model predictions within a range of charging voltages as presented in the following sections.

4.3.2 Applied overpotential

We compare the electrodeposition rates predicted by the free energy ($\tilde{\zeta}_+$) and grand canonical (μ) approaches under different applied voltages. Figure 4.5 displays the electrodeposition position ($\xi = 0.5$) over time for different applied voltages ($\phi_b = -0.45, -0.60, -0.75 [V]$).

Figure 4.5 shows the grand canonical approach (dotted lines) is more sensitive to changes in the applied voltage than the conventional free energy formulation (dashed lines). Taking the position of the electrode after $t = 20 [s]$ as an indication of the electrodeposition rate, we obtain relative position differences of 9.75%, 10.9%, and 11.5% for the free energy approach under -0.45, -0.60 and -0.75[V], respectively. The grand canonical approach results in larger relative position

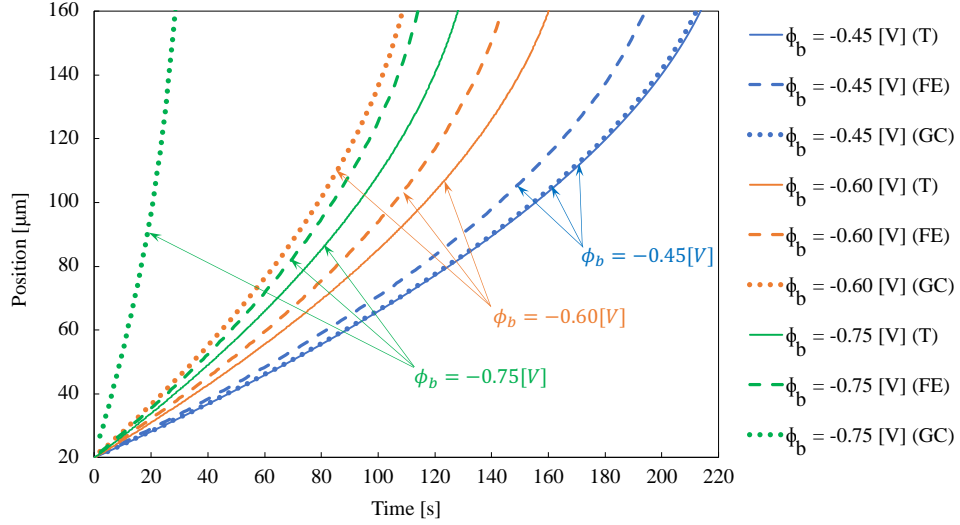


Figure 4.5: Interface position vs time for different applied voltages: theoretical rate (T) (4.2) (solid), simulation results under free energy (dashed), and grand canonical (dotted) approaches.

differences of 1.22%, 51.8%, and over 400% under identical charging conditions. Although we obtain good agreement with the Faradic theory (solid line) using the grand canonical approach to model the lowest applied voltage ($\phi_b = -0.45 [V]$), we obtain consistent reaction rates (with comparable position differences under various charging conditions) for the conventional free energy approach ($\tilde{\zeta}_+$).

4.3.3 Phase-field interface thickness

We select an appropriate phase-field interface thickness (δ_{PF}) by analyzing its effect on the simulated electrodeposition rate, which ultimately determines the evolution time scale (motion) of the electrodeposits. Figure 4.6 displays a comparative analysis of the simulated electrodeposit position ($\xi = 0.5$) over time for different values of interface thickness ($\delta_{PF} = 1, 5, 10 [\mu m]$) under an applied voltage of $\phi_b = -0.45 [V]$.

Figure 4.6 shows that the phase-field interface thickness significantly affects the simulated reaction rates; wider interfaces (larger δ_{PF}) induce extremely fast electrodeposition rates, up to 200% greater than theoretical results. These discrepancies have a physical justification: electrodeposition occurs at the electrode-

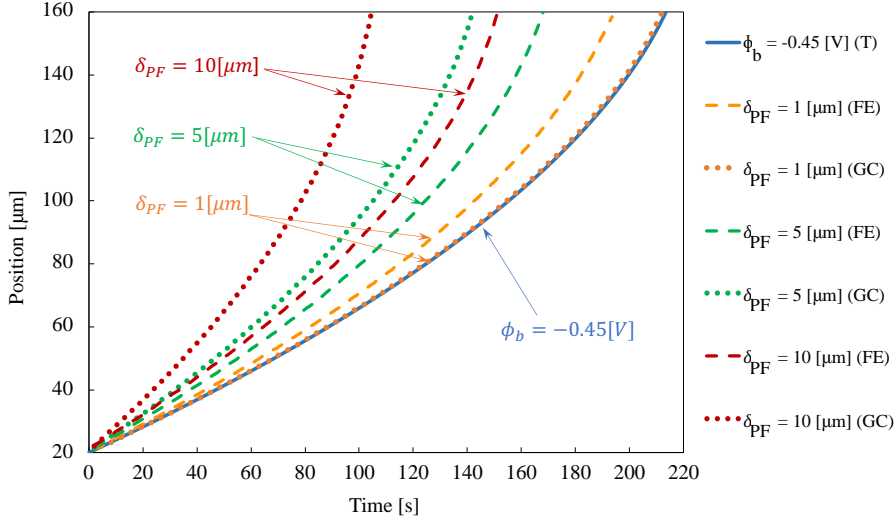


Figure 4.6: Interface position vs time for different phase-field interface thickness ($\delta_{PF} = 1, 5, 10 [\mu m]$) for applied voltage $\phi_b = -0.45 [V]$: theoretical rate (4.2) (solid), free energy (dashed), and grand canonical (dotted) approaches.

electrolyte interface; thus, expanding the interface for computational reasons (physical interfaces can be as small as $5 [nm]$ (ichi Morigaki, 2002)) increases the reactive area in the simulation, which induces faster than physical electrodeposition rates. However, as Figure 4.6 and the position analysis below illustrate, convergent electrodeposition rates (interface-thickness-independent growth) are possible well before reaching the nanometer width interfaces. Figure 4.6 includes results for the free energy and grand canonical approaches. Let the electrode position at $t = 100 [s]$ be a correlate of the electrodeposition rate, we compute position differences of 10.0%, 29.8%, and 47.2% for the free energy approach using 1, 5 and $10 [\mu m]$ interface thicknesses, respectively; alternatively, the grand canonical approach yields relative position differences of 0.43%, 62.6%, and 168% for the same interface thickness values. Therefore, the grand canonical results (dotted lines) are more sensitive to changes in δ_{PF} than those of the conventional free energy formulation (dashed lines).

In short, the grand canonical formulation has greater sensitivity to both the phase-field interface thickness and the applied electric potential value, which practically restricts when the negative applied voltages ($\phi_b < -0.50 [V]$) we may

simulate in 2D and 3D applications.

4.4 Tafel plot: Sharp-interface Butler-Volmer

Reaction rates sensitive to negative applied voltages (see Figure 4.5) guide our detailed analysis of the grand canonical approach using different phase-field interface thicknesses. We did not conduct a similar study of the free energy approach due to its significantly lower sensitivity to the interface thickness and applied voltage as per Figure 4.5 and Figure 4.6. We study the interface position plotting it as a function of time for different applied electric potential values in Figure 4.7. An interface thickness of $\delta_{PF} = 0.5 [\mu m]$ yields a good agreement with the theoretical Faradic rates under -0.40 , -0.45 , and $-0.50[V]$ applied voltages with a spatial resolution of $h = 0.125 [\mu m]$ (mesh size) allows for four elements to span the phase-field interface.

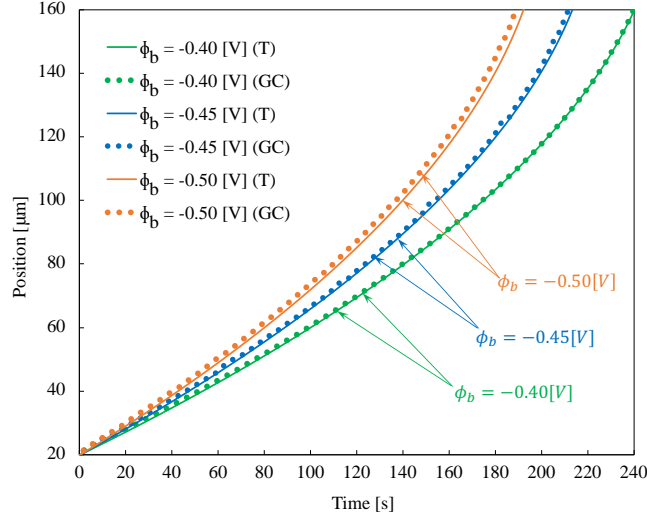


Figure 4.7: Interface position vs time for different applied voltages: theoretical electrodeposition rate (4.2) (solid); simulation results (grand canonical formulation; dotted). Phase-field interface thickness $\delta_{PF} = 0.5 [\mu m]$, and $h = 0.125 [\mu m]$ mesh size.

Figure 4.7 shows that the electrodeposition rate accelerates (curved) as the interface approaches the opposite electrode (battery short-circuit condition) (Liang

and Chen, 2014; Nishikawa et al., 2011; Monroe and Newman, 2003). This result agrees with the mathematical model (solid lines), where the deposition rate has a nonlinear relationship. We obtain larger electrodeposition rates under more negative electric potential values (faster battery charge).

We calculate the current density relation to the electrodeposition velocity v using (3.4). The current density increases as the electrode progresses to the opposite side, producing a nonlinear relationship with the total overpotential (η), as Figure 4.8 depicts; which satisfies the sharp-interface Butler-Volmer equation: $i = i_0 \left(e^{-\frac{\alpha n F \eta}{RT}} - e^{\frac{(1-\alpha) n F \eta}{RT}} \right)$. Figure 4.8 shows that as the deposit approaches the opposite electrode, the overpotential slightly increases with time (Subramanian et al., 2009), which corresponds to the reaction rate increase due to the Li^+ concentration increase at the electrode-electrolyte interface.

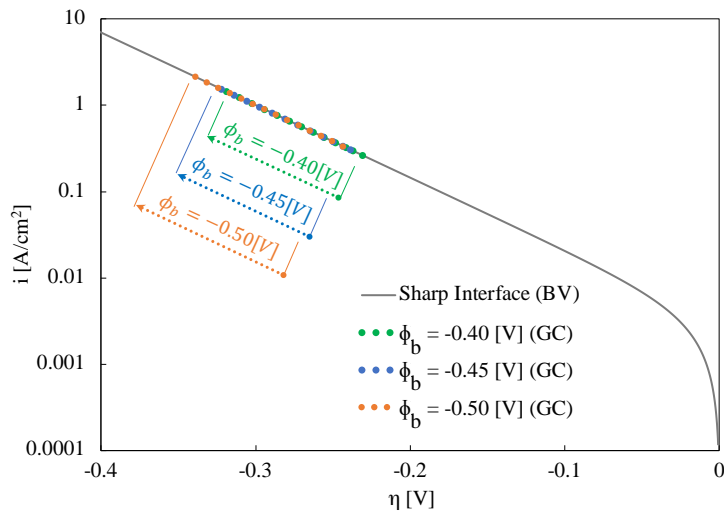


Figure 4.8: Tafel plot: Comparison of the phase-field model (dotted lines) with the sharp-interface Butler-Volmer equation (solid line) under different electric potential values.

4.5 Convergence test

We perform a spatial convergence analysis to verify the convergence rates and quantify the mesh-induced error. We compare flat interface simulation results for

different spatial resolutions, $n_x = 400, 800, 1600, 3200, 12800$; (with a domain size of $l_x = 200 [\mu m]$), using a small time-step size ($\Delta t = 6.25 \times 10^{-4} [s]$) to neglect the temporal error, such that $\frac{\Delta t/t_0}{h_{min}/h_0} \ll 1$, where $h_{min} = 0.015625 [\mu m]$ is the finest mesh size.

The position of the electrodeposit interface ($\xi = 0.5$) is the basis of our comparison, since it is the parameter that defines the reaction rate (time-scale) in our simulation. Starting with a $20 [\mu m]$ -thick metal anode, separated from the liquid electrolyte by a $1 [\mu m]$ interface; we compute the final phase-field interface position (electrode position) after $20 [s]$ of simulation under an applied electric potential value of $\phi_b = -0.45 [V]$, a commonly used electric potential in the literature (Chen et al., 2015; Cogswell, 2015; Hong and Viswanathan, 2018), using different mesh sizes. The spatial convergence analysis reveals that we obtain grid-independent results after sufficient mesh refinement (see Figure 4.9). The agreement between the $h = 0.015625 [\mu m]$ and $0.03125 [\mu m]$ results (finest and second finest meshes) is of 99.99% and 99.93%, for the free energy formulation and the grand canonical approach, respectively.

Figure 4.9 plots the relative error evolution over the mesh size (h). We compute the electrode position errors, relative to the finest mesh resolution (most accurate), as follows: $\varepsilon = \frac{X_{h_{min}} - X_{h_i}}{X_{h_{min}} - X_{IC}} \times 100$, where $X_{h_{min}}$, X_{h_i} and X_{IC} , are the electrode position of the finest spatial resolution, the current mesh result, and the electrode's initial thickness (initial position of the phase-field interface), respectively.

Hence, the mesh-induced errors we compute are lower than 5% for the grand canonical approach, and 1.5% for the free energy functional, when utilising the coarsest spatial resolution ($h = 0.5 [\mu m]$, and two linear elements spanning the phase-field interface) to simulate electrodeposition process under $\phi_b = -0.45 [V]$. The mesh-induced errors do not significantly affect the electrodeposition rate, compared to the previous ones when varying the phase-field interface thickness.

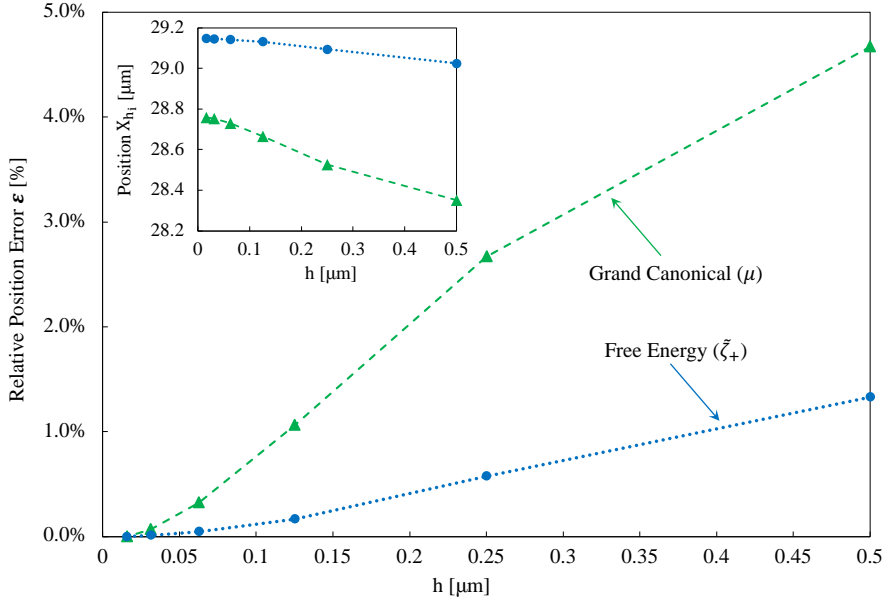


Figure 4.9: Relative position error “ ε ” at $t = 20$ [s] vs mesh sizes h [μm], using free energy (blue), and grand canonical (green) formulations. The inset shows the interface position “ X_{h_i} ” vs mesh sizes h [μm], using both formulations. Phase-field interface thickness $\delta_{PF} = 1$ [μm].

4.6 Conclusions on planar interface simulations

We perform phase-field simulations to describe the flat electrode evolution during metal (lithium) electrodeposition. We demonstrate the validity of the current model by comparing the simulation results with theoretical Faradic reactions and the kinetics of the sharp-interface Butler-Volmer model.

The comparison analysis between simulations using a phase-field model derived from either a free energy functional or a grand canonical approach allows us to assess each model’s sensitivity to the simulation and physical parameters and their robustness. In short, we obtain more consistent results (with comparable position differences under various charging conditions) for the conventional free energy approach. This model shows less sensitivity to changes in the phase-field interface thickness and under different applied voltages than the results obtained using the grand canonical formulation. In particular, we required smaller phase-field interface thicknesses (δ_{PF}), with higher mesh resolution, to

capture faster reaction rates under more negative electric potential values using the grand canonical formulation. Consequently, the computational cost significantly increases, making this class of models intractable for applications in two- or three-dimensions under large negative applied voltages involving dendrite growth under fast battery charge.

The higher sensitivity observed under the grand canonical approach can be explained by the effect of Li-metal diffusivity in the flux of Lithium species. The derivation of the grand canonical diffusion equation by Hong and Viswanathan (2018) does not consider the Li-metal diffusivity effect by assuming it to be much smaller than the diffusivity of Li-ion (Cogswell and Carter, 2011). This flux assumption creates an inconsistency in the diffusion equation via the grand canonical approach; where the chemical potential of all lithium species μ only considers the contribution of the flux of lithium-ion species \vec{J}_+ (please refer to Section 3.1.2 for further explanation).

Additionally, the spatial convergence analysis shows that the mesh-induced errors of up-to 5% for the grand canonical approach, and 1.5% in case of the free energy functional become grid independent (99.99% agreement) after sufficient refinement. Interestingly, these mesh-induced errors have a significantly lower impact in the electrodeposition rate, than those computed by varying the interface thickness (up to 47.2% and 168% relative position differences for the free energy and grand canonical approaches, respectively).

Finally, beyond lithium electrodeposition, this class of phase-field models can appropriately describe other metal deposits in metal-anode batteries, such as zinc anode batteries. The use of one-dimensional simulations as a tool to quantify the resolution requirements of the model under study is an effective strategy, that allows us to set ground rules for further 2D and 3D simulations.

Chapter 5

Phase-field simulations of dendrite formation in rechargeable lithium-metal batteries

This chapter ¹ discuss numerical simulations of dendrite growth in rechargeable lithium-metal batteries. Firstly, a two-dimensional model is verified in terms of dendrite propagation rates and spatial distribution analysis of the system's variables in comparison with phase-field simulation results reported in the literature. Furthermore, three-dimensional spike-like lithium structures that grow under high current density are simulated; these structure's growth is dangerous for battery operation. Single and multiple nuclei numerical experiments are carried out to study the 3D distribution of the electric field and the lithium-ion concentration

¹Parts of the content of this chapter are published in:

- Arguello, M. E., Labanda, N. A., Calo, V. M., Gumulya, M., Utikar, R., & Derksen, J. (2022). Dendrite formation in rechargeable lithium-metal batteries: Phase-field modeling using open-source finite element library. *Journal of Energy Storage*, 53, 104892.
- Arguello, M. E., Labanda, N. A., Calo, V. M., Gumulya, M., Utikar, R., & Derksen, J. (2022). Three-dimensional experimental-scale phase-field modelling of dendrite formation in rechargeable lithium-metal batteries. *Publication under review*.

to understand the mechanism behind spike-growing lithium morphologies better. Finally, a sensitivity analysis of 3D simulations under different mesh resolution and phase-field interface thickness is carried out.

5.1 System layout

Following the simulation set-up presented in Section 4.1, here we model a battery cell with a traditional sandwich architecture, undergoing a recharging process under fixed applied electro potential. We represent this cell as an $l_x \times l_y$ rectangular domain in 2D and as an $l_x \times l_y \times l_z$ hexagonal domain in 3D. The initial perturbation (dendrite nuclei) significantly impacts the simulation outcome. These nuclei are usually part of the problem’s initial conditions. In our experience, the shape of the initial seed and the noise levels have a major influence on the resulting dendrite morphology.

We study two different initial structures. The first structure consists of a $5\mu m$ -thick metal anode ($l_0 = 5 [\mu m]$), made up of pure Lithium, separated from the liquid electrolyte by a smooth interface, as Figure 5.1-a depicts. The initial condition derives from the equilibrium solution for a one-dimensional transition zone between solid ($\xi = 1$) and liquid ($\xi = 0$), where our variables $(\xi, \tilde{\zeta}_+, \phi)$ vary in the “ x ” spatial direction according to: $\frac{1}{2} \left[1 - \tanh \left(x \sqrt{\frac{W}{2\kappa_0}} \right) \right]$ (Boettinger et al., 2002).

In the second structure we assume that artificial nucleation regions, ellipsoidal protrusions (seeds) with semi-axes r_x, r_y, r_z , and center $(0, l_{0y}, l_{0z})$, exist at the surface of the anode undergoing electrodeposition (see Figure 5.1-b). This is a widely-used strategy in phase-field simulations of electrodeposition (Zhang et al., 2014; Chen et al., 2015; Yurkiv et al., 2018; Mu et al., 2019); since it reduces the computational cost as the lithium metal is only able to electrodeposit on the nuclei, enhancing dendrite growth and allowing for detailed study of its morphology. For the artificial nucleation case, we modify the initial condition formula, replac-

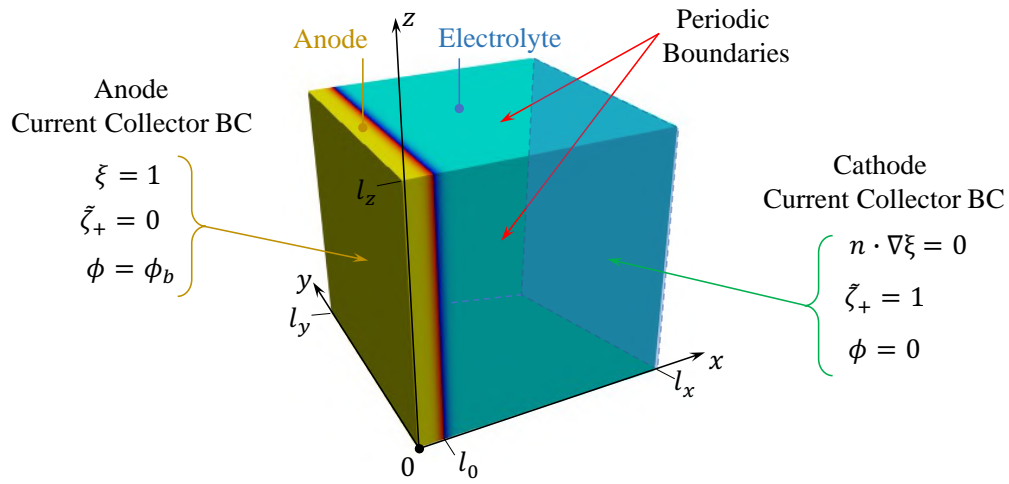
ing “ x ” by $h_0 \left[\left(\frac{x}{r_x} \right)^2 + \left(\frac{y-l_{0y}}{r_y} \right)^2 + \left(\frac{z-l_{0z}}{r_z} \right)^2 - 1 \right]$ within the hyperbolic tangent argument, to account for a smooth transition between the solid seed (lithium metal anode) and the surrounding liquid electrolyte region (Section 4.1).

We model the anode boundary as a Dirichlet boundary condition $\xi = 1$ at $x = 0$ for the phase-field parameter (solid electrode phase). In contrast, we use a no-flux Neumann boundary condition at $x = l_x$ (cathode) to allow the electrodeposition process to take place (ξ changing from 0 to 1) when the reaction front approaches the short-circuit condition (Section 4.1). For the Li-ion concentration, we apply Dirichlet boundary conditions setting $\tilde{\zeta}_+ = 0$ and $\tilde{\zeta}_+ = 1$ at the anode ($x = 0$) and cathode ($x = l_x$) boundaries, respectively. These boundary conditions allow the Li-ion flux into the battery (electrolyte side), ensuring that the Li deposited at the electrode-electrolyte interface equals the amount of Li^+ supplied to the electrolyte. Thus, these boundary conditions avoid the quick Li-ion depletion and keep the electrodeposition process running for the full simulation (Section 4.1). Finally, we apply periodic boundary conditions on the remaining faces; these are $(x, 0, z)$, (x, l_y, z) , $(x, y, 0)$, and (x, y, l_z) . Figure 5.1 summarizes the boundary conditions we apply.

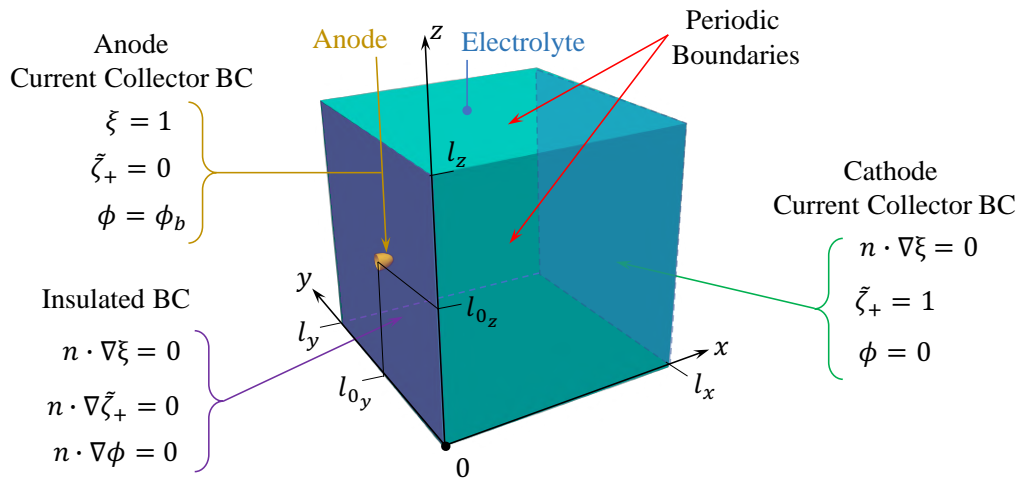
Additionally, Table 5.1 presents the parameters used in the current phase-field model. Note that Table 5.1 only includes those parameters that are missing or differ from Table 4.2. As a default set-up for our 2D and 3D simulations, we adopt $\delta_{PF} = 1.5 [\mu m]$ to achieve a balanced phase-field interface thickness to mesh resolution ratio.

Table 5.1: 2D & 3D Simulation’s Parameters

Description	Symbol	Real Value	Normalized	Source
Phase-field interface thickness	δ_{PF}	$1.5 \times 10^{-6} [m]$	1.5	Section 4.3.3
Barrier height	W	$4.45 \times 10^6 [J/m^3]$	1.78	computed
Gradient energy coefficient	κ_0	$1.25 \times 10^{-6} [J/m]$	0.5	computed
Anisotropy strength	δ_{aniso}	0.044	0.044	(Tran et al., 2016, 2019)
Anisotropy mode	ω	4	4	(Tran et al., 2019; Zheng et al., 2020)
Kinetic coefficient	L_η	$1.81 \times 10^{-3} [1/s]$	1.81×10^{-3}	computed



(a) Planar electrode.



(b) Artificial nucleation.

Figure 5.1: Boundary conditions for planar electrode (a) and artificial nucleation (b) simulations.

5.2 Two-dimensional simulations of lithium dendrite formation

5.2.1 Lithium dendrite propagation rate: Consistency with experimental data

Validation of phase-field models with experimental results is a well-known challenge of electrodeposition simulations (Cogswell, 2015); partly due to the computational cost of simulating the detailed lithium electrodeposition at the whole-cell scale (Yurkiv et al., 2018). One limiting factor is the domain size, defined by the inter-electrode separation distance in experimental cells, which ranges from 1 to 10[mm] (Nishikawa et al., 2011; Nishida et al., 2013; Yufit et al., 2019).

We perform 2D simulations to compare our simulations against experimental results obtained from thin-cell geometries. We use 2D simulation results to validate the predicted lithium dendrite propagation rates, assuming that the electrodeposition rates are not significantly affected by the problem’s dimensionality.

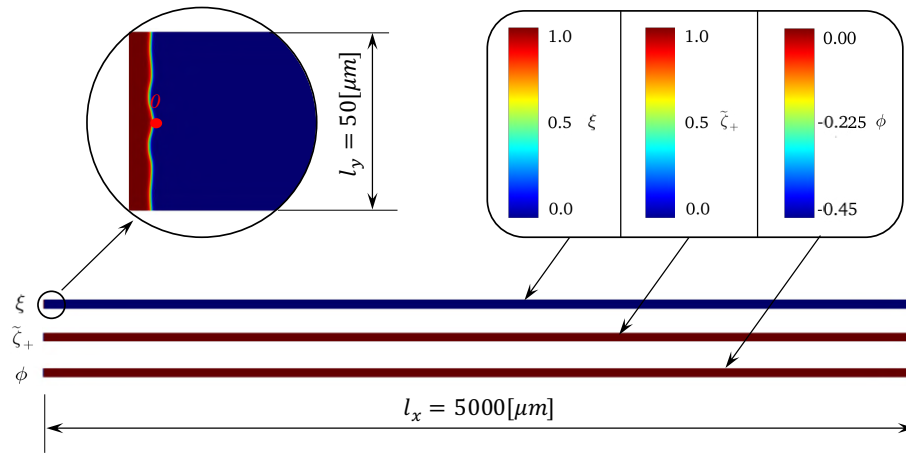
We achieve large domain sizes through several computational efficiency improvements. We use a sigmoid interpolating function (Chapter 3) instead of the polynomial interpolating function (Zhang et al., 2014; Liang and Chen, 2014; Chen et al., 2015). We use time-step size adaptivity and mesh mapping in the region of interest (close to the electrode-electrolyte interface). We also use parallel solution strategies and carefully select the phase-field interface thickness (δ_{PF}), given the interface thickness effect on the electrodeposition rate, which ultimately determines the evolution dynamics (motion) of the lithium electrodeposits (Chapter 4).

We compare the simulated lithium dendrite propagation rate against the experimental measurements of Nishikawa et al. (2011). Nishikawa et al. (2011) studied the dendritic electrodeposition of lithium as a function of total charge (electric current over time) using microscope observations. They reported den-

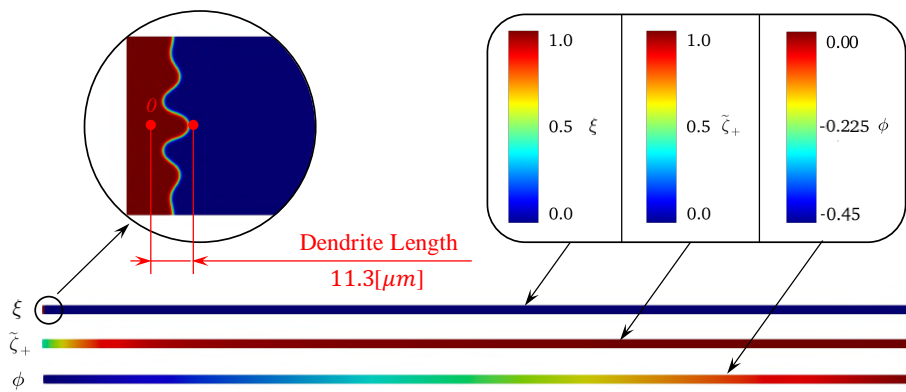
drite growth rates of $0.01 - 0.06 [\mu m s^{-1}]$ (Akolkar, 2014) using a 1M LiPF₆ electrolyte, establishing upper and lower bounds for comparison with our simulation results. The wide range of values reported in many studies (Crowther and West, 2008; Nishikawa et al., 2011, 2010) may be caused by the uneven current distribution on the electrode surface (Nishikawa et al., 2011).

We simulate a lithium electrodeposition process at an applied current density of $i = 10 [mA/cm^2]$ (Nishikawa et al., 2011). We use a 2D rectangular domain $l_x = 5000 [\mu m]$ long (distance between electrodes), and $l_y = 50 [\mu m]$ wide (sufficient width to allow dendrite formation). We use a mesh $8,000 \times 140$ elements, with mesh distribution that guarantees an x -spatial resolution of approximately $0.35 [\mu m]$ ($h < 4\delta_{PF}$) in the region of interest of the domain with square elements. We apply a charging electro potential of $\phi_b = -0.45 [V]$ to the cell (a common value in the literature (Chen et al., 2015; Hong and Viswanathan, 2018; Cogswell, 2015)), more negative than the threshold overpotential for dendrite growth $\phi_b = -0.37 [V]$ (Hong and Viswanathan, 2018). We perturb the initial electrode surface by $(\pm 0.5 [\mu m])$ in x -direction to promote dendrite formation at the center of the domain ($\frac{l_y}{2} = 25 [\mu m]$).

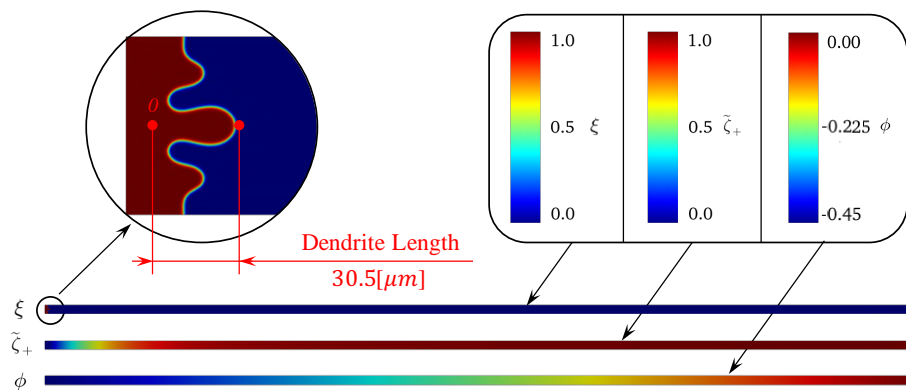
Figure 5.2 shows the initial conditions ($t = 0 [s]$) and the evolution of the system's variables $(\xi, \tilde{\zeta}_+, \phi)$. We zoom on the phase-field variable ξ at each instant to emphasize the growth of the lithium dendrite and show the instantaneous dendrite length measurement.



(a) $t = 0$ [s].



(b) $t = 400$ [s].



(c) $t = 800$ [s].

Figure 5.2: 2D phase-field simulation of lithium electrodeposition process at a current density of $i = 10$ [mA/cm²] with a distance of $l_x = 5000$ [μm] between electrodes.

Figure 5.3 shows the evolution of the simulated lithium morphology length over time, within the range of experimental data (Nishikawa et al., 2011). Further well-controlled experimental studies, with detailed characterization of the system parameters (transport and kinetic properties), may be necessary to improve the correlation (Akolkar, 2014).

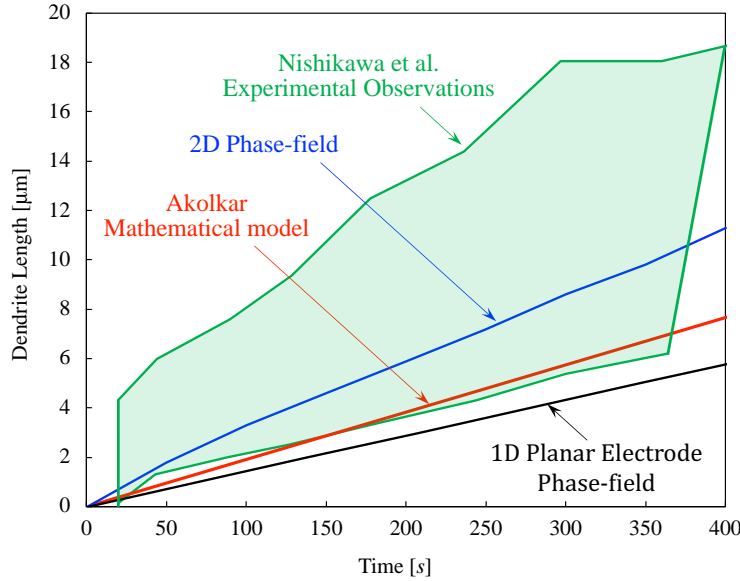


Figure 5.3: Comparison between 2D phase-field simulations of lithium dendrite growth at a current density of $i = 10 [mA/cm^2]$ (blue), experimental data taken from Nishikawa et al. (2011) (green), and the Akolkar (2014) analytical model predictions (red). 1D planar electrode phase field simulation for reference (black).

Additionally, Figure 5.3 includes analytical dendrite propagation results for the tip current density developed by Akolkar (Akolkar, 2014) for comparison. Akolkar’s model calculates the dendrite propagation rate by analyzing various overpotentials that develop at the dendrite tip and the flat electrode surface, assuming a current density of $i = 10 [mA/cm^2]$ applied and a constant radius of $r = 1 [\mu m]$ at the dendrite’s tip. This simplification constitutes departures from our phase-field model, where the dendrite’s tip radius is variable throughout the simulation. This difference explains the higher growth rate obtained in our simulations. Furthermore, we also include 1D planar electrode phase-field results using an identical set-up as to the 2D simulation (Chapter 4).

5.2.2 Bush-like lithium dendrite: Verification of 2D simulation results

The following 2D numerical experiment compares our model's features to other phase-field simulations reported in the literature. In this case, we use a 2D square domain set as $360 \times 360 [\mu m^2]$, within the range of typical distances between electrodes in metal anode batteries (Bai et al., 2018). We use a 500×720 structured mesh with a mapping in the x -direction to obtain square elements of size $0.5 \times 0.5 [\mu m^2]$ in the region of interest (see Section 5.3.1 for details). We apply a charging electro potential of $\phi_b = -0.7 [V]$ to the cell, with an artificial nucleation region with 3 protrusions (ellipsoidal seeds), equally spaced, growing from the left boundary, with semi-axes $4 [\mu m] \times 1 [\mu m]$. Figure 5.4 shows the evolution of our system's variables $(\xi, \tilde{\zeta}_+, \phi)$ at different time steps, with the ξ field showing the dendrite morphology. The 2D simulation presented here took about 15 hours to be completed, about 180 times longer than previous 1D simulations using the same computer.

Figure 5.4 shows the evolution of bush-like lithium dendrite formation, with morphological agreement to dendritic patterns reported in previous phase-field studies of dendrite growth (Yurkiv et al., 2018; Chen and Pao, 2021). The lithium dendrites grow from each nucleation site and move towards the opposite electrode, following the electric field ($\vec{E} = -\nabla\phi$). As the dendrite grows, side branches appear, growing across the electrolyte, in qualitative agreement with lithium dendrite experiments (Bai et al., 2016). The computed width range of lithium branches is between 5 and 13 $[\mu m]$. These bush-like morphologies grow fast across the electrolyte region and penetrate through porous separators, becoming potentially dangerous as they can produce battery short circuits (Bai et al., 2018). The lithium-ion concentration $\tilde{\zeta}_+$, and electric potential field ϕ , show similar spatial distribution as reported in other phase-field models of lithium dendrite growth (Yurkiv et al., 2018; Liang and Chen, 2014). The lithium-ion concentration remains equal to the bulk concentration, $\tilde{\zeta}_+ = 1$, through the electrolyte

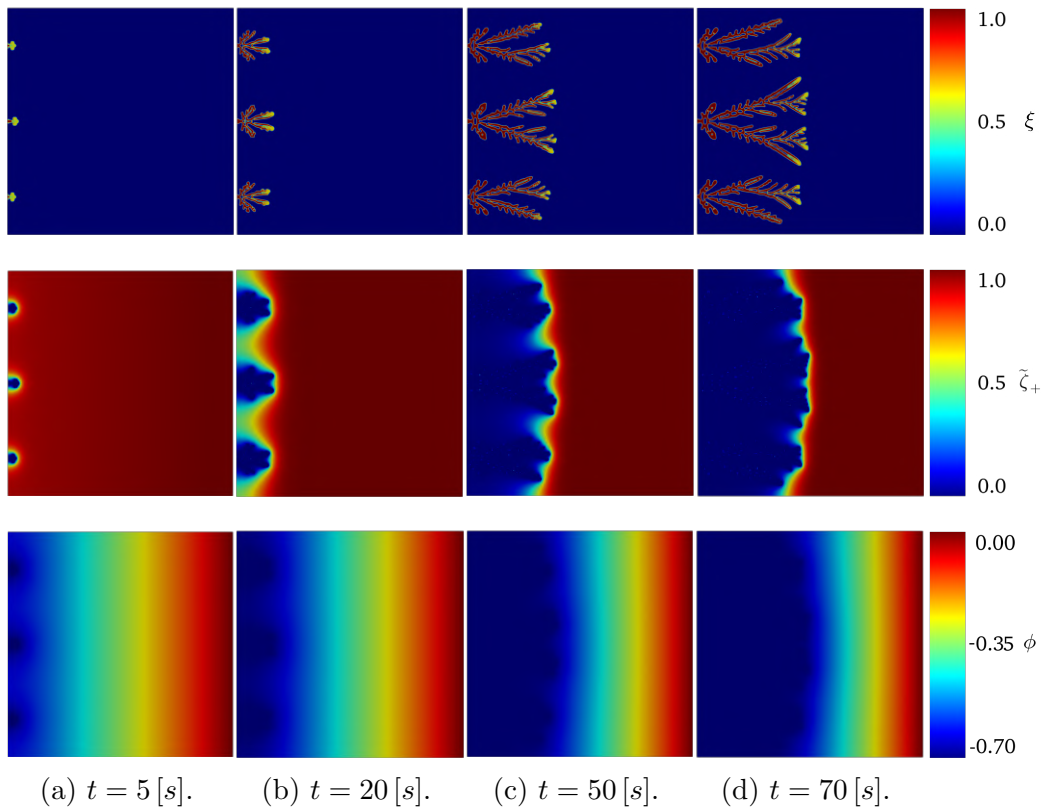


Figure 5.4: 2D phase-field simulation of bush-like lithium dendrite formation under $\phi_b = -0.7$ [V] charging potential. The upper row shows the lithium solid-phase evolution ξ ; the second row shows the lithium-ion distribution $\tilde{\zeta}_+$; and the third row shows the electric potential field ϕ . Square domain set as 360×360 [μm^2].

phase and decreases near the dendrite front (solid phase) due to the electrodeposition process (Chen et al., 2015). The electric potential has a small gradient that spreads over the electrolyte phase and remains constant and equal to ϕ_b at the electrode phase. As the lithium dendrite moves across the electrolyte region, the gradient of the electric potential (electric field) increases, in agreement with simulation results reported by Hong et al. (Liang and Chen, 2014).

Figure 5.5 illustrates the interplay between the weighted truncation error estimate e_{n+1} (3.49) (blue) and the time-step size evolution Δt_{n+1} (3.50) (red), throughout the 70 [s] of simulation. The figure shows that the simulation initially requires a small time-step size of $\Delta t_0 = 10^{-10}$ [s] to converge as the phase field develops its interface thickness and the ion concentration and electro potential

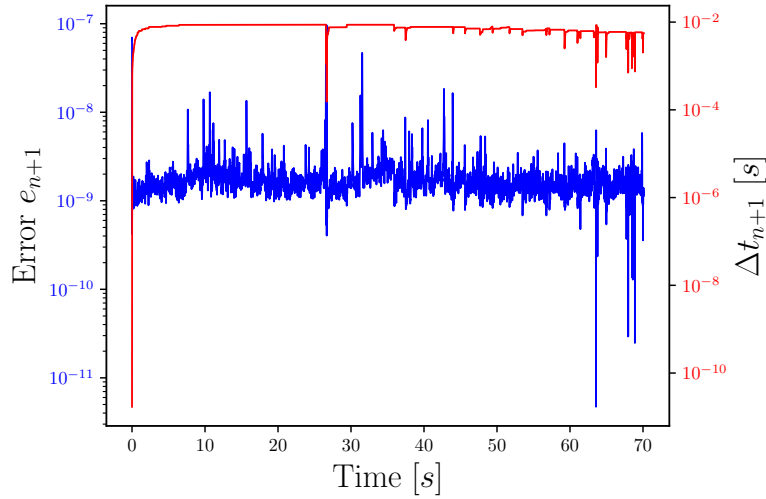


Figure 5.5: Performance of time-adaptive strategy in 2D lithium dendrite growth simulation. Weighted local truncation error (blue) and time-step size (red) vs time.

distributions achieve equilibrium. The time-step size increases sharply, achieving a stationary size of $\Delta t_{n+1} = 10^{-2}$ [s], after 5 [s] of simulation. In addition, the time-step size starts to decrease slightly after 40 [s], which corresponds with the acceleration of lithium dendrite propagation rate as it approaches the opposite electrode (Liang and Chen, 2014). The maximum and minimum tolerances for the time-adaptive scheme are 10^{-7} and 10^{-9} in this case, allowing the time-step size to decrease or increase accordingly when error tolerances bounds are reached.

In addition to previous 1D planar interface studies presented in Chapter 4, the current 2D simulations complete the groundwork setting for 3D phase-field simulations of lithium dendrite formation. This include successful 2D testing of the numerical parameters previously defined through 1D electrodeposition studies, such as phase field interface thickness and mesh resolution. The 2D numerical examples have assessed the framework’s effectiveness to capture the two-dimensional development of lithium electrodeposits, starting from a planar electrode configuration as well as using artificial nucleation sites. The validation of the predicted lithium dendrite propagation rates against experimental results obtained from thin-cell geometries has confirmed the reliability of the proposed model. Furthermore, the

agreement attained between the simulated lithium dendrite morphology, Li-ion and electric potential distribution with simulation results reported in other phase-field models of lithium dendrite growth, verifies our work as a preliminary step to continue with a series of larger and more complex 3D simulations of lithium dendrite growth in metal anode batteries next in this work.

5.3 Three-dimensional simulations of lithium dendrite formation

5.3.1 3D single nucleus simulation

This section describes 3D phase-field simulations of lithium dendrite formation to study highly branched "spike-like" dendritic patterns, commonly observed experimentally. These patterns form under high current density, which correspond to fast battery charge (Jana et al., 2019; Ding, 2016; Tatsuma et al., 2001). We select a geometrical unit that characterizes a real cell structure (Yurkiv et al., 2018; Trembacki et al., 2019). We choose a computational domain of $80 \times 80 \times 80 [\mu m^3]$. Consequently, given the domain size, we expect growth rates up-to two orders of magnitude faster than experimental results by Nishikawa et al. (2011); Nishida et al. (2013), due to the short separation between electrodes $l_x = 80 [\mu m]$ (close to short-circuit condition).

We use a 3D structured mesh with eight-node hexahedral elements. We distribute the mesh to focus the node's mapping on the area of interest (see Figure 5.6a). In particular, in the x -direction $x_r = (2/\pi) \arcsin(x_u)$; where x_u is the node's x coordinate normalized by l_x , before mapping (uniform distribution), and x_r is the node's mapped coordinate. The arcsin function transitions smoothly, inducing a relatively small variation in the mesh size within 50% of the physical domain where the lithium electrodeposit process occurs (Yurkiv et al., 2018; Mu et al., 2019; Zhang et al., 2021). The mapping produces a finer mesh to properly

capture the phase-field interface thickness (4 elements in the interface, as defined in Section 4.5) and the steepest gradients of $\tilde{\zeta}_+$ and ϕ . We use a 120^3 tensor-product mesh with a mesh size of $0.4 [\mu m]$ in the region of interest (bottom half of the domain). The mesh is divided in eight partitions, one for each processor. We verify that the computational efficiency achieved under the proposed number of partitions is close to optimal for the current 3D problem, in agreement with previous work performed by Mu et al. (2020).

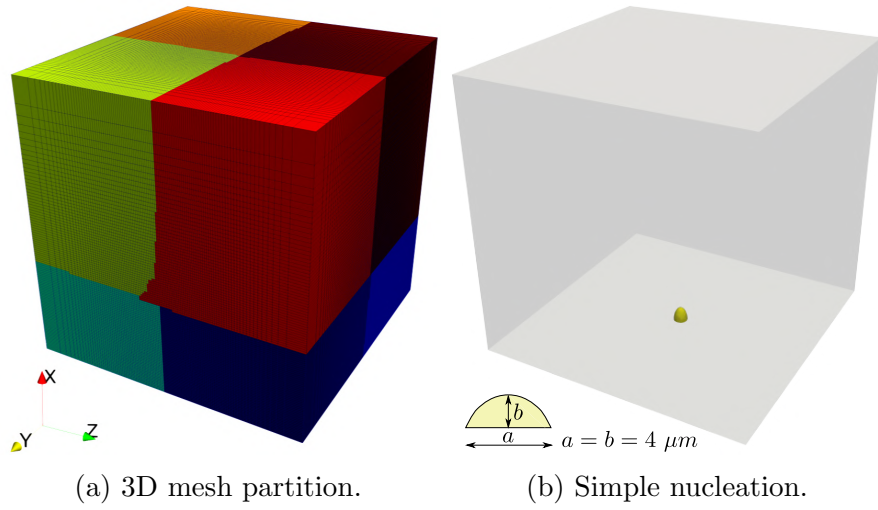


Figure 5.6: The mesh is divided in eight partitions, one for each processor, represented by a different color (a), and geometry of the initial protrusion for the simple nucleation experiment (b). Cube domain set as $80 \times 80 \times 80 [\mu m^3]$.

Figure 5.6a identifies each core with a different color, showing that the tensor-product mesh can efficiently allocate resources in the region of interest (more resources/colors allocated to the bottom half of the domain). We apply a charging electro-potential value of $\phi_b = -0.7 [V]$ to the cell, with an artificial nucleation region formed by a single protrusion (ellipsoidal seed), with its center at $(0; l_y/2; l_z/2)$, and semi-axes $4 [\mu m] \times 2 [\mu m] \times 2 [\mu m]$ as Figure 5.6b shows. For visualization purpose, here we rotate the 3D figures to depict a vertical x -axis, showing an upright lithium dendrite growth, in agreement with the convention used for lithium dendrite experiments (Nishikawa et al., 2011; Ding, 2016; Tatsuma et al., 2001).

Figure 5.7 shows the morphological evolution of the simulated lithium dendrite (isosurface plot of the phase-field variable ξ). The 3D simulation presented here took about 1 week to be completed, more than 10 times longer than previous 2D simulations using the same computer.

The simulation forms a spike-like, symmetric, and highly branched pattern, consisting of the main trunk and sets of four equal side branches growing in each horizontal direction. A result consistent with the body-centered cubic (bcc) crystallographic arrangement of lithium metal (Yurkiv et al., 2018). Our model includes the four folded surface anisotropy (3.10). In-situ optical microscopic investigations (Ding, 2016; Tatsuma et al., 2001) report spike-like lithium dendrite formation. These dendritic patterns grow when high (over-limiting) current densities are applied to the cell (Bai et al., 2018). In such cases, the rate of lithium deposition overcomes the rate of solid-electrolyte interface formation, allowing the lithium deposit to grow almost free from the influence of the interface (Bai et al., 2018).

The enrichment of lithium-ion concentration appears in the vicinity of dendrite tips, reaching peak values of up to $\tilde{\zeta}_+ = 2.1$, and triggering tip-growing dendritic lithium. Electrolyte regions with higher lithium-ion concentration ($\tilde{\zeta}_+ > 1$) are represented by orange volumes in Figure 5.7. It is worth mentioning that this phenomenon was previously reported by Hong et al. (Liang and Chen, 2014) in 2D simulations of lithium dendrite formation.

We calculate the electric field distribution by differentiation of the resolved electric potential $\vec{E} = -\nabla\phi$. The magnified view in Figure 5.8 shows how the electric field localizes in the vicinity of the dendrite tip, leading to an enriched concentration of the lithium-ion it induces due to the strong migration from the surrounding regions (see (3.22) and (Liang and Chen, 2014)).

Figure 5.9 shows the behaviour of the time-adaptive scheme, throughout the 0.6 [s] of simulation. Starting with a small time-step of $\Delta t_0 = 10^{-7}$ [s] to achieve convergence, followed by a rapid increase in size, until reaching a stationary value

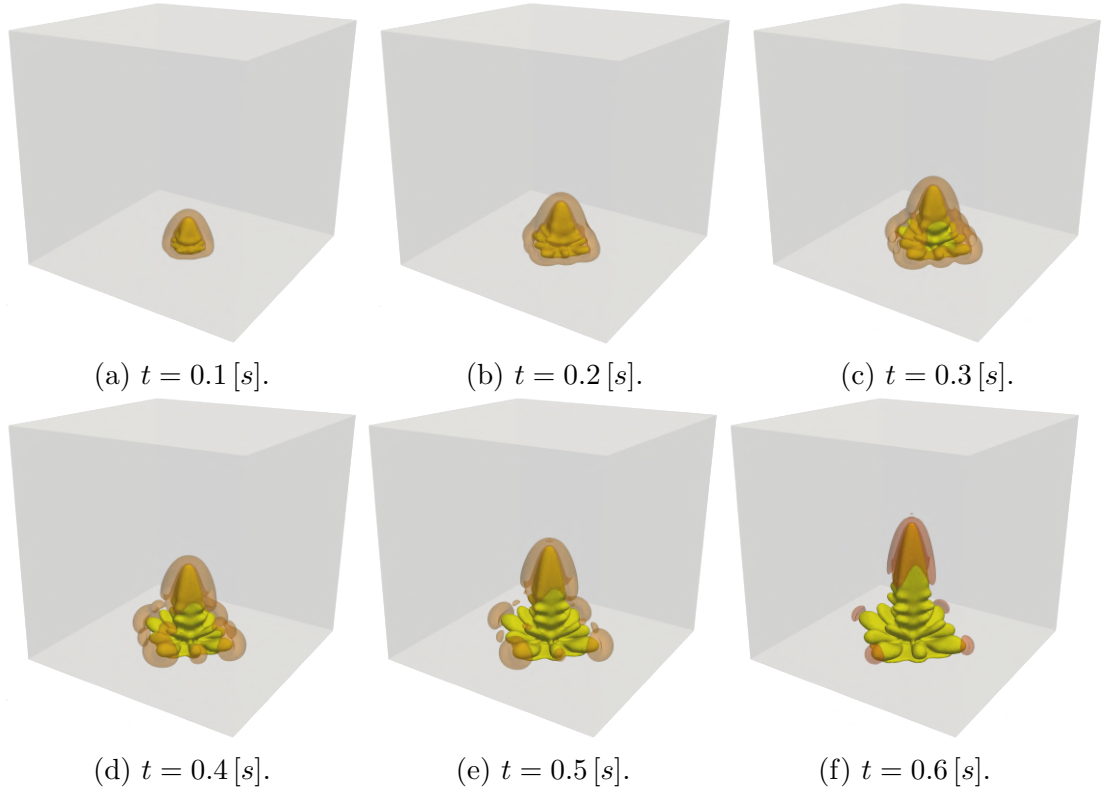


Figure 5.7: Spike-like lithium dendrite formation under $\phi_b = -0.7 [V]$ charging potential. The electrodeposited lithium is represented with a yellow isosurface plot of the phase-field variable ξ . Electrolyte regions with enriched concentration of lithium-ion ($\tilde{\zeta}_+ > 1$) represented with orange volumes. Cube domain set as $80 \times 80 \times 80 [\mu m^3]$.

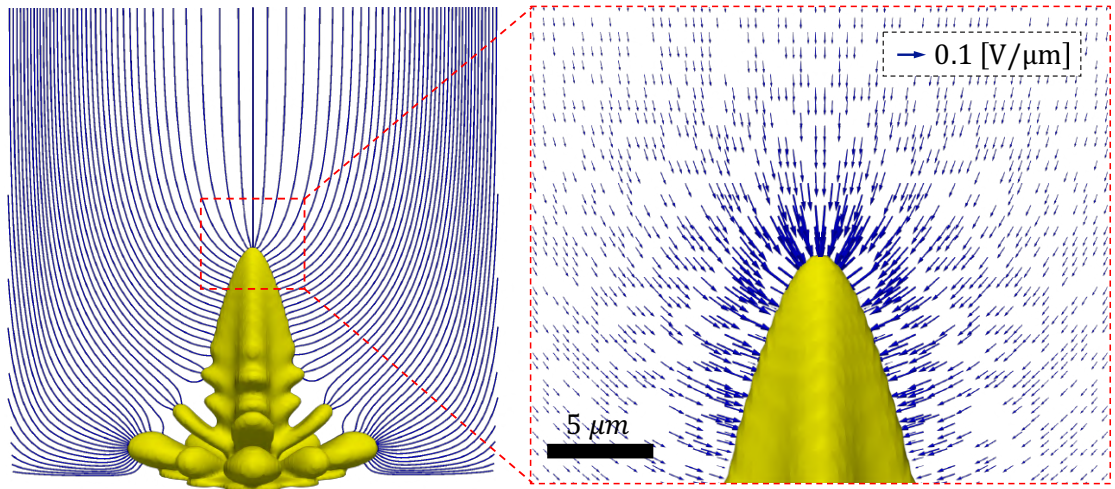


Figure 5.8: Overlay of electric field distribution (blue streamlines and vectors) with dendrite morphology at time $t = 0.5 [s]$. Streamline plane set at $y = 40 [\mu m]$.

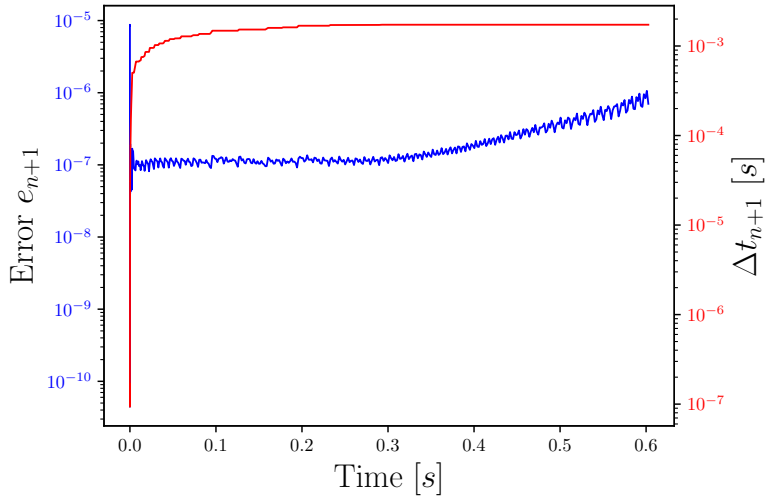


Figure 5.9: Time adaptivity for 3D spike-like dendrite growth simulation.

of about $\Delta t_{n+1} = 10^{-3} [s]$. The evolution of the weighted truncation error e_{n+1} (blue) stays close to the minimum tolerance limit (10^{-7}) during 0.3 [s] of simulation; beyond this point, the error estimate increases due to the acceleration of lithium dendrite propagation rate as the dendrites approach the positive electrode. The time-step size remains unchanged since the error estimate remains within the error bounds ($\text{tol}_{\max} = 10^{-6}$ and $\text{tol}_{\min} = 10^{-7}$, see Table 3.1).

The construction of phase-field models satisfies an a priori nonlinear stability relationship, expressed as a time-decreasing free-energy functional; nevertheless, standard discrete approximations do not inherit this stability property (see Section 3.3). Figure 5.10 shows the evolution of the Gibbs free energy of the system Ψ , see (3.6), using our adaptive time integration scheme. We plot the total energy curve, as well as three additional energy curves that correspond to each one of its terms, namely, the Helmholtz (chemical) free energy $\int_V f_{\text{ch}} dV$, surface energy $\int_V f_{\text{grad}} dV$, and electrostatic energy $\int_V f_{\text{elec}} dV$. Figure 5.10 shows that the total systems' discrete free energy does not increase with time. Therefore, we obtain discrete energy stable results using our second-order backward-difference (BDF2) time-adaptive marching scheme. Alternative, provably unconditionally stable second-order time accurate methods may deliver larger time-step sizes for

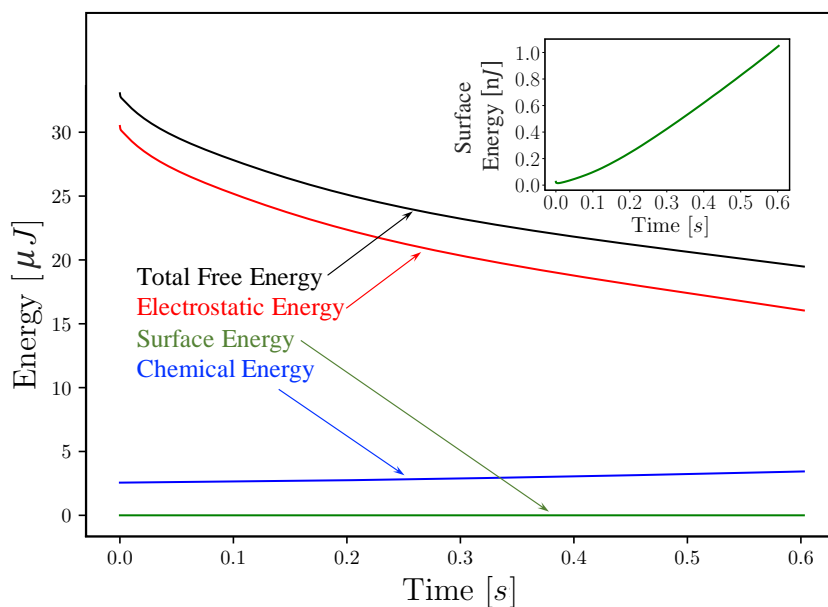


Figure 5.10: Energy time series for 3D spike-like dendrite growth simulation. The inset plots the increasing surface energy in smaller scale for better appreciation.

phase-field models (Gomez and Hughes, 2011; Sarmiento et al., 2018; Wu et al., 2014; Hawkins-Daarud et al., 2012; Vignal et al., 2017), but these are beyond the scope of this work. Additionally, the system’s chemical and surface energies increase as the lithium surface area grows as time progresses. In parallel, the electrostatic energy decreases in time. This interaction is consistent with the electrodeposition process, where the system stores the applied electrostatic energy as electrochemical energy as the battery charges.

5.3.2 3D multi-nuclei simulation

The lithium dendrite nucleation depends on local inhomogeneities that may arise from different causes, such as defects and impurities in the metal anode, imperfect contact between the electrode and electrolyte caused by the development of a solid-electrolyte interface, and variations in the local concentration or temperature in the electrolyte (Hong and Viswanathan, 2018). Given the random nature of the nucleation phenomenon, we need to deal with some degree of randomness and uncertainty when defining the artificial nuclei in the simulation. We study

the simulations' sensitivity to the artificial nuclei size, shape, and proximity as an extension of 2D studies that show this dependence (Chen et al., 2015; Ely et al., 2014; Yurkiv et al., 2018). Thus, the following 3D numerical experiment tests the simulation's sensitivity to the nuclei distribution and proximity by comparing four-nuclei morphological results with those previously obtained with a single artificial protrusion. The simulation setup is similar to the previous 3D experiment with a different nucleation arrangement. Therefore, we form the artificial nucleation region with four protrusions (ellipsoidal seeds), with semi-axes $4[\mu\text{m}] \times 2[\mu\text{m}] \times 2[\mu\text{m}]$, and centres located at $(y, x, z) = (0, 38, 38)$, $(0, 42, 38)$, $(0, 38, 42)$ and $(0, 42, 42)$.

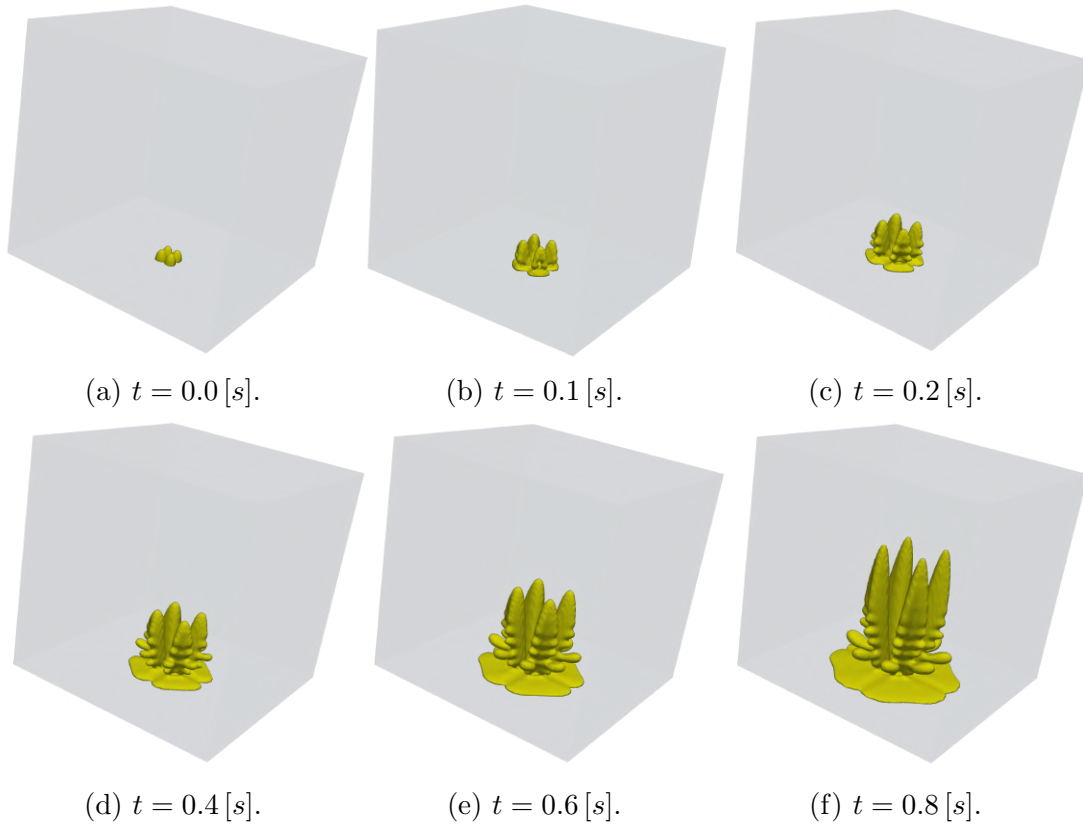


Figure 5.11: Spike-like lithium dendrite formation from multiple nucleation sites under $\phi_b = -0.7$ [V] charging potential. The electrodeposited lithium is represented with a yellow isosurface plot of the phase-field variable ξ . Cube domain set as $80 \times 80 \times 80$ [μm^3].

Figure 5.11 shows the morphological evolution of the simulated lithium den-

drite (isosurface plot of the phase-field variable $\xi = 0.5$). In agreement with previous numerical experiments, the simulation forms a spike-like, symmetric, and highly branched pattern. The dendrite morphology consists of four main trunks growing from each nucleus, with pairs of orthogonal branches developing to the sides.

The dendrite growth does not occur perpendicular to the stack but at an angle of about 20° between main trunks. The stacks seem to repel each other, showing morphological similarity with dendritic patterns observed in lithium experiments performed by Ding (2016) (see Figure 5.12a), and by Tatsuma et al. (2001) (see Figure 5.12b), under charging densities of $10 [mA/cm^2]$ and $3 [mA/cm^2]$, respectively. As a consequence of the reduced distance between electrodes (limited by the computational cost), the time scales we simulate are significantly shorter (by two orders of magnitude) than the experimental ones by Nishikawa et al. (2011); Ding (2016); Tatsuma et al. (2001).

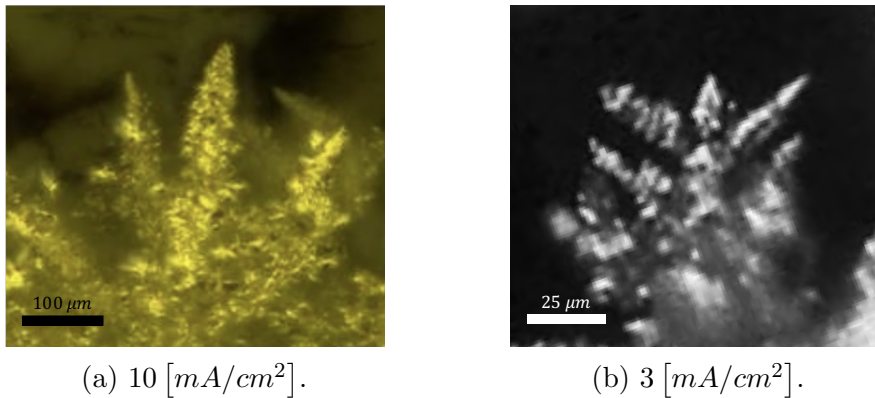


Figure 5.12: Photographs of lithium electrodes with electrochemical deposition of lithium. The deposition condition for (a), as performed by Ding (2016), consist of $10 [mA/cm^2]$ current density applied for 1 hour in 1M LiTFS/DME/DOL electrolyte, with working distance between electrodes set about $2 [mm]$. The deposition condition for (b), as performed by Tatsuma et al. (2001), consist of $3 [mA/cm^2]$ current density applied for 1 hour in 1M LiClO₄ electrolyte, with working distance between electrodes set about $3 [mm]$ (reproduced with Journal’s and author’s permission).

Figure 5.13a details the simulated dendritic morphology at time $t = 0.5 [s]$, together with the spatial distribution of the lithium-ion concentration $\tilde{\zeta}_+$ in the

electrolyte region. No side branches form facing the center of the nucleation arrangement (between the dendrites), where the deposition process depletes the lithium-ion concentration (shown in blue) (Liang and Chen, 2014). This creates a shadow that inhibits branching growth in the spatial proximity of more developed adjacent dendrites. As a consequence, the side branches do not grow dendrites facing the center of the nucleation arrangement (unfavorably oriented dendrites) due to the 3D interactions with other dendrites (adjacent to the main trunks) (Takaki et al., 2013). 2D phase-field models of dendrite electrodeposition cannot capture this 3D phenomenon.

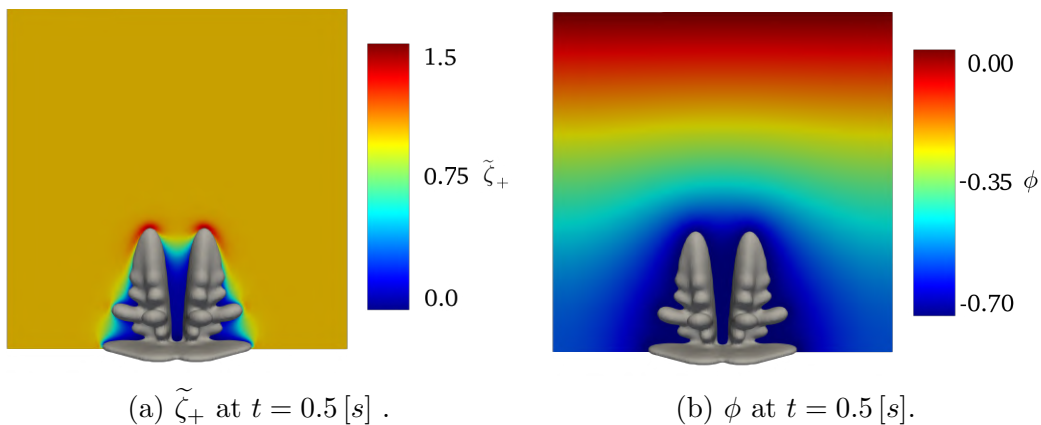


Figure 5.13: Spatial distribution overlay of lithium-ion concentration (a), and electric potential (b), with dendrite morphology at $t = 0.5 [s]$. Contour plane set at $y = 35 [\mu\text{m}]$.

Figure 5.13b shows the spatial distribution of the electric potential ϕ overlaid with the lithium dendrite at the same instant $t = 0.5 [s]$. In agreement with the 2D simulations of Section 5.2.2, the electric potential has a gradient over the electrolyte phase and its steepness increases as the lithium dendrite grows.

Figure 5.14 shows the evolution of the electric field $\vec{E} = -\nabla\phi$ and the enriched lithium-ion concentration ($\tilde{\zeta}_+ > 1$) in the vicinity of the dendrite tips (red volumes represent enriched concentration). As before, a larger electric field localizes in the vicinity of the dendrite tips, leading to a higher lithium-ion concentration with peak values of $\tilde{\zeta}_+ = 1.8$. The electric migration overcomes the diffusion due to the Li-ion concentration gradient, and drive lithium cations from surrounding

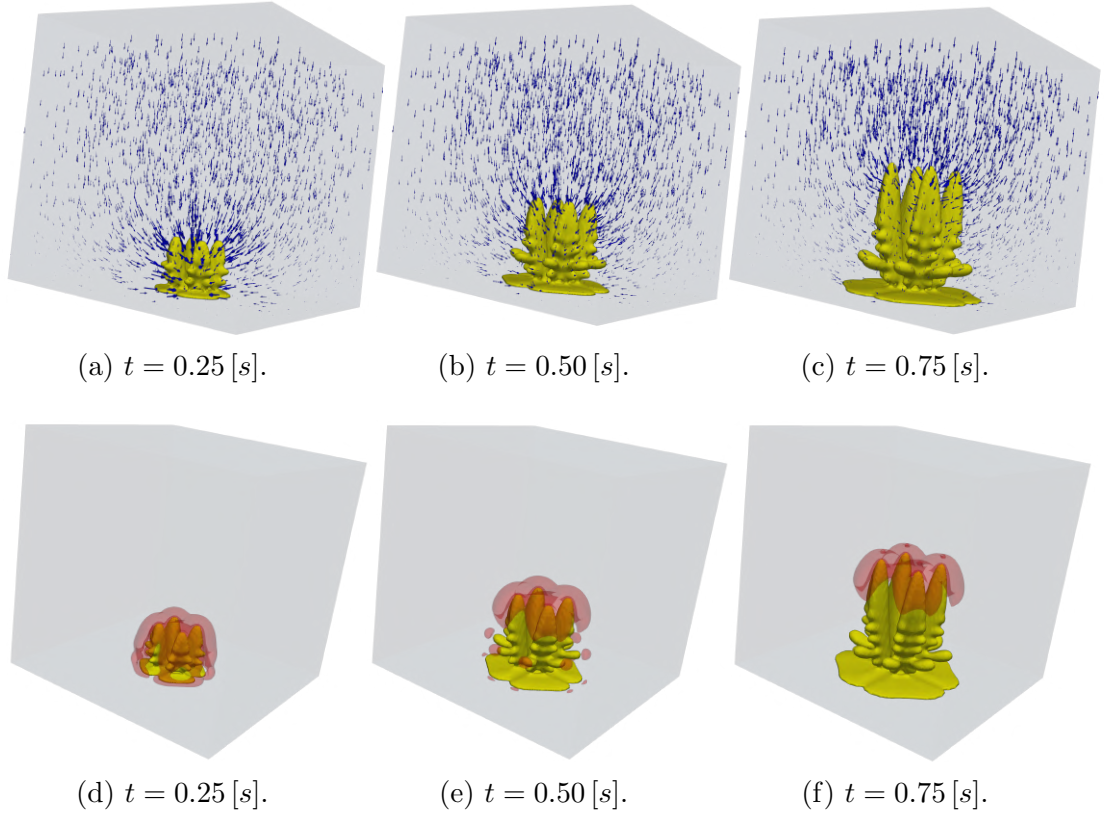
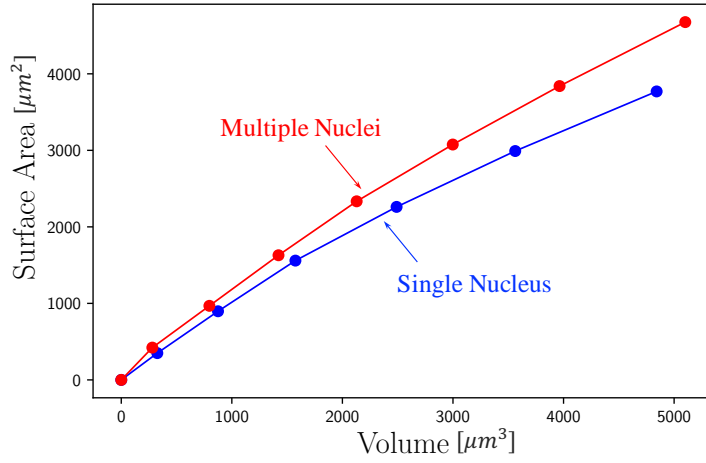


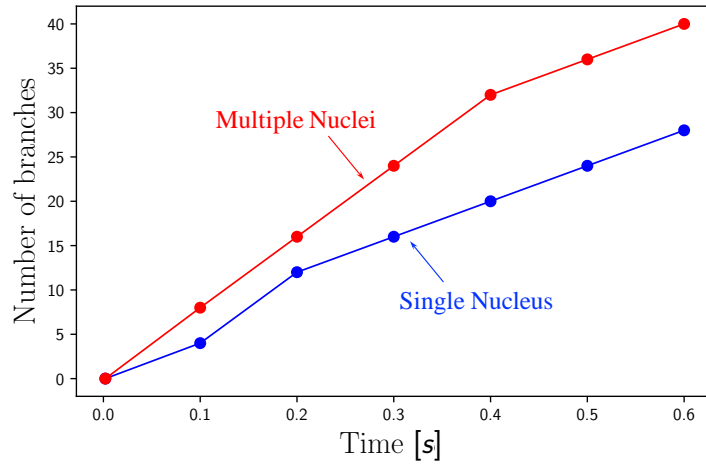
Figure 5.14: Simulation of spike-like lithium dendrite formation from multiple nucleation sites. The upper row shows the overlay of the electric field evolution $\vec{E} = -\nabla\phi$ (blue vectors) with dendrite morphology; the second row exhibit the lithium ion enrichment effect $\tilde{\zeta}_+ > 1$ (red volume) surrounding the dendrite tips.

regions with lower concentrations (i.e., Li-ion depletion of valley regions) to accumulate around dendrite tips, triggering tip-growth with highly branched dendritic lithium.

We analyze the dendritic patterns' morphology evolution using single and multiple nuclei. Following Yufit et al. (2019), we characterize the morphology by tracking the dendrites' volume-specific area ($\mu\text{m}^2/\mu\text{m}^3$) and the branch number evolution in time. Figure 5.15a plots the growth of the volume versus the surface area for the 3D lithium patterns we simulate. The volume-specific area average of 0.83 and 0.91 [$\mu\text{m}^2/\mu\text{m}^3$] of the single and multiple nuclei simulations, respectively; where a higher surface area/volume ratio is indicative of a more branched shape. Given the lack of experimental data available in the literature



(a) Volume vs Surface Area.



(b) Side branches vs t.

Figure 5.15: Comparison between 3D simulations of lithium dendrite growth (single and multiple-nuclei), in terms of the evolution of volume vs surface area **a**, and number of side branches developed over time **b**.

for quantitative characterization of the spike-like lithium morphologies, we rely on experimental results available for zinc dendrites. (Yufit et al., 2019) report values between 0.86 and 1.04 [$\mu\text{m}^2/\mu\text{m}^3$] for experimental formation of dendrites in zinc batteries. Figure 5.15b compares the number of branches developed over time in each case. The simulations produce ratios of 48 and 72 branches per second [1/s] for the single and multiple nuclei simulations, respectively. We compute the number of branches by visual inspection of the morphologies, where we consider

new protuberances (amplitudes larger than $2 [\mu m]$) as incipient branches under development. Direct comparison with dendrite experiments was impractical in this case, due to the faster dynamics of the simulation (small distance between electrodes).

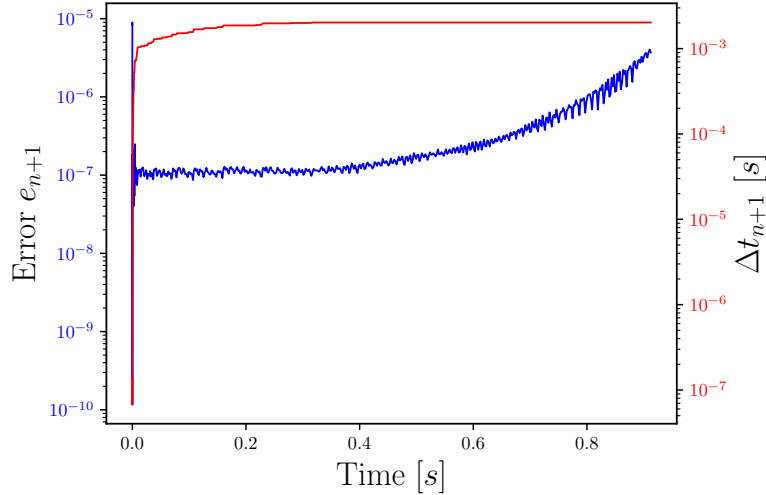


Figure 5.16: Time adaptivity plot for 3D spike-like four-nuclei dendrite growth simulation.

Figure 5.16 shows the behaviour of the time-adaptive scheme, throughout the $> 0.8 [s]$ of the simulation. Starting with a small time-step of $\Delta t_0 = 10^{-7} [s]$ to initially achieve convergence, followed by a rapid increase in size, until reaching a stationary value of about $\Delta t_{n+1} = 10^{-3} [s]$. As we can observe, the timestepping behaves similarly than the previous 3D simulation (compare with Figure 5.9).

Figure 5.17 shows the systems' energy evolution. The total energy curve (black) does not increase with time, showing energy stable results. As before, we observe that the process transforms electrostatic energy and stores it as electrochemical energy (battery charge). Figure 5.17 shows that the surface energy for the four-nuclei simulation is almost four times larger than the single nucleus surface energy of Figure 5.10. The proportionately larger surface area due to the four seeds explains this scaling.

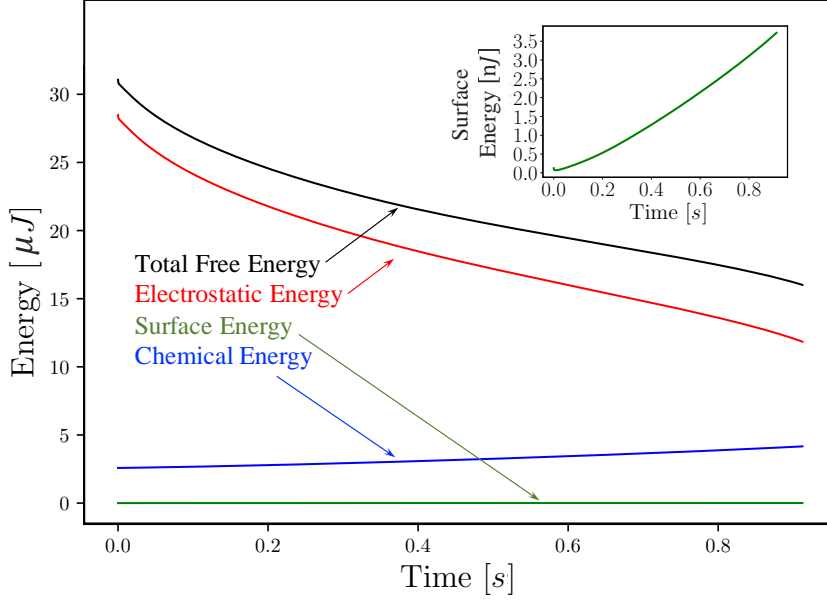


Figure 5.17: Energy time series for 3D spike-like four-nuclei dendrite growth simulation. The inset plots the increasing surface energy in smaller scale for better appreciation.

5.3.3 Phase-field interface thickness to mesh resolution ratio: A sensitivity analysis

In this section, we perform a sensitivity analysis to study possible mesh-induced effects on the simulated 3D dendrite morphology, propagation rates (dendrite’s height vs time), electrodeposition rates (dendrite’s volume vs time), and energy levels. We compare 3D simulation results for different spatial resolutions and phase-field interface thicknesses.

The symmetric nature of spike-like lithium morphology Tatsuma et al. (2001); Jana et al. (2019) allows us to reduce the computational cost by using symmetry boundary conditions to model only one-quarter of the domain. Thus, we split the domain in four, and apply Neumann boundary conditions ($\nabla\xi \cdot \mathbf{n} = 0$; $\nabla\tilde{\zeta}_+ \cdot \mathbf{n} = 0$; $\nabla\phi \cdot \mathbf{n} = 0$) to those boundaries facing the center of the domain as depicted in Figure 5.18. Therefore, we reduce the size of our computational domain to 25% ($l_x, l_y/2, l_z/2$).

We verify our strategy by comparing the previous 3D simulation result using

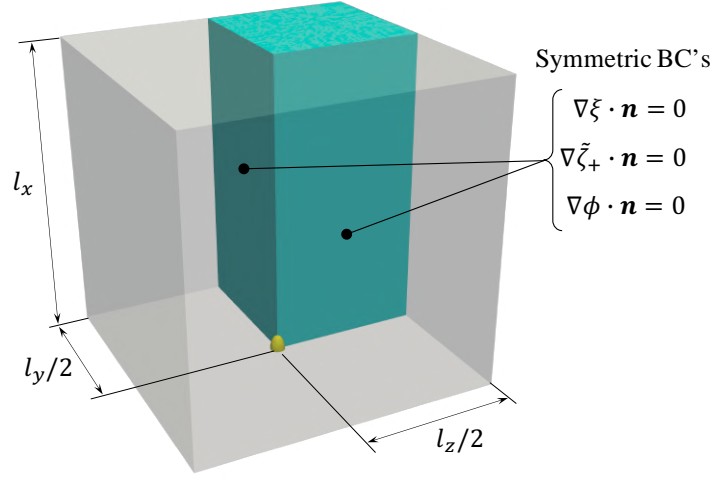


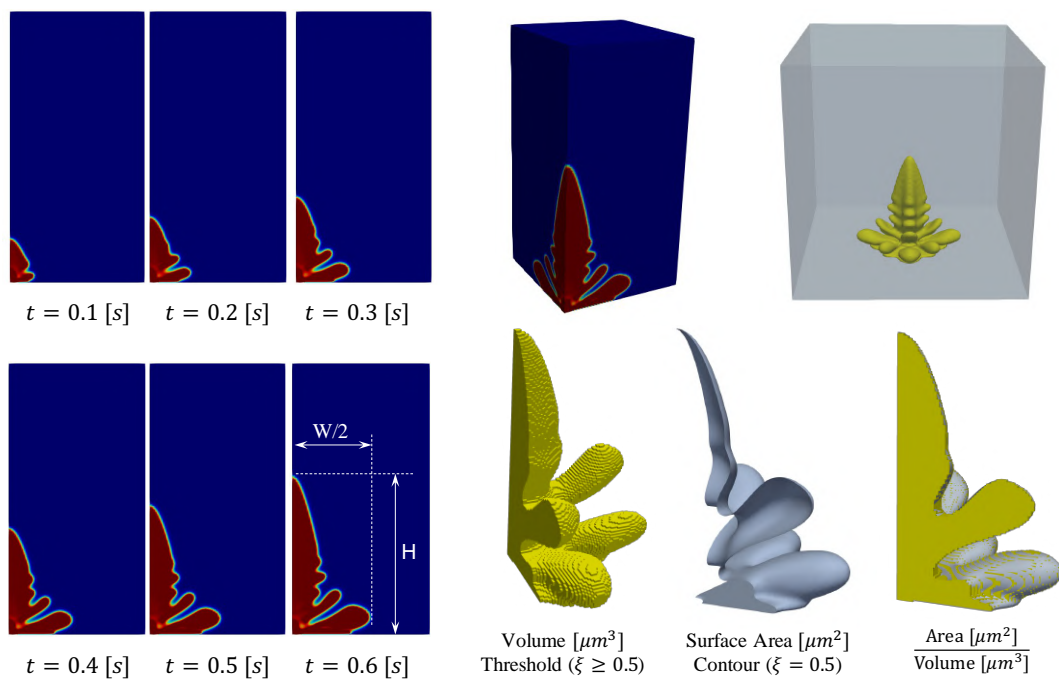
Figure 5.18: Symmetric boundary conditions for 3D spike-like simulations.

the whole domain (see Figure 5.7), and those obtained using symmetric boundary conditions (see Figure 5.19).

We simulate the evolution of the geometrical features that define the dendrite's morphology, such as the maximum semi-width ($W/2$), height (H), and volume-specific area ratio. Figure 5.19b depicts the threshold of $\xi \geq 0.5$ to calculate the volume of deposited lithium ($\int_V \xi dV$), and a smoothed contour $\xi = 0.5$ to estimate the dendrite's surface area at each time set. Figure 5.19 shows the same morphological structures shown in Figure 5.7 by modelling the whole domain. Thus, the symmetric boundary conditions reduce the computational cost, which allows us to use finer meshes in the sensitivity analysis.

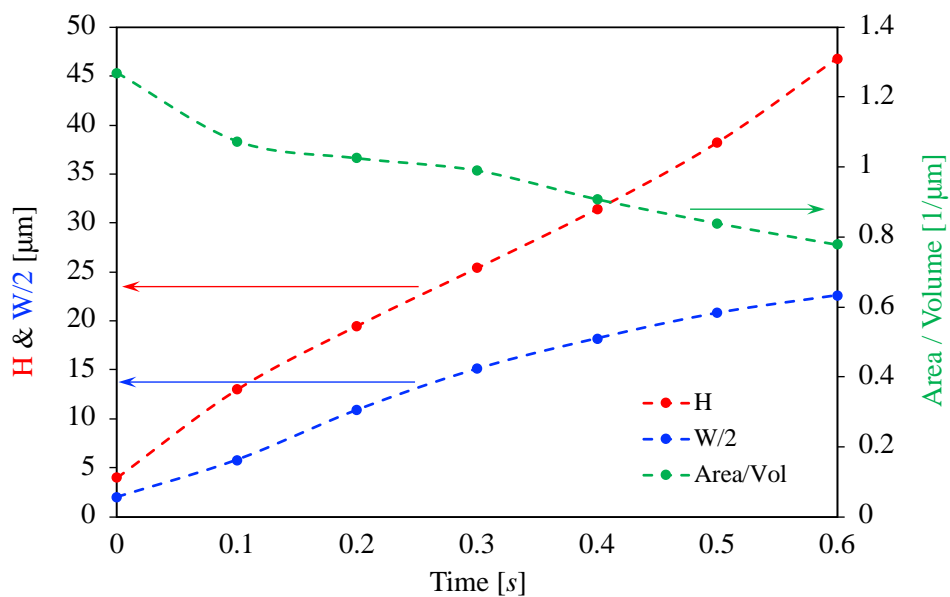
As discussed in Section 4.3.3, the phase-field interface thickness significantly affects the simulated reaction rates. Wider interfaces (larger δ_{PF}) increase the reactive area in the simulation, which induces faster electrodeposition rates. Numerical evidence shows that 1D interface-thickness-independent growth (convergent results) are possible well before reaching the physical nanometer interface width (ichi Morigaki, 2002) (see Section 4.3.3).

Figure 5.20 presents a collection of 3D spike-like lithium dendrite morphologies (isosurface plot of the phase-field variable $\xi = 0.5$), obtained by varying the phase-



(a) Width & height.

(b) Volume & surface area measurement.



(c) Evolution plot of morphological parameters.

Figure 5.19: Morphological analysis of symmetric boundary conditions in terms of dendrite's width & height (a), volume / surface area ratio (b). We plot the evolution of the dendrite's maximum semi-width ($W/2$ - blue), height (H - red), and volume-specific area ratio (green) (c).

field interface thickness ($\delta_{PF} = 1, 1.5$ and $2 [\mu m]$), and mesh sizes ($h = 0.5, 0.375$ and $0.25 [\mu m]$). Thus, we test different combinations of phase-field interface thickness to mesh resolution ratios ($\mathcal{R} = \delta_{PF}/h = 3$ to 8). We compare dendrite morphologies at the moment they reach a height of $H = 45 [\mu m]$.

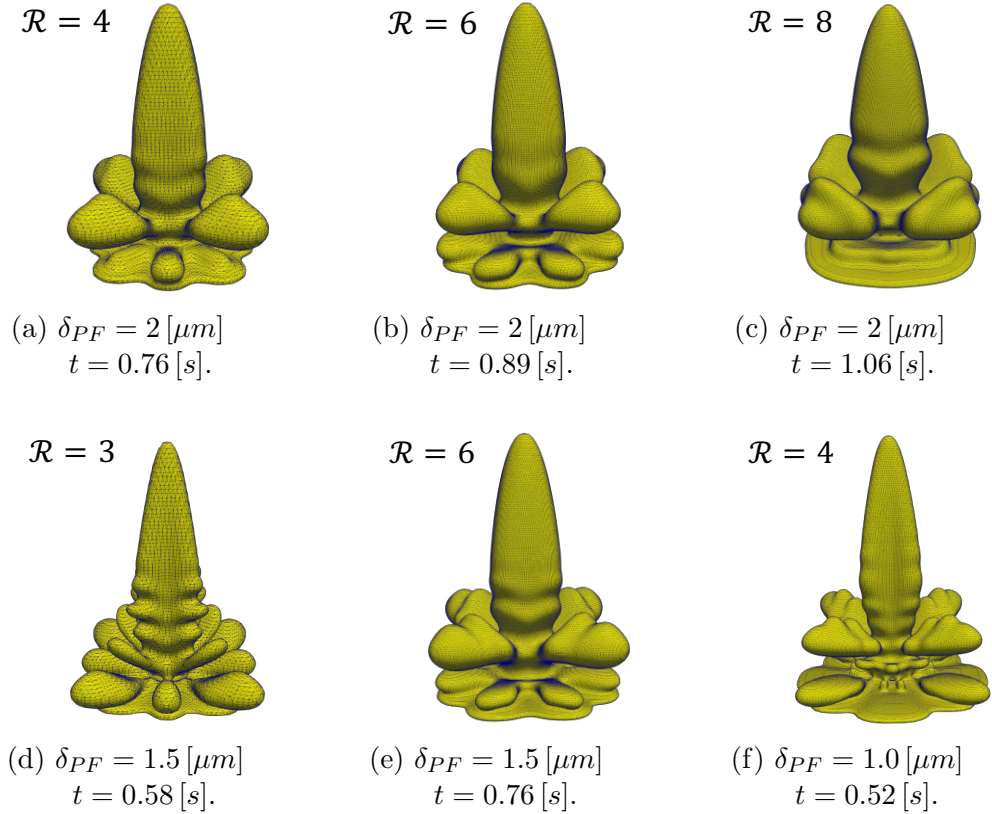


Figure 5.20: Sensitivity analysis of 3D spike-like lithium dendrite morphology, for different phase-field interface thickness to mesh resolution ratios ($\mathcal{R} = \delta_{PF}/h$), under $\phi_b = -0.7 [V]$ charging potential. Simulated morphologies for $\delta_{PF} = 2, 1.5$ and $1 [\mu m]$ phase-field interface thickness; mesh grid overlaid with dendrite's morphology. We use dendrite's common height ($H = 45 [\mu m]$) as the basis of our comparison.

Figure 5.20 shows spike-like patterns that exhibit morphological similarity. Each consists of the main trunk and four side branches growing in each horizontal direction (as a result of the body-centered cubic (bcc) crystallographic arrangement of lithium metal (Yurkiv et al., 2018)). Smaller phase-field interface thicknesses produce more slender dendritic morphologies (cf. Figures 5.20f ($\delta_{PF} = 1 [\mu m]$) and 5.20c ($\delta_{PF} = 2 [\mu m]$)). We use Paraview's mean curvature

measurement (Ayachit, 2015) to analyse the dendrite’s tip radius (isosurface plot of the phase-field variable $\xi = 0.5$). Thus, the measured dendrite’s tip radius in Figure 5.20f ($\delta_{PF} = 1 [\mu m]$) is about $r_{tip_1} = 2.7 [\mu m]$, while the computed dendrites’ tip radius in Figure 5.20c ($\delta_{PF} = 2 [\mu m]$) is about $r_{tip_2} = 5.3 [\mu m]$ (49% larger). The dendrite’s maximum cross sectional area, main trunk, in Figure 5.20f ($\delta_{PF} = 1 [\mu m]$) is approximately $A_{max_1} = 154 [\mu m^2]$, while the computed cross sectional area in Figure 5.20f ($\delta_{PF} = 2 [\mu m]$) is about $A_{max_2} = 254 [\mu m^2]$ (40% larger). In addition, Figure 5.20 shows that increasing the resolution ratio delivers thicker dendritic morphologies ($\mathcal{R} = \delta_{PF}/h$), keeping the phase-field interface thickness constant (more elements at the interface). We compare the morphologies in the first row of Figure 5.20 ($\delta_{PF} = 2 [\mu m]$), against those on the second row of Figure 5.20 ($\delta_{PF} = 1.5 [\mu m]$); in both cases finer mesh resolutions (higher \mathcal{R}) lead to less slender and less branched dendritic morphologies.

Figure 5.21 shows the evolution of the Gibbs free energy of the system Ψ , see (3.6). We plot the total energy curve for different simulation set-ups (phase-field interface thickness δ_{PF} and mesh resolution ratio \mathcal{R}), as the figure indicates. Figure 5.21 shows that in all cases, the systems’ discrete free energy does not increase with time (adaptivity delivers discrete energy stable results). We obtain a maximum energy difference of about 9% ($t = 0.6 [s]$) between the simulations with the maximum ($\delta_{PF} = 2 [\mu m]$ & $\mathcal{R} = 8$) and minimum ($\delta_{PF} = 1 [\mu m]$ & $\mathcal{R} = 4$) total energy levels (see Figure 5.21). In addition, those dendrites sharing a similar level of total energy (represented in green, orange, and purple) exhibit closer morphological resemblance, as the figure shows.

Figure 5.22 shows the effect of the phase-field interface thickness and mesh resolution ratio on the dendrite’s propagation rate (H vs t). Smaller phase-field interface thickness produces significantly faster propagation rates. For example, simulation using smaller interface thickness ($\delta_{PF} = 1 [\mu m]$) exhibits up-to 100% faster growth rates than those obtained under larger interface thickness ($\delta_{PF} = 2 [\mu m]$). Figure 5.22 shows that slower dendrite propagation rates occur

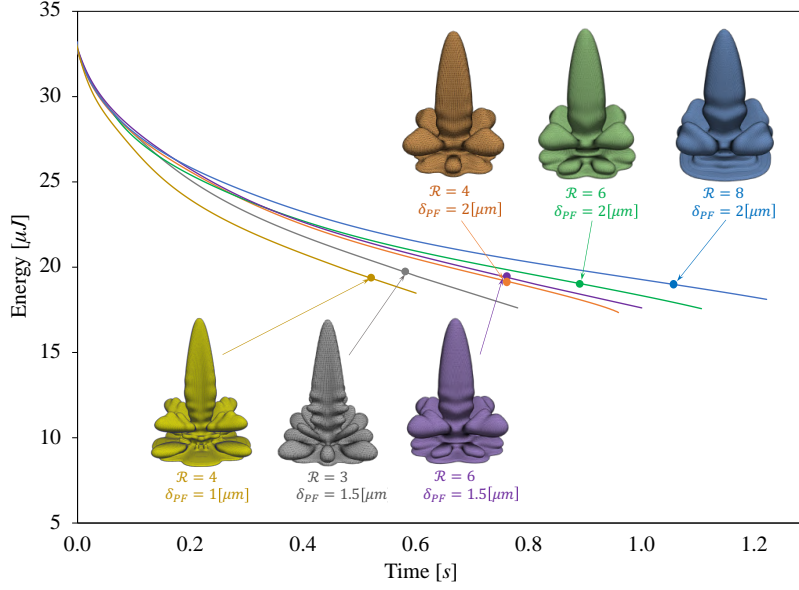


Figure 5.21: Comparison of energy time series for 3D spike-like dendrite growth simulations, for different phase-field interface thickness to mesh resolution ratios ($\mathcal{R} = \delta_{PF}/h$), under $\phi_b = -0.7$ [V] charging potential. Dendrite morphologies at height $H = 45$ [μm] for reference (colours by phase-field interface thickness and mesh size).

as we increase the mesh resolution ratio ($\mathcal{R} = \delta_{PF}/h$), keeping the phase-field interface thickness constant. The inset in Figure 5.22 plots the maximum Li-ion concentration surrounding the dendrite's tips for $\delta_{PF} = 2$ [μm] where the enriched Li-ion concentration decreases as we increase the mesh resolution $\mathcal{R} = \delta_{PF}/h$ (more accurate solution), leading to slower propagation rates (H vs t).

Figure 5.23 shows the dendrite's volume evolution as a proxy of the overall electrodeposition rate (volume of lithium metal deposited over time). The effect of the phase-field interface thickness and mesh resolution ratio on the overall electrodeposition rate is less significant (percentage-wise) than it is for the dendrite's propagation rate (dendrite's height over time). For example, Figure 5.23 shows a maximum electrodeposition rate difference of less than 20% (volume vs time) between the fastest and slowest simulation results. Thus, higher dendrite's propagation rates occur for smaller phase-field interface thicknesses due to the lithium metal being deposited / spread over a smaller surface area (more slender

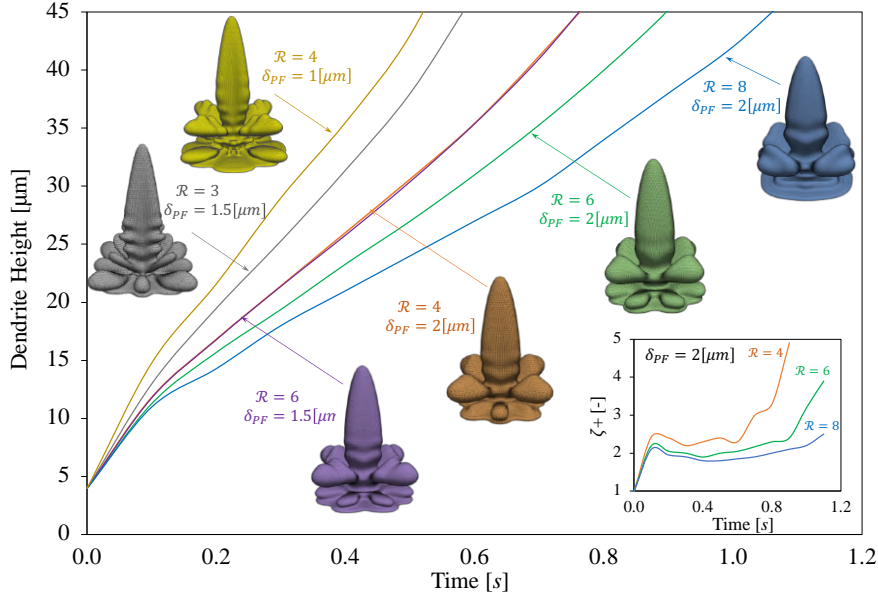


Figure 5.22: Comparison of 3D spike-like dendrite propagation rate, for different phase-field interface thickness to mesh resolution ratios ($\mathcal{R} = \delta_{PF}/h$), under $\phi_b = -0.7$ [V] charging potential. Dendrite morphologies at common height $H = 45$ [μm] for reference (colours by phase-field interface thickness and mesh size). The inset shows maximum Li-ion concentration as a function of time for different $\mathcal{R} = \delta_{PF}/h$ ratios, using the same phase-field interface thickness ($\delta_{PF} = 2$ [μm]).

dendritic morphologies), rather than differences in the overall electrodeposition rate (minor effect).

This analysis shows (see Figure 5.23) that for phase field interface thickness 2 [μm] or smaller, the simulated electrodeposition rate (volume of lithium metal deposited over time) is relatively insensitive to the numerical parameters (δ_{PF} and \mathcal{R}). On the other hand, the simulated dendrite propagation rate shows stronger numerical dependencies (see Figure 5.22), affecting the level of realism of our results. Thus, propagation predictions presented here should only be taken as a comparison indicator between numerical tests, as we work towards smaller phase-field interface thickness to increase the accuracy of our simulations.

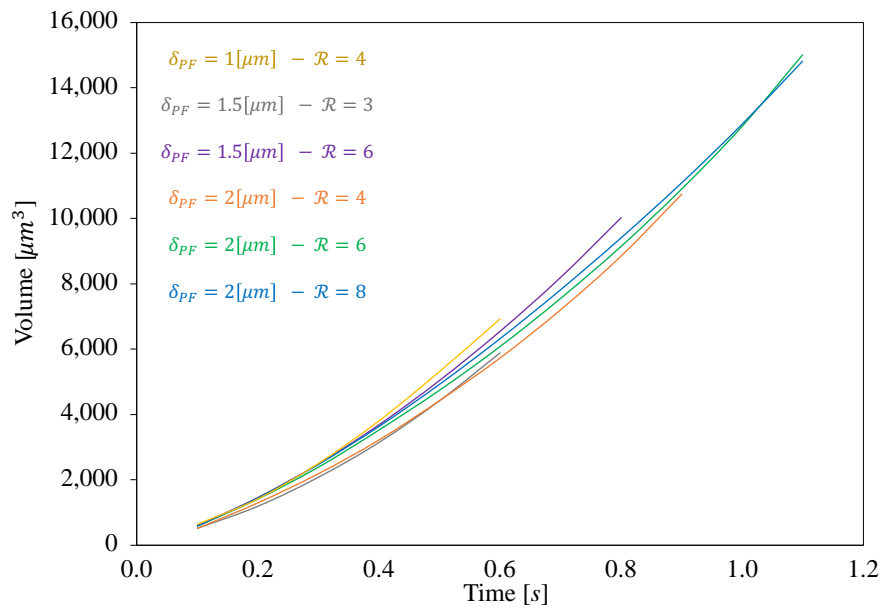


Figure 5.23: Comparison electrodeposited volume for 3D spike-like dendrite growth simulation, for different phase-field interface thickness to mesh resolution ratios ($\mathcal{R} = \delta_{PF}/h$), under $\phi_b = -0.7$ [V] charging potential.

Chapter 6

Three-dimensional experimental-scale phase-field modelling of dendrite formation in rechargeable lithium-metal batteries

Lithium dendrite simulations presented in Chapter 5 enabled the development of our phase-field framework and gave insights into the mechanism behind spike-growing lithium morphologies. This chapter ¹ resume the work by addressing some of the shortcomings identified towards the goal of experimental scale simulations. Here, a modified surface anisotropy representation is introduced to the model. Firstly, numerical test are performed to gain insight into the benefits of this modification compared with the results previously obtained in Chapter 5. Secondly, we enlarge the domain size to achieve experimental inter-electrode dis-

¹The content of this chapter is published in: Arguello, M. E., Labanda, N. A., Calo, V. M., Gumulya, M., Utikar, R., & Derksen, J. (2022). Three-dimensional experimental-scale phase-field modelling of dendrite formation in rechargeable lithium-metal batteries. *Publication under review*.

tances. We map the nodal distribution concentrating the nodes in the region of interest, inspired by experimental and simulation results. The increased domain size affects the lithium electrodeposition behavior by increasing the interelectrode distance. We discuss the lithium dendrite propagation rates and morphologies for different charging voltages, and give insight into strategies of dendrite suppression.

6.1 3D simulations using modified surface anisotropy

We evaluate the performance of the surface anisotropy representation model for metal anode battery simulations (see Section 6.1.1). These studies consist of 3D phase-field simulations of lithium dendrite formation during battery charge state to explore three-dimensional highly branched "spike-like" dendritic patterns, commonly observed experimentally. These patterns form under high current density loads, which correspond to fast battery charge (Jana et al., 2019; Ding, 2016; Tatsuma et al., 2001).

6.1.1 Surface anisotropy representation for phase-field electrodeposition models

In this section, we present a modified representation of the 3D surface anisotropy of lithium crystal. We start by considering the surface energy expression, following (3.8) $f_{\text{grad}} = \frac{1}{2}\kappa(\xi)(\nabla\xi)^2$, where its variational derivative (surface anisotropy of lithium crystal) (3.11) is: $\frac{\delta f_{\text{grad}}}{\delta \xi} = \kappa(\xi)\nabla^2\xi$, consistent with most recent phase-field models of dendritic electrodeposition (Zhang et al., 2014; Chen et al., 2015; Cogswell, 2015; Hong and Viswanathan, 2018; Mu et al., 2019; Chen and Pao, 2021). However, a more accurate representation of $\frac{\delta f_{\text{grad}}}{\delta \xi}$ may include an additional term, as originally derived by Kobayashi (1993) for 2D crystal growth. In 3D, we use the variational derivative version derived by George and Warren

(2002) to simulate the surface anisotropy of crystal growth

$$\frac{\delta f_{\text{grad}}}{\delta \xi} = \frac{\delta}{\delta \xi} \left[\frac{1}{2} a^2 (\nabla \xi)^2 \right] = \nabla \cdot (a^2 \nabla \xi) + \sum_{i=1}^3 \frac{\partial}{\partial x_i} \left[a \frac{\partial a}{\partial \left(\frac{\partial \xi}{\partial x_i} \right)} (\nabla \xi)^2 \right], \quad (6.1)$$

where $a^2 = \kappa(\xi)$ is the three-dimensional surface anisotropy or gradient coefficient (3.10). The first term after the last equality remains the same as in the previous surface anisotropy expression; however, we add a second term (derivation due to κ as a function of ξ). We calculate the partial derivative $\frac{\partial a}{\partial \left(\frac{\partial \xi}{\partial x_i} \right)}$ in (6.1). We express the 3D surface anisotropy coefficient (3.10) (four-fold anisotropy), presented in Chapter 3 (George and Warren, 2002), as:

$$a(\xi) = \sqrt{\kappa_0} (1 - 3\delta_{\text{aniso}}) \left[1 + \frac{4\delta_{\text{aniso}}}{1 - 3\delta_{\text{aniso}}} \left(\frac{\sum_{i=1}^3 \left(\frac{\partial \xi}{\partial x_i} \right)^4}{\|\nabla \xi\|^4} \right) \right], \quad (6.2)$$

where $x_1 = x$, $x_2 = y$, and $x_3 = z$; κ_0 relates to the Lithium surface tension γ ; and δ_{aniso} is the strength of anisotropy (Tran et al., 2019; Zheng et al., 2020). Thus, we apply the quotient derivative rule to (6.2) and arrive at the partial derivative expression we use in (6.1); subsequently:

$$\begin{aligned} \frac{\partial a}{\partial \left(\frac{\partial \xi}{\partial x_i} \right)} &= 4\sqrt{\kappa_0} \delta_{\text{aniso}} \left[\frac{4 \left(\frac{\partial \xi}{\partial x_i} \right)^3 \|\nabla \xi\|^4 - \left(\frac{\partial \xi}{\partial x_i} \right)^4 4 \|\nabla \xi\|^3 \frac{\partial \|\nabla \xi\|}{\partial \left(\frac{\partial \xi}{\partial x_i} \right)}}{\|\nabla \xi\|^8} \right] \\ &= 4\sqrt{\kappa_0} \delta_{\text{aniso}} \left[\frac{4 \left(\frac{\partial \xi}{\partial x_i} \right)^3 \|\nabla \xi\|^4 - 4 \left(\frac{\partial \xi}{\partial x_i} \right)^4 \|\nabla \xi\|^3 \frac{\frac{\partial \xi}{\partial x_i}}{\|\nabla \xi\|}}{\|\nabla \xi\|^8} \right] \\ &= 4\sqrt{\kappa_0} \delta_{\text{aniso}} \left[\frac{4 \left(\frac{\partial \xi}{\partial x_i} \right)^3 \|\nabla \xi\|^2 - 4 \left(\frac{\partial \xi}{\partial x_i} \right)^5}{\|\nabla \xi\|^6} \right] \\ &= 4\sqrt{\kappa_0} \delta_{\text{aniso}} \left[\frac{4(n_i^3 - n_i^5)}{\|\nabla \xi\|} \right] \text{ for } i = 1, 2, 3, \end{aligned} \quad (6.3)$$

where $n_i = \frac{\frac{\partial \xi}{\partial x_i}}{\|\nabla \xi\|}$ for $i = 1, 2, 3$.

Although its extensive use in phase-field models of crystal growth (solidification) (George and Warren, 2002; Takaki et al., 2013), only Wang et al. (2015) apply these models to a 2D phase-field simulation of dendrite growth in the recharging process of zinc–air batteries. This limited use of this known model is because it induces only minor morphological changes in 2D electrodeposition process; compare the similarity of the 2D dendritic morphologies reported by Wang et al. (2015) including the additional surface anisotropy term, and Zhang et al. (2014) not using it. However, as we show later, its effect is crucial when modelling 3D dendritic growth.

We modify the phase-field Butler-Volmer equation (3.17) (reactive Allen-Cahn) Chen et al. (2015) by including the additional surface anisotropy term:

$$\frac{\partial \xi}{\partial t} = -L_\sigma \left\{ \frac{\partial g(\xi)}{\partial \xi} - \nabla \cdot (a^2 \nabla \xi) - \sum_{i=1}^3 \frac{\partial}{\partial x_i} \left[a \frac{\partial a}{\partial \left(\frac{\partial \xi}{\partial x_i} \right)} (\nabla \xi)^2 \right] \right\} \quad (6.4)$$

$$- L_\eta \frac{\partial h(\xi)}{\partial \xi} \left[e^{\left(\frac{(1-\alpha)nF\phi}{RT} \right)} - \tilde{\zeta}_+ e^{\left(\frac{-\alpha nF\phi}{RT} \right)} \right].$$

6.1.2 Comparison of simulated patterns: Surface anisotropy model

We study the performance of the modified surface anisotropy representation (6.4) using a 3D numerical experiment and comparing the resulting morphologies with those obtained for single nucleus simulations using the standard anisotropy representation (see Figure 5.7). We use the same simulation set-up as described in Section 5.3.1.

Figure 6.1 shows the morphological evolution of the simulated lithium dendrite and the enriched lithium-ion concentration ($\tilde{\zeta}_+ > 1$) in the vicinity of the dendrite tips, with peak values of $\tilde{\zeta}_+ = 2.3$. In agreement with previous numerical experiments, the simulation forms a spike-like, symmetric, and branched pattern. The dendrite morphology consists of the main trunk and sets of four equal orthogonal branches developing to the sides. The side branches grow up to

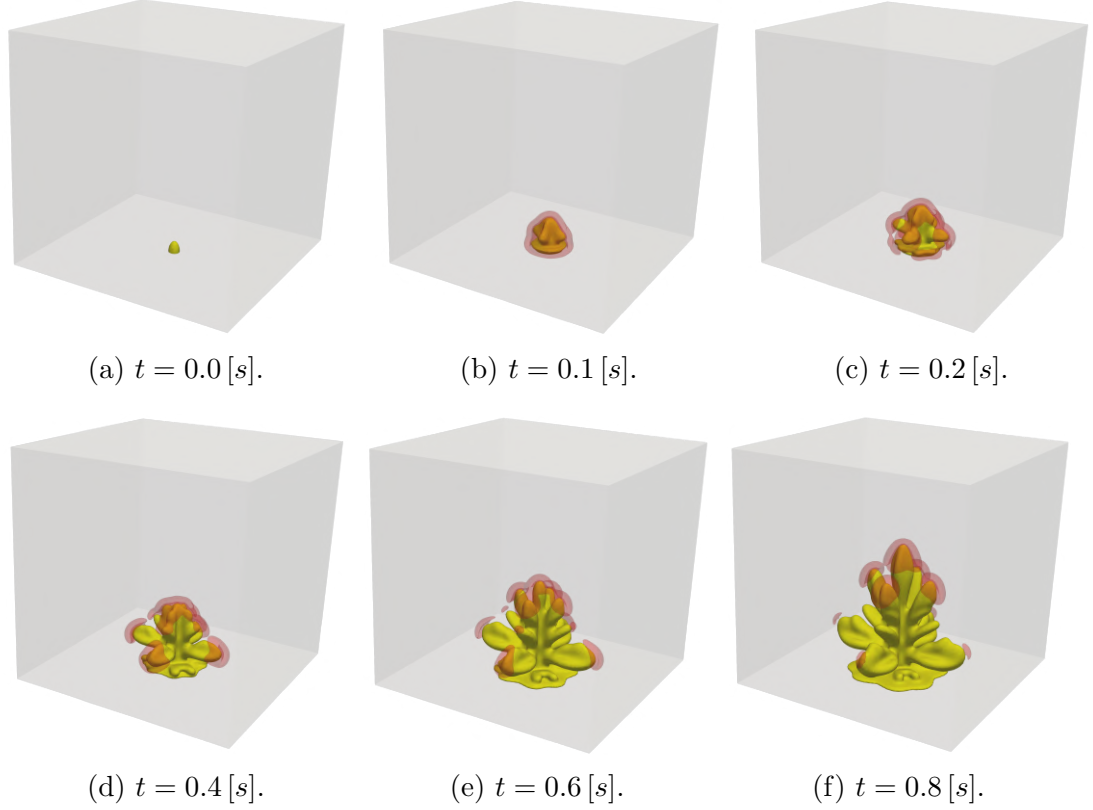


Figure 6.1: Spike-like lithium dendrite formation with modified surface anisotropy representation, under $\phi_b = -0.7 [V]$ charging potential. The electrodeposited lithium is represented with a yellow isosurface plot of the phase-field variable $\xi = 0.5$. Electrolyte regions with enriched concentration of lithium-ion ($\tilde{\zeta}_+ > 1$) represented with orange volumes. Cube domain set as $80 \times 80 \times 80 [\mu m^3]$. Phase-field interface thickness $\delta_{PF} = 1.5 [\mu m]$ & mesh size $h = 0.5 [\mu m]$.

$18 [\mu m]$ long (60% longer than in previous simulations), and 5 to $10 [\mu m]$ width. Furthermore, the side branches growth is not perpendicular to the main trunk but at an angle of about 25° to 50° , with a separation of about 4 to $8 [\mu m]$ between branches. These results show improved morphological similarity with dendritic patterns observed in lithium experiments performed by Tatsuma et al. (2001) (see Figure 5.12b).

Figure 6.2a plots the evolution of the surface energy for the 3D lithium patterns we simulate, revealing equivalent energy levels (less than 4% difference) when compared against the results previously obtained using the initial, non-modified, anisotropy representation. Thus, the numerical experiment demon-

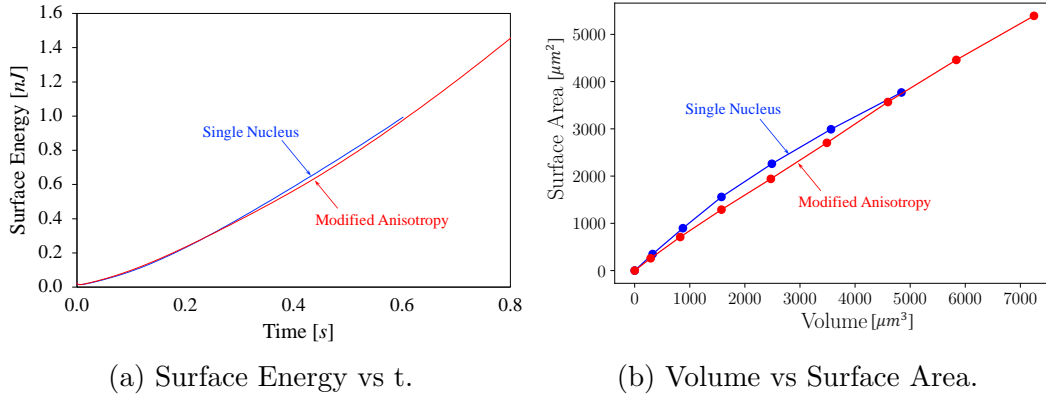


Figure 6.2: Comparison between 3D simulations of lithium dendrite growth (single nucleus initial vs modified surface anisotropy), in terms of the evolution of the surface energy **a**, and volume vs surface area ratio over time **b**.

states that the modified anisotropy representation did not significantly affect the surface energy. Additionally, Figure 6.2b characterizes the morphology by tracking the dendrites' volume-specific area ($\mu\text{m}^2/\mu\text{m}^3$). We compute the volume-specific area average ratios of 0.83 and 0.78 [$\mu\text{m}^2/\mu\text{m}^3$] for the single nucleus and modified anisotropy simulations, respectively. The slightly lower surface area/volume ratio of the modified anisotropy representation (-6%) indicates the dendrite growth has fewer but larger branches.

6.1.3 Mesh orientation effect for different surface anisotropy representations

We further compare the behavior of the standard and modified anisotropy representation behavior by studying the mesh orientation's effect on each simulated pattern. So far, the simulations results use structured meshes aligned with the Cartesian axes. Unlike previous 3D simulations, we now proceed to redistribute the mesh (node's mapping) by performing a 25° rotation around the x -axis, as depicted in Figure 6.3. Thus, here we test the dendrite's sensitivity to the mesh orientation. Figure 6.4 compares the dendrite morphologies using the standard anisotropy representation, using Cartesian, as well as 25° rotated mesh distri-

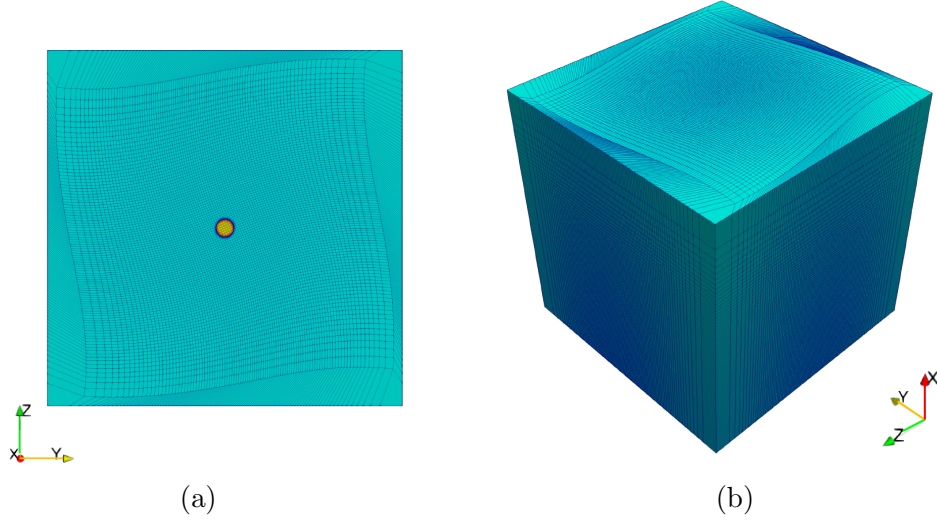


Figure 6.3: Bottom **a** & perspective **b** views of the 3D mesh with 25° rotation around the x -axis (node's mapping). Cube domain set as $80 \times 80 \times 80 [\mu m^3]$.

bution (see Figure 6.3). We compare dendrite's cross sections (horizontal slices) at positions $L_O = 5, 10, 15$ & $25[\mu m]$. The analysis reveals an alignment of dendrites' side branches to the mesh orientation (angular offset), with no major differences in terms of the simulated dendrite's shapes.

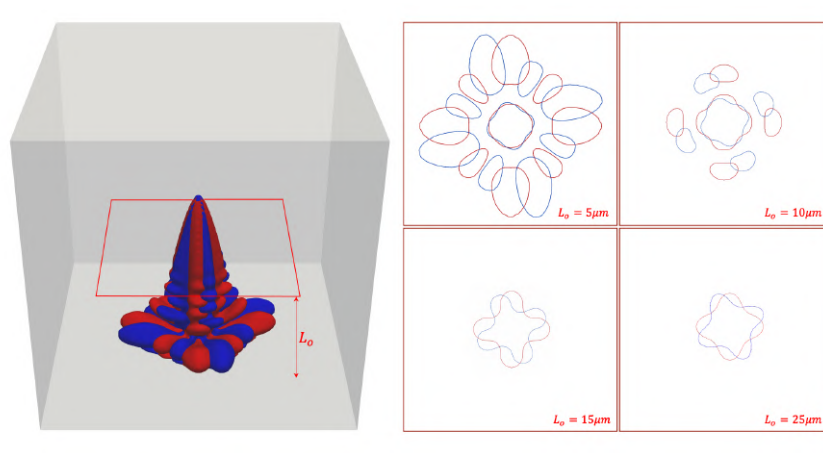
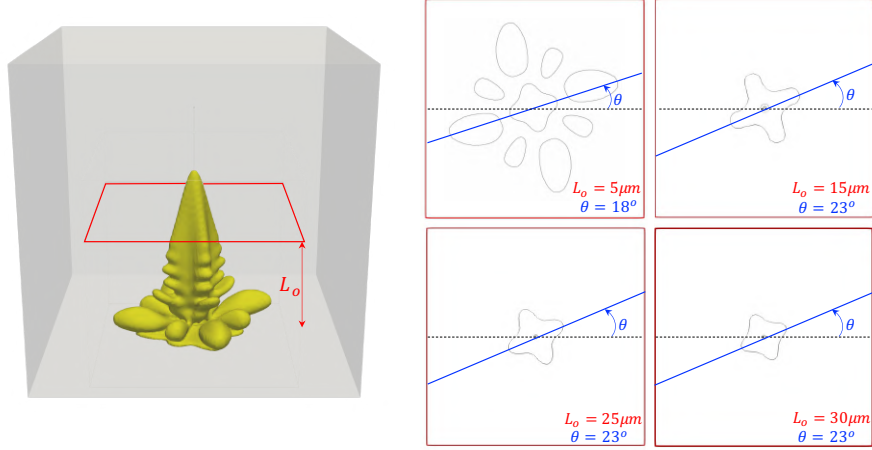
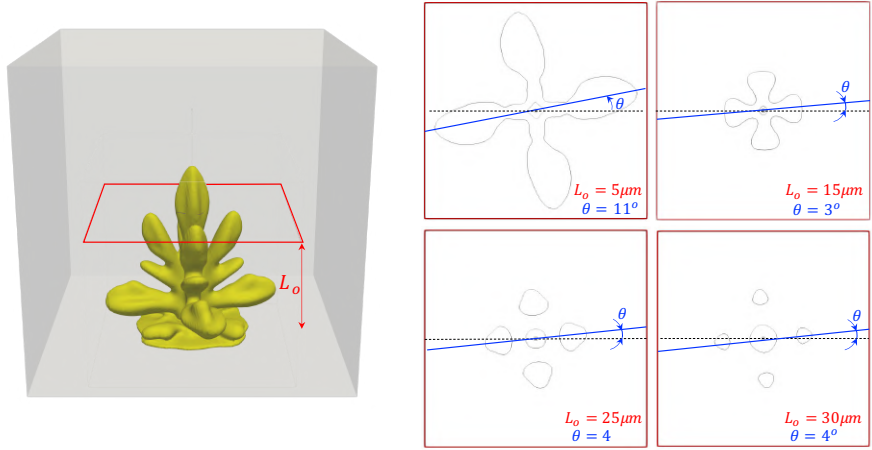


Figure 6.4: Overlay of 3D simulated dendrite morphologies (non-modified anisotropy representation), obtained under Cartesian mesh (red), and 25° rotated mesh around the x -axis (blue). Horizontal slices of the dendrite's contour plots at positions $L_O = 5, 10, 15$ & $25[\mu m]$ depict the angular offset between the morphologies.

Figure 6.5 shows simulated dendrite morphologies under the rotated mesh



(a) $t = 0.58 [s]$.



(b) $t = 0.80 [s]$.

Figure 6.5: 3D simulation results using a single artificial protrusion with the initial **a** and the modified surface anisotropy representation **b**, under a 25° rotated mesh around the x-axis (longitudinal). Horizontal slices of the dendrite's contour plot at positions $L_O = 5, 15, 25$ & $30[\mu m]$ depict the orientation θ of the side branches. We use dendrite's common height ($H = 45 [\mu m]$) as the basis of our comparison.

distribution, using the standard and modified surface anisotropy representations. Now, we analyze the dendrite's side branches orientation θ at fixed positions $L_O = 5, 15, 25$ & $30[\mu m]$ (horizontal slices of dendrite's contour plot). We define the orientation θ as the inclination of the line that crosses the geometry by passing through its center and connecting the two farthest points of the contour (see Figure 6.5). We compare dendrite morphologies at the moment they reach a height

of $H = 45 [\mu m]$. The analysis of the dendrite's side branches (horizontal slices) in Figure 6.5 reveals that the standard anisotropy representation is more sensitive to the orientation of the mesh. For example, orientation analysis in Figure 6.5a depicts dendrite's rotation angles of around $\theta = 23^\circ$, evidently aligned with the 25° of rotation imposed to the mesh. The side branches, due to the modified surface anisotropy representation (6.4) exhibit significantly smaller rotations of about $\theta = 4^\circ$, using the same simulation conditions (see Figure 6.5b). Thus, the modified anisotropy model shows reduced sensitivity with respect to the mesh.

6.1.4 3D Orientation of lithium crystal: A surface anisotropy-based strategy

Given the random nature of the nucleation process, we need to deal with some degree of randomness and uncertainty when determining the preferred growth direction of the dendrite's crystal in the battery. The orientation of the crystal, determined by the orientation of the surface anisotropy, will direct the preferred direction of growth of the lithium dendrite. Thus, we adapt this well-known crystal growth model for solidification in (Takaki et al., 2013) to electrodeposition dendrite growth. We define a material system of coordinates $(\tilde{x}, \tilde{y}, \tilde{z})$, in which each axis corresponds to the $\langle 100 \rangle$ direction of a cubic lattice. The following coordinate transformation \mathbb{T} is used between the coordinate systems of (x, y, z) and $(\tilde{x}, \tilde{y}, \tilde{z})$:

$$\underbrace{\begin{Bmatrix} \frac{\delta \xi}{\delta \tilde{x}} \\ \frac{\delta \xi}{\delta \tilde{y}} \\ \frac{\delta \xi}{\delta \tilde{z}} \end{Bmatrix}}_{\frac{\partial \xi}{\partial \tilde{x}_i}} = \underbrace{\begin{bmatrix} 1 & 0 & 0 \\ 0 & \cos \theta_x & \sin \theta_x \\ 0 & -\sin \theta_x & \cos \theta_x \end{bmatrix} \begin{bmatrix} \cos \theta_y & 0 & \sin \theta_y \\ 0 & 1 & 0 \\ -\sin \theta_y & 0 & \cos \theta_y \end{bmatrix} \begin{bmatrix} \cos \theta_z & \sin \theta_z & 0 \\ -\sin \theta_z & \cos \theta_z & 0 \\ 0 & 0 & 1 \end{bmatrix}}_{\mathbb{T}} \underbrace{\begin{Bmatrix} \frac{\delta \xi}{\delta x} \\ \frac{\delta \xi}{\delta y} \\ \frac{\delta \xi}{\delta z} \end{Bmatrix}}_{\frac{\partial \xi}{\partial x_i}}. \quad (6.5)$$

where θ_x , θ_y , and θ_z are the rotation angles around the x, y, and z axes,

respectively.

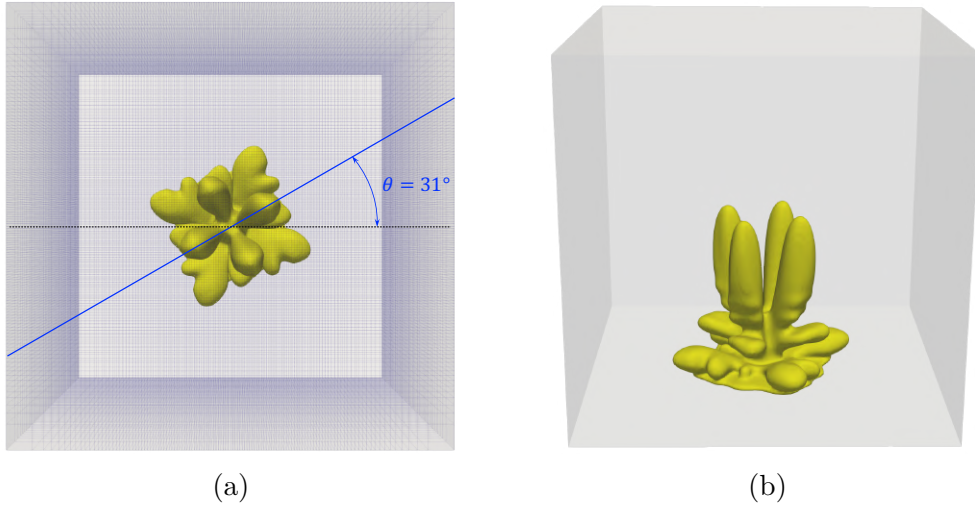


Figure 6.6: Top **a** & perspective **b** views of the 3D spike-like lithium dendrite simulation, with $\theta_x = 35^\circ$ rotation of the surface anisotropy. Top view overlaid with mesh shows that dendrite's orientation is not aligned with the Cartesian axes.

We use (6.5) to compute the gradient of the phase-field variable ($\nabla\xi$) and use it in the surface anisotropy expression (6.1). Therefore, we can assign random values to each of the rotation angles ($\theta_x, \theta_y, \theta_z$) to control the preferred growth direction of the lithium dendrite and side branches. We test the proposed strategy by applying a $\theta_x = 35^\circ$ rotation ($\theta_y = \theta_z = 0^\circ$) to the lithium surface anisotropy when using a Cartesian mesh. Figure 6.6 shows the simulated spike-like lithium dendrite morphology after $t = 0.7$ [s]. The top-view analysis 6.6a reveals that this rotation resulted in a dendrite rotation of about $\theta = 31^\circ$ under the applied anisotropy angle, showing the effectiveness of the proposed strategy.

6.1.5 Mesh size effect for different surface anisotropy representations

Following Section 5.3.3, we study the spatial sensitivity of the modified surface representation under mesh refinement. Given spike-like lithium dendrite symmetry (see Figure 6.1), we use symmetry condition of Section 5.3.3 to reduce the

computation cost and improve the mesh resolution. Thus, we model only one-quarter of the domain, using a $200 \times 100 \times 100$ tensor-product mesh with a mesh spacing of $0.25 [\mu m]$ in the region of interest (bottom half of the domain). The node mapping produces a finer mesh to properly capture the smaller phase-field interface thickness $\delta_{PF} = 1 [\mu m]$ (4 elements in the interface; see Sections 4.3.3 and 5.3.3) and the steepest gradients of $\tilde{\zeta}_+$ and ϕ .

Figure 6.7 shows the simulated lithium dendrite (isosurface plot of the phase-field variable $\xi = 0.5$). The simulation forms a spike-like and highly branched pattern. We calculate the electric field distribution by differentiating the resolved electric potential $\vec{E} = -\nabla\phi$. Figure 6.7 shows how the electric field localizes in the vicinity of the dendrite tip (see (3.22)). In agreement with previous numerical experiments (cf. Figure 5.8), the electric field distribution leads to an enriched concentration of the lithium-ion it induces due to the strong migration from the surrounding regions (Liang and Chen, 2014). The dendrite growth does not occur perpendicular to the stack but at an angle of about 22° between main trunks (cf. Figure 6.6)). The stacks repel each other, similar to previous multiple-nuclei results (cf. Figure 5.11).

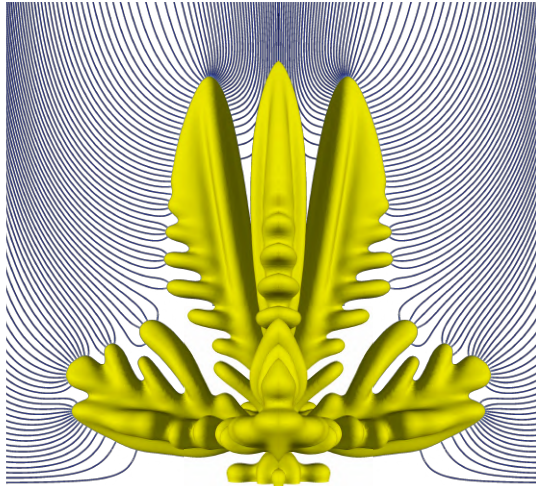


Figure 6.7: Overlay of electric field distribution (blue streamlines) with dendrite morphology under the modified surface anisotropy representation at time $t = 0.7 [s]$. We combine in this figure 4 symmetric copies. Streamline plane set at $y = 40 [\mu m]$.

Figure 6.8 compares the effect of the mesh resolution and phase-field interface thickness on the simulated morphologies, with and without the presence of the modified surface anisotropy term. For the modified surface anisotropy representation, smaller phase-field interface thickness (δ_{PF}) and finer mesh resolution (h) lead to more branched and detailed dendritic patterns. However, in the standard case, higher mesh resolution leads to less branched micorstructures (see Figure 6.8c).

Despite the morphological differences mentioned above, the computed lithium electrodeposition average rate in this case (10,800 [$\mu m^3/s$]) is within analogous simulation results under coarser mesh resolution (9,150 [$\mu m^3/s$], see Figure 6.2b), as well as simulation result using the standard anisotropy representation, using coarse and fine mesh options (10,100 to 12,400 [$\mu m^3/s$], see Figure 5.23). These results show that using the modified surface anisotropy representation is robust in relation to the rate of electrodeposition (volume of lithium metal deposited over time), showing relatively low sensitivity to numerical parameters of our choice (δ_{PF} and \mathcal{R}). In practice, the amount of dendritic lithium directly reduces the Coulombic efficiency of the battery (Adams et al., 2018). Therefore, we envisage a future application of our model in evaluating Coulombic efficiency reduction due dendite’s formation in rechargeable lithium batteries.

6.2 Experimental-scale three-dimensional simulations of lithium dendrite formation

This section evaluates the performance of the modified surface anisotropy model (see Section 6.1.1) in experimental-scale interelectrode distances.

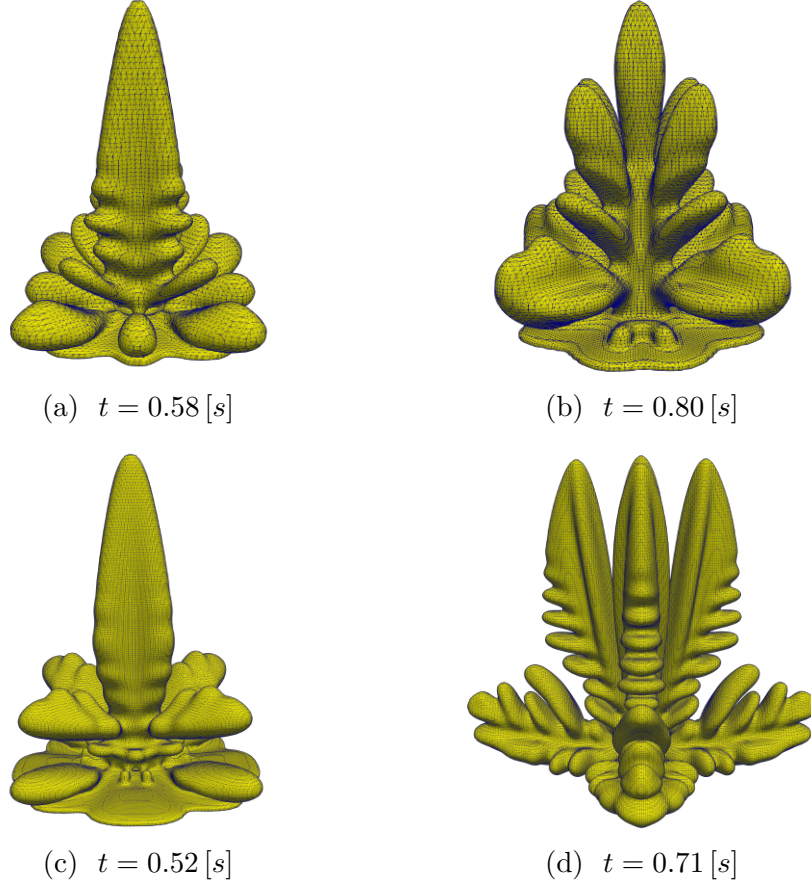


Figure 6.8: Comparison of fully developed lithium dendrite morphologies under $\phi_b = -0.7[V]$ charging potential. The electrodeposited lithium is represented with a yellow isosurface plot of the phase-field variable ξ , overlaid with the mesh grid. Top row (a & b) presents simulation results obtained under coarser mesh resolution ($h=0.5[\mu m]$ & $\delta_{PF} = 1.5[\mu m]$). Bottom row (c & d) depicts results obtained under finer resolution ($h=0.25[\mu m]$ & $\delta_{PF} = 1[\mu m]$). Left column (a & c) correspond to simulated morphologies using the non-modified surface anisotropy representation, and the right column (b & d) allocates dendritic patterns under the modified anisotropy representation. We use dendrite's common height ($H = 45[\mu m]$) as the basis of our comparison. Cube domain set as $80 \times 80 \times 80[\mu m^3]$ in all cases.

6.2.1 Meshing strategy for experimental-scale 3D simulations

The high computational cost of detailed 3D simulations of lithium electrodeposition at the whole-cell scale is a well-known challenge of electrodeposition simulations (Cogswell, 2015; Yurkiv et al., 2018). A limiting factor is the domain

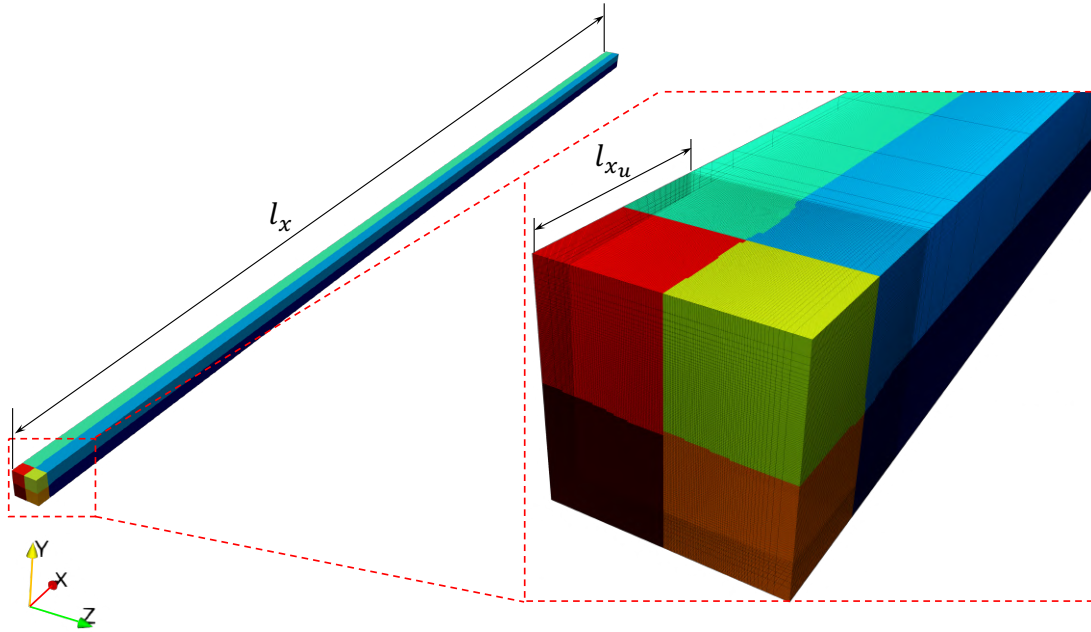


Figure 6.9: 3D mesh partition in 8 processors, each one represented by a different color. Magnified view of the region of interest ($l_{x_u} \ll l_x$), showing a uniform to exponential mapping transition while moving into the bulk region of the domain.

size, which imposes practical restrictions on the 3D simulations. Previously, we chose a domain size of $(80 \times 80 \times 80 [\mu m^3])$ that ensures the simulation volume at an affordable computational cost. But this short domain (electrode separation of $l_x = 80 [\mu m]$) induces dendrite growth rates that are two orders of magnitude higher than those observed experimentally.

A detailed analysis of lithium dendrite experiments reveals that, despite the interelectrode separation distance in experimental cells, which ranges from 1 to $10[mm]$ (Nishikawa et al., 2011; Nishida et al., 2013; Yufit et al., 2019), the lithium dendrites effectively occupy up to 20% of the interelectrode space. Thus, we focus on this area of interest, the region/volume of the experimental cell where lithium dendrites develop, near the anode surface. Furthermore, previous simulation results show that the spatial distribution of the variables in the bulk region (outside the area of interest) exhibit either constant values, such as $\xi = 0$ and $\tilde{\zeta}_+ = 1$, or small electric potential gradients $\nabla\phi$. This weak variation indicates that only a few elements may adequately capture the bulk behavior. At

the same time, we assign most computational resources to the area presenting the steepest gradients of ξ , $\tilde{\zeta}_+$ and ϕ , representing a small portion of the whole domain.

This section applies the modified anisotropy representation in 3D simulations targeting experimental time and length scales. We describe a simple meshing strategy that exploits the aforementioned distribution by combining uniform node's mapping in the portion of the physical domain where the lithium electrodeposition process occurs (finer and regular mesh), with an exponential increment of the mesh size as we move away from the electrode into the electrolyte's bulk region. Thus, we use a 3D structured mesh with eight-node hexahedral elements. Within the bulk region, in particular in the x -direction $x_r = 2^j \times x_u$ with $j = 1, 2, \dots, n$; where x_u is the node's x coordinate normalized by l_x , before mapping (uniform distribution), and x_r is the node's mapped coordinate. The exponential function transitions smoothly by doubling the element size when moving away from the area of interest into the bulk region. This focussed-mesh distribution in the area of interest and subsequent stretching allow us to achieve experimental interelectrode distances with only a few additional elements. Consequently, although the detailed portion of our domain (l_{x_u}) remains the same ($80 \times 80 \times 80 [\mu m^3]$), we are now able to avoid simulations with higher-than-normal dendrite's growth rates, by achieving experimental interelectrode distances (l_x up-to $5000 [\mu m]$).

Thus, we select a geometrical unit that characterizes a real cell structure (Yurkiv et al., 2018; Trembacki et al., 2019). We choose a computational domain of $5000 \times 80 \times 80 [\mu m^3]$. Figure 5.1b summarizes the boundary conditions we apply. Lateral dimensions remain unchanged in this case ($l_y = l_z = 80 [\mu m^3]$), which along with periodic boundary conditions applied on the lateral faces, generates a $80 [\mu m] \times 80 [\mu m]$ nucleation arrangement surrounding the simulated morphology (neighbouring dendrites). The implemented approach constitutes a more realistic alternative than modelling a single isolated dendrite (Nishikawa et al., 2011;

Nishida et al., 2013). Furthermore, neighboring dendrites act as a barrier (charge repulsion effect) that limits the side development of the simulated electrodeposit beyond the domain’s boundaries.

We use a $180 \times 100 \times 100$ tensor-product mesh, with a mesh size of $0.4 [\mu m]$ in the region of interest (l_{x_u}). We partition the mesh into eight processors. Figure 6.9 identifies each core with a different color, showing that the tensor-product mesh can efficiently allocate resources in the region of interest (l_{x_u}).

6.2.2 Experimental-scale 3D simulations

This section presents 3D phase-field simulations of lithium dendrite formation to study dendritic patterns formed under $\phi_b = -0.7 [V]$ and $\phi_b = -1.4 [V]$ charging potential, using experimental-scale interelectrode distance ($l_x = 5000 [\mu m]$). We use artificial nucleation regions, ellipsoidal protrusions (seeds) with semi-axes $4 [\mu m] \times 2 [\mu m] \times 2 [\mu m]$, and centres located at $(y, x, z) = (0, 38, 38)$, $(0, 42, 38)$, $(0, 38, 42)$ and $(0, 42, 42)$. We modify the initial condition, by introducing a constant electric potential gradient in the liquid electrolyte region, from $\phi = \phi_b$ at the electrode-electrolyte interface, to $\phi = 0$ at $x = l_x$ (cathode), which corresponds to the experimental observations by Nishida et al. (2013). They measured the initiation periods (time transient) for dendrite precursors to start to grow (become visible under an optical microscope) between 4 to 140 s (Nishida et al., 2013); shorter initiation times occur under larger applied current density. Therefore, sufficiently developed dendrite nuclei may take several seconds to appear, depending on the electrodeposition conditions. This time is sufficient for developing the electric potential gradient in the electrolyte. In addition, the initial conditions for ξ and $\tilde{\zeta}_+$ remain the same, with a smooth transition between the solid seed (lithium metal anode) and the surrounding liquid electrolyte region (see Section 5.1).

Figure 6.10 shows the morphological evolution of the simulated lithium dendrite (isosurface plot of the phase-field variable ξ) under $\phi_b = -0.7 [V]$ charging

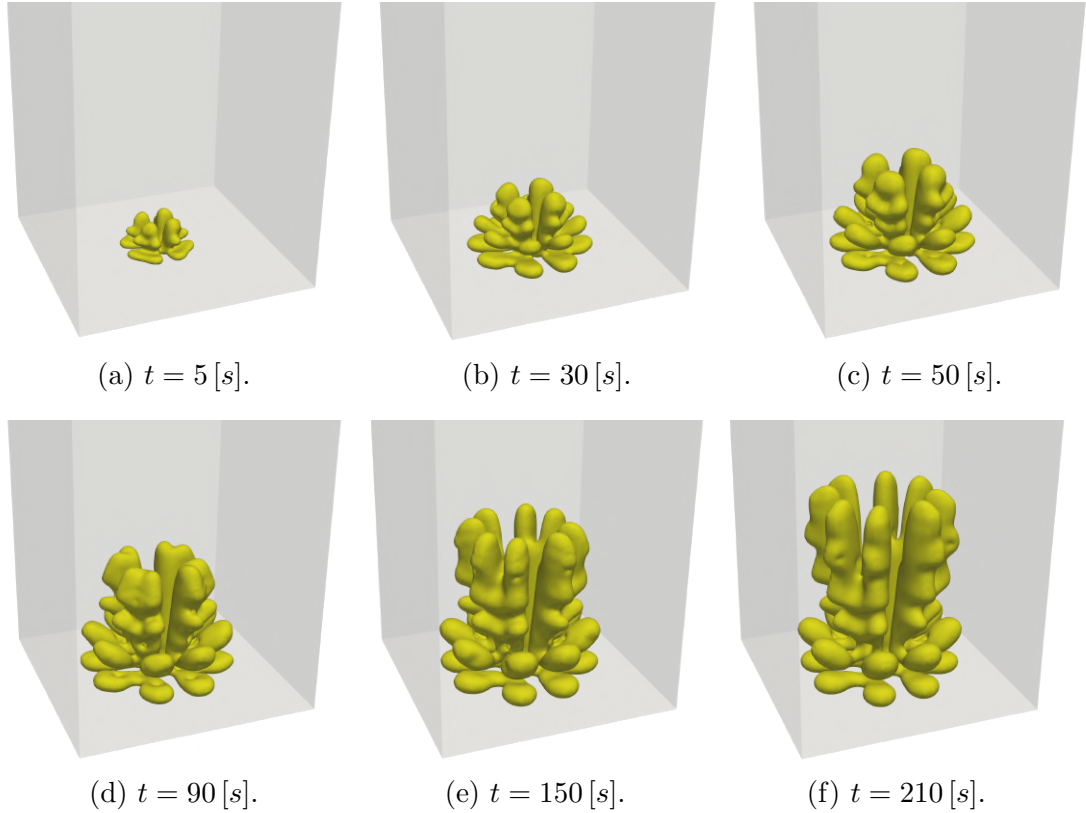


Figure 6.10: 3D lithium dendrite simulation with modified anisotropy representation, under $\phi_b = -0.7 [V]$ charging potential. The electrodeposited lithium is represented with a yellow isosurface plot of the phase-field variable $\xi = 0.5$. Hexagonal domain set as $5000 \times 80 \times 80 [\mu m^3]$.

potential. This setup yields realistic simulation time scales due to the larger interelectrode distance we employ (Nishikawa et al., 2011). Stationary propagation rates (dendrite’s tip speed) of around $0.2 [\mu m/s]$ are reached after 70 s of simulation (see Figure 6.13a). The simulated growth rates are larger than those reported by Nishikawa et al. (2011) in experimental measurements of lithium dendrite growth in 1M $LiPF_6$ electrolyte ($0.06 [\mu m/s]$) due in part to the higher (almost double) applied current density in our model. Our results are within the range of lithium dendrite growth rates reported by Nishida et al. (2013) ($0.25 - 0.55 [\mu m s^{-1}]$) using a different electrolyte type (LiTFSI). Therefore, further well-controlled experimental studies, with detailed characterization of the system parameters, combined with modelling will be necessary to improve the

correlation (Akolkar, 2014). Unlike previous 3D simulations, forming spike-like patterns (cf. Figure 5.11), this case yields less branched, blunt tip, finger-like morphologies. The dendrite morphology consists of four main trunks growing from each nucleus, with pairs of orthogonal branches developing to the sides. The observed morphological difference is a consequence of the spatial distribution of the electrostatic potential in the electrolyte (ϕ). Although the applied electric potential remains the same ($\phi_b = -0.7 [V]$) the larger interelectrode distance results in a significantly different electric field distribution ($\vec{E} = -\nabla\phi$). The electric field surrounding the electrodeposit region can be 60 times smaller than in previous simulations lowering the current density (consistent with the change ratio in the interelectrode distance $5000 [\mu m] / 80 [\mu m] = 62.5$). This weaker current density results in a weaker action of the electric migration forces over the distribution of lithium ions in the electrolyte. Thus, lithium ions are less prone to accumulate around dendrite tips due to the counteracting influence of diffusion due to the concentration gradient (3.22), producing less branched and blunt morphologies.

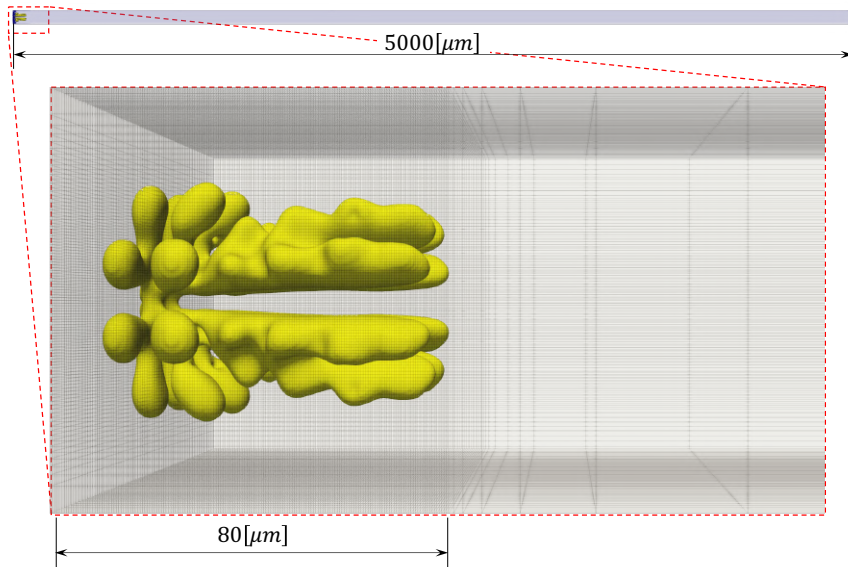


Figure 6.11: 3D mesh overlaid with simulated lithium dendrite morphology at $t = 210 [s]$ ($\phi_b = -0.7 [V]$). Magnified view of the region of interest ($l_{x_u} \ll l_x$), showing a uniform to exponential mapping transition while moving into the bulk region.

The lower electric field effect is in agreement with experimental observations

by Chae et al. (2022), where a variation of the separation between the electrodes revealed a considerable difference in the electrochemical deposition of lithium (experiments under $1[mA/cm^{-2}]$ applied current density). Chae et al. (2022) observed that the lithium deposition behavior and morphology changed from "hazardous" needle- and moss-like dendritic structures to "safer" morphologies (smooth and round shaped surface) as interelectrode spacing increases. The variation of lithium deposition behavior was ascribed to a difference in the Li-ion concentration distribution. Thus, when under shorter interelectrode separation ($< 500 [\mu m]$), lithium electrodeposition occurs closer to the high Li-ion concentration regions (formed by the release of Li-ions from the counter electrode), producing a non-uniform directional deposition of lithium. Sharp dendritic structures can grow and penetrate porous separators, which are potentially dangerous as they can create a short battery circuit (Bai et al., 2018). On the other hand, larger electrode separations (2000 and 4000 $[\mu m]$) lead to a more uniform deposition, without any angular edges or sharp tips, due to lower Li-ion concentration and electric potential gradients (Chae et al., 2022). Although the current density applied in the present simulation is lower than in previous numerical examples, it remains well above the limiting current density of the system, about $i_{lim} = 2 [mA/cm^{-2}]$ (Bai et al., 2016). For over-limiting current densities applied to the cell, the rate of lithium deposition overcomes the rate of solid-electrolyte interface formation, allowing the lithium deposit to grow almost free from the influence of the SEI (Bai et al., 2018).

Figure 6.11 shows that the fully developed lithium dendrite morphology ($t = 210 [s]$) resides within the region of interest (well-resolved portion of the domain: $\leq 80 [\mu m]$), which makes-up only 1.6% of the whole domain. Although the system size is similar to previous 3D simulations presented in this work (5,400,000 degrees of freedom), the temporal evolution is slower, increasing the computational time by four times.

Next, we present a 3D phase-field simulation of lithium dendrite formation

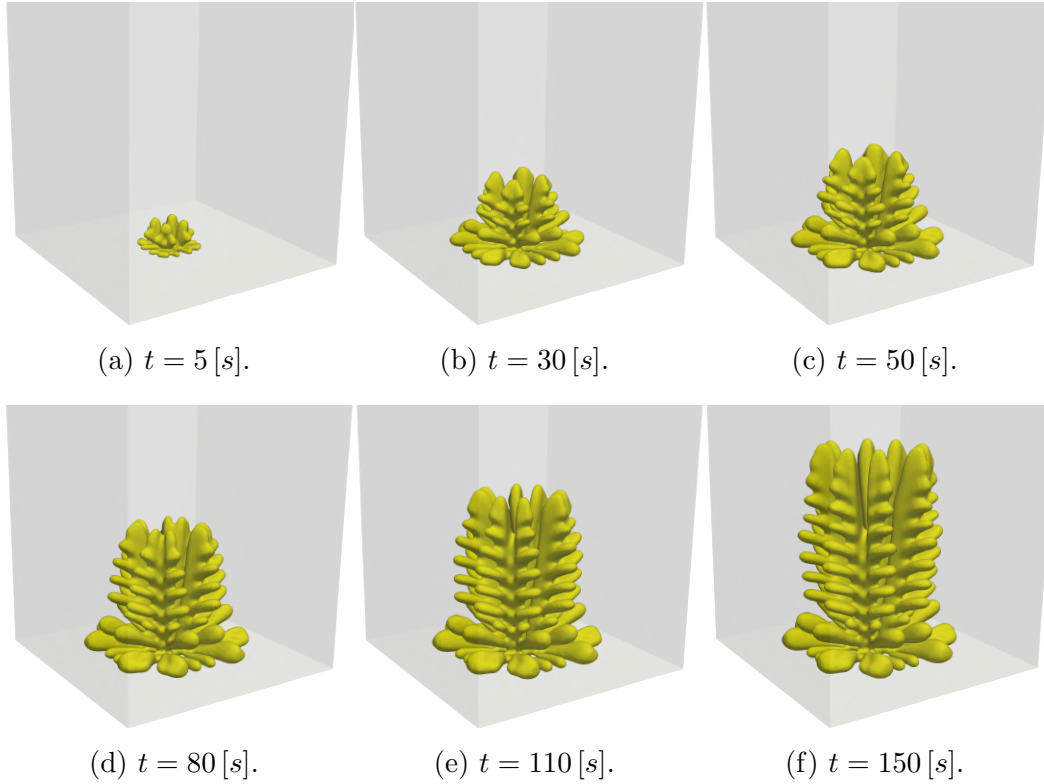


Figure 6.12: 3D lithium dendrite simulation with modified anisotropy representation, under $\phi_b = -1.4 [V]$ charging potential. The electrodeposited lithium is represented with a yellow isosurface plot of the phase-field variable ξ . Hexagonal domain set as $5000 \times 80 \times 80 [\mu m^3]$.

under more negative applied voltage $\phi_b = -1.4 [V]$. We use the setup of the previous experiment, with the sole difference of the applied voltage ϕ_b . We adjust the interfacial mobility parameter L_σ (3.19) to the newly applied electro potential to achieve the right balance between the phase-field interface energy term and the electrochemical reaction contribution (see Section 3.1.1). Figure 6.12 depicts the evolution of the lithium dendrite (ξ isosurface). As in the previous experimental-scale case, we obtain realistic simulated time scale, with stationary dendrite propagation rates of about $0.4 [\mu m/s]$ (see Figure 6.13b). The higher propagation rate in this case is due to the higher applied current density (from $\phi_b = -0.7$ to $-1.4 [V]$ charging potential), which agrees with experimental results, where higher current densities produce faster electrodeposition and dendrite propagation rates (Monroe and Newman, 2003; Nishikawa et al., 2011; Akolkar,

2013). Furthermore, we see that computed dendrite propagation rates are within the range of lithium dendrite experiments reported by Nishida et al. (2013).

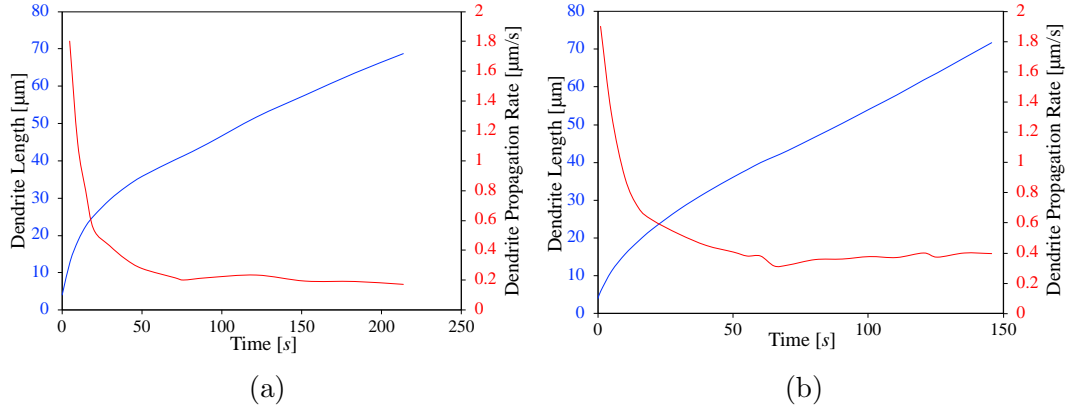


Figure 6.13: Simulated 3D lithium dendrite propagation plot. Dendrite length (blue) & propagation rate (red) vs time for applied voltages: (a) $\phi_b = -0.7 [V]$, and (b) $\phi_b = -1.4 [V]$.

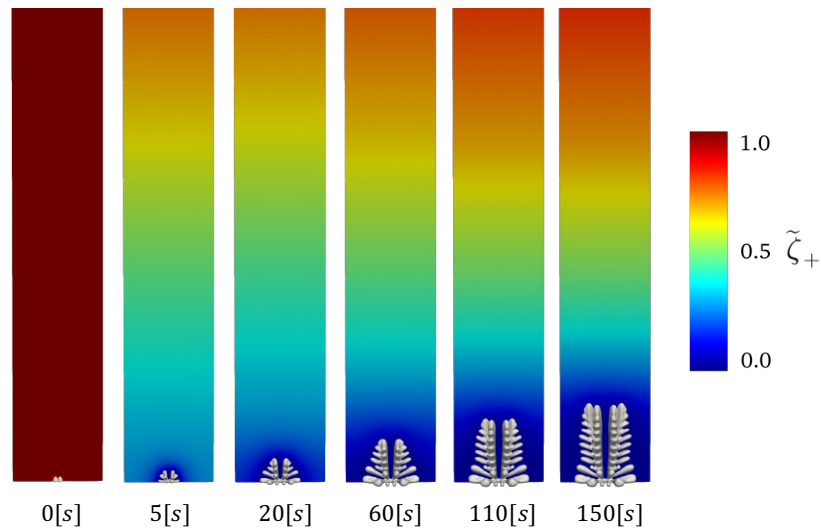


Figure 6.14: Evolution of the spatial distribution of lithium-ion concentration, overlaid with dendrite morphology. Contour plane set at $y = 35 [\mu m]$, display of first $400 [\mu m]$ portion of the domain. Experimental interelectrode distance $l_x = 5000 [\mu m]$, and applied voltage $\phi_b = -1.4 [V]$.

The simulation produces a spike-like, symmetric, and highly branched pattern, with morphological resemblance to previous dendritic deposits obtained under shorter interelectrode distance (cf. Figure 5.11). The microstructure consists of four main trunks growing from each nucleus, with pairs of orthogonal branches

developing to the sides. Figure 6.14 depicts the evolution of the simulated spike-like dendritic morphology, together with the spatial distribution of the lithium-ion concentration $\tilde{\zeta}_+$ in the electrolyte region.

Figure 6.14 shows the evolution of the Li-ion concentration profile extending over $400 [\mu m]$ in the stack direction (x); where the deposition process depletes the lithium-ion concentration close to the electrode (shown in blue). This behavior contrasts with smaller-scale simulations presented earlier in this work, where Li-ion concentration enriches the dendrite tips due to large electric migration forces (see Figure 6.2). This dendrite-tip enrichment can happen in a close-to-short-circuit condition (short interelectrode distance). Nevertheless, our simulations indicate that lower electro-potential gradients, such as those obtained under experimental-scale interelectrode distances, do not generate high Li-ion concentration around the dendrite tips (competition between electric migration and diffusion due to the Li-ion concentration gradient). This observation is in agreement with experimental measurements of Li-ion surface concentration by Nishida et al. (2013), where the concentration of Li-ion near the electrode surface was reduced from 1 M (initially) to less than 0.1 M, after a few tens of seconds of electrodeposition, depending on the experiment's conditions.

We obtain apparent morphological differences from the previous dendritic lithium electrodeposition simulation under the experimental-scale domain (cf. Figure 6.10). Although in this case, the electric field ($\vec{E} = -\nabla\phi$) surrounding the electrodeposit region remains low relative to previous simulations with shorter interelectrode separation ~ 30 times smaller; the larger charging voltage ($\phi_b = -1.4 [V]$) induces a spike-like and highly branched dendrite (over-limiting current density condition). This result agrees with previous two-dimensional phase-field studies investigating the effect of the applied voltage on the electrodeposit's morphological structure. Increasing the applied voltage produces faster dendrite formation with the tip splitting phenomenon (Chen et al., 2015), changing from a needle or finger-like structure to a tip splitting or spike-like pattern (Mu

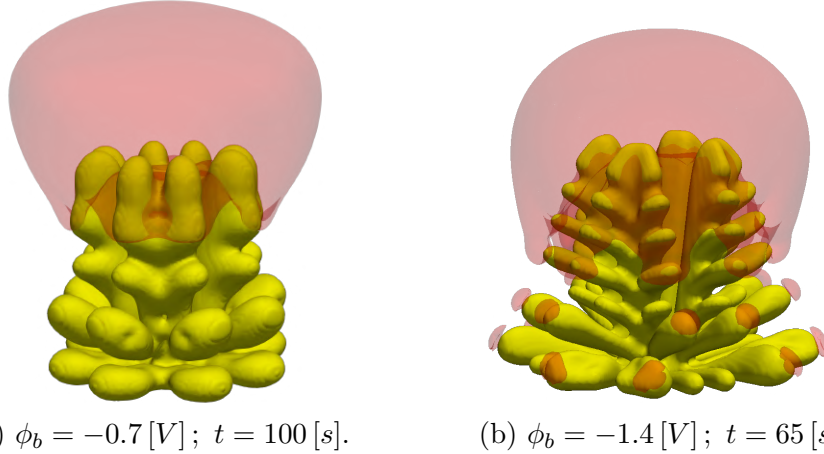


Figure 6.15: Comparison of lithium-ion concentration gradients for (a) $\phi_b = -0.7 [V]$, and (b) $\phi_b = -1.4 [V]$, applied voltage. Electrolyte regions with higher lithium-ion concentration gradient ($\|\nabla\tilde{\zeta}_+\| > 0.005$) represented with red volumes. Interelectrode distance $l_x = 5000 [\mu m]$. We use dendrite's common height ($H = 45 [\mu m]$) as the basis of our comparison.

et al., 2019). The reactive term of the phase-field equation, see (6.4), is exponentially affected by the electric potential through $\eta_a = \phi - E^\ominus$. The applied voltage increases the degree of polarization on the electrode, affecting the deposition and accumulation of lithium on the anode surface, which leads to changes in the morphology of lithium dendrites (Mu et al., 2019). One verifies this by inspecting the Li-ion concentration gradient $\|\nabla\tilde{\zeta}_+\|$ in the electrolyte region surrounding the dendrites morphologies. Figure 6.15 shows a comparison between the experimental-scale simulation results obtained under different charging voltages: $\phi_b = -0.7 [V]$ (Figure 6.15a), and $\phi_b = -1.4 [V]$ (Figure 6.15b). Electrolyte regions with higher lithium-ion concentration gradients ($\|\nabla\tilde{\zeta}_+\| > 0.005$) are represented with red volumes. Thus, higher lithium-ion concentration gradients appear in the vicinity of the dendrites' tips and side branches in Figure 6.15b leading to a spike-like, highly branched dendritic lithium (resembling the previously observed electric-migration versus diffusion due to the Li-ion concentration gradient competition happening here at a smaller scale). In contrast, Figure 6.15a, under lower applied voltage, only presents higher lithium-ion concentration gradients in the vicinity of upper tips of the dendrite triggering vertical and less

branched growth. Therefore, the spike-like lithium morphologies forming under over-limiting current density (fast battery charge) (Jana et al., 2019) can occur either using a large electric field ($\vec{E} = -\nabla\phi$) surrounding the electrodeposit region (close-to-short-circuit condition) or under a large applied voltage ϕ_b (fast battery charge). This forcing produces strong electric migration forces, causing lithium cations to move from less concentrated surrounding regions (i.e., lithium-ion depletion of valley regions) and accumulate around dendrite tips, triggering spike-growing and highly branched dendritic lithium.

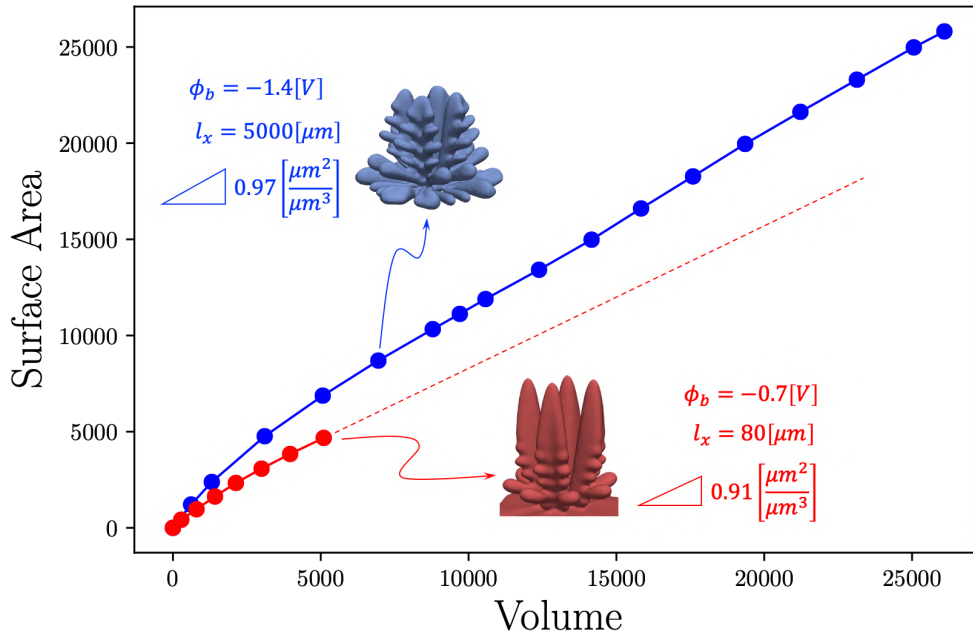


Figure 6.16: Morphological comparison between 3D simulations of spike-like multi-nuclei dendrite growth, smaller-scale with non-modified anisotropy representation (red - Section 5.3.2), and experimental-scale with modified anisotropy representation (blue), in terms of the evolution of volume vs surface area ratio.

Following (Yufit et al., 2019), we characterize the morphology by tracking the dendrites' volume-specific area ($\mu\text{m}^2/\mu\text{m}^3$). Figure 6.16 compares the growth of the deposited volume versus the surface area for the 3D spike-like lithium pattern we simulate (short interelectrode separation vs experimental-scale results).

Despite differences in the time and length scales between these simulations, we obtain similar volume-specific area average ratios; 0.91 and 0.97 [$\mu\text{m}^2/\mu\text{m}^3$],

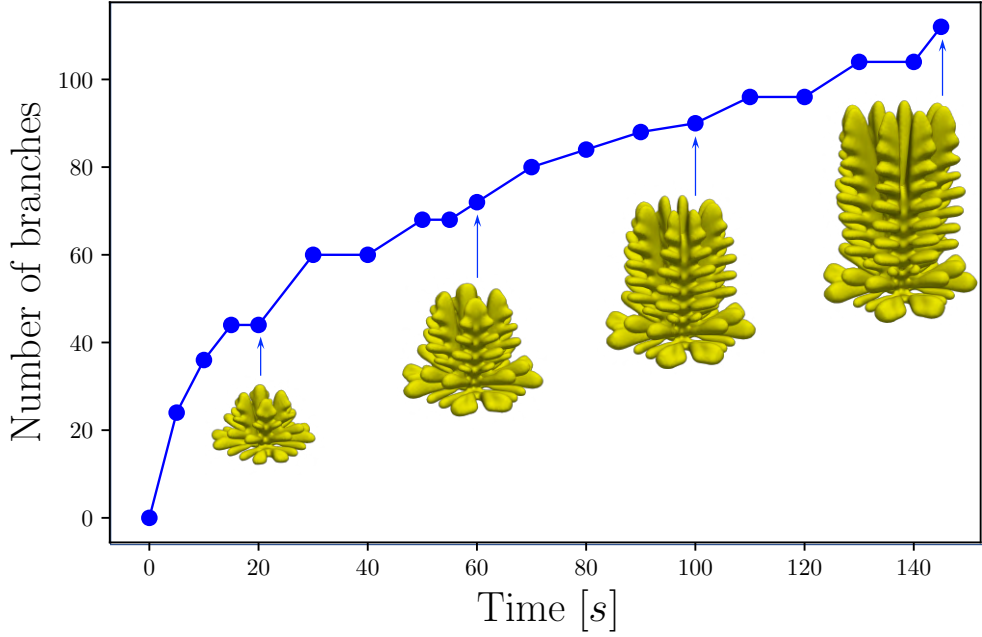


Figure 6.17: Morphological analysis of 3D spike-like dendrite growth simulation in terms of number of side branches developed over time. Experimental interelectrode distance $l_x = 5000 [\mu m]$, and applied voltage $\phi_b = -1.4 [V]$.

for smaller-scale and experimental-scale simulations, respectively. The higher surface area/volume ratio indicates a more branched shape in the experimental-scale simulation. Both cases are within the volume-specific results reported for experimental formation of dendrites in zinc batteries (0.86 and $1.04 [\mu m^2/\mu m^3]$) (Yufit et al., 2019) (the literature lacks experimental data for quantitative characterization of the spike-like lithium morphologies).

Remark 1 *The similar area/volume average ratios between the dendritic microstructures formed using the experimental-scale simulation domain and the deposition patterns obtained under the short interelectrode distance setup (close-to-short-circuit condition) opens the possibility of using small-scale (lower-cost) 3D simulations. For example, the earlier ones in this work may be a useful testing tool to assess and adjust different 3D strategies before moving into more expensive, well-resolved larger-scale 3D simulations.*

Figure 6.17 tracks the number of side branches formed over time. The simula-

tion produces stationary ratios of about 0.5 branch per second $[1/s]$. We compute the number of branches by visual inspection of the simulated morphologies, where we consider new protuberances as incipient branches. Given the lack of experimental data in the literature for quantitative characterization of the spike-like lithium morphologies, we rely on experimental results for zinc dendrites. Yufit et al. (2019) report values between 0.19 and 0.92 branches per second $[1/s]$ for experimental formation of "spruce tree"-like dendrites in zinc batteries under $\phi_b = -1.6 [V]$ applied voltage, and $3000 [\mu m]$ interelectrode separation. Thus, we observe agreement between the simulated branching dynamic and experimental data.

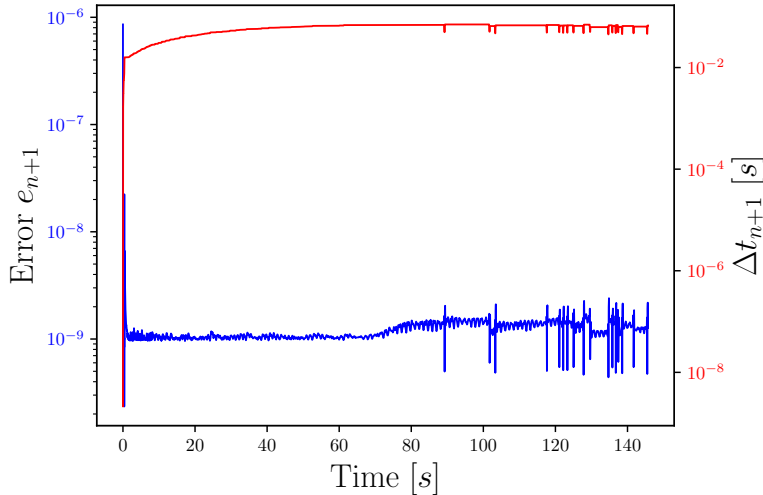


Figure 6.18: Time adaptivity plot for 3D lithium dendrite growth simulation under $\phi_b = -1.4 [V]$ charging potential, and experimental-scale interelectrode distance ($5000 [\mu m]$).

Figure 6.18 shows the behaviour of the time-adaptive scheme, throughout the 150 $[s]$ of the simulation. Starting with a small time-step of $\Delta t_0 = 10^{-8} [s]$ to initially achieve convergence, followed by an increase in size, until reaching a stationary value of about $\Delta t_{n+1} = 0.05 [s]$ (almost two orders of magnitude larger than previous simulations under smaller interelectrode distance). The weighted truncation error e_{n+1} (blue) stays close to the minimum tolerance limit (10^{-9}) during the whole simulation. The estimated error does not grow exponentially

as in previous cases (cf. Figure 5.16) since the lithium dendrite remains far away from the positive electrode (propagation rate does not accelerate).

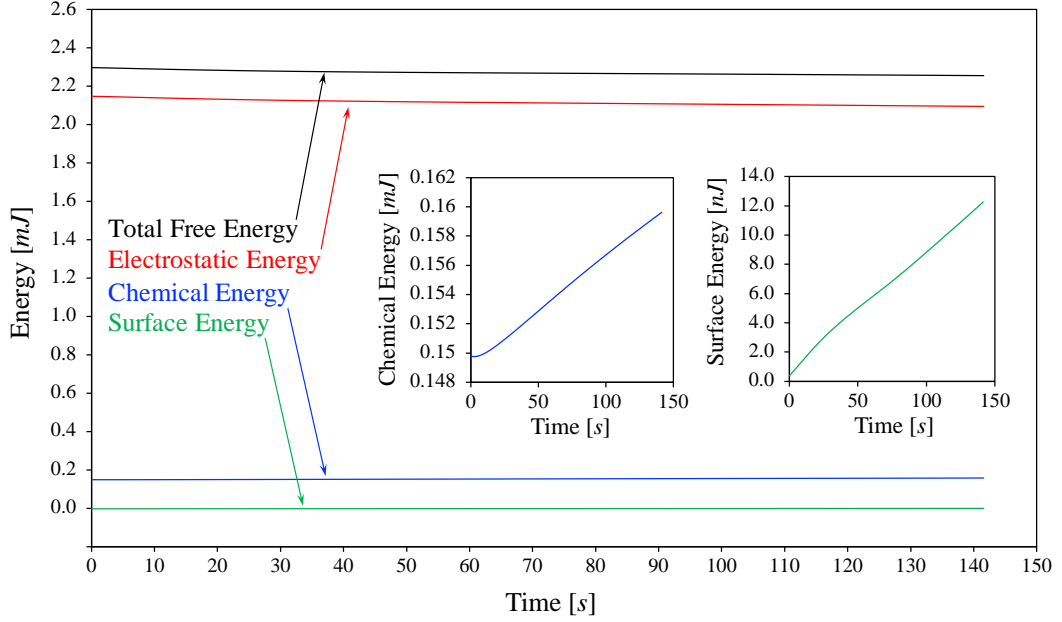


Figure 6.19: Energy time series for 3D spike-like dendrite growth simulation with modified anisotropy representation, under $\phi_b = -1.4 [V]$ applied voltage, and interelectrode distance $l_x = 5000 [\mu m]$. The insets plot the increasing chemical and surface energy in smaller scale for better appreciation.

Standard discrete approximations do not inherit the a priori nonlinear stability relationship satisfied by phase-field models, expressed as a time-decreasing free-energy functional (see, e.g., Gomez and Hughes (2011); Sarmiento et al. (2018); Vignal et al. (2017) for discussions on energy stable time-marching methods). Therefore, we study the energetic evolution of our system. Figure 6.19 shows the evolution of the Gibbs free energy of the system Ψ , using our adaptive time integration scheme for the experimental-scale phase-field simulation. We plot the total energy curve (black), as well as three additional energy curves that correspond to each one of its terms, namely, the Helmholtz (chemical) free energy $\int_V f_{ch} dV$ (blue), surface energy $\int_V f_{grad} dV$ (green), and electrostatic energy $\int_V f_{elec} dV$ (red), as the figure indicates. Figure 6.19 shows that the total systems' discrete free energy does not increase with time. Thus, we obtain discrete energy

stable results in experimental-scale simulations using our second-order backward-difference (BDF2) time-adaptive marching scheme, although the method is not provably stable energetically. Moreover, while the system’s surface and chemical energies grow as the area of the lithium deposit increase, the electrostatic energy decreases in time. This behaviour, previously observed in smaller scale 3D simulations, is consistent with the electrodeposition process, where the system stores the applied electrostatic energy as electrochemical energy as the battery charges. The inset in Figure 6.19 shows that the surface energy of the fully developed pattern is almost four times larger than the surface energy computed in Figure 5.17 for the smaller-scale simulation. The proportionately four-times larger surface area in the experimental-scale case (see Figure 6.16) explains this scaling.

In conclusion, well-resolved experimental-scale simulations using a modified 3D surface anisotropy representation of lithium crystal have been performed. The modified model improves the simulation results being less sensitive to the mesh orientation. We simulate two charging voltages ($\phi_b = -0.7 [V]$ and $\phi_b = -1.4 [V]$), revealing details about the mechanism behind spike-like dendrite growth at experimental scale. Furthermore, we verify measured morphological parameters, such as simulated dendrite propagation rates, volume-specific area, and side branching rates, within the reported ranges for experimental electrodeposition of spike- or tree-like metal dendrites. Our experimental-scale analysis confirms the connection between lithium dendrite formation and the competition effect between lithium cations diffusion and electrical migration, generating an uneven distribution of Li^+ on the electrode surface that increases under more negative applied voltages (fast battery charge). This fact reaffirms our insight into strategies of dendrite suppression, focusing on achieving a more uniform distribution of Li-ion concentration on the anode surface as an effective approach to reduce the dendrite formation propensity.

Chapter 7

Conclusions and research perspectives

7.1 Conclusions

A computational investigation of lithium electrodeposition in rechargeable metal-anode batteries has been performed, having major technological significance for modern battery systems.¹ Enhancing the energy density and life cycle of energy storage systems is a major driving force for research into new battery technologies. Novel rechargeable lithium-metal batteries (LMBs) can achieve ultra-high energy densities (Figure 1.2) by avoiding the use of a graphite anode structure (compare conventional Li-ion and LMB structures and charging mechanisms in Figure 1.3). The greatest challenge to achieve the commercial realisation of LMBs is related to

¹Parts of the content of this chapter are published in:

- Arguello, M. E., Gumulya, M., Derksen, J., Utikar, R., & Calo, V. M. (2022). Phase-field modeling of planar interface electrodeposition in lithium-metal batteries. *Journal of Energy Storage*, 50, 104627.
- Arguello, M. E., Labanda, N. A., Calo, V. M., Gumulya, M., Utikar, R., & Derksen, J. (2022). Dendrite formation in rechargeable lithium-metal batteries: Phase-field modeling using open-source finite element library. *Journal of Energy Storage*, 53, 104892.
- Arguello, M. E., Labanda, N. A., Calo, V. M., Gumulya, M., Utikar, R., & Derksen, J. (2022). Three-dimensional experimental-scale phase-field modelling of dendrite formation in rechargeable lithium-metal batteries. *Publication under review*.

the unstable, nonuniform deposition of lithium during battery charge (Figure 1.4). Thus, controlling the morphology of the electrodeposited material is a serious challenge, which drastically affects the capacity, stability and safety of LMBs.

Within computational research, based on classical chemical reaction kinetics, our literature review work reveals that the phase-field method is a suitable modeling technique for studying mesoscale (μm) electro-kinetic phenomena, such as dendritic electrodeposition of lithium, with a reasonable computational cost (see Figure 2.4). Phase-field (diffuse-interface) models can simulate the morphology evolution of lithium electrodeposit due to reaction-driven phase transformation within metal anode batteries (Figure 2.6) and rationalize morphology patterns of dendrites observed experimentally (Figure 2.2).

Thus, we develop a computational model based on the framework of phase-field models, to investigate the electrodeposition process that forms dendrites within metal-anode batteries. We derive the free energy functional model, arriving at a system of partial differential equations that elucidates the evolution of a phase field (ξ), the lithium-ion concentration ($\tilde{\zeta}_+$), and an electric potential (ϕ); a summary of the dendrite growth model is presented in Section 3.1.4. We formulate, discretize (Section 3.2), and solve the set of partial differential equations describing the coupled electrochemical interactions during a battery charge cycle using an open-source finite element library that allows us to use parallel solvers. We apply a time-adaptive strategy and detail its implementation and parametrization (Section 3.3). The implemented time-adaptive strategy produces energy stable results, expressed as a time-decreasing free-energy functional.

We use one-dimensional (planar interface) simulations (Figure 4.1) as an effective strategy to quantify the resolution requirements of the model under study, that allows us to set ground rules for further 2D and 3D simulations. We perform phase-field simulations to describe the flat electrode evolution during metal (lithium) electrodeposition. We demonstrate the validity of the current model by comparing the simulation results with theoretical Faradic reactions (4.2) and the

kinetics of the sharp-interface Butler-Volmer model (3.3).

The planar interface simulations also allowed us to compare 2 alternate formulations of the phase field model, derived from either a free energy functional (3.22) or a grand canonical approach (3.26). We assess each model’s sensitivity to the numerical and physical parameters and their robustness. Our results showed that while both formulations demonstrated a dependency of electrodeposition rate on the phase-field interface thickness (and the applied voltage), a lower degree of sensitivity was obtained with the case of the conventional free energy approach (see Figure 4.5).

We show that 1D interface-thickness-independent growth (convergent results) are possible well before reaching the physical nanometer interfaces width (ichi Morigaki, 2002). In general, wider interfaces ($\delta_{PF} > 1 [\mu m]$) increase the reactive area in the simulation, which induces faster electrodeposition rates (see Figure 4.6). We required smaller phase-field interface thickness ($\delta_{PF} = 0.5 [\mu m]$), with higher mesh resolution ($h = 0.125 [\mu m]$), to capture reaction rates under more negative electric potential values ($\phi_b = -0.5 [V]$) using the grand canonical formulation (Figures 4.7 and 4.8). Consequently, the computational cost significantly increases, making this class of models intractable for applications in three-dimensions under large negative applied voltages involving dendrite growth under fast battery charge. Thus, we select the free energy formulation (3.8) as the approach to proceed with 2D and 3D simulations.

In addition to planar interface studies, further 2D simulations complete the groundwork setting for 3D phase-field simulations of lithium dendrite formation. This include 2D testing of the numerical parameters previously defined through 1D electrodeposition studies, such as phase field interface thickness ($\delta_{PF} = 1.5 [\mu m]$) and mesh resolution ($h = 0.5 [\mu m]$ - Figure 4.9). These numerical examples assessed the framework’s effectiveness to capture the two-dimensional development of lithium electrodeposits, starting from a planar electrode configuration (Figure 5.1a) as well as using artificial nucleation sites (Figure 5.1b).

The validation of the predicted lithium dendrite propagation rates against experimental results obtained from thin-cell geometries confirmed the reliability of the proposed model (Figure 5.3) depicts the propagation comparison plot). Furthermore, the agreement attained between the simulated lithium dendrite morphology, Li-ion and electric potential distribution (Figure 5.4) with simulation results reported in other phase-field models of lithium dendrite growth, verifies our work as a preliminary step to move into more complex 3D simulations.

The realisation of 3D simulations, such as those presented in this work, is an important milestone for the study and understanding of the three-dimensional effects triggering spike-like lithium dendrite formation (inherently three dimensional patterns (Jana et al., 2019; Ding, 2016; Tatsuma et al., 2001)). These dendritic patterns are known to grow rapidly across the electrolyte region and penetrate through porous separators, becoming hazardous for battery operation (Bai et al., 2018). A central challenge towards the goal of 3D simulations is the large computational cost involved in solving the highly non-linear set of equations (PDE's) describing coupled electrochemical interactions during a battery charge cycle. This was also evident from the scarcity of three-dimensional phase field results identified in our literature review (Mu et al., 2020; Liu et al., 2021).

We use several computational efficiency improvements to deliver the 3D simulations at a reasonable cost, such as time step adaptivity strategy (Section 3.3), parallel computation (up-to 8 partitions) (Figure 5.6a), nodes' mapping to concentrate the mesh in the region of interest (*arcsin* and exponential distributions), and a balanced selection of the phase-field interface thickness (δ_{PF} between 1 and $2[\mu m]$). The flexibility provided by the open source finite element library (Alnæs et al., 2015; Kirby, 2004; Balay et al., 2021) was essential to achieve these improvements (Hong and Viswanathan, 2020). Additional cost reduction was attained by assuming artificial nucleation regions at the anode surface (Figure 5.6b). This strategy is widely-used in phase-field simulations of electrodeposition (Zhang

et al., 2014; Chen et al., 2015; Yurkiv et al., 2018; Mu et al., 2019); it reduces the cost of the simulation since lithium metal can only be electroplated onto the artificial nuclei, which enhances the growth of dendrites and allows a detailed study of their morphology. We verify that the computational efficiency achieved under 8 partitions is close to optimal for the current problem, in agreement with previous work performed by Mu et al. (2020)

Three-dimensional simulations were performed in two stages according to the size of the domain under study. In first place, electrodeposition under short inter-electrode distance was investigated in Sections 5.3 and 6.1. These simulations represent a close-to-short-circuit condition, where the dendrite propagation rates obtained are up to two orders of magnitude faster than those that occur in physical scale cells under the same applied voltage, due to the short separation between electrodes $l_x = 80 [\mu m]$. These small-scale (lower-cost) 3D simulations are a useful testing ground to assess and adjust different 3D strategies before moving into more expensive, well-resolved larger-scale 3D simulations. We mimic the cubic crystal structure and surface anisotropy of lithium by using a 3D four-fold anisotropy model (3.10) to simulate crystal growth. We implement a modified 3D representation of the surface anisotropy (6.4), delivering improved simulation results with less sensitivity to the mesh orientation (Figure 6.5). Furthermore, a surface anisotropy-based strategy has been introduced in Section 6.1.4 to deal with randomness and uncertainty when determining the preferred growth direction of the dendrite crystal in the battery.

Through a resolution sensitivity analysis, we assess the mesh-induced effect on the simulated 3D dendrite morphology (Figures 5.20 and 6.8), energy levels (Figure 5.21), propagation rates (dendrite's height vs time - Figure 5.22), and electrodeposition rates (dendrite's volume vs time - Figure 5.23). The use of symmetry boundary conditions (Figure 5.18) is adequate to exploit the symmetric nature of the spike-like lithium morphologies (Tatsuma et al., 2001), reducing the computational cost down to 25% of the original requirement, which allows us

to use finer meshes in the sensitivity analysis. The simulated electrodeposition rate (volume of lithium metal deposited over time) is the least sensitive to the numerical parameters of our choice (δ_{PF} and \mathcal{R}), while dendrite’s propagation rate shows the strongest sensitivity. Thus, lithium average electrodeposition rates between 10,100 and 12,400 [$\mu\text{m}^3/\text{s}$] (less than 20% difference) were computed for the coarsest ($h = 2 [\mu\text{m}]$) and finest ($h = 1 [\mu\text{m}]$) mesh sizes, respectively. These results have practical significance since the amount of dendritic lithium produced during charge is directly linked to the reduction in Coulombic efficiency of the battery (Adams et al., 2018), and the growth rate is related to battery short-circuit predictions (Rosso et al., 2006). Therefore, future work may evaluate the Coulombic efficiency reduction due to dendrite formation in rechargeable lithium batteries.

The second stage of three-dimensional simulations evaluates the performance of the model in experimental-scale interelectrode distances ($l_x = 5000 [\mu\text{m}]$ - Section 6.2). We map the nodal distribution concentrating the nodes in the region of interest (Figure 6.9), inspired by experimental and simulation results. Although the size of the system used to perform 3D experimental-scale simulations is similar to that of short inter-electrode distance simulations (about 5,400,000 degrees of freedom), the computational time increases significantly (up-to 4 times longer) due to the larger simulated time scale, which is only partly compensated by increasing time steps (compare Figures 5.16 and 6.18). For example, 3D experimental-scale simulations presented in this work took up-to 4 weeks to be completed using a regular computer (laptop with a 2.4 GHz processor with 8-core Intel Core i9 and 16 GB 2667 MHz DDR4 RAM). The computational time is almost 45 times longer than previous 2D simulations presented in this work.

We simulate two charging voltages ($\phi_b = -0.7 [\text{V}]$ and $\phi_b = -1.4 [\text{V}]$), revealing details about the mechanism behind spike-like dendrite growth at experimental scale (non-uniform Li-ion concentration distribution on the anode surface leading to an uneven deposition of lithium). Furthermore, we verify mea-

sured morphological parameters, such as simulated dendrite propagation rates ($0.4 [\mu\text{m}/\text{s}]$ - Figure 6.13b), volume-specific area ($0.97 [\mu\text{m}^2/\mu\text{m}^3]$ - Figure 6.16), and side branching rates ($0.5 [1/\text{s}]$ - Figure 6.17), within the reported ranges for experimental electrodeposition of spike- or tree-like metal dendrites (Nishida et al., 2013; Yufit et al., 2019).

The 3D distribution of the electric field ($\vec{E} = -\nabla\phi$) and lithium-ion concentration ($\tilde{\zeta}_+$), has been studied in detail to better understand the mechanism behind spike-like dendrite growth. In the case of short inter-electrode separation ($80 [\mu\text{m}]$), we observe that the electric field increases in the vicinity of the dendrite tips (Figure 5.8), increasing the lithium-ion concentration that peaks at $\tilde{\zeta}_+ = 2.1$ (Figure 5.7). Thus, electric migration overcomes the concentration diffusion gradient, causing lithium cations to move from less concentrated surrounding regions (i.e., lithium-ion depletion of valley regions) and accumulate around dendrite tips, triggering spike-growing and highly branched dendritic lithium (Figure 5.13a). Unlike simulations using shorter interelectrode separation, we observe in Figure 6.14 no enrichment of Li-ion concentration surrounding the dendrite morphology at experimental scale ($\tilde{\zeta}_+ < 1$). However, electric migration forces continue to cause lithium cations to move from less concentrated surrounding regions and accumulate around dendrite tips (identified as higher lithium-ion concentration gradients $\|\nabla\tilde{\zeta}_+\| > 0.005$), triggering spike-growing and highly branched dendritic lithium in the case of $\phi_b = -1.4 [\text{V}]$ charging potential (Figure 6.15b). In contrast, under 50% lower applied voltage ($\phi_b = -0.7 [\text{V}]$), high lithium-ion concentration gradients are only present in the vicinity of the upper tips of the dendrite, triggering vertical and less branched growth, with smoother and rounder surface shapes (Figure 6.15a), in agreement with Chae et al. (2022) experimental work.

Thus, our analysis at the experimental scale confirms what was previously observed under smaller-scale simulations: dendrite formation is connected to the competition between the lithium cation diffusion and electric migration, gener-

ating an uneven distribution of Li^+ on the electrode surface (3.22). This fact gives insight into inhibition strategies that focus on achieving a more uniform concentration field on the anode surface, leading to lower dendrite formation propensity. For example, the use of pulse charging in lithium batteries can shift the competition in favour of cation diffusion (concentration gradient), by allowing resting times (milliseconds) for lithium cations to diffuse from dendrites' tips to less concentrated surrounding regions (valleys), leading to dendrite inhibition (Mayers et al., 2012; Yang et al., 2014; Qiao et al., 2022). Furthermore, other strategies such as the application of electrolyte flow, increment of the internal temperature, or improvements in the electrolyte composition, can enhance the diffusion of lithium ions to achieve a more uniform concentration field on the anode surface, leading to lower dendrite formation propensity (Sundström and Bark, 1995; Li et al., 2017; Zheng et al., 2017; Qian et al., 2015; Suo et al., 2013; Kim et al., 2018; Cheng et al., 2016; Yang et al., 2005; Wang et al., 2019; Tan and Ryan, 2016; Crowther and West, 2008; Wlasenko et al., 2010; Li et al., 2018; Iverson and Garimella, 2008).

In conclusion, the developed phase-field modelling framework provides a way for dendrite growth evaluation within metal anode batteries. The present model has been carefully validated using theoretical as well as publicly available experimental data. Simulation results presented in this work provide valuable insight into the mechanisms dominating spike-like dendrite growth in rechargeable lithium-metal batteries. Thus, it can be applied to interpret experimental observation and guide strategies to extend lithium metal batteries lifespan. This work constitute a significant contribution towards the physics-based, quantitative models to achieve the commercial realisation of Li-metal batteries. In order to encourage expansion of this field, we make our open-source finite element framework available to enable future studies and developments (see Appendix A).

7.2 Research outlook

In this section we discuss the research perspectives deriving from this project. Firstly, the dendritic lithium simulated in this work correspond to hazardous patterns growing under high (over-limiting) current densities; for example during fast battery charge. In such conditions, the rate of lithium deposition overcomes the rate of solid-electrolyte interface (SEI) formation, allowing the lithium deposit to grow almost free from the influence of the interface (Bai et al., 2018). Therefore in this work the electrode phase was assumed as pure solid and, thus, neglecting the presence of a SEI. Future work may consider incorporating SEI presence into the 3D model to study dendrite formation under lower current density conditions, and evaluating the coulombic efficiency reduction due to dendrite and SEI formation in rechargeable lithium batteries. Modelling the SEI presence may imply higher computational cost by incorporating an electrochemical-mechanical model to explore the role of stress development in lithium dendrites, such as the hydrostatic stress of lithium metal and residual stress in the SEI (Yurkiv et al., 2018; Liu and Guan, 2019; Jana et al., 2019; Zhang et al., 2021). Furthermore, the SEI film can create anisotropic diffusion pathways, defects and change of elastic modulus (Fang, 2022).

Although significant progress was attained in terms of understanding of the mechanism behind spike-like dendrite formation, the current model only considered three main variables, namely, the phase-field order parameter (ξ), the lithium-ion concentration ($\tilde{\zeta}_+$), and an electric potential (ϕ). In future work, our 3D phase-field model can be coupled with additional fields to gain insight into a particular aspect of dendrite formation as well as assessing some of the proposed strategies for dendrite suppression. To this end, some of the strategies already implemented in other 2D phase-field models available in the literature could be followed. For example, the current model does not consider temperature field to simulate the thermal effect during the lithium dendrite growth process. Thermal induced ion-diffusion may be included to assess dendrite suppression under high

operating temperatures (Yan et al., 2018; Qiao et al., 2022). Flow field (forced advection) can be induced to study the effect of electrolyte hydrodynamics on the dendrite morphology in flow batteries (Wang et al., 2019; Parekh et al., 2020), and electrochemical-mechanical phase-field models can be explored to study the role of stress in lithium dendrites (Jana et al., 2019; Yurkiv et al., 2018).

The large computational cost involved in solving the highly non-linear set of equations, has imposed a practical limitation on the size and number of lithium dendrites that we could model, as well as on the mesh resolution we utilised. Furthermore, additional computational resources may be required to accomplish future work as described above, such as coupling of additional fields, or simulation of dendrite formation during several charge-discharge cycles. Thus, acceleration of the solution is an urgent matter. Different strategies can be explored, such as the development of provably unconditionally stable second-order time accurate methods that may deliver larger time-step sizes for phase-field models (Gomez and Hughes, 2011; Sarmiento et al., 2018; Wu et al., 2014; Hawkins-Daarud et al., 2012; Vignal et al., 2017), adaptive mesh refinement strategies (Sakane et al., 2022), and improvement of the parallel computation efficiency (Sakane et al., 2022; Mu et al., 2020).

Given the lack of experimental data available in the literature for quantitative characterization of the spike-like lithium morphologies, in some cases we rely on experimental results available for zinc dendrites, such as (Yufit et al., 2019). Thus, there is an urgent need for the development of effective in-situ detection methods to deal with the high reactivity of lithium, and allow further well-controlled experimental studies, with detailed characterization of the system parameters (transport and kinetic properties) and lithium morphologies.

We can also mention a wider range of opportunities and challenges in computational modelling of rechargeable batteries, in general, and phase-field simulations, in particular. Currently, phase-field simulations in rechargeable batteries, including those presented in this work, focus on the description of the microstructure

evolution of materials (i.e. dendritic electrodeposition of lithium, formation of unstable solid electrolyte interphase, volume expansion of metal anode), and its comparison against experimental results, which involves a combination of qualitative, semi-quantitative and quantitative research. Progress of phase-field simulations for rechargeable batteries toward quantification is needed to forecast the performance properties of battery cells, such as evaluation of system's energy density, Coulombic efficiency, and life cycle. Thus, taking the analysis to the next level will require evaluating the connection between microstructure development and its effect on battery performance, predicting and improving battery system performance according to simulation results, which can be anticipated as a combination of semi-quantitative and quantitative analysis (Wang et al., 2020).

To achieve this goal, phase-field models like the one presented here can be developed into a multiscale model (MSM), where physical parameters in the simulations, such as changes in local diffusivity and conductivity of the electrolyte due to temperature and concentration fluctuations, can be obtained using molecular level simulations (molecular dynamics (MD) and density functional theory (DFT)) (Franco et al., 2019). Additionally, the outputs obtained using larger scale simulations can be used as an input for smaller scales to foster the development of improved materials (i.e. anode stability effect expanded across different scales, from molecular to battery cells) (Pannala et al., 2015). This will require further development of the physics linking these scales in order to study complex microstructures which undergo electrochemical reactions, charge, mass, and heat transport, and mechanical stresses at various time and length scales (Figure 2.3 shows length-scale dependent physics affecting lithium battery simulation). This approach will allow a better understanding of the influence of material properties and structure on the behaviour of the battery system as a whole (Hyeonggeon et al., 2021).

Furthermore, it would be useful to train neural networks (machine learning algorithms) by means of MSM, so that they can be applied to predict the effect of

different parameters on battery materials, components and properties (Diddens et al., 2022). Additionally, relevant cases identified by neural networks can be verified by MSM (machine learning assisted multiscale modelling) (Kolodziejczyk et al., 2021). MSM can also be combined with a web-based real-time data acquisition system (voltage, internal resistance, temperature) of a wide range of operating battery systems (real-time database), so as to implement interactive corrections of the MSM parametrization to improve accuracy of simulations (similar approach used today with weather forecast models) (Franco et al., 2019; Talib et al., 2022).

In conclusion, we note many attractive opportunities for future research actions to overcome current battery modelling challenges. Thus, in accordance with the rapid development of computational capacities and lower research cost, computational investigation is on its way to becoming a critical driving force in improving the design, energy density, life cycle and safety levels of new battery systems.

Appendices

Appendix A

Computational Framework

This section presents our open-source finite element framework, together with recommended system requirements and instructions for user:

- Minimum hardware requirements (recommended): 2.4 GHz 8-core Intel Core i9 & 16 GB 2667 MHz DDR4 RAM
- Install C++ core and Python interface, along with their respective dependencies: <https://docs.fenicsproject.org/dolfinx/main/python/installation.html#source>
- Download the latest release of legacy FEniCS (2019.1.0) from <https://fenicsproject.org/download/archive/>. Follow the installation instructions in the website according to different operating systems.
- For FEniCS project (Alnæs et al., 2015) first-time users we suggest exploring "The FEniCS Tutorial Volume I" <https://fenicsproject.org/pub/tutorial/sphinx1/>.
- Execute following commands in terminal to run the code provided (framework.py):

```
source activate fenicsproject
mpirun -n 8 python3 framework.py
```

```
from __future__ import division, print_function
import sys
from fenics import *
from dolfin import MPI
import pylab as plt
from datetime import datetime
import numpy as np
import math
import mpi4py
import os

"""
PARAMETERS
"""

# Domain size
lox= 5000 #Interelectrode distance
loy= 80
loz= 80

# Mesh size
nx, ny, nz = 180, 100, 100

# Applied voltage
phie = -1.4

# Normalized Parameters
L = Constant(625e6)
kappa_0 = Constant(0.707)
```

```

delta = Constant(0.05)
Ls = Constant(0.0018)
alpha = Constant(0.5)
AA = Constant(38.69) # nF/RT
W = Constant(1.78)
A = Constant(1.0) # R*T/R*T
M1 = Constant (0.3179)
M2 = Constant(317.9)
S1 = Constant(10000000)
S2 = Constant(1.19)
ft2 = Constant(0.0074)

# Numerical Parameters
t=0.0
Tf= 200
dt= 1e-7
tol_DT = 1.0e-6
tol_DT_min = 1.0e-9
rho_0 = 0.9
save_every = 5 # Save every 5 seconds
deg_L2 = 4
deg_grad = 2
num_steps=int(Tf/dt)
k , k_n , k_n_1 , eta_n = Constant(dt), Constant(0.0), Constant(0.0),
    Constant(0.0)
Type_int = 'BDF2'
Type_switch = 'SIGMOID'
#Type_switch = 'POLY'
# Type_Truc = 'BDF122'
Type_Truc = 'BDF223'
Type_kappa = 'Vble'

```

```

#Type_kappa = 'Cte'
TrialTypeDir = os.path.join(f'data/sim{n_sim+1}')
if not os.path.isdir(TrialTypeDir): os.makedirs(TrialTypeDir)

parameters["form_compiler"]["optimize"] = True
parameters["form_compiler"]["cpp_optimize"] = True
parameters["form_compiler"]["representation"] = "uflacs"

"""
MESH AND FUNCTIONS
"""

# Create mesh and define function space
elem = CellType.Type.hexahedron

mesh = UnitCubeMesh.create(nx,ny,nz,CellType.Type.hexahedron)

xmesh = mesh.coordinates()

#####

#Uniform to Exponential Node Mapping in "x" Direction (80um)

for xx in range(0, len(xmesh[:,0])):
    if xmesh[xx,0] < 1:
        xmesh[xx,0] = xmesh[xx,0]/62.5

for xx in range(0, len(xmesh[:,0])):
    if xmesh[xx,0] == (1-1/nx)/62.5:
        xmesh[xx,0] = 0.378844444

```



```

elif xmesh[xx,0] == (1-2/nx)/62.5:
    xmesh[xx,0] = 0.1968
elif xmesh[xx,0] == (1-3/nx)/62.5:
    xmesh[xx,0] = 0.105777778
elif xmesh[xx,0] == (1-4/nx)/62.5:
    xmesh[xx,0] = 0.060266667
elif xmesh[xx,0] == (1-5/nx)/62.5:
    xmesh[xx,0] = 0.037511111
elif xmesh[xx,0] == (1-6/nx)/62.5:
    xmesh[xx,0] = 0.026133333
elif xmesh[xx,0] == (1-7/nx)/62.5:
    xmesh[xx,0] = 0.020444444
elif xmesh[xx,0] == (1-8/nx)/62.5:
    xmesh[xx,0] = 0.0176
elif xmesh[xx,0] == (1-9/nx)/62.5:
    xmesh[xx,0] = 0.016177778
elif xmesh[xx,0] == (1-10/nx)/62.5:
    xmesh[xx,0] = 0.015466667
elif xmesh[xx,0] == (1-11/nx)/62.5:
    xmesh[xx,0] = 0.015111111

```

```
#####
```

```
#Arcsin Node Mapping in "y" and "z" Directions
```

```

xmesh[:,1] = 2*xmesh[:,1]-1
xmesh[:,1] = (np.arcsin((xmesh[:,1]))/(pi)+0.5)

xmesh[:,2] = 2*xmesh[:,2]-1
xmesh[:,2] = (np.arcsin((xmesh[:,2]))/(pi)+0.5)

```

```
#####
```

```
mesh.coordinates()[:,0] = mesh.coordinates()[:,0]*lox  
mesh.coordinates()[:,1] = mesh.coordinates()[:,1]*loy  
mesh.coordinates()[:,2] = mesh.coordinates()[:,2]*loz
```

```
#####
```

```
#Define Periodic Boundary Conditions (Lateral faces)
```

```
class PeriodicBoundary(SubDomain):
```

```
    # Left boundary is "target domain" G
```

```
    def inside(self, x, on_boundary):
```

```
        # return True if on left or bottom boundary AND NOT on one of  
        the two slave edges
```

```
        return bool ((near(x[0], 0) or near(x[1], 0) or near(x[2], 0))  
                    and
```

```
                    (not ((near(x[0], lox) and near(x[2], loz)) or
```

```
                        (near(x[0], lox) and near(x[1], loy)) or
```

```
                        (near(x[1], loy) and near(x[2], loz)))) and
```

```
                    on_boundary)
```

```
    # Map right boundary (H) to left boundary (G)
```

```
    def map(self, x, y):
```

```
        #### define mapping for a single point in the box, such that 3  
        mappings are required
```

```
        if near(x[0], lox) and near(x[1], loy) and near(x[2], loz):
```

```
            y[0] = x[0]
```

```
            y[1] = x[1] - loy
```

```
            y[2] = x[2] - loz
```

```

##### define mapping for edges in the box, such that mapping in
      2 Cartesian coordinates are required
if near(x[0], lox) and near(x[2], loz):
    y[0] = x[0]
    y[1] = x[1]
    y[2] = x[2] - loz
elif near(x[1], loy) and near(x[2], loz):
    y[0] = x[0]
    y[1] = x[1] - loy
    y[2] = x[2] - loz
elif near(x[0], lox) and near(x[1], loy):
    y[0] = x[0]
    y[1] = x[1] - loy
    y[2] = x[2]

#### right maps to left: left/right is defined as the
      x-direction
elif near(x[0], lox):
    y[0] = x[0]
    y[1] = x[1]
    y[2] = x[2]

### back maps to front: front/back is defined as the y-direction
elif near(x[1], loy):
    y[0] = x[0]
    y[1] = x[1] - loy
    y[2] = x[2]

#### top maps to bottom: top/bottom is defined as the
      z-direction
elif near(x[2], loz):
    y[0] = x[0]
    y[1] = x[1]
    y[2] = x[2] - loz

```

```

pbc = PeriodicBoundary()

# Space Functions
P1 = FiniteElement('P', mesh.ufl_cell(), 1)
PDG = FunctionSpace(mesh, 'DG', 0)
V = FunctionSpace(mesh, MixedElement([P1,P1,P1]),
    constrained_domain=pbc)

# Define trial and test functions
v_1, v_2, v_3 = TestFunctions(V)

# Define functions for solutions at previous and at current time
u = Function(V)      # At current time
u_n = Function(V)
u_n_1 = Function(V)
u_n_2 = Function(V)
LTE = Function(V)

# Split system function to access the components
xi, w, phi = split(u)
xi_n, w_n, phi_n = split(u_n)
xi_n_1, w_n_1, phi_n_1 = split(u_n_1)
xi_n_2, w_n_2, phi_n_2 = split(u_n_2)

metadata = {"quadrature_scheme": "default", 'quadrature_degree':
    deg_grad}
dx = dx(metadata=metadata)
metadata = {"quadrature_scheme": "default", 'quadrature_degree':
    deg_L2}

```

```

dxm = dx(metadata=metadata)

"""
INITIAL CONDITIONS
"""

# Create initial conditions (multiple nuclei)
ruido1 = Expression('-1.0 + pow((x[2]-42.)/2.,2.0) +
    pow((x[1]-42.)/2.,2.0) + pow(x[0]/4.,2.0)', degree=deg_L2)
ruido2 = Expression('-1.0 + pow((x[2]-38.)/2.,2.0) +
    pow((x[1]-38.)/2.,2.0) + pow(x[0]/4.,2.0)', degree=deg_L2)
ruido3 = Expression('-1.0 + pow((x[2]-42.)/2.,2.0) +
    pow((x[1]-38.)/2.,2.0) + pow(x[0]/4.,2.0)', degree=deg_L2)
ruido4 = Expression('-1.0 + pow((x[2]-38.)/2.,2.0) +
    pow((x[1]-42.)/2.,2.0) + pow(x[0]/4.,2.0)', degree=deg_L2)
u_init =
    Expression(('0.5*(1.0-1.0*tanh(4*(ruido1)))+0.5*(1.0-1.0*tanh(4*(ruido2)))
+0.5*(1.0-1.0*tanh(4*(ruido3)))+0.5*(1.0-1.0*tanh(4*(ruido4)))',
    '0.5*(1.0+tanh(4*(ruido1)))+0.5*(1.0+tanh(4*(ruido2)))
+0.5*(1.0+tanh(4*(ruido3)))+0.5*(1.0+tanh(4*(ruido4)))-3.0',
    'x[0] >= 5.0 ? (- phie / (lox-5.0) * x[0] + (phie * lox) / (lox-5.0))
: phie'),
    degree=deg_L2, ruido1=ruido1, ruido2=ruido2, ruido3=ruido3,
    ruido4=ruido4, phie=phie, lox=lox)
u_init_xi =
    Expression(('0.5*(1.0-1.0*tanh(4*(ruido1)))+0.5*(1.0-1.0*tanh(4*(ruido2)))
+0.5*(1.0-1.0*tanh(4*(ruido3)))+0.5*(1.0-1.0*tanh(4*(ruido4)))'),
    degree=deg_L2, ruido1=ruido1, ruido2=ruido2, ruido3=ruido3,
    ruido4=ruido4)
u_init_w =
    Expression(('0.5*(1.0+tanh(4*(ruido1)))+0.5*(1.0+tanh(4*(ruido2)))

```

```

+0.5*(1.0+tanh(4*(ruido3)))+0.5*(1.0+tanh(4*(ruido4)))-3.0'),
degree=deg_L2, ruido1=ruido1, ruido2=ruido2, ruido3=ruido3,
    ruido4=ruido4)
u_init_phi =
    Expression(('phi_*(1.0-tanh(4*(ruido1)))+phi_*(1.0-tanh(4*(ruido2)))
+phi_*(1.0-tanh(4*(ruido3)))+phi_*(1.0-tanh(4*(ruido4)))')
, degree=deg_L2, ruido1=ruido1, ruido2=ruido2, ruido3=ruido3,
    ruido4=ruido4, phi_=phie*0.5)
u.interpolate(u_init)
u_n.interpolate(u_init)

"""
BOUNDARY CONDITIONS
"""

# Define boundary conditions

# Boundaries y=0, y=Ly
def boundary0(x, on_boundary):
    return on_boundary and near(x[0], 0)
def boundaryL(x, on_boundary):
    return on_boundary and near(x[0], lxx)
def boundary1phi(x, on_boundary):
    return on_boundary and near(x[0], 0) and abs(x[1]-42)<1.0 and
        abs(x[2]-42)<1.0
def boundary2phi(x, on_boundary):
    return on_boundary and near(x[0], 0) and abs(x[1]-38)<1.0 and
        abs(x[2]-38)<1.0
def boundary3phi(x, on_boundary):
    return on_boundary and near(x[0], 0) and abs(x[1]-38)<1.0 and
        abs(x[2]-42)<1.0

```

```

def boundary4phi(x, on_boundary):
    return on_boundary and near(x[0], 0) and abs(x[1]-42)<1.0 and
        abs(x[2]-38)<1.0

# Boundary conditions for xi
bc_xi1 = DirichletBC(V.sub(0), u_init_xi, boundary0)
bc_xi5 = DirichletBC(V.sub(0), Constant(0.0), boundaryL)

# Boundary conditions for Cli
bc_c1 = DirichletBC(V.sub(1), u_init_w, boundary1phi)
bc_c2 = DirichletBC(V.sub(1), u_init_w, boundary2phi)
bc_c3 = DirichletBC(V.sub(1), u_init_w, boundary3phi)
bc_c4 = DirichletBC(V.sub(1), u_init_w, boundary4phi)
bc_c5 = DirichletBC(V.sub(1), Constant(1), boundaryL)

# Boundary conditions for phi
bc_phi1 = DirichletBC(V.sub(2), u_init_phi, boundary1phi)
bc_phi2 = DirichletBC(V.sub(2), u_init_phi, boundary2phi)
bc_phi3 = DirichletBC(V.sub(2), u_init_phi, boundary3phi)
bc_phi4 = DirichletBC(V.sub(2), u_init_phi, boundary4phi)
bc_phi5 = DirichletBC(V.sub(2), Constant(0.0), boundaryL)

# Gather all boundary conditions in a variable
bcs = [bc_xi1, bc_xi5, bc_c1, bc_c2, bc_c3, bc_c4, bc_c5, bc_phi1,
        bc_phi2, bc_phi3, bc_phi4, bc_phi5 ] # Dirichlet

"""
FUNCITONS DEFINITION
"""

```

```

# Surface Normal
def n_call(x):
    num = grad(x)
    den = sqrt(inner(num, num))
    n = conditional(gt((den),1e-16), num/den, as_vector([0,0,0]))
    return n

# Surface Anisotropy Gradient Coefficient
def kappa(x):
    if Type_kappa == 'Cte':
        kappa = kappa_0
    if Type_kappa == 'Vble':
        n = n_call(x)
        kappa = kappa_0 * ( 1.0 - 3.0 * delta ) * ( 1 + 4.0 * delta * (
            n[0]**(4) + n[1]**(4) + n[2]**(4) ) / (1 - 3.0 * delta) )
    return kappa

def kappa_dev(x):
    if Type_kappa == 'Cte':
        kappa_x = 0
        kappa_y = 0
        kappa_z = 0
    if Type_kappa == 'Vble':
        n = n_call(x)
        den = sqrt(inner(grad(x),grad(x)))
        kappa_x = conditional(gt((den),1e-16), kappa_0 * ( 1.0 - 3.0 *
            delta ) * ( 4.0 * delta * ( 4 * ( n[0]**(3) - n[0]**(5) ) /
            den ) / (1 - 3.0 * delta)), 0.0)
        kappa_y = conditional(gt((den),1e-16), kappa_0 * ( 1.0 - 3.0 *
            delta ) * ( 4.0 * delta * ( 4 * ( n[1]**(3) - n[1]**(5) ) /
            den ) / (1 - 3.0 * delta)), 0.0)

```



```

        kappa_z = conditional(gt((den),1e-16), kappa_0 * ( 1.0 - 3.0 *
            delta ) * ( 4.0 * delta * ( 4 * ( n[2]**(3) - n[2]**(5)) /
            den ) / (1 - 3.0 * delta)), 0.0)
    return as_vector([kappa_x,kappa_y,kappa_z])

# Switching Function Material
def h(_x):
    if Type_switch == 'POLY':
        h = _x**3*(Constant(6.0)*_x**2 - Constant(15.0)*_x +
            Constant(10.0))
    if Type_switch == 'SIGMOID':
        h = exp(Constant(20.0)*(Constant(1.0)*_x-Constant(0.5)))
            /(1+exp(Constant(20.0)*(Constant(1.0)*_x-Constant(0.5))))
    return h

def dh(_x):
    if Type_switch == 'POLY':
        dh = Constant(30.0)*_x*_x*(_x-Constant(1.0))*(_x-Constant(1.0))
    if Type_switch == 'SIGMOID':
        dh =
            Constant(20.0)*exp(Constant(20.0)*(Constant(1.0)*_x-Constant(0.5)))
            /(1+exp(Constant(20.0)*(Constant(1.0)*_x-Constant(0.5))))**2
    return dh

# Barrier Function Material
def g(_x):
    return W*_x**2.0*(Constant(1.0) - _x)**2
def dg(_x):
    return W*Constant(2.0)*(_x * (Constant(1.0) - _x) ** 2 -
        (Constant(1.0) - _x) * _x ** 2)

```

```
# Effective Diffusivity
```

```
def D(_xi):  
    return M1*h(_xi)+M2*(Constant(1.0)-h(_xi))
```

```
# Effective Conductivity
```

```
def Le1(_xi):  
    return S1*h(_xi)+S2*(Constant(1.0)-h(_xi))
```

```
# Select Time Integrator
```

```
def Time_integrator(var,var_n,var_n_1,eta_n,DT,type):  
    if type == 'BDF1':  
        dot_var = (var-var_n)/DT  
    if type == 'BDF2':  
        c1 = (1+eta_n)**2/(1+2*eta_n)  
        c2 = eta_n**2/(1+2*eta_n)  
        dot_var = (1+2*eta_n)/(1+eta_n)*(var-c1*var_n+c2*var_n_1)/DT  
    return dot_var
```

```
"""
```

```
VARIATIONAL PROBLEM
```

```
"""
```

```
# Time Adaptiviy
```

```
def
```

```
    Update_next_step(u,u_n,u_n_1,u_n_2,k_n_1,k_n,k,eta_n,t,count>Error,Time,DeltaT,Type_int)
```

```
    xi_ =
```

```
        MPI.comm_world.gather(u.split()[0].vector().get_local(),root=0)
```

```
    xi_n_ =
```

```
        MPI.comm_world.gather(u_n.split()[0].vector().get_local(),root=0)
```

```

xi_n_1_ =
    MPI.comm_world.gather(u_n_1.split()[0].vector().get_local(),root=0)
xi_n_2_ =
    MPI.comm_world.gather(u_n_2.split()[0].vector().get_local(),root=0)

w_ = MPI.comm_world.gather(u.split()[1].vector().get_local(),root=0)
w_n_ =
    MPI.comm_world.gather(u_n.split()[1].vector().get_local(),root=0)
w_n_1_ =
    MPI.comm_world.gather(u_n_1.split()[1].vector().get_local(),root=0)
w_n_2_ =
    MPI.comm_world.gather(u_n_2.split()[1].vector().get_local(),root=0)

WLT = tol_DT

if mpi_rank == 0:

    WLT1 = truncation(xi_,xi_n_,xi_n_1_,xi_n_2_,k,k_n,k_n_1)
    WLT2 = truncation(w_,w_n_,w_n_1_,w_n_2_,k,k_n,k_n_1)
    WLT = max(WLT1,WLT2)

WLT = cpp.MPI.comm_world.bcast(WLT, root=0)

if (WLT >= tol_DT or math.isnan(WLT) or aux2 == False):

    Mult = (tol_DT/WLT)**(0.5)
    if (Mult >= 1.):
        Mult = 1.
    if aux2 == False:
        Mult = 0.8
    if math.isnan(Mult):

```

```

    Mult = 0.1

k.assign(rho_0*Mult*k.values()[0])
dt = k.values()[0]
u.assign(u_n)
if (k_n.values()[0] > 0):
    eta_n.assign(k/k_n)

if mpi_rank == 0:
    print("--- Reducing Time Step ---", k.values()[0], 'Error',
          WLT)
    sys.stdout.flush()

else:

    # Update previous solution
    u_n_2, u_n_1, u_n, k_n_1, k_n, eta_n =
        Update_var(u,u_n,u_n_1,u_n_2,k_n_1,k_n,k,eta_n,Type_int)

    # Update time
    t+= k.values()[0]
    count += k.values()[0]

Error.append(WLT)
Time.append(t)
DeltaT.append(k.values()[0])

if mpi_rank == 0:
    print("*****")
    print("*** Finishing Time Step ***", t, "** Error **", WLT)
    print("*****")

```

```

        sys.stdout.flush()

    if (WLT < tol_DT_min):
        Mult = (tol_DT_min/WLT)**(0.5)
        k.assign(Mult*k.values()[0])
        dt = k.values()[0]
        eta_n.assign(k/k_n)

        if mpi_rank == 0:
            print("---- Increasing Time Step ----",
                  k.values()[0], 'Error', WLT)
            sys.stdout.flush()

    return u_n_2, u_n_1, u_n, k_n_1, k_n, eta_n, t , count, Error,
           Time, DeltaT

def Update_var(u,u_n,u_n_1,u_n_2,k_n_1,k_n,k,eta_n,type):
    k_n_1.assign(k_n)
    k_n.assign(k)
    u_n_2.assign(u_n_1)
    u_n_1.assign(u_n)
    u_n.assign(u)
    eta_n.assign(k/k_n)
    return u_n_2, u_n_1, u_n, k_n_1, k_n, eta_n

# Time Adaptivi Truncation Error Estimator
def truncation(u,u_n,u_n_1,u_n_2,k,k_n,k_n_1):
    Tau_abs = 1e2
    Tau_rel = 1e2
    if Type_Truc == 'BDF122':

```

```

eta = (k.values()[:]+k_n.values()[:])/k.values()[:]
if (eta-1.)==0:
    WLTE = (tol_DT+tol_DT_min)/2
else:
    LTE =
        np.concatenate((-1/eta)*u+(1/(eta-1))*u_n-(1/(eta*(eta-1)))*u_n_1)
    u = np.concatenate(u)
    WLTE = np.sqrt(np.sum((LTE / (Tau_abs + Tau_rel *
        np.max(np.abs(u)+np.abs(LTE))))**2)/LTE.size)
if Type_Truc == 'BDF223':
    if (k_n.values()[:])==0:
        WLTE = (tol_DT+tol_DT_min)/2
    elif (k_n_1.values()[:])==0:
        eta = (k.values()[:]+k_n.values()[:])/k.values()[:]
        LTE =
            np.concatenate((-1/eta)*u+(1/(eta-1))*u_n-(1/(eta*(eta-1)))*u_n_1)
        u = np.concatenate(u)
        WLTE = np.sqrt(np.sum((LTE / (Tau_abs + Tau_rel *
            np.max(np.abs(u)+np.abs(LTE))))**2)/LTE.size)
    else:
        c1 = (k.values()[:]+k_n.values()[:])/6
        c2 = 1/k.values()[:]
        c3 = (1+k.values()[:]/k_n.values()[:])/k_n.values()[:]
        c4 = k.values()[:]/(k_n.values()[:]*k_n_1.values()[:])
        LTE =
            np.concatenate(c1*(c2*u-c2*u_n-c3*u_n+c3*u_n_1+c4*u_n_1-c4*u_n_2))
        u = np.concatenate(u)
        WLTE = np.sqrt(np.sum((LTE / (Tau_abs + Tau_rel *
            np.max(np.abs(u)+np.abs(LTE))))**2)/LTE.size)
return WLTE

```

```

# Solver Parameters
def Solver_NR(F,u,bcs,J):
    problem =NonlinearVariationalProblem(F,u,bcs,J=J)
    solver=NonlinearVariationalSolver(problem)
    solver.parameters['nonlinear_solver'] = 'snes'
    solver.parameters["snes_solver"]["maximum_iterations"] = 8
    solver.parameters["snes_solver"]["absolute_tolerance"] = 1.0e-5
    solver.parameters["snes_solver"]["relative_tolerance"] = 1.0e-7
    solver.parameters["snes_solver"]["report"] = True
    solver.parameters["snes_solver"]["error_on_nonconvergence"] = False
    solver.parameters["snes_solver"]["linear_solver"]= "bicgstab"
    solver.parameters["snes_solver"]["krylov_solver"]["maximum_iterations"]
        = 1000
    solver.parameters["snes_solver"]["krylov_solver"]["error_on_nonconvergence"]
        = False
    return solver

# Weak Variational Formulation
def
Functional(u,xi,xi_n,xi_n_1,w,w_n,w_n_1,phi,v_1,v_2,v_3,k,Type_int):
F1 = Time_integrator(xi,xi_n,xi_n_1,eta_n,k,Type_int)*v_1*dx +
    L*kappa(xi)*kappa(xi)*dot(grad(xi),grad(v_1))*dx +
    L*dg(xi)*v_1*dx +
    Ls*(exp(phi*AA/Constant(2.0))-w*exp(-phi*AA/Constant(2.0)))*dh(xi)*v_1*dxm
F1 +=
    inner(L*kappa(xi)*kappa_dev(xi)*dot(grad(xi),grad(xi)),grad(v_1))*dx
F2 = Time_integrator(w,w_n,w_n_1,eta_n,k,Type_int)*v_2*dx +
    D(xi)*dot(grad(w),grad(v_2))*dx +
    D(xi)*w*AA*dot(grad(phi),grad(v_2))*dx +
    76.4*Time_integrator(xi,xi_n,xi_n_1,eta_n,k,Type_int)*v_2*dx
F3 = Le1(xi)*dot(grad(phi),grad(v_3))*dx +

```

```

        ft2*Time_integrator(xi,xi_n,xi_n_1,eta_n,k,Type_int)*v_3*dx
F=F1+F2+F3
J = derivative(F,u)
return F, J

"""
SOLVE AND SAVE SOLUTIONS
"""

# Timestamp before solving
mpi_rank = MPI.comm_world.Get_rank()
mpi_size = MPI.comm_world.Get_size()
if mpi_rank == 0:
    t1 = datetime.fromtimestamp(datetime.timestamp(datetime.now()))
    print("timestamp =", t1)

# Solve
F,J =
    Functional(u,xi,xi_n,xi_n_1,w,w_n,w_n_1,phi,v_1,v_2,v_3,k,Type_int)
solver = Solver_NR(F,u,bcs,J)

# Time Integrator Output Variables
Error = []
Time = []
DeltaT = []

n_count = 0
count = 0

# Time step
while t<=Tf:

```



```

# Solve problem
aux1, aux2 = solver.solve()

u_n_2, u_n_1, u_n, k_n_1, k_n, eta_n, t, count , Error, Time,
    DeltaT = Update_next_step(u,u_n,u_n_1,u_n_2,k_n_1,k_n,k,eta_n,
    t, count>Error, Time, DeltaT, Type_int)

# Save solution every 5 seconds of simulation
if (count>=save_every):
    count = 0
    n_count += 1
    fileResults = XDMFFile(f"saved2D/sim{n_sim+1}/u_t_" +
        str(n_count) + ".xdmf")
    fileResults.parameters["flush_output"] = True
    fileResults.parameters['rewrite_function_mesh'] = False
    fileResults.parameters["functions_share_mesh"] = True
    var1 = u.split()[0]
    var2 = u.split()[1]
    var3 = u.split()[2]
    var1.rename("xi", "tmp")
    var2.rename("w", "tmp")
    var3.rename("phi", "tmp")
    fileResults.write(var1,t)
    fileResults.write(var2,t)
    fileResults.write(var3,t)
    all_data = np.array(4,dtype=np.object)
    all_data = Error, Time, DeltaT
    data_filename = os.path.join(TrialTypeDir, 'data')
    np.save(data_filename, all_data)
    np.savetxt("Data.csv", np.transpose(all_data), delimiter=",")

```

```


# Save last solution
n_count += 1
fileResults = XDMFFile(f"saved2D/sim{n_sim+1}/u_t_" + str(n_count) +
    ".xdmf")
fileResults.parameters["flush_output"] = True
fileResults.parameters['rewrite_function_mesh'] = False
fileResults.parameters["functions_share_mesh"] = True
var1 = u.split()[0]
var2 = u.split()[1]
var3 = u.split()[2]
var1.rename("xi", "tmp")
var2.rename("w", "tmp")
var3.rename("phi", "tmp")
fileResults.write(var1,t)
fileResults.write(var2,t)
fileResults.write(var3,t)

# Timestamp
if mpi_rank == 0:
    print("timestamp =", t1, " ... ",
        datetime.fromtimestamp(datetime.timestamp(datetime.now())))

```

Appendix B

Copyright Information



Phase-field modeling of planar interface electrodeposition in lithium-metal batteries

Author:
Marcos Exequiel Arguello, Monica Gumulya, Jos Derksen, Ranjeet Utikar, Victor Manuel Calo

Publication: Journal of Energy Storage

Publisher: Elsevier

Date: June 2022

© 2022 Elsevier Ltd. All rights reserved.

Journal Author Rights

Please note that, as the author of this Elsevier article, you retain the right to include it in a thesis or dissertation, provided it is not published commercially. Permission is not required, but please ensure that you reference the journal as the original source. For more information on this and on your other retained rights, please visit: <https://www.elsevier.com/about/our-business/policies/copyright#Author-rights>

BACK **CLOSE WINDOW**

Copyright clearance for published paper from Journal of Energy Storage



Dendrite formation in rechargeable lithium-metal batteries: Phase-field modeling using open-source finite element library

Author:

Marcos E. Arguello, Nicolás A. Labanda, Victor M. Calo, Monica Gumulya, Ranjeet Utikar, Jos Derksen

Publication: Journal of Energy Storage

Publisher: Elsevier

Date: September 2022

© 2022 Elsevier Ltd. All rights reserved.

Journal Author Rights

Please note that, as the author of this Elsevier article, you retain the right to include it in a thesis or dissertation, provided it is not published commercially. Permission is not required, but please ensure that you reference the journal as the original source. For more information on this and on your other retained rights, please visit: <https://www.elsevier.com/about/our-business/policies/copyright#Author-rights>

BACK

CLOSE WINDOW

Copyright clearance for published paper from Journal of Energy Storage

Phase-field modeling of planar interface electrodeposition in lithium-metal batteries Journal of Energy Storage	
Investigation	
Conceptualization	X
Methodology	
Writing – Original Draft	
Writing – Review & Editing	
Resources	
Supervision	X

Name: Ranjeet Utikar

Signature:.....

Date:..... 3 August 2022

Dendrite formation in rechargeable lithium-metal batteries: Phase-field modeling using open-source finite element library Journal of Energy Storage	
Investigation	
Conceptualization	X
Methodology	
Writing – Original Draft	
Writing – Review & Editing	
Resources	
Supervision	X

Name: Ranjeet Utikar

Signature:.....

Date:..... 3 August 2022

Three-dimensional experimental-scale phase-field modelling of dendrite formation in rechargeable lithium-metal batteries	
Investigation	
Conceptualization	X
Methodology	
Writing – Original Draft	
Writing – Review & Editing	
Resources	
Supervision	X

Name: Ranjeet Utikar

Signature:.....

Date:..... 24/08/2022

Copyright clearance from Dr Ranjeet Utikar

Phase-field modeling of planar interface electrodeposition in lithium-metal batteries Journal of Energy Storage	
Investigation	
Conceptualization	
Methodology	X
Writing – Original Draft	
Writing – Review & Editing	X
Resources	X
Supervision	

Name: Víctor Manuel Calo

Signature: 

Date: 27/07/2022

Dendrite formation in rechargeable lithium-metal batteries: Phase-field modeling using open-source finite element library Journal of Energy Storage	
Investigation	
Conceptualization	
Methodology	X
Writing – Original Draft	
Writing – Review & Editing	X
Resources	X
Supervision	

Name: Víctor Manuel Calo

Signature: 

Date: 27/07/2022

Three-dimensional experimental-scale phase-field modelling of dendrite formation in rechargeable lithium-metal batteries	
Investigation	
Conceptualization	
Methodology	X
Writing – Original Draft	
Writing – Review & Editing	X
Resources	X
Supervision	

Name: Víctor Manuel Calo

Signature: 

Date: 24/8/2022

Copyright clearance from Prof Victor Manuel Calo

Phase-field modeling of planar interface electrodeposition in lithium-metal batteries Journal of Energy Storage	
Investigation	
Conceptualization	X
Methodology	
Writing – Original Draft	
Writing – Review & Editing	X
Resources	
Supervision	

Name: Monica Gumulya

Signature: M. Gumulya 

Date: 12/07/2022

Dendrite formation in rechargeable lithium-metal batteries: Phase-field modeling using open-source finite element library Journal of Energy Storage	
Investigation	
Conceptualization	X
Methodology	
Writing – Original Draft	
Writing – Review & Editing	X
Resources	
Supervision	

Name: Monica Gumulya

Signature: M. Gumulya 

Date: 12/07/2022

Three-dimensional experimental-scale phase-field modelling of dendrite formation in rechargeable lithium-metal batteries	
Investigation	
Conceptualization	X
Methodology	
Writing – Original Draft	
Writing – Review	X
Resources	
Supervision	

Name: Monica Gumulya

Signature: 

Date: 31/08/2022

Copyright clearance from Dr Monica Gumulya

Phase-field modeling of planar interface electrodeposition in lithium-metal batteries Journal of Energy Storage	
Investigation	
Conceptualization	X
Methodology	
Writing – Original Draft	
Writing – Review & Editing	X
Resources	
Supervision	

Name: Jos Derksen

Signature:.....

Date:.....

Dendrite formation in rechargeable lithium-metal batteries: Phase-field modeling using open-source finite element library Journal of Energy Storage	
Investigation	
Conceptualization	X
Methodology	
Writing – Original Draft	
Writing – Review & Editing	X
Resources	
Supervision	

Name: Jos Derksen

Signature:.....

Date:.....

Three-dimensional experimental-scale phase-field modelling of dendrite formation in rechargeable lithium-metal batteries	
Investigation	
Conceptualization	X
Methodology	
Writing – Original Draft	
Writing – Review & Editing	X
Resources	
Supervision	

Name: Jos Derksen

Signature:.....

Date:.....

Copyright clearance from Prof Jos Derksen

Dendrite formation in rechargeable lithium-metal batteries: Phase-field modeling using open-source finite element library Journal of Energy Storage	
Investigation	X
Conceptualization	
Methodology	X
Writing – Original Draft	X
Writing – Review & Editing	
Resources	
Supervision	

Name: Nicolás Agustín Labanda

Signature: 

Date: 07/07/2022

Three-dimensional experimental-scale phase-field modelling of dendrite formation in rechargeable lithium-metal batteries	
Investigation	X
Conceptualization	
Methodology	X
Writing – Original Draft	X
Writing – Review & Editing	
Resources	
Supervision	

Name: Nicolás Agustín Labanda

Signature: 

Date: 24/08/2022

Copyright clearance from Dr Nicolas Agustin Labanda

Before Li Ion Batteries

Author: Martin Winter, Brian Barnett, Kang Xu
 Publication: Chemical Reviews
 Publisher: American Chemical Society
 Date: Dec 1, 2018
 Copyright © 2018, American Chemical Society

PERMISSION/LICENSE IS GRANTED FOR YOUR ORDER AT NO CHARGE

This type of permission/license, instead of the standard Terms and Conditions, is sent to you because no fee is being charged for your order. Please note the following:

- Permission is granted for your request in both print and electronic formats, and translations.
- If figures and/or tables were requested, they may be adapted or used in part.
- Please print this page for your records and send a copy of it to your publisher/graduate school.
- Appropriate credit for the requested material should be given as follows: "Reprinted (adapted) with permission from (COMPLETE REFERENCE CITATION). Copyright (YEAR) American Chemical Society." Insert appropriate information in place of the capitalized words.
- One-time permission is granted only for the use specified in your RightsLink request. No additional uses are granted (such as derivative works or other editions). For any uses, please submit a new request.

If credit is given to another source for the material you requested from RightsLink, permission must be obtained from that source.

BACK
CLOSE WINDOW

Permission request for reproducing Figure 1.2 from American Chemical Society

Permissions

All articles published in this journal are made available under the terms of the [Creative Commons Attribution License \(CC-BY\)](#). The CC-BY license permits use, distribution and reproduction in any medium, provided the original work is properly cited and allows the commercial use of published articles. Covers are published under the [Creative Commons Attribution-Non Commercial License \(CC-BY-NC\)](#). The CC-BY-NC license permits use, distribution and reproduction in any medium, for noncommercial purposes only, provided the original work is properly cited.

Permission request for reproducing Figure 1.4 from Advanced Science

This is a License Agreement between Curtin University - Marcos Exequiel Arguello ("User") and Copyright Clearance Center, Inc. ("CCC") on behalf of the Rightsholder identified in the order details below. The license consists of the order details, the Marketplace Order General Terms and Conditions below, and any Rightsholder Terms and Conditions which are included below.

All payments must be made in full to CCC in accordance with the Marketplace Order General Terms and Conditions below.

Order Date	14-Jul-2022	Type of Use	Republish in a thesis/dissertation
Order License ID	1247230-1	Publisher	Nature Research
ISSN	1476-4687	Portion	Image/photo/illustration

LICENSED CONTENT

Publication Title	Nature	Publication Type	e-Journal
Article Title	Cryo-STEM mapping of solid-liquid interfaces and dendrites in lithium-metal batteries.	Start Page	345
Date	01/01/1995	End Page	349
Language	English	Issue	7718
Country	United States of America	Volume	560
Rightsholder	Springer Nature BV	URL	http://www.nature.com/nature/

REQUEST DETAILS

Portion Type	Image/photo/illustration	Distribution	Worldwide
Number of images / photos / illustrations	1	Translation	Original language of publication
Format (select all that apply)	Print, Electronic	Copies for the disabled?	No
Who will republish the content?	Academic institution	Minor editing privileges?	No
Duration of Use	Life of current and all future editions	Incidental promotional use?	No
Lifetime Unit Quantity	Up to 499	Currency	USD
Rights Requested	Main product		

NEW WORK DETAILS

Title	Computational modelling of reactive processes in lithium-metal batteries	Institution name	Curtin University
Instructor name	Marcos Exequiel Arguello	Expected presentation date	2022-09-30

ADDITIONAL DETAILS

The requesting person / organization to appear on the license	Curtin University - Marcos Exequiel Arguello
---	--

REUSE CONTENT DETAILS

Title, description or numeric reference of the portion(s)	Figure 1. Characterization of dendrite morphologies by cryo-FIB	Title of the article/chapter the portion is from	Cryo-STEM mapping of solid-liquid interfaces and dendrites in lithium-metal batteries.
Editor of portion(s)	Archer, Lynden A; Choudhury, Snehashis; Kourkoutis, Lena F; Tu, Zhengyuan; Zachman, Michael J	Author of portion(s)	Archer, Lynden A; Choudhury, Snehashis; Kourkoutis, Lena F; Tu, Zhengyuan; Zachman, Michael J
Volume of serial or monograph	560	Publication date of portion	2018-08-15
Page or page range of portion	345-349		

RIGHTSHOLDER TERMS AND CONDITIONS

If you are placing a request on behalf of for a corporate organization, please use RightsLink. For further information visit <http://www.nature.com/reprints/permission-requests.html> and <https://www.springer.com/gp/rights-permissions/obtaining-permissions/882>. If the content you are requesting to reuse is under a CC-BY 4.0 licence (or previous version), you do not need to seek permission from Springer Nature for this reuse as long as you provide appropriate credit to the original publication. <https://creativecommons.org/licenses/by/4.0/> STM Permissions Guidelines STM Permissions Guidelines (2022) - STM (stm-assoc.org) will complement the Terms & Conditions on this page CCC Payment T&Cs (copyright.com)

Permission request for reproducing Figure 2.1 from Nature

This is a License Agreement between Curtin University - Marcos Exequiel Arguello ("User") and Copyright Clearance Center, Inc. ("CCC") on behalf of the Rightsholder identified in the order details below. The license consists of the order details, the Marketplace Order General Terms and Conditions below, and any Rightsholder Terms and Conditions which are included below.

All payments must be made in full to CCC in accordance with the Marketplace Order General Terms and Conditions below.

Order Date	14-Jul-2022	Type of Use	Republish in a thesis/dissertation
Order License ID	1247240-1	Publisher	RSC Publishing
ISSN	1754-5706	Portion	Chart/graph/table/figure

LICENSED CONTENT

Publication Title	Energy & environmental science	Publication Type	e-Journal
Article Title	Electrochemomechanics of lithium dendrite growth	Start Page	3595
Author/Editor	Royal Society of Chemistry (Great Britain)	End Page	3607
Date	01/01/2008	Issue	12
Language	English	Volume	12
Country	United Kingdom of Great Britain and Northern Ireland	URL	http://www.rsc.org/Publishing/Journals/E...
Rightsholder	Royal Society of Chemistry		

REQUEST DETAILS

Portion Type	Chart/graph/table/figure	Distribution	Worldwide
Number of charts / graphs / tables / figures requested	1	Translation	Original language of publication
Format (select all that apply)	Print, Electronic	Copies for the disabled?	No
Who will republish the content?	Academic institution	Minor editing privileges?	Yes
Duration of Use	Life of current edition	Incidental promotional use?	No
Lifetime Unit Quantity	Up to 499	Currency	USD
Rights Requested	Main product		

NEW WORK DETAILS

Title	Computational modelling of reactive processes in lithium-metal batteries	Institution name	Curtin University
Instructor name	Marcos Exequiel Arguello	Expected presentation date	2022-09-30

ADDITIONAL DETAILS

Order reference number	N/A	The requesting person / organization to appear on the license	Curtin University - Marcos Exequiel Arguello
------------------------	-----	---	--

REUSE CONTENT DETAILS


Title, description or numeric reference of the portion(s)	Figure 1	Title of the article/chapter the portion is from	Electrochemomechanics of lithium dendrite growth
Editor of portion(s)	Jana, Aniruddha; Woo, Sang Inn; Vikrant, K. S. N.; García, R. Edwin	Author of portion(s)	Jana, Aniruddha; Woo, Sang Inn; Vikrant, K. S. N.; García, R. Edwin
Volume of serial or monograph	12	Issue, if republishing an article from a serial	12
Page or page range of portion	3595-3607	Publication date of portion	2019-01-01

Permission request for reproducing Figure 2.2 from Energy & Environmental Science

Nanoscale Nucleation and Growth of Electrodeposited Lithium Metal

Author: Allen Pei, Guangyuan Zheng, Feifei Shi, et al
Publication: Nano Letters
Publisher: American Chemical Society
Date: Feb 1, 2017

Copyright © 2017, American Chemical Society



PERMISSION/LICENSE IS GRANTED FOR YOUR ORDER AT NO CHARGE

This type of permission/license, instead of the standard Terms and Conditions, is sent to you because no fee is being charged for your order. Please note the following:

- Permission is granted for your request in both print and electronic formats, and translations.
- If figures and/or tables were requested, they may be adapted or used in part.
- Please print this page for your records and send a copy of it to your publisher/graduate school.
- Appropriate credit for the requested material should be given as follows: "Reprinted (adapted) with permission from (COMPLETE REFERENCE CITATION), Copyright (YEAR) American Chemical Society." Insert appropriate information in place of the capitalized words.
- One-time permission is granted only for the use specified in your RightsLink request. No additional uses are granted (such as derivative works or other editions). For any uses, please submit a new request.

If credit is given to another source for the material you requested from RightsLink, permission must be obtained from that source.

[BACK](#) [CLOSE WINDOW](#)

Permission request for reproducing Figure 2.2a from American Chemical Society

This is a License Agreement between Curtin University - Marcos E Arguello ("User") and Copyright Clearance Center, Inc. ("CCC") on behalf of the Rightsholder identified in the order details below. The license consists of the order details, the Marketplace Order General Terms and Conditions below, and any Rightsholder Terms and Conditions which are included below.

All payments must be made in full to CCC in accordance with the Marketplace Order General Terms and Conditions below.

Order Date	18-Jul-2022	Type of Use	Republish in a thesis/dissertation
Order License ID	1248345-1	Publisher	Nature Research
ISSN	1748-3395	Portion	Chart/graph/table/figure

LICENSED CONTENT

Publication Title	Nature nanotechnology	Publication Type	e-Journal
Article Title	Interconnected hollow carbon nanospheres for stable lithium metal anodes.	Start Page	618
Date	01/01/2006	End Page	623
Language	English	Issue	8
Country	United States of America	Volume	9
Rightsholder	Springer Nature BV	URL	http://www.nature.com/nnano

REQUEST DETAILS

Portion Type	Chart/graph/table/figure	Distribution	Worldwide
Number of charts / graphs / tables / figures requested	1	Translation	Original language of publication
Format (select all that apply)	Print, Electronic	Copies for the disabled?	No
Who will republish the content?	Academic institution	Minor editing privileges?	No
Duration of Use	Life of current and all future editions	Incidental promotional use?	No
Lifetime Unit Quantity	Up to 499	Currency	USD
Rights Requested	Main product		

NEW WORK DETAILS

Title	Computational modelling of reactive processes in lithium-metal batteries	Institution name	Curtin University
Instructor name	Marcos Exequiel Arguello	Expected presentation date	2022-09-30

ADDITIONAL DETAILS

The requesting person / organization to appear on the license	Curtin University - Marcos E Arguello
---	---------------------------------------

REUSE CONTENT DETAILS

Title, description or numeric reference of the portion(s)	Figure 3	Title of the article/chapter the portion is from	Interconnected hollow carbon nanospheres for stable lithium metal anodes.
Editor of portion(s)	Zheng, Guangyuan; Lee, Seok Woo; Liang, Zheng; Lee, Hyun-Wook; Yan, Kai; Yao, Hongbin; Wang, Haotian; Li, Weiyang; Chu, Steven; Cui, Yi	Author of portion(s)	Zheng, Guangyuan; Lee, Seok Woo; Liang, Zheng; Lee, Hyun-Wook; Yan, Kai; Yao, Hongbin; Wang, Haotian; Li, Weiyang; Chu, Steven; Cui, Yi
Volume of serial or monograph	9	Publication date of portion	2014-08-01
Page or page range of portion	618-623		

RIGHTSHOLDER TERMS AND CONDITIONS

If you are placing a request on behalf of for a corporate organization, please use RightsLink. For further information visit <http://www.nature.com/reprints/permission-requests.html> and <https://www.springer.com/gp/rights-permissions/obtaining-permissions/882>. If the content you are requesting to reuse is under a CC-BY 4.0 licence (or previous version), you do not need to seek permission from Springer Nature for this reuse as long as you provide appropriate credit to the original publication. <https://creativecommons.org/licenses/by/4.0/> STM Permissions Guidelines STM Permissions Guidelines (2022) - STM (stm-assoc.org) will complement the Terms & Conditions on this page CCC Payment T&Cs (copyright.com)

Permission request for reproducing Figure 2.2b from Nature Nanotechnology

This is a License Agreement between Curtin University - Marcos E Arguello ("User") and Copyright Clearance Center, Inc. ("CCC") on behalf of the Rightsholder identified in the order details below. The license consists of the order details, the Marketplace Order General Terms and Conditions below, and any Rightsholder Terms and Conditions which are included below.

All payments must be made in full to CCC in accordance with the Marketplace Order General Terms and Conditions below.

Order Date	18-Jul-2022	Type of Use	Republish in a thesis/dissertation
Order License ID	1248348-1	Publisher	RSC Publishing
ISSN	1754-5706	Portion	Chart/graph/table/figure

LICENSED CONTENT

Publication Title	Energy & environmental science	Publication Type	e-Journal
Article Title	Transition of lithium growth mechanisms in liquid electrolytes	Start Page	3221
Author/Editor	Royal Society of Chemistry (Great Britain)	End Page	3229
Date	01/01/2008	Issue	10
Language	English	Volume	9
Country	United Kingdom of Great Britain and Northern Ireland	URL	http://www.rsc.org/Publishing/Journals/E...
Rightsholder	Royal Society of Chemistry		

REQUEST DETAILS

Portion Type	Chart/graph/table/figure	Distribution	Worldwide
Number of charts / graphs / tables / figures requested	1	Translation	Original language of publication
Format (select all that apply)	Print, Electronic	Copies for the disabled?	No
Who will republish the content?	Academic institution	Minor editing privileges?	No
Duration of Use	Life of current edition	Incidental promotional use?	No
Lifetime Unit Quantity	Up to 499	Currency	USD
Rights Requested	Main product		

NEW WORK DETAILS

Title	Computational modelling of reactive processes in lithium-metal batteries	Institution name	Curtin University
Instructor name	Marcos Arguello	Expected presentation date	2022-09-30

ADDITIONAL DETAILS

Order reference number	N/A	The requesting person / organization to appear on the license	Curtin University - Marcos E Arguello
------------------------	-----	---	---------------------------------------

REUSE CONTENT DETAILS

Title, description or numeric reference of the portion(s)	Figure 1	Title of the article/chapter the portion is from	Transition of lithium growth mechanisms in liquid electrolytes
Editor of portion(s)	Bai, Peng; Li, Ju; Brushett, Fikile R.; Bazant, Martin Z.	Author of portion(s)	Bai, Peng; Li, Ju; Brushett, Fikile R.; Bazant, Martin Z.
Volume of serial or monograph	9	Issue, if republishing an article from a serial	10
Page or page range of portion	3221-3229	Publication date of portion	2016-10-05

Permission request for reproducing Figure 2.2c from Energy & Environmental Science

ELSEVIER LICENSE
TERMS AND CONDITIONS

Jul 14, 2022

This Agreement between Mr. Marcos Arguello ("You") and Elsevier ("Elsevier") consists of your license details and the terms and conditions provided by Elsevier and Copyright Clearance Center.

License Number	5347531182007
License date	Jul 14, 2022
Licensed Content Publisher	Elsevier
Licensed Content Publication	Electrochimica Acta
Licensed Content Title	Inhibition effect of covalently cross-linked gel electrolytes on lithium dendrite formation
Licensed Content Author	Tetsu Tatsuma, Makoto Taguchi, Noboru Oyama
Licensed Content Date	Jan 31, 2001
Licensed Content Volume	46
Licensed Content Issue	8
Licensed Content Pages	5
Start Page	1201
End Page	1205
Type of Use	reuse in a thesis/dissertation
Portion	figures/tables/illustrations
Number of figures/tables/illustrations	1
Format	both print and electronic
Are you the author of this Elsevier article?	No
Will you be translating?	No
Title	Computational modelling of reactive processes in lithium-metal batteries
Institution name	Curtin University
Expected presentation date	Sep 2022
Portions	Figure 4
Requestor Location	Mr. Marcos Arguello 15 Mary Street Claremont, WA 6010 Australia Attn: Mr. Marcos Arguello
Publisher Tax ID	GB 494 6272 12
Total	0.00 USD

Permission request for reproducing Figures 2.2d and 5.12b from Electrochimica Acta

ELSEVIER LICENSE
TERMS AND CONDITIONS

Jul 17, 2022

This Agreement between Marcos E Arguello ("You") and Elsevier ("Elsevier") consists of your license details and the terms and conditions provided by Elsevier and Copyright Clearance Center.

License Number	5351660547825
License date	Jul 17, 2022
Licensed Content Publisher	Elsevier
Licensed Content Publication	Journal of Power Sources
Licensed Content Title	Safety focused modeling of lithium-ion batteries: A review
Licensed Content Author	S. Abada,G. Marlair,A. Lecocq,M. Petit,V. Sauvant-Moynot,F. Huet
Licensed Content Date	Feb 29, 2016
Licensed Content Volume	306
Licensed Content Issue	n/a
Licensed Content Pages	15
Start Page	178
End Page	192
Type of Use	reuse in a thesis/dissertation
Portion	figures/tables/illustrations
Number of figures/tables/illustrations	1
Format	both print and electronic
Are you the author of this Elsevier article?	No
Will you be translating?	No
Title	Computational modelling of reactive processes in lithium-metal batteries
Institution name	Curtin University
Expected presentation date	Sep 2022
Portions	Figure 2. Length scale dependent physics impacting battery modeling
Requestor Location	Marcos E Arguello 15 Mary Street Claremont, WA 6010 Australia Attn: Mr. Marcos Arguello
Publisher Tax ID	GB 494 6272 12
Total	0.00 USD

Permission request for reproducing Figure 2.3 from Journal of Power Sources

ELSEVIER LICENSE
TERMS AND CONDITIONS

Jul 17, 2022

This Agreement between Marcos E Arguello ("You") and Elsevier ("Elsevier") consists of your license details and the terms and conditions provided by Elsevier and Copyright Clearance Center.

License Number	5351660781429
License date	Jul 17, 2022
Licensed Content Publisher	Elsevier
Licensed Content Publication	Journal of Power Sources
Licensed Content Title	A review of modeling and simulation techniques across the length scales for the solid oxide fuel cell
Licensed Content Author	Kyle N. Grew, Wilson K.S. Chiu
Licensed Content Date	Feb 1, 2012
Licensed Content Volume	199
Licensed Content Issue	n/a
Licensed Content Pages	13
Start Page	1
End Page	13
Type of Use	reuse in a thesis/dissertation
Portion	figures/tables/illustrations
Number of figures/tables/illustrations	1
Format	both print and electronic
Are you the author of this Elsevier article?	No
Will you be translating?	No
Title	Computational modelling of reactive processes in lithium-metal batteries
Institution name	Curtin University
Expected presentation date	Sep 2022
Portions	Figure 2
Requestor Location	Marcos E Arguello 15 Mary Street Claremont, WA 6010 Australia Attn: Mr. Marcos Arguello
Publisher Tax ID	GB 494 6272 12
Total	0.00 USD

Permission request for reproducing Figure 2.4 from Journal of Power Sources

ELSEVIER LICENSE
TERMS AND CONDITIONS

Jul 14, 2022

This Agreement between Mr. Marcos Arguello ("You") and Elsevier ("Elsevier") consists of your license details and the terms and conditions provided by Elsevier and Copyright Clearance Center.

License Number	5347520961900
License date	Jul 14, 2022
Licensed Content Publisher	Elsevier
Licensed Content Publication	Energy Storage Materials
Licensed Content Title	Simulation of 3-D lithium dendritic evolution under multiple electrochemical states: A parallel phase field approach
Licensed Content Author	Zhenliang Mu,Zhipeng Guo,Yuan-Hua Lin
Licensed Content Date	Sep 1, 2020
Licensed Content Volume	30
Licensed Content Issue	n/a
Licensed Content Pages	7
Start Page	52
End Page	58
Type of Use	reuse in a thesis/dissertation
Portion	figures/tables/illustrations
Number of figures/tables/illustrations	1
Format	both print and electronic
Are you the author of this Elsevier article?	No
Will you be translating?	No
Title	Computational modelling of reactive processes in lithium-metal batteries
Institution name	Curtin University
Expected presentation date	Sep 2022
Portions	Figure 2
Requestor Location	Mr. Marcos Arguello 15 Mary Street Claremont, WA 6010 Australia Attn: Mr. Marcos Arguello
Publisher Tax ID	GB 494 6272 12
Total	0.00 USD

Permission request for reproducing Figure 2.5 from Energy Storage Materials

ELSEVIER LICENSE
TERMS AND CONDITIONS

Jul 14, 2022

This Agreement between Mr. Marcos Arguello ("You") and Elsevier ("Elsevier") consists of your license details and the terms and conditions provided by Elsevier and Copyright Clearance Center.

License Number	5347521447596
License date	Jul 14, 2022
Licensed Content Publisher	Elsevier
Licensed Content Publication	Journal of Energy Storage
Licensed Content Title	Quantitative analysis of the inhibition effect of rising temperature and pulse charging on Lithium dendrite growth
Licensed Content Author	Dongge Qiao,Xunliang Liu,Ruifeng Dou,Zhi Wen,Wenming Zhou,Lin Liu
Licensed Content Date	May 1, 2022
Licensed Content Volume	49
Licensed Content Issue	n/a
Licensed Content Pages	1
Start Page	104137
End Page	0
Type of Use	reuse in a thesis/dissertation
Portion	figures/tables/illustrations
Number of figures/tables/illustrations	1
Format	both print and electronic
Are you the author of this Elsevier article?	No
Will you be translating?	No
Title	Computational modelling of reactive processes in lithium-metal batteries
Institution name	Curtin University
Expected presentation date	Sep 2022
Portions	Figure 6
Requestor Location	Mr. Marcos Arguello 15 Mary Street Claremont, WA 6010 Australia Attn: Mr. Marcos Arguello
Publisher Tax ID	GB 494 6272 12
Total	0.00 USD

Permission request for reproducing Figure 2.7a from Journal of Energy Storage

ELSEVIER LICENSE
TERMS AND CONDITIONS

Jul 14, 2022

This Agreement between Mr. Marcos Arguello ("You") and Elsevier ("Elsevier") consists of your license details and the terms and conditions provided by Elsevier and Copyright Clearance Center.

License Number	5347530508218
License date	Jul 14, 2022
Licensed Content Publisher	Elsevier
Licensed Content Publication	Energy Storage Materials
Licensed Content Title	The dendrite growth in 3D structured lithium metal anodes: Electron or ion transfer limitation?
Licensed Content Author	Rui Zhang,Xin Shen,Xin-Bing Cheng,Qiang Zhang
Licensed Content Date	Dec 1, 2019
Licensed Content Volume	23
Licensed Content Issue	n/a
Licensed Content Pages	10
Start Page	556
End Page	565
Type of Use	reuse in a thesis/dissertation
Portion	figures/tables/illustrations
Number of figures/tables/illustrations	1
Format	both print and electronic
Are you the author of this Elsevier article?	No
Will you be translating?	No
Title	Computational modelling of reactive processes in lithium-metal batteries
Institution name	Curtin University
Expected presentation date	Sep 2022
Portions	Figure 4
Requestor Location	Mr. Marcos Arguello 15 Mary Street Claremont, WA 6010 Australia Attn: Mr. Marcos Arguello
Publisher Tax ID	GB 494 6272 12
Total	0.00 USD

Permission request for reproducing Figure 2.7b from Energy Storage Materials

ELSEVIER LICENSE
TERMS AND CONDITIONS

Jul 14, 2022

This Agreement between Mr. Marcos Arguello ("You") and Elsevier ("Elsevier") consists of your license details and the terms and conditions provided by Elsevier and Copyright Clearance Center.

License Number	5347530807168
License date	Jul 14, 2022
Licensed Content Publisher	Elsevier
Licensed Content Publication	Journal of Energy Storage
Licensed Content Title	Numerical simulation of the factors affecting the growth of lithium dendrites
Licensed Content Author	Wenyu Mu,Xunliang Liu,Zhi Wen,Lin Liu
Licensed Content Date	Dec 1, 2019
Licensed Content Volume	26
Licensed Content Issue	n/a
Licensed Content Pages	1
Start Page	100921
End Page	0
Type of Use	reuse in a thesis/dissertation
Portion	figures/tables/illustrations
Number of figures/tables/illustrations	1
Format	both print and electronic
Are you the author of this Elsevier article?	No
Will you be translating?	No
Title	Computational modelling of reactive processes in lithium-metal batteries
Institution name	Curtin University
Expected presentation date	Sep 2022
Portions	Figure 8
Requestor Location	Mr. Marcos Arguello 15 Mary Street Claremont, WA 6010 Australia Attn: Mr. Marcos Arguello
Publisher Tax ID	GB 494 6272 12
Total	0.00 USD

Permission request for reproducing Figure 2.7c from Journal of Energy Storage

Bibliography

- Abada, S., G. Marlair, A. Lecocq, M. Petit, V. Sauvant-Moynot, and F. Huet (2016). Safety focused modeling of lithium-ion batteries: A review. *Journal of Power Sources* 306, 178–192.
- Adams, B. D., J. Zheng, X. Ren, W. Xu, and J.-G. Zhang (2018). Accurate determination of coulombic efficiency for lithium metal anodes and lithium metal batteries. *Advanced Energy Materials* 8(7), 1702097.
- Akolkar, R. (2013). Mathematical model of the dendritic growth during lithium electrodeposition. *Journal of Power Sources* 232, 23–28.
- Akolkar, R. (2014). Modeling dendrite growth during lithium electrodeposition at sub-ambient temperature. *Journal of Power Sources* 246, 84–89.
- Allen, S. and J. Cahn (1972). Ground state structures in ordered binary alloys with second neighbor interactions. *Acta Metallurgica* 20(3), 423–433.
- Alnæs, M. S., J. Blechta, J. Hake, A. Johansson, B. Kehlet, A. Logg, C. Richardson, J. Ring, M. E. Rognes, and G. N. Wells (2015). The FEniCS project version 1.5. *Archive of Numerical Software* 3(100), 9–23.
- Aryanfar, A., D. Brooks, B. V. Merinov, W. A. Goddard, A. J. Colussi, and M. R. Hoffmann (2014). Dynamics of lithium dendrite growth and inhibition: Pulse charging experiments and monte carlo calculations. *The Journal of Physical Chemistry Letters* 5(10), 1721–1726.

- Ayachit, U. (2015). *The paraview guide: A parallel visualization application*. Kitware, Inc.
- Bai, P., J. Guo, M. Wang, A. Kushima, L. Su, J. Li, F. R. Brushett, and M. Z. Bazant (2018). Interactions between lithium growths and nanoporous ceramic separators. *Joule* 2(11), 2434–2449.
- Bai, P., J. Li, F. R. Brushett, and M. Z. Bazant (2016). Transition of lithium growth mechanisms in liquid electrolytes. *Energy Environ. Sci.* 9, 3221–3229.
- Balay, S., S. Abhyankar, M. Adams, J. Brown, P. Brune, K. Buschelman, L. Dalcin, A. Dener, V. Eijkhout, W. Gropp, D. Karpeyev, D. Kaushik, M. Knepley, D. May, L. C. McInnes, R. Mills, T. Munson, K. Rupp, P. Sanan, B. Smith, S. Zampini, H. Zhang, and H. Zhang (2021). *PETSc Users Manual, ANL-95/11 - Revision 3.15*.
- Bard, A. J. and L. R. Faulkner (Eds.) (2001). *Electrochemical Methods: Fundamentals and Applications*. Wiley.
- Barton, J. L., J. O. Bockris, and A. R. J. P. Ubbelohde (1962). The electrolytic growth of dendrites from ionic solutions. *Proceedings of the Royal Society of London. Series A. Mathematical and Physical Sciences* 268(1335), 485–505.
- Bazant, M. Z. (2013). Theory of chemical kinetics and charge transfer based on nonequilibrium thermodynamics. *Accounts of Chemical Research* 46(5), 1144–1160.
- Bieker, G., M. Winter, and P. Bieker (2015). Electrochemical in situ investigations of SEI and dendrite formation on the lithium metal anode. *Phys. Chem. Chem. Phys.* 17, 8670–8679.
- Boettinger, W. J., J. A. Warren, C. Beckermann, and A. Karma (2002). Phase-field simulation of solidification. *Annual Review of Materials Research* 32(1), 163–194.

- Bruce, P. G., S. A. Freunberger, L. J. Hardwick, and J.-M. Tarascon (2012). Li-O₂ and Li-S batteries with high energy storage. *Nature materials* 11(1), 19–29.
- Cahn, J. W. and J. E. Hilliard (1959). Free energy of a nonuniform system. III. Nucleation in a two-component incompressible fluid. *The Journal of Chemical Physics* 31(3), 688–699.
- Celaya, E. A., J. J. A. Aguirrezabala, and P. Chatzipantelidis (2014). Implementation of an adaptive BDF2 formula and comparison with the MATLAB Ode15s. *Procedia Computer Science* 29, 1014–1026.
- Chae, O. B., J. Kim, and B. L. Lucht (2022). Modification of lithium electrodeposition behavior by variation of electrode distance. *Journal of Power Sources* 532, 231338.
- Chai, M., K. Luo, C. Shao, and J. Fan (2017). An efficient level set remedy approach for simulations of two-phase flow based on sigmoid function. *Chemical Engineering Science* 172, 335–352.
- Chazalviel, J.-N. (1990, Dec). Electrochemical aspects of the generation of ramified metallic electrodeposits. *Phys. Rev. A* 42, 7355–7367.
- Chen, C.-H. and C.-W. Pao (2021). Phase-field study of dendritic morphology in lithium metal batteries. *Journal of Power Sources* 484, 229203.
- Chen, L., X. Fan, X. Ji, J. Chen, S. Hou, and C. Wang (2019). High-energy li metal battery with lithiated host. *Joule* 3(3), 732–744.
- Chen, L., H. W. Zhang, L. Y. Liang, Z. Liu, Y. Qi, P. Lu, J. Chen, and L.-Q. Chen (2015). Modulation of dendritic patterns during electrodeposition: A nonlinear phase-field model. *Journal of Power Sources* 300, 376–385.
- Cheng, X.-B., T.-Z. Hou, R. Zhang, H.-J. Peng, C.-Z. Zhao, J.-Q. Huang, and Q. Zhang (2016). Dendrite-free lithium deposition induced by uniformly dis-

- tributed lithium ions for efficient lithium metal batteries. *Advanced Materials* 28(15), 2888–2895.
- Cheng, X.-B., R. Zhang, C.-Z. Zhao, and Q. Zhang (2017). Toward safe lithium metal anode in rechargeable batteries: A review. *Chemical reviews* 117(15), 10403–10473.
- Cimrman, R., V. Lukeš, and E. Rohan (2019). Multiscale finite element calculations in python using sfepy. *Advances in Computational Mathematics* 45(4), 1897–1921.
- Cogswell, D. A. (2015). Quantitative phase-field modeling of dendritic electrodeposition. *Phys. Rev. E* 92, 011301.
- Cogswell, D. A. and W. C. Carter (2011, Jun). Thermodynamic phase-field model for microstructure with multiple components and phases: The possibility of metastable phases. *Phys. Rev. E* 83, 061602.
- Crowther, O. and A. C. West (2008). Effect of electrolyte composition on lithium dendrite growth. *Journal of The Electrochemical Society* 155(11), A806.
- Dalcin, L. and Y.-L. L. Fang (2021). mpi4py: Status update after 12 years of development. *Computing in Science Engineering* 23(4), 47–54.
- Dalcin, L. D., R. R. Paz, P. A. Kler, and A. Cosimo (2011). Parallel distributed computing using Python. *Advances in Water Resources* 34(9), 1124–1139. New Computational Methods and Software Tools.
- Dalcín, L., R. Paz, and M. Storti (2005). MPI for Python. *Journal of Parallel and Distributed Computing* 65(9), 1108–1115.
- Dalcín, L., R. Paz, M. Storti, and J. D’Elía (2008). MPI for Python: Performance improvements and MPI-2 extensions. *Journal of Parallel and Distributed Computing* 68(5), 655–662.

- de Groot, S. R. and P. Mazur (1984). *Non-equilibrium Thermodynamics*. Courier Corporation.
- DeWitt, S., S. Rudraraju, D. Montiel, W. B. Andrews, and K. Thornton (2020). Prisms-pf: A general framework for phase-field modeling with a matrix-free finite element method. *npj Computational Materials* 6(1), 1–12.
- Diddens, D., W. A. Appiah, Y. Mabrouk, A. Heuer, T. Vegge, and A. Bhowmik (2022). Modeling the solid electrolyte interphase: Machine learning as a game changer? *Advanced Materials Interfaces* 9(8), 2101734.
- Ding, T. (2016). In-situ optical microscopic investigation of the dendrite formation on lithium anode under different electrolyte conditions in Li-S battery.
- Dollé, M., L. Sannier, B. Beaudoin, M. Trentin, and J.-M. Tarascon (2002). Live scanning electron microscope observations of dendritic growth in lithium/polymer cells. *Electrochemical and solid-state letters* 5(12), A286.
- Echebarria, B., R. Folch, A. Karma, and M. Plapp (2004, Dec). Quantitative phase-field model of alloy solidification. *Phys. Rev. E* 70, 061604.
- Elder, K. R., M. Grant, N. Provatas, and J. M. Kosterlitz (2001, Jul). Sharp interface limits of phase-field models. *Phys. Rev. E* 64, 021604.
- Elezgaray, J., C. Léger, and F. Argoul (1998). Linear stability analysis of unsteady galvanostatic electrodeposition in the two-dimensional diffusion-limited regime. *Journal of The Electrochemical Society* 145, 2016–2024.
- Ely, D. R., A. Jana, and R. E. García (2014). Phase field kinetics of lithium electrodeposits. *Journal of Power Sources* 272, 581–594.
- Fan, L., H. L. Zhuang, W. Zhang, Y. Fu, Z. Liao, and Y. Lu (2018). Stable lithium electrodeposition at ultra-high current densities enabled by 3D PMF/Li composite anode. *Advanced Energy Materials* 8(15), 1703360.

- Fang, Q. (2022). *Phase-field simulation of dendrite growth in Li-metal batteries*. Ph. D. thesis, Queensland University of Technology.
- Franco, A. A., A. Rucci, D. Brandell, C. Frayret, M. Gaberscek, P. Jankowski, and P. Johansson (2019). Boosting rechargeable batteries r&d by multiscale modeling: myth or reality? *Chemical reviews* 119(7), 4569–4627.
- Frenck, L., G. K. Sethi, J. A. Maslyn, and N. P. Balsara (2019). Factors that control the formation of dendrites and other morphologies on lithium metal anodes. *Frontiers in Energy Research* 7, 115.
- Fu, J., Z. P. Cano, M. G. Park, A. Yu, M. Fowler, and Z. Chen (2017). Electrically rechargeable zinc–air batteries: Progress, challenges, and perspectives. *Advanced Materials* 29(7), 1604685.
- Gao, L. and Z. Guo (2020). Phase-field simulation of li dendrites with multiple parameters influence. *Computational Materials Science* 183, 109919.
- Gao, X., Y.-N. Zhou, D. Han, J. Zhou, D. Zhou, W. Tang, and J. B. Goodenough (2020). Thermodynamic understanding of li-dendrite formation. *Joule* 4(9), 1864–1879.
- Garche, J., C. Dyer, P. T. Moseley, Z. Ogumi, D. A. Rand, and B. Scrosati (2013). *Encyclopedia of electrochemical power sources*. Newnes.
- García, R., C. M. Bishop, and W. Carter (2004). Thermodynamically consistent variational principles with applications to electrically and magnetically active systems. *Acta Materialia* 52(1), 11–21.
- George, W. L. and J. A. Warren (2002). A parallel 3D dendritic growth simulator using the phase-field method. *Journal of Computational Physics* 177(2), 264–283.

- Gireaud, L., S. Grugeon, S. Laruelle, B. Yrieix, and J.-M. Tarascon (2006). Lithium metal stripping/plating mechanisms studies: A metallurgical approach. *Electrochemistry Communications* 8(10), 1639–1649.
- Gomez, H. and T. J. Hughes (2011). Provably unconditionally stable, second-order time-accurate, mixed variational methods for phase-field models. *Journal of Computational Physics* 230(13), 5310–5327.
- Gomez, H. and K. G. van der Zee (2017). Computational phase-field modeling.
- Grew, K. N. and W. K. Chiu (2012). A review of modeling and simulation techniques across the length scales for the solid oxide fuel cell. *Journal of Power Sources* 199, 1–13.
- Guan, P., L. Liu, and Y. Gao (2018). Phase-field modeling of solid electrolyte interphase (SEI) cracking in lithium batteries. *ECS Transactions* 85(13), 1041.
- Guan, P., L. Liu, and X. Lin (2015). Simulation and experiment on solid electrolyte interphase (SEI) morphology evolution and lithium-ion diffusion. *Journal of The Electrochemical Society* 162(9), A1798.
- Guyer, J. E., W. J. Boettinger, J. A. Warren, and G. B. McFadden (2004a). Phase field modeling of electrochemistry. I. Equilibrium. *Phys. Rev. E* 69, 021603.
- Guyer, J. E., W. J. Boettinger, J. A. Warren, and G. B. McFadden (2004b, Feb). Phase field modeling of electrochemistry. II. Kinetics. *Phys. Rev. E* 69, 021604.
- Gómez, H., V. M. Calo, Y. Bazilevs, and T. J. Hughes (2008). Isogeometric analysis of the Cahn–Hilliard phase-field model. *Computer Methods in Applied Mechanics and Engineering* 197(49), 4333 – 4352.
- Hairer, E. and G. Wanner (2010). *Solving Ordinary Differential Equations II: Stiff and Differential-Algebraic Problems*, Volume 14. Springer.

- Han, B., A. Van der Ven, D. Morgan, and G. Ceder (2004). Electrochemical modeling of intercalation processes with phase field models. *Electrochimica Acta* 49(26), 4691–4699.
- Hannah Ritchie, M. R. and P. Rosado (2020). Energy. *Our World in Data*. <https://ourworldindata.org/energy>.
- Hawkins-Daarud, A., K. G. van der Zee, and J. Tinsley Oden (2012). Numerical simulation of a thermodynamically consistent four-species tumor growth model. *International journal for numerical methods in biomedical engineering* 28(1), 3–24.
- Hong, Z. and V. Viswanathan (2018). Phase-field simulations of lithium dendrite growth with open-source software. *ACS Energy Letters* 3(7), 1737–1743.
- Hong, Z. and V. Viswanathan (2020). Open-sourcing phase-field simulations for accelerating energy materials design and optimization. *ACS Energy Letters* 5(10), 3254–3259.
- Hughes, T. J. (2012). *The finite element method: linear static and dynamic finite element analysis*. Courier Corporation.
- Hyeonggeon, L., S. Niranjana, H. Sungwon, and J. S.-I. Kwon (2021). Multi-scale modeling of dendrite formation in lithium-ion batteries. *Cocomputers & Chemical Engineering* 153, 107415.
- ichi Morigaki, K. (2002). Analysis of the interface between lithium and organic electrolyte solution. *Journal of Power Sources* 104(1), 13–23.
- IEA (2021). Global energy review 2021. Paris.[Online] <https://www.iea.org/reports/global-energy-review-2021> [Accessed: 2021-06-07].

- IEA (2022). Global energy review: Co2 emissions in 2021. *Paris*. [Online] <https://www.iea.org/reports/global-energy-review-co2-emissions-in-2021-2> [Accessed: 2021-06-07].
- Iverson, B. D. and S. V. Garimella (2008, Aug). Recent advances in microscale pumping technologies: A review and evaluation. *Microfluidics and Nanofluidics* 5(2), 145–174.
- Jana, A. and R. E. García (2017). Lithium dendrite growth mechanisms in liquid electrolytes. *Nano Energy* 41, 552–565.
- Jana, A., S. I. Woo, K. Vikrant, and R. E. García (2019). Electrochemomechanics of lithium dendrite growth. *Energy & Environmental Science* 12(12), 3595–3607.
- Jang, I. and A. Yethiraj (2021). Effect of diffusion constant on the morphology of dendrite growth in lithium metal batteries. *The Journal of Chemical Physics* 154(23), 234705.
- Jiang, K., X. Liu, X. Yi, G. Lou, Z. Wen, and L. Liu (2022). Modeling of solid-state lithium-oxygen battery with porous $\text{Li}_{1.3}\text{Al}_{0.3}\text{Ti}_{1.7}(\text{PO}_4)_3$ -based cathode. *Journal of Energy Storage* 45, 103747.
- Jiao, S., J. Zheng, Q. Li, X. Li, M. H. Engelhard, R. Cao, J.-G. Zhang, and W. Xu (2018). Behavior of lithium metal anodes under various capacity utilization and high current density in lithium metal batteries. *Joule* 2(1), 110–124.
- Jäckle, M. and A. Groß (2014). Microscopic properties of lithium, sodium, and magnesium battery anode materials related to possible dendrite growth. *The Journal of Chemical Physics* 141(17), 174710.
- Karma, A. (2001, Aug). Phase-field formulation for quantitative modeling of alloy solidification. *Phys. Rev. Lett.* 87, 115701.

- Kim, P. J., K. Kim, and V. G. Pol (2018). Uniform metal-ion flux through interface-modified membrane for highly stable metal batteries. *Electrochimica Acta* 283, 517–527.
- Kirby, R. C. (2004). Algorithm 839: FIAT, a new paradigm for computing finite element basis functions. *ACM Trans. Math. Softw.* 30(4), 502–516.
- Klinsmann, M., F. E. Hildebrand, M. Ganser, and R. M. McMeeking (2019). Dendritic cracking in solid electrolytes driven by lithium insertion. *Journal of Power Sources* 442, 227226.
- Kobayashi, R. (1993). Modeling and numerical simulations of dendritic crystal growth. *Physica D: Nonlinear Phenomena* 63(3), 410–423.
- Kolodziejczyk, F., B. Mortazavi, T. Rabczuk, and X. Zhuang (2021). Machine learning assisted multiscale modeling of composite phase change materials for li-ion batteries’ thermal management. *International Journal of Heat and Mass Transfer* 172, 121199.
- Kumar, M. (2020). Social, economic, and environmental impacts of renewable energy resources. In K. E. Okedu, A. Tahour, and A. G. Aissaou (Eds.), *Wind Solar Hybrid Renewable Energy System*, Chapter 11. Rijeka: IntechOpen.
- Kuznetsov, A. M. and J. Ulstrup (1999). *Electron Transfer in Chemistry and Biology: An Introduction to the Theory*. Wiley.
- Labanda, N. A., L. Espath, and V. M. Calo (2022). A spatio-temporal adaptive phase-field fracture method. *Computer Methods in Applied Mechanics and Engineering* 392, 114675.
- Lang, J. (1995). Two-dimensional fully adaptive solutions of reaction-diffusion equations. *Applied Numerical Mathematics* 18(1), 223 – 240.
- Li, G., Y. Gao, X. He, Q. Huang, S. Chen, S. H. Kim, and D. Wang (2017, Oct). Organosulfide-plasticized solid-electrolyte interphase layer enables stable

- lithium metal anodes for long-cycle lithium-sulfur batteries. *Nature Communications* 8(1), 850.
- Li, G., Z. Liu, Q. Huang, Y. Gao, M. Regula, D. Wang, L.-Q. Chen, and D. Wang (2018, Dec). Stable metal battery anodes enabled by polyethylenimine sponge hosts by way of electrokinetic effects. *Nature Energy* 3(12), 1076–1083.
- Li, H., D. Chao, B. Chen, X. Chen, C. Chuah, Y. Tang, Y. Jiao, M. Jaroniec, and S.-Z. Qiao (2020). Revealing principles for design of lean-electrolyte lithium metal anode via in situ spectroscopy. *Journal of the American Chemical Society* 142(4), 2012–2022.
- Li, J., Z. Kong, X. Liu, B. Zheng, Q. H. Fan, E. Garratt, T. Schuelke, K. Wang, H. Xu, and H. Jin (2021). Strategies to anode protection in lithium metal battery: a review. *InfoMat* 3(12), 1333–1363.
- Li, N., Q. Ye, K. Zhang, H. Yan, C. Shen, B. Wei, and K. Xie (2019). Normalized lithium growth from the nucleation stage for dendrite-free lithium metal anodes. *Angewandte Chemie International Edition* 58(50), 18246–18251.
- Li, Y. and J. Lu (2017). Metal–air batteries: Will they be the future electrochemical energy storage device of choice? *ACS Energy Letters* 2(6), 1370–1377.
- Li, Y., G. Zhang, B. Chen, W. Zhao, L. Sha, D. Wang, J. Yu, and S. Shi (2022). Understanding the separator pore size inhibition effect on lithium dendrite via phase-field simulations. *Chinese Chemical Letters* 33(6), 3287–3290.
- Li, Z., J. Huang, B. Y. Liaw, V. Metzler, and J. Zhang (2014). A review of lithium deposition in lithium-ion and lithium metal secondary batteries. *Journal of power sources* 254, 168–182.
- Liang, L. and L.-Q. Chen (2014). Nonlinear phase field model for electrodeposition in electrochemical systems. *Applied Physics Letters* 105(26), 263903.

- Liang, L., Y. Qi, F. Xue, S. Bhattacharya, S. J. Harris, and L.-Q. Chen (2012). Nonlinear phase-field model for electrode-electrolyte interface evolution. *Phys. Rev. E* 86, 051609.
- Liao, H.-l., B. Ji, and L. Zhang (2020, 11). An adaptive BDF2 implicit time-stepping method for the phase field crystal model. *IMA Journal of Numerical Analysis* 42(1), 649–679.
- Lin, D., Y. Liu, and Y. Cui (2017). Reviving the lithium metal anode for high-energy batteries. *Nature nanotechnology* 12(3), 194–206.
- Lindsay, A. D., D. R. Gaston, C. J. Permann, J. M. Miller, D. Andrš, A. E. Slaughter, F. Kong, J. Hansel, R. W. Carlsen, C. Icenhour, L. Harbour, G. L. Giudicelli, R. H. Stogner, P. German, J. Badger, S. Biswas, L. Chapuis, C. Green, J. Hales, T. Hu, W. Jiang, Y. S. Jung, C. Matthews, Y. Miao, A. Novak, J. W. Peterson, Z. M. Prince, A. Rovinelli, S. Schunert, D. Schwen, B. W. Spencer, S. Veeraraghavan, A. Recuero, D. Yushu, Y. Wang, A. Wilkins, and C. Wong (2022). 2.0 - MOOSE: Enabling massively parallel multiphysics simulation. *SoftwareX* 20, 101202.
- Ling, C., D. Banerjee, and M. Matsui (2012). Study of the electrochemical deposition of Mg in the atomic level: Why it prefers the non-dendritic morphology. *Electrochimica Acta* 76, 270–274.
- Liu, B., J.-G. Zhang, and W. Xu (2018). Advancing lithium metal batteries. *Joule* 2(5), 833–845.
- Liu, H., X.-B. Cheng, Z. Jin, R. Zhang, G. Wang, L.-Q. Chen, Q.-B. Liu, J.-Q. Huang, and Q. Zhang (2019). Recent advances in understanding dendrite growth on alkali metal anodes. *EnergyChem* 1(1), 100003.
- Liu, L. and P. Guan (2019). Phase-field modeling of solid electrolyte interphase (SEI) evolution: Considering cracking and dissolution during battery cycling. *ECS Transactions* 89(1), 101.

- Liu, Y., D. Lin, P. Y. Yuen, K. Liu, J. Xie, R. H. Dauskardt, and Y. Cui (2017). An artificial solid electrolyte interphase with high Li-ion conductivity, mechanical strength, and flexibility for stable lithium metal anodes. *Advanced Materials* 29(10), 1605531.
- Liu, Y., X. Xu, M. Sadd, O. O. Kapitanova, V. A. Krivchenko, J. Ban, J. Wang, X. Jiao, Z. Song, J. Song, S. Xiong, and A. Matic (2021). Insight into the critical role of exchange current density on electrodeposition behavior of lithium metal. *Advanced Science* 8(5), 2003301.
- Lu, D., Y. Shao, T. Lozano, W. D. Bennett, G. L. Graff, B. Polzin, J. Zhang, M. H. Engelhard, N. T. Saenz, W. A. Henderson, P. Bhattacharya, J. Liu, and J. Xiao (2015). Failure mechanism for fast-charged lithium metal batteries with liquid electrolytes. *Advanced Energy Materials* 5(3), 1400993.
- Mayers, M. Z., J. W. Kaminski, and T. F. Miller (2012). Suppression of dendrite formation via pulse charging in rechargeable lithium metal batteries. *The Journal of Physical Chemistry C* 116(50), 26214–26221.
- Monroe, C. and J. Newman (2003). Dendrite growth in lithium/polymer systems. *Journal of The Electrochemical Society* 150(10), A1377.
- Monroe, C. and J. Newman (2004). The effect of interfacial deformation on electrodeposition kinetics. *Journal of The Electrochemical Society* 151(6), A880.
- Mu, W., X. Liu, Z. Wen, and L. Liu (2019). Numerical simulation of the factors affecting the growth of lithium dendrites. *Journal of Energy Storage* 26, 100921.
- Mu, Z., Z. Guo, and Y.-H. Lin (2020). Simulation of 3-d lithium dendritic evolution under multiple electrochemical states: A parallel phase field approach. *Energy Storage Materials* 30, 52–58.
- Multiphysics, C. (2022). 3.4, comsol ab, stockholm, sweden.

- Natsiavas, P., K. Weinberg, D. Rosato, and M. Ortiz (2016). Effect of prestress on the stability of electrode–electrolyte interfaces during charging in lithium batteries. *Journal of the Mechanics and Physics of Solids* 95, 92–111.
- Nishida, T., K. Nishikawa, M. Rosso, and Y. Fukunaka (2013). Optical observation of li dendrite growth in ionic liquid. *Electrochimica acta* 100, 333–341.
- Nishikawa, K., T. Mori, T. Nishida, Y. Fukunaka, and M. Rosso (2011). Li dendrite growth and Li^+ ionic mass transfer phenomenon. *Journal of Electroanalytical Chemistry* 661(1), 84–89.
- Nishikawa, K., T. Mori, T. Nishida, Y. Fukunaka, M. Rosso, and T. Homma (2010). In situ observation of dendrite growth of electrodeposited Li metal. *Journal of The Electrochemical Society* 157(11), A1212.
- Nishikawa, K., H. Naito, M. Kawase, and T. Nishida (2012). Morphological variation of electrodeposited li in ionic liquid. *ECS Transactions* 41(41), 3.
- Okajima, Y., Y. Shibuta, and T. Suzuki (2010). A phase-field model for electrode reactions with Butler–Volmer kinetics. *Computational Materials Science* 50(1), 118–124.
- Ozhabes, Y., D. Gunceler, and T. A. Arias (2015). Stability and surface diffusion at lithium-electrolyte interphases with connections to dendrite suppression.
- Pannala, S., J. A. Turner, S. Allu, W. R. Elwasif, S. Kalnaus, S. Simunovic, A. Kumar, J. J. Billings, H. Wang, and J. Nanda (2015). Multiscale modeling and characterization for performance and safety of lithium-ion batteries. *Journal of Applied Physics* 118(7), 072017.
- Pardo, D., P. J. Matuszyk, V. Puzyrev, C. Torres-Verdin, M. J. Nam, and V. M. Calo (2021). *Modeling of Resistivity and Acoustic Borehole Logging Measurements Using Finite Element Methods*. Elsevier.

- Parekh, M. N., C. D. Rahn, and L. A. Archer (2020). Controlling dendrite growth in lithium metal batteries through forced advection. *Journal of Power Sources* 452, 227760.
- Pei, A., G. Zheng, F. Shi, Y. Li, and Y. Cui (2017). Nanoscale nucleation and growth of electrodeposited lithium metal. *Nano letters* 17(2), 1132–1139.
- Pires, V. F., E. Romero-Cadaval, D. Vinnikov, I. Roasto, and J. Martins (2014). Power converter interfaces for electrochemical energy storage systems—a review. *Energy conversion and management* 86, 453–475.
- Plapp, M. (2011). Unified derivation of phase-field models for alloy solidification from a grand-potential functional. *Phys. Rev. E* 84, 031601.
- Powell, A. C. and R. Arroyave (2008). Open source software for materials and process modeling. *JOM* 60(5), 32–39.
- Qian, J., W. A. Henderson, W. Xu, P. Bhattacharya, M. Engelhard, O. Borodin, and J.-G. Zhang (2015, Feb). High rate and stable cycling of lithium metal anode. *Nature Communications* 6(1), 6362.
- Qiao, D., X. Liu, R. Dou, Z. Wen, W. Zhou, and L. Liu (2022). Quantitative analysis of the inhibition effect of rising temperature and pulse charging on lithium dendrite growth. *Journal of Energy Storage* 49, 104137.
- Rosso, M., C. Brissot, A. Teyssot, M. Dollé, L. Sannier, J.-M. Tarascon, R. Bouchet, and S. Lascaud (2006). Dendrite short-circuit and fuse effect on Li/polymer/Li cells. *Electrochimica Acta* 51(25), 5334–5340.
- Sakane, S., T. Takaki, and T. Aoki (2022). Parallel-gpu-accelerated adaptive mesh refinement for three-dimensional phase-field simulation of dendritic growth during solidification of binary alloy. *Materials Theory* 6(1), 1–19.

- Sarmiento, A., L. Espath, P. Vignal, L. Dalcin, M. Parsani, and V. Calo (2018). An energy-stable generalized- α method for the Swift–Hohenberg equation. *Journal of Computational and Applied Mathematics* 344, 836–851.
- Shibuta, Y., Y. Okajima, and T. Suzuki (2007). Phase-field modeling for electrodeposition process. *Science and Technology of Advanced Materials* 8(6), 511–518. Nanoionics - Present and future prospects.
- Silber, S. A. and M. Karttunen (2022). Symphas—general purpose software for phase-field, phase-field crystal, and reaction-diffusion simulations. *Advanced Theory and Simulations* 5(1), 2100351.
- Smil, V. (2016). *Energy transitions: global and national perspectives*. ABC-CLIO.
- Steiger, J., G. Richter, M. Wenk, D. Kramer, and R. Mönig (2015). Comparison of the growth of lithium filaments and dendrites under different conditions. *Electrochemistry Communications* 50, 11–14.
- Steinbach, I., F. Pezzolla, B. Nestler, M. Seeßelberg, R. Prieler, G. Schmitz, and J. Rezende (1996). A phase field concept for multiphase systems. *Physica D: Nonlinear Phenomena* 94(3), 135–147.
- Subramanian, V. R., V. Boovaragavan, V. Ramadesigan, and M. Arabandi (2009). Mathematical model reformulation for lithium-ion battery simulations: Galvanostatic boundary conditions. *Journal of The Electrochemical Society* 156(4), A260.
- Sundström, L.-G. and F. H. Bark (1995). On morphological instability during electrodeposition with a stagnant binary electrolyte. *Electrochimica Acta* 40(5), 599–614.
- Suo, L., Y.-S. Hu, H. Li, M. Armand, and L. Chen (2013, Feb). A new class of solvent-in-salt electrolyte for high-energy rechargeable metallic lithium batteries. *Nature Communications* 4(1), 1481.

- Takaki, T., T. Shimokawabe, M. Ohno, A. Yamanaka, and T. Aoki (2013). Unexpected selection of growing dendrites by very-large-scale phase-field simulation. *Journal of Crystal Growth* 382, 21–25.
- Talib, A. N., K. Hafeez, M. J. Mnati, and S. A. Khan (2022). Design and implementation of new battery monitoring system for photovoltaic application. In *2022 4th Global Power, Energy and Communication Conference (GPECOM)*, pp. 1–7. IEEE.
- Tan, J. and E. M. Ryan (2016). Computational study of electro-convection effects on dendrite growth in batteries. *Journal of Power Sources* 323, 67–77.
- Tan, P., W. Kong, Z. Shao, M. Liu, and M. Ni (2017). Advances in modeling and simulation of Li–air batteries. *Progress in Energy and Combustion Science* 62, 155–189.
- Tang, C.-Y. and S. J. Dillon (2016). In situ scanning electron microscopy characterization of the mechanism for li dendrite growth. *Journal of The Electrochemical Society* 163(8), A1660.
- Tatsuma, T., M. Taguchi, and N. Oyama (2001). Inhibition effect of covalently cross-linked gel electrolytes on lithium dendrite formation. *Electrochimica Acta* 46(8), 1201–1205.
- Tegeler, M., O. Shchyglo, R. D. Kamachali, A. Monas, I. Steinbach, and G. Suttmann (2017). Parallel multiphase field simulations with openphase. *Computer physics communications* 215, 173–187.
- Tikekar, M. D., L. A. Archer, and D. L. Koch (2014). Stability analysis of electrodeposition across a structured electrolyte with immobilized anions. *Journal of The Electrochemical Society* 161(6), A847–A855.
- Tran, R., X.-G. Li, J. H. Montoya, D. Winston, K. A. Persson, and S. P. Ong

- (2019). Anisotropic work function of elemental crystals. *Surface Science* 687, 48–55.
- Tran, R., Z. Xu, B. Radhakrishnan, D. Winston, W. Sun, K. A. Persson, and S. P. Ong (2016). Surface energies of elemental crystals. *Scientific data* 3(1), 1–13.
- Trembacki, B., E. Duoss, G. Oxberry, M. Stadermann, and J. Murthy (2019). Mesoscale electrochemical performance simulation of 3D interpenetrating lithium-ion battery electrodes. *Journal of The Electrochemical Society* 166(6), A923–A934.
- Valoen, L. O. and J. N. Reimers (2005). Transport properties of LiPF₆-based Li-ion battery electrolytes. *Journal of The Electrochemical Society* 152(5), A882.
- Vetter, K. J. (Ed.) (1967). *Electrochemical Kinetics*. Academic Press.
- Vignal, P., N. Collier, L. Dalcin, D. Brown, and V. Calo (2017). An energy-stable time-integrator for phase-field models. *Computer Methods in Applied Mechanics and Engineering* 316, 1179–1214. Special Issue on Isogeometric Analysis: Progress and Challenges.
- Vitos, L., A. Ruban, H. Skriver, and J. Kollár (1998). The surface energy of metals. *Surface Science* 411(1), 186–202.
- Wang, A., Q. Deng, L. Deng, X. Guan, and J. Luo (2019). Eliminating tip dendrite growth by lorentz force for stable lithium metal anodes. *Advanced Functional Materials* 29(25), 1902630.
- Wang, D., W. Zhang, W. Zheng, X. Cui, T. Rojo, and Q. Zhang (2016). Towards high-safe lithium metal anodes: Suppressing lithium dendrites via tuning surface energy. *Advanced science (Weinheim, Baden-Wuerttemberg, Germany)* 4(1), 1600168–1600168.

- Wang, K., P. Pei, Z. Ma, H. Chen, H. Xu, D. Chen, and X. Wang (2015). Dendrite growth in the recharging process of zinc–air batteries. *Journal of Materials Chemistry A* 3(45), 22648–22655.
- Wang, K., Y. Xiao, P. Pei, X. Liu, and Y. Wang (2019). A phase-field model of dendrite growth of electrodeposited zinc. *Journal of The Electrochemical Society* 166(10), D389.
- Wang, Q., B. Liu, Y. Shen, J. Wu, Z. Zhao, C. Zhong, and W. Hu (2021). Confronting the challenges in lithium anodes for lithium metal batteries. *Advanced Science* 8(17), 2101111.
- Wang, Q., G. Zhang, Y. Li, Z. Hong, D. Wang, and S. Shi (2020). Application of phase-field method in rechargeable batteries. *npj Computational Materials* 6(1), 1–8.
- Wheeler, D., J. Guyer, and J. Warren (2005, 2005-09-01). Fipy: A finite volume pde solver using python.
- Winter, M., B. Barnett, and K. Xu (2018). Before li ion batteries. *Chemical reviews* 118(23), 11433–11456.
- Wlasenko, A., F. Soltani, D. Zakopcan, D. Sinton, and G. M. Steeves (2010, Feb). Diffusion-limited and advection-driven electrodeposition in a microfluidic channel. *Phys. Rev. E* 81, 021601.
- Wu, X., G. J. van Zwieten, and K. G. van der Zee (2014). Stabilized second-order convex splitting schemes for Cahn–Hilliard models with application to diffuse-interface tumor-growth models. *International Journal for Numerical Methods in Biomedical Engineering* 30(2), 180–203.
- Xu, L., Z. Yu, and J. Zheng (2021). Dendrite-free lithium electrodeposition enabled by 3D porous lithiophilic host toward stable lithium metal anodes. *Oxford Open Materials Science* 1(1), itab013.

- Xu, R., S. Zhang, X. Wang, Y. Xia, X. Xia, J. Wu, C. Gu, and J. Tu (2018). Recent developments of all-solid-state lithium secondary batteries with sulfide inorganic electrolytes. *Chemistry—A European Journal* 24(23), 6007–6018.
- Xu, W., J. Wang, F. Ding, X. Chen, E. Nasybulin, Y. Zhang, and J.-G. Zhang (2014). Lithium metal anodes for rechargeable batteries. *Energy Environ. Sci.* 7, 513–537.
- Yan, C., X.-Q. Zhang, J.-Q. Huang, Q. Liu, and Q. Zhang (2019). Lithium-anode protection in lithium–sulfur batteries. *Trends in Chemistry* 1(7), 693–704.
- Yan, H., Y. Bie, X. Cui, G. Xiong, and L. Chen (2018). A computational investigation of thermal effect on lithium dendrite growth. *Energy Conversion and Management* 161, 193–204.
- Yang, C.-P., Y.-X. Yin, S.-F. Zhang, N.-W. Li, and Y.-G. Guo (2015). Accommodating lithium into 3D current collectors with a submicron skeleton towards long-life lithium metal anodes. *Nature communications* 6(1), 1–9.
- Yang, H., E. O. Fey, B. D. Trimm, N. Dimitrov, and M. S. Whittingham (2014). Effects of pulse plating on lithium electrodeposition, morphology and cycling efficiency. *Journal of Power Sources* 272, 900–908.
- Yang, X., Z. Wen, X. Zhu, and S. Huang (2005). Electrodeposition of lithium film under dynamic conditions and its application in all-solid-state rechargeable lithium battery. *Solid State Ionics* 176(11-12), 1051–1055.
- Yufit, V., F. Tariq, D. S. Eastwood, M. Biton, B. Wu, P. D. Lee, and N. P. Brandon (2019). Operando visualization and multi-scale tomography studies of dendrite formation and dissolution in zinc batteries. *Joule* 3(2), 485–502.
- Yurkiv, V., T. Foroozan, A. Ramasubramanian, R. Shahbazian-Yassar, and F. Mashayek (2018). Phase-field modeling of solid electrolyte interface (SEI) influence on Li dendritic behavior. *Electrochimica Acta* 265, 609–619.

- Zachman, M. J., Z. Tu, S. Choudhury, L. A. Archer, and L. F. Kourkoutis (2018). Cryo-stem mapping of solid–liquid interfaces and dendrites in lithium-metal batteries. *Nature* 560(7718), 345–349.
- Zhang, C., S. Liu, G. Li, C. Zhang, X. Liu, and J. Luo (2018). Incorporating ionic paths into 3D conducting scaffolds for high volumetric and areal capacity, high rate lithium-metal anodes. *Advanced Materials* 30(33), 1801328.
- Zhang, H. and Y. Qi (2022). Investigating lithium metal anodes with nonaqueous electrolytes for safe and high-performance batteries. *SUSTAINABLE ENERGY & FUELS* 6(4), 954–970.
- Zhang, H.-W., Z. Liu, L. Liang, L. Chen, Y. Qi, S. J. Harris, P. Lu, and L.-Q. Chen (2014, sep). Understanding and predicting the lithium dendrite formation in Li-ion batteries: Phase field model. *ECS Transactions* 61(8), 1–9.
- Zhang, J., Y. Liu, C. Wang, and H. Tan (2021). An electrochemical-mechanical phase field model for lithium dendrite. *Journal of The Electrochemical Society* 168(9), 090522.
- Zhang, R., X. Shen, X.-B. Cheng, and Q. Zhang (2019). The dendrite growth in 3d structured lithium metal anodes: Electron or ion transfer limitation? *Energy Storage Materials* 23, 556–565.
- Zhang, R., X. Shen, H.-T. Ju, J.-D. Zhang, Y.-T. Zhang, and J.-Q. Huang (2022). Driving lithium to deposit inside structured lithium metal anodes: A phase field model. *Journal of Energy Chemistry* 73, 285–291.
- Zhang, Y., T.-T. Zuo, J. Popovic, K. Lim, Y.-X. Yin, J. Maier, and Y.-G. Guo (2020). Towards better li metal anodes: challenges and strategies. *Materials Today* 33, 56–74.
- Zhang, Z., K. Smith, R. Jervis, P. R. Shearing, T. S. Miller, and D. J. Brett (2020). Operando electrochemical atomic force microscopy of solid–electrolyte

interphase formation on graphite anodes: the evolution of sei morphology and mechanical properties. *ACS applied materials & interfaces* 12(31), 35132–35141.

Zhao, Y., B. Zhang, W. Chen, H. Wang, M. Wang, and H. Hou (2018). Simulation for the influence of interface thickness on the dendritic growth of nickel- copper alloy by a phase-field method. *ES Materials & Manufacturing* 2, 45–50.

Zheng, G., S. W. Lee, Z. Liang, H.-W. Lee, K. Yan, H. Yao, H. Wang, W. Li, S. Chu, and Y. Cui (2014). Interconnected hollow carbon nanospheres for stable lithium metal anodes. *Nature nanotechnology* 9(8), 618–623.

Zheng, H., X.-G. Li, R. Tran, C. Chen, M. Horton, D. Winston, K. A. Persson, and S. P. Ong (2020). Grain boundary properties of elemental metals. *Acta Materialia* 186, 40–49.

Zheng, J., M. H. Engelhard, D. Mei, S. Jiao, B. J. Polzin, J.-G. Zhang, and W. Xu (2017, Mar). Electrolyte additive enabled fast charging and stable cycling lithium metal batteries. *Nature Energy* 2(3), 17012.

Zhu, B., Y. Jin, X. Hu, Q. Zheng, S. Zhang, Q. Wang, and J. Zhu (2017). Poly(dimethylsiloxane) thin film as a stable interfacial layer for high-performance lithium-metal battery anodes. *Advanced Materials* 29(2), 1603755.

Zhu, R., J. Feng, and Z. Guo (2019). In situ observation of dendrite behavior of electrode in half and full cells. *Journal of the Electrochemical Society* 166(6), A1107.

Every reasonable effort has been made to acknowledge the owners of copyright material. I would be pleased to hear from any copyright owner who has been omitted or incorrectly acknowledged.